University of Alberta

CHARACTERIZATION OF METAL AND SEMICONDUCTOR NANOMILLING AT NEAR THRESHOLD INTENSITIES USING FEMTOSECOND LASER PULSES

by

Sean Eric Kirkwood

©

A dissertation submitted to the Faculty of Graduate Studies and Research
in partial fulfillment of the requirements for the degree of:

Doctor of Philosophy

Department of Electrical and Computer Engineering
Edmonton, Alberta

Spring 2007

Library and Archives Canada

Published Heritage Branch

395 Wellington Street
Ottawa ON K1A 0N4
Canada

Bibliothèque et Archives Canada

Direction du Patrimoine de l'édition

395, rue Wellington
Ottawa ON K1A 0N4
Canada

Your file Votre référence
ISBN: 978-0-494-29699-8
Our file Notre référence
ISBN: 978-0-494-29699-8

NOTICE:
The author has granted a non-exclusive license allowing Library and Archives Canada to reproduce, publish, archive, preserve, conserve, communicate to the public by telecommunication or on the Internet, loan, distribute and sell theses worldwide, for commercial or non-commercial purposes, in microform, paper, electronic and/or any other formats.

The author retains copyright ownership and moral rights in this thesis. Neither the thesis nor substantial extracts from it may be printed or otherwise reproduced without the author's permission.

AVIS:
L'auteur a accordé une licence non exclusive permettant à la Bibliothèque et Archives Canada de reproduire, publier, archiver, sauvegarder, conserver, transmettre au public par télécommunication ou par l'Internet, prêter, distribuer et vendre des thèses partout dans le monde, à des fins commerciales ou autres, sur support microforme, papier, électronique et/ou autres formats.

L'auteur conserve la propriété du droit d'auteur et des droits moraux qui protège cette thèse. Ni la thèse ni des extraits substantiels de celle-ci ne doivent être imprimés ou autrement reproduits sans son autorisation.

In compliance with the Canadian Privacy Act some supporting forms may have been removed from this thesis.

While these forms may be included in the document page count, their removal does not represent any loss of content from the thesis.

Conformément à la loi canadienne sur la protection de la vie privée, quelques formulaires secondaires ont été enlevés de cette thèse.

Bien que ces formulaires aient inclus dans la pagination, il n'y aura aucun contenu manquant.

Canada

It's over. Now, where was I?

FOR

KATHLYN AND LIAM

Abstract

Two novel techniques were developed: nanomilling and direct writing of metal surfaces with self-assembled monolayers. This thesis first details the nanomilling of metal surfaces with 800 nm wavelength, femtosecond laser pulses and initial modeling of the microscopic processes in silicon. A careful study of the single shot ablation threshold for copper was carried out yielding an incident single-shot ablation threshold and a reduction in this ablation threshold for multiple shots consistent with an incubation phenomenon. A two-temperature model was used to model the single-shot ablation threshold by describing the coupling of the laser energy to the electron subsystem and the relaxation of this energy to the lattice subsystem through a temperature-dependent energy-coupling equation with a pre-factor commonly referred to as the *g*-parameter. The *g*-parameter was similar for all noble metals when the electron thermal conductivity was modeled using the plasma electron conductivity model. The plasma electron thermal conductivity resulted in the independence of the single-shot ablation threshold on pulse width below the electron-lattice thermal coupling time and the adequate prediction of the single-shot ablation threshold for copper.

Nanomilling to depths of less than 10 nanometers required determining the single-shot ablation threshold, incubation coefficient and surface reflectivity. These laser parameters established that surface nanomilling occurred close to the multiple-pulse ablation threshold. Photomultiplier tube measurements of atomic emission during the nanomilling process showed photons emitted once every several shots. The results were consistent with a model that ablation occurred in bursts after a number of intervening incubation energy storage shots.

A methodology was developed to manipulate the surface properties of a self-assembled monolayer (SAM) of alkanethiol on a gold film by using nanomilling. CW laser patterned SAM surfaces created minimum line widths of 4 μm. SAM patterning with femtosecond pulses achieved minimum line widths of (375 ± 25) nm.

A molecular dynamics simulation of silicon for femtosecond laser pulse ablation was extended to include an electron subsystem to model the avalanche ionization mechanism. The inclusion of avalanche ionization and a parametric study showed the potential of the model to predict the single-shot ablation threshold of silicon over a larger femtosecond pulse range.

Acknowledgements

Great colleagues and great friends have made these past seven years successful.

First to Dr. Bob Fedosejevs, your guidance goes beyond this thesis, though I am grateful for your help and constant humbling. Your extensive knowledge in physics has always been impressive and your diverse research projects in optics have given me an extensive knowledge in the field. I will always remember our conversation in Puebla.

To Dr. Ying Tsui, who has been my check and balance system in this work ensuring that I did not deviate too far from my objectives. Thank you for all your patience in my energetic mental riffings. You are right; I am an excitable person.

To Blair Harwood, your contribution cannot be weighed. You have been a great friend and a great teacher in the technical aspects of laser systems and optical design. I wish you all the best, you are a patient, caring and supportive person and I am definitely a better person for having known you.

To Dr. Alidad Amirfazli, I have enjoyed our collaboration and conversations, thank you very much for approaching our group with your project and to Dr. Reza Shadnam for your contributions. I would also like to thank Dr. David Wilson for the use of his laboratory in the earlier work of the SAM project.

To my lab mates, especially Dr. Matt Reid, James Gospodyn, Dr. Mike Taschuk and Mike Argument, who were great friends that made those "truthful" moments easier to handle. To the newer people who joined our lab that became good friends: Rick Conrad, Dr. Craig Unick, Roman Holenstein, Yogesh Godwal and Zahid Chowdhury, you made it easy to cope with dealing yourself a 13-spade hand that you ended up opening as 7 NT.

To the Campus Rec. group, and in particular to Mike Chow, for an excellent recreation program that embraces all level of "skill", especially our Laser Mob Unit. Your activities have helped keep many people fit and given us a stress outlet. Through your organization, I found a great group of friends outside of my academic sphere. To the most over-educated soccer team, Taps Thunderheads, thank you for taking on a relatively weak player and turning him into somewhat of a soccer player. Especially to Dr. Dave Bressler, Dr. Dan Barreda, Doug McFarlane, Matt Bryman and Jeremy Wakaruk, you have been great friends and I wish you and your growing families all the best.

I am thankful to the Natural Sciences and Engineering Research Council (NSERC), the Canadian Institute for Photonic Innovations (CIPI), the Informatics Circle of Research Excellence (iCORE), the Faculty of Graduate Studies and Research and the Department of Electrical and Computer Engineering for their funding support.

A special note of appreciation to Melissa Haveroen, Dr. Jon van Hamme, Roz Young and Nelson Young (thanks for helping with the MD project).

An important, final note of appreciation goes to my family for their love and support. To my wonderfully patient and caring wife, Dr. Kathlyn Kirkwood: she beat me to the finish but was still supportive while raising our newborn son Liam while I finished this thesis. And to our parents, this thesis could not have been completed without your help, and I am forever grateful for their help in this achievement.

Contents

1. Introduction 1
   - 1.1 Background 1
   - 1.2 Research objectives and thesis overview 2
   - 1.3 Contributions 4
2. Femtosecond Laser Pulse Heating and Ablation 5
   - 2.1 Femtosecond laser pulse interaction with noble metals 7
   - 2.2 Two-temperature model of femtosecond laser pulse interaction with metals 15
     - 2.2.1 Introduction 15
     - 2.2.2 TTM parameters 17
   - 2.3 Femtosecond laser pulse ablation of silicon 25
   - 2.4 Molecular dynamics modeling of femtosecond laser pulse ablation of silicon 30
3. Materials and Methods 46
   - 3.1 Experimental tools 46
     - 3.1.1 Femtosecond nanomilling and ablation threshold experiments 46
     - 3.1.2 CW laser patterning of self-assembled monolayers 51
   - 3.2 Materials 53
     - 3.2.1 Target samples and substrates 53
     - 3.2.2 SAM deposition chemicals 54
   - 3.3 Femtosecond laser experiment techniques 55
     - 3.3.1 Preliminary notes on Ti:Sapphire laser performance 55
     - 3.3.2 Initial steps in the femtosecond laser experiments 57
     - 3.3.3 Focal spot calibration 60

3.3.4 Femtosecond laser ablation threshold and incubation experiments.....62
3.3.5 Femtosecond laser pulse nanomilling.....63
3.3.6 Femtosecond laser pulse patterning of SAMs.....64
3.3.7 Reflectivity calibrations.....65
3.3.8 Transient reflection dynamics of incident femtosecond laser pulses...67
3.4 Patterning SAMs with the Argon ion laser.....69
3.5 SAM substrate preparation.....71
3.5.1 Patterning of SAMs with the Argon Ion laser.....71
3.5.2 Patterning of SAMs with femtosecond laser pulses.....72
4. Femtosecond laser pulse nanomilling of metal surfaces.....74
4.1 Determining the single-shot ablation threshold for a material using Gaussian spatially-shaped laser pulses.....74
4.2 Femtosecond laser pulse ablation threshold and incubation of copper.....77
4.3 Nanomilling copper surfaces.....82
4.4 Two-temperature modeling of femtosecond laser pulse interaction with metals.....86
4.4.1 Discretization of the TTM.....87
4.4.2 TTM results for the ablation threshold and nanomilling of copper.....90
4.5 Discussion.....94
4.6 Engineering application: Smart micromachining.....101
5. Laser patterning of metal surfaces with self-assembled monolayers.....102
5.1 Self-assembled monolayers of alkanethiols on metal surfaces.....103
5.2 Patterning metal surfaces with self-assembled monolayers by thermally-induced desorption.....109
5.3 Modeling thermally induced self-assembled monolayer desorption from thin gold film surfaces.....114
5.4 Patterning metal surfaces with self-assembled monolayers by femtosecond laser pulse nanomilling of thin gold film surfaces.....116
5.5 Discussion.....123
5.6 Engineering application: Self-assembled monolayer patterning of glass substrates with femtosecond laser pulses.....126

6. Femtosecond laser pulse ablation of silicon 128
6.1 Pulse dependent single-shot ablation threshold of silicon 129
6.2 Modeling femtosecond laser pulse ablation of silicon with molecular dynamics 134
6.2.1 Modeling avalanche ionization 134
6.2.2 Dynamics of conduction band electron generation in the avalanche MD simulation 137
6.3 Discussion 141
7. General Discussion 150
7.1 The nanomilling mechanism 150
7.2 Incubation and fatigue 152
7.3 Future experimental directions in nanomilling, incubation and fatigue 156
8. Conclusion 159
References 161
A. Discretization of the TTM 176
A.1 Formula development 176
A.2 Procedure for running the TTM 182
A.3 TTM filenames 182
B. Derivation of the Gaussian Beam Limiting Technique 185
C. Reporting of the ablation threshold and incubation coefficient 188
C.1 Error in the beam waist and the threshold energy for ablation 188
C.2 Error in the incubation coefficient 190
C.3 An example 191

List of Tables

Table 2.1: Thermophysical properties at room temperature of metals of interest in laser ablation and TTM 8

Table 2.2: L_{HAZ} during the laser pulse in laser machining using equation (2.1) and the room-temperature thermophysical properties of materials 9

Table 2.3: Optical properties of metals and ballistic electron range for typical laser wavelengths 10

Table 2.4: Published incident ablation threshold fluences, $\phi_{th,inc}$, and incubation coefficients for noble metals 13

Table 2.5: Experimentally derived and theoretically calculated electron-phonon coupling coefficients (g-parameter) for metals 22

Table 2.6: Published, experimentally measured, incident single-shot ablation thresholds of silicon. 28

Table 2.7: Published, theoretically derived, absorbed single-shot ablation thresholds of silicon. 35

List of Figures

Figure 2.1: Example of the temperature dynamics of the electron and lattice subsystems from interaction with a femtosecond laser pulse over several picoseconds 6

Figure 2.2: Example of the ablation threshold for a metal with a single-shot ablation threshold of 1 J/cm^2 and an incubation coefficient of 0.80 15

Figure 2.3: Electron thermal conductivity of copper calculated using the proportional and plasma electron thermal conductivity models 20

Figure 2.4: Comparison of the full equation and the approximation of the energy coupling equation in the TTM 23

Figure 2.5: HF-MD simulation of the single-shot ablation threshold of silicon with 800 nm wavelength, femtosecond laser pulses as compared with experimental results reported in the literature 33

Figure 2.6: HF-MD simulation of the single-shot ablation threshold of silicon with 800 nm wavelength, femtosecond laser pulses as compared with theoretical results reported in the literature 34

Figure 2.7: Impact ionization rate of conduction band electrons for silicon calculated using collisional integrals and the Keldysh ionization rate 43

Figure 3.1: Block diagram of the femtosecond laser system with the energy selection optics, pulse width characterization and spatial characterization 47

Figure 3.2: Example of the beam profile measured on the SP-980 CCD camera in the equivalent focal plane system 49

Figure 3.3: Circuit diagram of the biasing of the FND-100 silicon photodiodes 50

Figure 3.4: Schematic of the SAM microscope slide mount 52

Figure 3.5: Polarization of the main pulse and the pre-pulse from the output of the Ti:Sapphire laser 56

Figure 3.6: Contrast ratio of the Ti:Sapphire laser after the half-wave plate and Glan polarizer 57

Figure 3.7: Experimental setup for nanomilling and femtosecond SAM laser patterning 58
Figure 3.8: General experimental setup for measuring the specular reflectivity 65
Figure 3.9: Setup for measuring the diffuse reflectivity 67
Figure 3.10: Experimental setup measuring the transient reflectivity of a laser pulse incident on a target with a specular reflective surface 67
Figure 3.11: Experimental setup for the CW Ar^+ direct laser writing of SAMs 70
Figure 4.1: SEM images of GF copper foil ablation spots 78
Figure 4.2: An example of the determination of the major and minor axes diameter and energy ablation threshold of GF copper foil for 1- and 10-shot ablation spots measured by SEM 79
Figure 4.4: Determination of the ablation threshold for the 250 nm copper thin film for 1, 5 and 20 shots measured by SEM 81
Figure 4.5: Nanostructured surface profiles measured by optical interferometric profilometry 84
Figure 4.6: White light interferometric profilometry measurement and PMT traces of nanomilled results 85
Figure 4.7: Illustration of the heated region by an ultrashort laser pulse modeled by the TTM 87
Figure 4.8: Discretization of the one-dimensional TTM in space and time 88
Figure 4.9: TTM results for copper using the proportional electron thermal conductivity heated by a 800 nm, 130 fs FWHM Gaussian-shaped laser pulse at 93.54 mJ/cm^2 (absorbed) with $g = 10 \times 10^{16}$ W/(m^3·K) 91
Figure 4.10: TTM results for copper using the plasma electron thermal conductivity for copper heated by a 800 nm, 130 fs FWHM Gaussian-shaped laser pulse at 60.7 mJ/cm^2 (absorbed) with $g = 3 \times 10^{16}$ W/(m^3·K) 93
Figure 4.11: Prediction of the absorbed single-shot ablation threshold for copper using the PTS-TTM 94
Figure 5.1: Schematic representation of a 1-hexadecanethiol monolayer coating on a thin gold film surface 104
Figure 5.2: The SAM system with the thiol chemically bound to a gold-coated glass substrate 110
Figure 5.3: An OM image of gold film damage by overheating the glass slide 111
Figure 5.4: SEM images of two regions scanned with a +10 cm lens 111
Figure 5.5: An OM image of a 70 μm wide hydrophilic line written with a 90 mW Ar^+ beam focused by a +10 cm BK7 plano-convex lens 112
Figure 5.6: SAM line widths created by scanning the focal spot of a CW Ar^+ laser at 200 μm/s to induce thermal desorption 113

Figure 5.7: SAM line widths created by scanning the focal spot of a CW Ar^+ laser at 200 μm/s compared to the steady-state thermal model 115

Figure 5.8: Schematic of the mechanism differences between the two SAM laser patterning techniques 117

Figure 5.9: Determination of the ablation threshold of GF gold foil for 1, 10 and 1000 shot ablation measured by SEM 119

Figure 5.10: Determination of the ablation threshold of a 30 nm thin gold film with the hydrophobic monolayer surface for 1, 10, 100 and 1000 shot ablation measured by SEM 120

Figure 5.11: SEM image of a region on the gold-coated substrate scanned with an incident peak fluence of 150 mJ/cm^2, a repetition rate of 1 kHz and a scanning speed of 50 μm/s 121

Figure 5.12: Sub-micrometer line widths of SAMs on gold-coated substrate using NIR femtosecond laser pulse nanomilling 122

Figure 6.1: WLI images of intrinsic silicon ablation spots. 130

Figure 6.2: Enhancement of the WLI image of Figure 6.1(c) to expose the region on the native oxide silicon sample labeled as B in Figure 6.1(a and c).. 131

Figure 6.3: Line out of an ablation spot made on the intrinsic silicon with a native oxide measured using the WLI 131

Figure 6.4: Close up of the rim of the ablation spot made on the intrinsic silicon with a native oxide measured using the WLI 132

Figure 6.5: Determination of the single-shot ablation threshold for intrinsic and p-type silicon with femtosecond pulse widths at 800 nm 134

Figure 6.6: Plot of the avalanche MD simulation with the experimental single-shot ablation thresholds for different silicon wafers 137

Figure 6.7: Strength of the conduction band electron generation mechanisms during the laser pulse in the avalanche MD simulation near the single-shot ablation threshold at 41 fs, 83 fs, 166 fs and 333 fs Gaussian FWHM pulse widths 138

Figure 6.8: Conduction band electron density in the avalanche MD simulation volume for a 41.6 fs Gaussian FWHM pulse with an absorbed fluence of 100 mJ/cm^2 140

Figure 6.9: Conduction band electron density in the avalanche MD simulation volume for a 333 fs Gaussian FWHM pulse with an absorbed fluence of 330 mJ/cm^2 141

Figure 6.10: Transient reflectivity of the 800 nm, 140 fs to 150 fs FWHM Gaussian main pulse from silicon measured over a range of incident peak fluences for (upper graph) p-type silicon and (lower) BOE etched intrinsic silicon 142

Figure 6.11: Absorption coefficient of silicon from the Drude model modified dielectric constants with a Drude dampening time of 1 fs and the approximation of the FCA contribution from the two approximations at the 800 nm wavelength 148

Figure C.1: Example of an energy calibration curve for a photodiode and beam waist measurement for a 100 nm thin copper film sample used in the nanomilling experiments.....191

Abbreviations, Variables and Units

Abbreviations

AFM	Atomic force microscope (or microscopy)
AOI	Angle of incidence
BOE	Buffered oxide etch
CCD	Charge-coupled detector (or device)
CW	Continuous-wave
e^-	electrons (used in units)
ECE	Department of Electrical and Computer Engineering
EP	Electric probe
ESEM	Environmental SEM (see SEM)
evap	Evaporated thin film
FCA	Free-carrier absorption
FWHM	Full width at half maximum
GBLT	Gaussian beam limiting technique
GF	Goodfellow [1]
HAZ	Heat-affected zone
HF-MD	MD simulation with Langevin heat-flow dynamics (see MD)
MD	Molecular dynamics
MecE	Department of Mechanical Engineering
n/a	Not available (or not applicable)
NanoFab	Nanofabrication Facility in the ECE Dept. at the U of A
NG	Neutral glass (Schott filters for visible wavelengths) [2]
NIR	Near-infrared
NIST	National Institute for Standards and Technology
OM	Optical microscope (or microscopy)
PDMS	polydimethylsiloxane
PTFE	polytetrafluoroethylene
PMT	Photomultiplier tube
PTS	Parabolic two-step
QCM	Quartz crystal microbalance
ref.	reference
SAM	Self-assembled monolayer
SEM	Scanning electron microscope (or microscopy)
STM	Scanning tunneling microscope (or microscopy)
SW	Stillinger-Weber (potential function in MD)
TOF	Time-of-flight
TPA	Two-photon absorption
TTM	Two-temperature model
U of A	University of Alberta
UV	Ultraviolet
UVGSFS	UV-grade synthetic fused silica
WLI	White light interferometer (interferometry)
x-tal	crystal/crystalline

Variables: Greek

α	general absorption coefficient (m^{-1})
α_{FCA}	free-carrier absorption coefficient (m^{-1})
α_0	linear absorption coefficient (m^{-1})
β	two-photon absorption coefficient (cm/GW)
γ	Sommerfeld parameter ($J/[m^3 \cdot K^2]$)
ε_0	permittivity of free space (F/m)
ε_R	real part of the dielectric constant
ε_I	imaginary part of the dielectric constant
$\eta(E)$	electric-field dependent avalanche coefficient
λ	wavelength (m)
ϕ_{pk}	peak fluence (J/cm^2)
$\phi_{th}(1)$	single-shot ablation threshold (J/cm^2)
$\phi_{th}(N)$	N-shot ablation threshold (J/cm^2)
κ_0	thermal conductivity coefficient (W/[m·K])
μ_h	hole mobility (m/[V·s])
μ_e	electron mobility (m/[V·s])
ν_{eff}	effective collision frequency
ξ	incubation coefficient (unitless)
ρ	density (kg/m^3)
τ_{coll}	collision time (s)
τ_p	laser pulse width (s)
ω_L	laser angular frequency (rad/s)
ω_{pe}	electron plasma frequency (rad/s)

Variables: Roman

C_e	electron heat capacity ($J/[m^3 \cdot K]$)
C_L	lattice volumetric heat capacity ($J/[m^3 \cdot K]$)
c_0	vacuum speed of light (m/s)
D	diffusivity (m^2/s)
D_{Rsq}	normalized beam diameter (unitless)
E	electric field
e	charge (C)
g	g-parameter (W/[m·K])
h	Planck's constant
k	extinction coefficient
k_{AR}	ablation rate absorption depth
k_B	Boltzmann's constant
I	intensity (W/m^2)
m_e	electron rest mass (kg)
m_{opt}	optical or effective mass of the electron (kg)
N	number of laser pulses
N_{crit}	critical electron density (e^-/cm^3)
n	index of refraction

n_{CB}	conduction band electron density (e^-/cm^3)
n_e	density of electrons (e^-/cm^3)
n_{VB}	valence band electron density (e^-/cm^3)
$O(\Delta i)$	order of the equation for variable i
pk	peak
R	reflectivity
T	temperature (K)
T_D	Debye temperature (K)
T_e	electron temperature (K)
T_F	Fermi temperature (K)
U_i^n	finite-difference lattice temperature in TTM (K)
U	energy (J or eV)
U_F	Fermi energy
U_G	band gap energy (eV)
U_I	ionization energy (eV)
w	laser beam waist (m)

Units and Constants

All the units in this thesis, with a couple of exceptions and unless otherwise specified, are in Système Internationale (SI) or meter-kilogram-second (MKS) units. Units that are not SI are used for their familiarity and ubiquitous use in the literature. One unit in this thesis that does not conform to SI is Torr for reporting vacuum pressures. The SI unit for vacuum pressure is the Pascal (Pa) but is often reported in bar or Torr.

Some important relationships are listed below:

760 Torr = 1.01293 bar = 101.293 kPa	
1 eV = 1.2398 μm [3]	energy associated with wavelength
1 eV = 1.6022×10^{-19} J [3]	energy in Joules associated with 1 eV
1 eV = 11 604 K	temperature associated with 1 eV
$N_{crit} = 1.11 \times 10^{21}/\lambda_{\mu m}^2$ cm^{-3}	critical plasma electron density for an electron mass of m_e

The symbols and values used for the fundamental constants and the significant digits used throughout the calculations in this thesis are from the NRL Plasma Formulary [3] and repeated here for the benefit of the reader.

$c_0 = 2.9979 \times 10^8$ m/s	speed of light in a vacuum
$\varepsilon_0 = 8.8542 \times 10^{-12}$ F/m	permittivity of free space
$e = 1.6022 \times 10^{-19}$ C	charge
$h = 6.6261 \times 10^{-34}$ J·s	Planck's constant
$k_B = 1.3807 \times 10^{-23}$ J/K	Boltzmann's constant
$m_e = 9.1094 \times 10^{-31}$ kg	rest mass of the electron

Chapter 1

Introduction

1.1 Background

Precision micromachining has been an active research topic with the availability of commercial femtosecond laser sources. Qualitative studies have shown that metals ablated with femtosecond laser pulses have limited residual damage features as a result of the interaction, allowing for precision drilling of metals and ceramics [4]. Metals can be structured on nanometer length scales into gratings [5], complex patterns like medical implants [6], and sub-wavelength features [7]. Much of the research and industrial focus in precision laser micromachining has been to eliminate collateral damage features and optimize the lateral feature sizes to the nanometer scale.

Laser micromachining of surfaces for nanotechnology applications requires the controlled removal of nanometer-scale size *surface layers* from a material substrate with little subsurface damage. The ablation threshold intensity, the ablation rate in the near threshold intensity regime, the incubation of damage through multiple laser pulses and the resultant surface morphology all need to be investigated when nanomilling metal, semiconductor and dielectric surfaces. In many cases, the ablation threshold is equivalent to the damage threshold.

High precision laser interaction with materials can be achieved with femtosecond laser pulses since little detrimental feedback occurs during their interaction with the

surface. The coupling of energy from the electronic subsystem to the lattice occurs on the picosecond time scale and longer pulse widths enhance the propagation of the heat into the bulk creating a region called the heat-affected zone (HAZ). If the pulse width of the laser is nanoseconds long, then the laser pulse can interact with the evolving plasma plume from the surface and drive the plasma to higher temperatures that result in additional pressure acting on the molten surface leading to spallation.

Metal surface nanomilling using femtosecond laser pulses is a more controlled technique that requires investigation into the laser interaction parameters dependent upon one or more pulses at near-threshold energy densities. Surface material removal at intensities near the ablation threshold can be controlled to remove material at an effective rate of sub-nanometers with each laser shot using near-infrared (NIR) femtosecond laser pulses. Understanding this phenomenon and controlling the parameters at the nanometer level is required for applications in fine tuning device operation on the sub-micrometer scale. For example, microelectronic devices, microelectromechanical systems and interdigitated surface acoustic wave devices can be tuned to exact operating parameters or frequencies by adjusting their size or adjusting the mass of the metal electrodes.

1.2 Research objectives and thesis overview

The goal of the thesis was to demonstrate nanomilling, defined as precision micromachining into the depth of the material to less than 10 nm with no restriction on the lateral feature sizes. When this work began, this depth resolution was yet to be realized in femtosecond laser interaction research. I expected that the single-shot ablation threshold, $\phi_{th}(1)$, and the incubation coefficient, ξ, would be the main control variables in nanomilling. Copper was chosen as the main substrate since it is a commonly used material in technological devices. Careful characterization of its ablative properties was undertaken in this study.

Temperature dynamics have been modeled using the two-temperature model (TTM), a set of coupled partial differential equations that has been used in femtosecond laser pulse interaction studies with metals for decades [8]. This model predicts the single-shot ablation threshold by using the melting temperature as the predictor for the threshold. The temperature dynamics in metals is also an important feature in examining

the incubation phenomenon so numerical modeling has been carried out in this work. Temperature dynamics in femtosecond pulse patterning of self-assembled monolayers (SAMs) on thin gold film surfaces was also important since the heating rates may determine the removal pathway. The use of the noble metals, copper and gold, makes the modeling straight-forward due to their simpler electron dynamics.

Temperature dynamics provides a macroscopic model of the heating and ablation process in metals but microscopic particle dynamics would provide more information on the restructuring of the lattice and particle removal, useful for insight into the incubation phenomenon during femtosecond laser ablation. An initial approach was carried out in adapting an existing molecular dynamics (MD) simulation for silicon to include an electronic subsystem to model avalanche ionization. The electronic subsystem dynamics was required before modeling a metal with MD.

The thesis is divided into five main parts. The first part is a review chapter of the physics and literature leading up to the proposed research project. The next part is a chapter on materials and methods, giving a detailed account of the major experimental techniques used to demonstrate that nanomilling can be done on metal surfaces using NIR femtosecond laser pulses.

The third part is the development of metal surface nanomilling and its applicability in engineering the surface layer. This part is broken into two chapters with the first chapter detailing the experiments and calibrations necessary to nanomill a copper surface as the test standard. Two-temperature modeling explores the temperature dynamics of nanomilling and shows the ability of the model to predict the single-shot ablation threshold and the scaling of the threshold with the laser pulse width.

The next chapter details the development of a novel nanometer-scale gold surface patterning technique using a continuous-wave (CW) laser and SAMs. SAMs are used to alter the surface properties of a metal. The end product of this work was to create barrier-free microfluidic channels defined as the confinement of a liquid by surface wetting without physical walls. The reduction of the channel widths to the nanometer scale to create sub-diffraction limited SAM line widths is developed with nanomilling.

The fourth part is an initial study to adapt an MD simulation of silicon to provide insight into the particle dynamics in nanomilling. The milestone of this chapter was the

development of an electronic subsystem as an initial step to modeling femtosecond metal interactions at nanomilling laser intensities.

The final part is a general discussion that hypothesizes on the dynamics of nanomilling from the results presented in the thesis and proposes a mechanism for incubation, the mechanism inherent to nanomilling.

1.3 Contributions

The thesis presents two novel techniques in the field of laser-matter interactions. Controlled nanomilling of metal surfaces to depths of less than 10 nm was realized experimentally using near-infrared femtosecond laser pulses at near-ablation-threshold intensities [9]. CW laser patterning for heterogeneous metal surface functionality using SAMs is the second novel technique presented in this thesis [10-12].

Over the course of this research, I have published the results of a single-shot ablation threshold study on copper surfaces [13] that clarified the spread reported in the literature. Knowledge of the single-shot ablation threshold was a key parameter in nanomilling metal surfaces. The nanomilling technique was presented the Conference on Laser Ablation (COLA) in Banff, Alberta, 2005 and was accepted for publication [9]. Initial results in the adaptation of an MD simulation of silicon to include electron dynamics for the first time, for the development of a microscopic nanomilling model, were presented at COLA 2005.

The CW direct laser surface patterning technique using SAMs, developed to create barrier-free microfluidic channels in collaboration with researchers in the Mechanical Engineering Department (MecE) at the University of Alberta (U of A), was first presented at the International Conference on MEMS, Nano and Smart Systems (ICMENS) in Banff, Alberta, 2003 and published in the associated conference journal [10]. Follow-up theoretical work done by our collaborators was published in Langmuir [11] and the Journal of Physical Chemistry B [12]. This technique was further developed in our laboratory to create sub-diffraction limited features using nanomilling and presented at COLA 2005 and was accepted for publication in the associated refereed conference publication [14].

Chapter 2

Femtosecond Laser Pulse Heating and Ablation

Extensive reviews exist on laser matter interactions and I refer you to such references [15, 16] for further discussions on the material presented in this section since the review given here is not a complete overview of material already discussed adequately in the literature.

In short, the physics of interaction between an NIR femtosecond laser pulse and a metal surface initiates with the photon energy being transferred to the conduction band electrons. The electrons absorb the energy through collisions with other electrons, forming a distribution in tens of femtoseconds that represents a temperature increase of the electronic subsystem. After the laser pulse, the electron energy relaxes to the lattice atoms through collisions at a transfer rate defined by the properties of the lattice.

Electrons have a very small heat capacity and a very large thermal conductivity as compared to the lattice. The temperature rise of the electrons is quite high for femtosecond interactions, usually several thousand Kelvin, and the high conductivity means the heat eventually propagates several hundred nanometers into the substrate with a majority of the energy coupled from the laser beam occurring in the optical penetration depth of a few tens of nanometers. The lattice atoms have a high heat capacity and low conductivity compared to the electrons, so the energy coupled from the electrons does not result in a very large temperature increase. These dynamics can be seen in Figure 2.1.

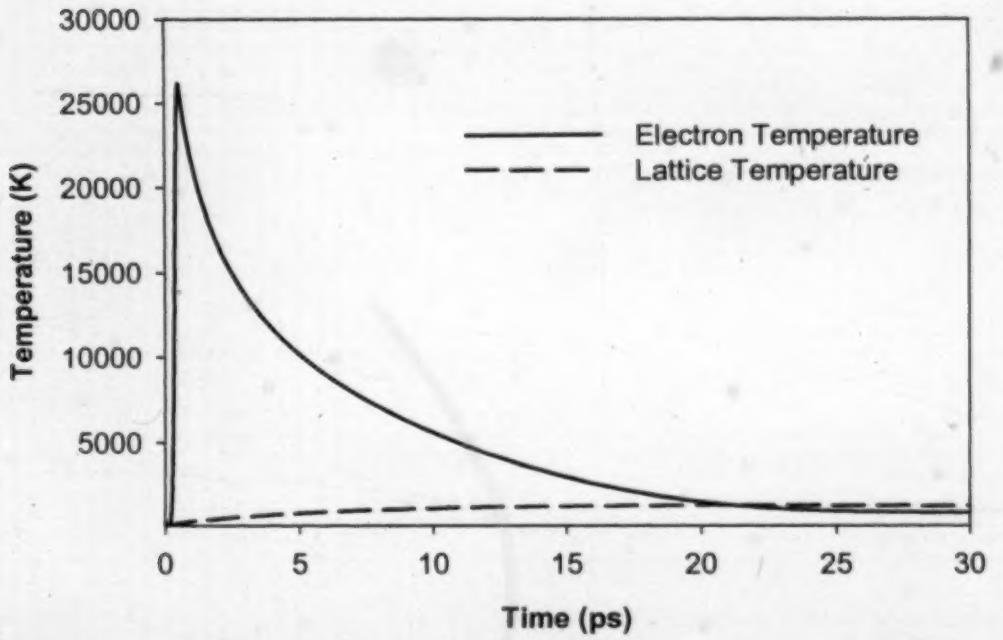

Figure 2.1: Example of the temperature dynamics of the electron and lattice subsystems from interaction with a femtosecond laser pulse over several picoseconds.

If the temperature of the electrons exceeds the work function of the metal, then electrons can leave the surface and a positively charged region will remain. The work function of the noble metals is usually about 5 eV (about 58 000 K) so it takes a significant amount of laser energy to reach this electron temperature. Whether the remaining positively charged material is neutralized by the nearly infinite electrical conductivity of the metal with free electrons shielding the charge or whether the charged cores repulse each other leading to Coulomb explosion is currently debated in the field of femtosecond laser pulse ablation. The latter phenomenon has been observed in semiconductors and dielectrics where the conductivity is not sufficient to neutralize the ionic cores before the ions respond to the force of Coulomb repulsion.

The high electron temperatures that can be reached may be enough to melt or vapourize the metal once all the electron energy has coupled to the lattice. Extremely high electron temperatures that lead to lattice temperatures above the melting and vapourization temperatures is called "superheating" because the material is relatively

cold when all the energy has been coupled to the electron subsystem. The thermal energy contained in the electrons can be sufficient to reach lattice temperatures that induce melting and eventually plasma formation. If the electron temperatures are not high enough to reach melting or vapourization, then the metal will heat up, expand, and recrystallize as though heated by conventional sources, but at a much higher rate.

Semiconductors have the same laser coupling pathways when heated by NIR laser pulses except that semiconductors do not have a high density of conduction band electrons as do metals. The low conduction band electron density gives semiconductors a long optical absorption depth at NIR wavelengths and requires more *absorbed* energy than metals to lead to melting, vapourization and plasma formation. Femtosecond laser pulses have the intensity to be very efficient free electron generators in semiconductors and dielectrics. To generate conduction band electrons that lead to heating, electrons are promoted from the valence band by multiphoton absorption, which decreases the absorption depth. Subsequent heating comes from electron-electron collisions (or Joule heating) of the conduction band electrons.

Femtosecond laser pulses are useful material diagnostic systems since they do not interact beyond the electron subsystem. If the pulse width gets longer than a picosecond, then heating of the lattice occurs during laser interaction leading to motion and coupling to lattice atoms and ions. If the pulse width is longer than several picoseconds, then the laser pulse interacts with the developing plasma that forms from intense heating of the metal, heating the plasma further and driving shock waves back into the material. The absence of these effects is why femtosecond laser pulses are seen as a high precision tool for manufacturing precision devices on the micrometer and nanometer scale.

2.1 Femtosecond laser pulse interaction with noble metals

Within the transition metals, copper, silver and gold are the only metals that have a full *d*-shell and the Fermi surface passing through the *s*-shell [17] and are referred to as the noble metals [18-20]. The electronic structure for each metal is:

Cu: [Ar] $3d^{10}\ 4s^{1}$
Ag: [Kr] $4d^{10}\ 5s^{1}$
Au: [Xe] $4f^{14}\ 5d^{10}\ 6s^{1}$

This structure results in noble metals having free electrons that do not interact very well with the bound electrons (*d*-shell electrons), that are weakly scattered by the lattice vibrations [19], and that are simple to model because the Fermi surface passes through the spherical *s*-shell; parabolic band structures are used to approximate the energy of the free electrons [21]. The free electrons in the noble metals can travel more easily than in other metals where the Fermi surface passes through the more complex bands. The physical properties of the noble metals and other metals in the periodic table are shown in Table 2.1.

Table 2.1: Thermophysical properties at room temperature of metals of interest in laser ablation and TTM [19, 22, 23].

Metal	Atomic Weight (amu)	ρ (g/cm^3)	γ (J/[m^3·K^2])	κ_0 (W/[m·K])	C_L (J/[cm^3·K])	T_{melt} (K)	T_D (K)	U_F (eV)
Cu	63.546	8.96	98.1	401	3.44	1357.8	343	7.04
Ag	107.87	10.5	62.9	429	2.47	1234.9	225	5.48
Au	196.97	19.3	71.4	317	2.49	1337.3	165	5.53
Al	26.98	2.70	135	237	2.42	933	428	11.66
Ti	47.88	4.51	316	21.9	2.35	1940	420	---
Cr	52.00	7.15	190	93.7	3.23	2180	630	---
Fe	55.85	7.87	702	80.2	3.53	1811	470	11.15
Ni	58.69	8.90	1060	90.7	3.96	1728	450	11.74
W	183.84	19.3	136	174	2.55	3687	400	---
Pt	195.08	21.5	750	71.6	2.86	2041.4	240	---

ρ is the density of the metal, γ is the Sommerfeld parameter, κ_0 is the electron thermal conductivity, C_L is the lattice volumetric heat capacity, T_{melt} is the melting temperature, T_D is the Debye temperature and U_F is the Fermi energy

Aluminum, a main group metal, and the other transition metals have electron thermal conductivities consistently smaller than the noble metals, demonstrating that the electrons in the noble metals travel more freely. The Sommerfeld parameter, γ, used as a measure of the thermal mass of the electron, shows that the noble metals have lighter electrons that are closer to the rest mass than in the other metals.

Laser machining of metals usually results in a significant HAZ, which is the result of a thermal field driven by interaction with a laser field. The HAZ is dependent on the

laser pulse width and the extent of this zone in metals can be several micrometers because of the high thermal diffusivity, D, of metals shown in equation (2.1) below:

$$L_{HAZ} \approx 2\sqrt{D\tau_p} = 2\sqrt{\frac{\kappa_0}{C_L}\tau_p} \quad \text{(m)} \tag{2.1}$$

where κ_0 is the electron thermal conductivity, ρ is the density, C_L is the lattice volumetric heat capacity and τ_p is the laser pulse width. The factor of two is a geometric factor for a spatial point source in an infinite medium and is most often used to get the 1 e-folding ($1/e$) length of the HAZ (p.20 in ref. [15]). In Table 2.2, the advantage of *femtosecond* pulse laser machining of metals is evident since the length of the HAZ extends less than 1 μm, allowing for high quality results with limited modification outside the machining region compared to longer pulse widths. The HAZ for other non-metallic material is calculated from the diffusivity given in Table II of ref. [15]. One should be careful, however, because the thermal interaction time may be significantly longer than the laser pulse length, particularly for ultrashort pulses.

Table 2.2: L_{HAZ} during the laser pulse in laser machining using equation (2.1) and the room-temperature thermophysical properties of materials; the data for the non-metallic materials are from ref. [15].

	D (cm^2/s)	L_{HAZ} by pulse width (nm) 1 ns	10 ps	100 fs
Cu	1.17	680	68	6.8
Ag	1.74	830	83	8.3
Au	1.27	710	71	7.1
Al	0.98	630	63	6.3
Ti	0.093	190	19	1.9
Fe	0.23	300	30	3.0
Pt	0.25	320	32	3.2
c-Si	0.85	580	58	5.8
SiO_2	0.086	180	18	1.8
PMMA	0.0011	21	2.1	0.21
PI	0.0008	18	1.8	0.18

PI is polyimide (Kapton™) and PMMA is polymethylmethacrylate

The *s*-shell conduction band of the noble metals and the limited interaction of the free electrons with the bound electrons and lattice leads to higher electron penetration depths than predicted by the optical skin depth. Electrons take longer to thermalize in noble metals resulting in longer penetration depths, called the ballistic absorption depth, δ_b [24-26]. Table 2.3 shows that the electron penetration depth of the ballistic electrons is greater than the optical skin depth for the noble metals, which then requires special treatment of energy transport as will be shown in Section 2.2.2 when discussing the source term in the TTM.

Table 2.3: Optical properties of metals and ballistic electron range for typical laser wavelengths [23]

λ	Reflectivity (%)				Skin Depth (nm)				δ_b	δ_b
(nm):	248	266	400	800	248	266	400	800	(nm)	Refs
Cu	36.6	33.7	48.8	96.3	11.1	12.6	14.9	12.6	70	[25]
Ag	25.7	24.7	84.4	96.6	14.5	16.0	15.2	11.4	142	[25]
Au	31.9	35.8	37.1	98.7	12.7	12.8	17.7	13.4	100	[27, 28]
Al	92.4	92.5	92.4	87.4	6.7	6.7	6.5	7.5	46	[25]
Ti	23.6	25.8	44.2	55.8	16.3	16.7	14.8	19.2	n/a	
Cr	54.2	59.1	68.2	63.4	9.8	9.5	9.0	14.7	14	[25]
Fe	43.5	47.1	58.0	59.3	10.6	10.5	10.5	17.4	n/a	
Ni	44.9	42.5	48.0	68.3	9.4	10.1	13.5	14.5	11	[25]
W	50.5	46.1	46.0	49.7	6.9	8.6	13.2	23.3	n/a	
Pt	37.2	40.8	55.5	71.1	11.2	11.0	11.2	12.9	n/a	

The reflectivity and optical skin depth is linearly interpolated from adjacent points if the value at the desired wavelength did not exist.

Nanomilling noble metals requires knowledge of specific parameters for laser ablation: the single-shot ablation threshold, the incubation coefficient (defines the decrease of the single-shot ablation threshold in multishot irradiation), the laser wavelength, λ, the laser pulse shape, the laser pulse width, the laser energy penetration depth, k, and absorption at the wavelength of interest. As seen in Table 2.1 and Table 2.3, the properties among the metals can vary significantly so noble metals were targeted for measuring and modeling the nanomilling process since they had similar properties. These laser ablation parameters determine the nanomilling regime and in this

thesis, the femtosecond ablation threshold of copper was the primary goal to understanding some of the controlling parameters for the interaction.

Many values for the ablation threshold of copper have been determined by a variety of experimental procedures. Extrapolation of ablation rates [29-34], measurement of emitted particles by electric probes (EP) [35] and time-of-flight (TOF) techniques [36, 37], and the Gaussian beam limiting technique (GBLT) pioneered by Liu [38] have been employed to experimentally determine the ablation threshold; however, except for recent ion and electron expulsion studies using TOF by Amoruso *et al.* [36, 37], all reported ablation thresholds for NIR femtosecond laser pulses were measured using multiple-shot interactions [30, 31, 33] yet the ablation threshold decreases with the number of laser shots [39]. The published ablation thresholds for copper and gold are presented in Table 2.4 and will be discussed further in Sections 4.5 and 5.5.

Laser surface milling, at first glance, would appear to be limited to a minimum depth defined by either the optical penetration depth of the metal (Table 2.3) or the extent of the HAZ (Table 2.2). Multiple-shot ablation threshold experiments, $\phi_{th}(N)$ where N is the number of incident pulses, indicate that the feature sizes are limited to the optical penetration depth at low fluences since the evolution of the depth of a crater scales with the incident fluence as shown below:

$$h = k_{AR} \ln\left(\frac{\phi_{pk}}{\phi_{th}}\right) \text{ (m)} \tag{2.2}$$

where h is the ablation depth per pulse (or ablation rate) and k_{AR} is the effective penetration depth. The ablation rate plotted against the incident peak fluence, ϕ_{pk}, provides a threshold value by extrapolation of the ablation rate to the abscissa.

Multiple-pulse laser drilling experiments on noble metals have shown two ablation regimes, referred to as the "gentle" and "strong" regimes, with respect to the incident fluence. In the "gentle" regime, just above the ablation threshold, the effective optical penetration depth was similar to the optical skin depth. In the "strong" regime the effective penetration depth was similar to the ballistic electron penetration depths (compare k_{AR} with values in Table 2.3, and see, for example, refs. [33, 40]). The fluence

dependence of the optical penetration depths indicates that the nanomilling regime, near the ablation threshold for noble metals, may be limited to depths similar to the optical penetration depth as shown in Table 2.4 for femtosecond pulse nanomilling in the NIR.

Although multiple-pulse laser drilling experiments indicate that the ultimate depth per pulse is limited to the optical penetration depths in the "gentle" regime, the reduction of the ablation threshold with the number of incident laser pulses attributed to the cumulative effect of thermal cycling in metals by nanosecond laser pulses [39] may be another pathway of material removal that could further reduce the ablation rate to achieve sub-optical skin depth results (below 10 nm). Repetitive nanosecond laser interaction with a metal was described as promoting the slip-line defect formation in metal surfaces similar to mechanical fatigue and the multiple-pulse ablation threshold allowed characterization of the incubation of damage. Incubation was observed as a reduction in ablation threshold for an increasing number of shots. This reduction was described by an incubation coefficient given as [39]:

$$\phi_{th}(N) = \phi_{th}(1) N^{\xi - 1} \quad (\mathrm{J/cm^2}) \tag{2.3}$$

If $\xi = 1$, then no incubation is observed. An increase in the observed incubation of damage shows as a decrease in ξ.

If the incubation effect with femtosecond laser pulses is a thermal cycling event, then it may be possible to interact in a region smaller than the optical skin depth since the temperature profile always has a maximum at the surface. The interaction region would occur very close to the ablation threshold. The effect of incubation is shown in Figure 2.2 where the change in the ablation threshold with respect to incident shot number is highlighted by plotting equation (2.3) with $\phi_{th}(1) = 1$ J/cm^2 and $\xi = 0.80$.

The most striking feature in Figure 2.2 is the rapid decrease in the ablation threshold over the initial 1000 pulses that appears to asymptotically approach the abscissa as though an ultimate ablation threshold exists, as has been assumed in studies on the ablation threshold for metals using the ablation rate. This expectation is likely the cause for lack of studies on the single-shot ablation threshold and incubation coefficient for femtosecond laser ablation as shown in Table 2.4.

Table 2.4: Published incident ablation threshold fluences, $\phi_{th,inc}$, and incubation coefficients for noble metals with the measurement error in brackets. The detection methods (Det. Method) column indicates whether EP, TOF, material reflectivity changes (R), QCM, the GBLT (XXX-1), where XXX defines whether AFM, SEM or OM was used to measure the crater diameters, or ablation rate (XXX-2) where additionally a stylus profilometer (SP) measures the crater depth were used.

Metal	(condition)	Thick. (μm)	Env.	λ (nm)	k_{AR} (nm)	τ_p	$\phi_{th,inc}$ (mJ/cm^2)	N	ξ	Det. Method	Ref.
Cu	poly x-tal	n/a	Air	248	n/a	23 ps	1800	1	n/a	EP	[35]
Cu	n/a	n/a	Air	248	n/a	23 ps	1130	> 1	n/a	AFM-2	[32]
Cu	n/a	n/a	10^{-5}	248	14.3	500 fs	170	n/a	n/a	SP-2	[29]
Cu	foil	127	Air	775	150	150 fs	580(50)$^{\blacklozenge}$	1	0.87	SEM-1	[41]
Cu	GF foil	1000	10^{-3}	780	57	14.4 ps	423	> 100	n/a	OM-2	[31]
Cu	GF foil	1000	10^{-3}	780	60	9.6 ps	375	> 100	n/a	OM-2	[31]
Cu	GF foil	1000	10^{-3}	780	65	7.6 ps	345	> 100	n/a	OM-2	[31]
Cu	bulk x-tal	n/a	10^{-5}	780	n/a	840 fs	1100†	> 1	n/a	SEM-2	[33]
Cu	bulk x-tal	n/a	10^{-5}	780	n/a	590 fs	1150†	> 1	n/a	SEM-2	[33]
Cu	bulk x-tal	n/a	10^{-5}	780	n/a	350 fs	950†	> 1	n/a	SEM-2	[33]
Cu	GF foil	1000	10^{-3}	780	10	150 fs	140	> 100	n/a	OM-2	[31]
Cu	GF foil	1000	10^{-3}	780	80	150 fs	460	~1000	n/a	OM-2	[31]
Cu	99.99% purity	n/a	10^{-7}	780	n/a	120 fs	$557_L(17)^{*\ddagger}$	1	n/a	TOF	[36]
Cu	99.99% purity	n/a	10^{-7}	780	n/a	120 fs	$854_H(26)^{*\ddagger}$	1	n/a	TOF	[36]
Cu	bulk x-tal	n/a	10^{-5}	780	n/a	120 fs	430	> 1	n/a	SEM-2	[33]
Cu	n/a	n/a	Air	780	0.01	70 fs	18	> 10^5	n/a	SP-2	[42]
Cu	n/a	n/a	Air	780	7	70 fs	220	> 128	n/a	SP-2	[42]
Cu	n/a	n/a	Air	780	80	70 fs	1000	> 1	n/a	SP-2	[42]
Cu	evap/fused silica	1	Air	1053	67	40 ps	172	1	n/a	SEM-1	[43]
Cu	(110) polished	n/a	Air	1064	n/a	10 ns	8000	1	0.92	SEM-1	[39]
Cu	(110) polished	n/a	Air	1064	n/a	10 ns	10 500	1	0.92	SEM-1	[39]
Cu	(110) polished	n/a	Air	1064	n/a	10 ns	11 300	1	0.92	SEM-1	[39]

Metal	(condition)	Thick. (μm)	Env.	λ (nm)	k_{AR} (nm)	τ_p	ϕ_{th} (mJ/cm^2)	N	ξ	Det. Method	Ref.
Cu	(110) polished	n/a	Air	1064	n/a	10 ns	12 700	1	0.92	SEM-1	[39]
Cu	n/a	n/a	10^{-6}	9300	n/a	ps	8000	> 100	n/a	R,OM-2	[44]
Ag	x-tal	n/a	10^{-5}	780	n/a	775 fs	1700†	>1	n/a	SEM-2	[33]
Ag	x-tal	n/a	10^{-5}	780	n/a	540 fs	1460†	> 1	n/a	SEM-2	[33]
Ag	x-tal	n/a	10^{-5}	780	n/a	350 fs	1360†	> 1	n/a	SEM-2	[33]
Ag	x-tal	n/a	10^{-5}	780	20	120 fs	93	> 1	n/a	SEM-2	[33]
Ag	x-tal	n/a	10^{-5}	780	102.5	120 fs	397	> 1	n/a	SEM-2	[33]
Ag	poly x-tal	n/a	Air	800	n/a	120 fs	140(4)*	1	n/a	R	[45]
Au	QCM	0.54	Ar	UV	n/a	26 ns	800(100)	n/a	n/a	QCM	[46]
Au	n/a	n/a	10^{-5}	248	47	500 fs	210	n/a	n/a	SP-2	[29]
Au	evap film	n/a	vac.	248	18(2)	500 fs	145	n/a	n/a	SP-2	[47]
Au	QCM	0.3	n/a	355	n/a	10 ns	600	n/a	n/a	QCM	[48]
Au	film/UVGSFS	0.03	n/a	400	n/a	200 fs	2.5§	7500	0.922	R	[49]
Au	QCM	0.3	n/a	532	n/a	10 ns	500	n/a	n/a	QCM	[48]
Au	x-tal	n/a	10^{-5}	780	n/a	750 fs	1700†	> 1	n/a	SEM-2	[33]
Au	x-tal	n/a	10^{-5}	780	n/a	550 fs	1460†	> 1	n/a	SEM-2	[33]
Au	x-tal	n/a	10^{-5}	780	n/a	325 fs	1200†	> 1	n/a	SEM-2	[33]
Au	99.99% purity	n/a	10^{-7}	780	n/a	120 fs	$470_L(14)^{*\ddagger}$	1	n/a	TOF	[36]
Au	99.99% purity	n/a	10^{-7}	780	n/a	120 fs	$570_H(18)^{*\ddagger}$	1	n/a	TOF	[36]
Au	x-tal	n/a	10^{-5}	780	n/a	120 fs	950†	> 1	n/a	SEM-2	[33]
Au	poly x-tal	n/a	Air	800	n/a	120 fs	189(6)*	1	n/a	R	[45]

* average value calculated from the published intensity threshold using the pulse width as a $1/e$ and a FWHM pulse width (since it was not indicated in the text) and the spread given in brackets

† measured in the "strong" ablation regime ($\phi_{th} > 1$ J/cm^2)

‡ 50° AOI with 'L' indicating Low threshold and 'H' High threshold of thermally excited plasma plume

§ absorbed fluence where scaling by reflectivity is inappropriate

♦ reflectivity of sample not known

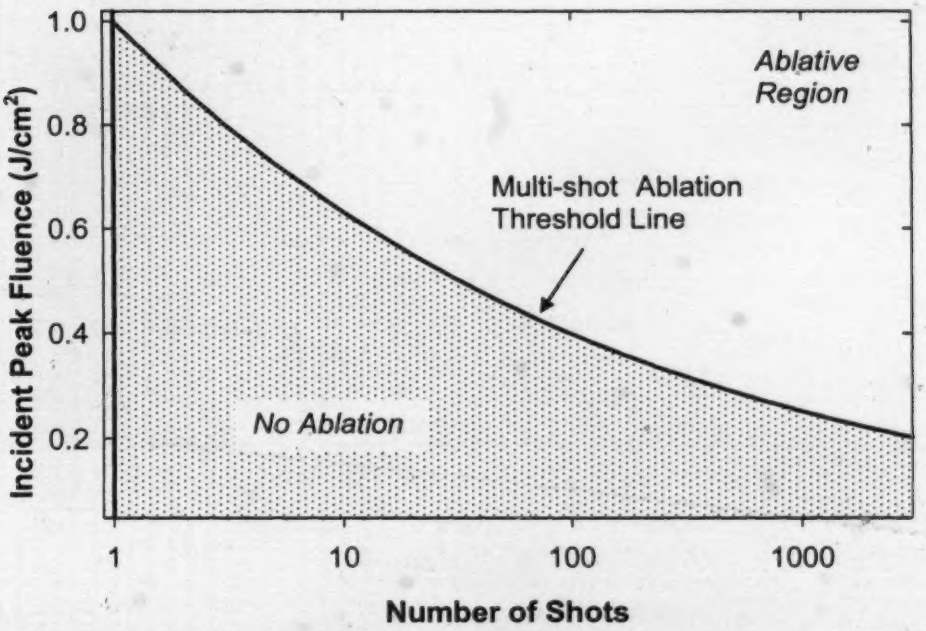

Figure 2.2: Example of the ablation threshold for a metal with a single-shot ablation threshold of 1 J/cm^2 and an incubation coefficient of 0.80.

The hypothesis in this thesis is that nanomilling occurs close to the multiple-shot ablation threshold line where the depth of interaction is close to the optical penetration depth of the metal. The main parameters for determining the multiple-shot ablation threshold line are the single-shot ablation threshold and the incubation coefficient as discussed. A theoretical model that can be used to compare the single-shot ablation threshold values for a noble metal is the TTM discussed in the following section.

2.2 Two-temperature model of femtosecond laser pulse interaction with metals

2.2.1 Introduction

Heating of a metal by a femtosecond laser pulse is often modeled using the TTM. The TTM is a coupled partial differential equation that describes the transport and relaxation of energy deposited by an ultrashort laser pulse to the electron subsystem that couples to the lattice subsystem of a metal. The model includes a coupling coefficient that quantifies the transfer of energy between the two subsystems. Overall, the TTM is a

formulation describing the *macroscopic* states of the electron and lattice subsystems by their individual temperatures given by:

$$C_e \frac{\partial T_e}{\partial t} = \frac{\partial}{\partial z}\left(\kappa(T_e, T_L)\frac{\partial T_e}{\partial z}\right) - g(T_e - T_L) + S(z,t)$$
$$C_L \frac{\partial T_L}{\partial t} = g(T_e - T_L) \tag{2.4}$$

where T_e is the electron temperature, T_L is the temperature of the lattice, C_e is the electronic heat capacity, C_L is the lattice heat capacity, $\kappa(T_e,T_L)$ is the temperature-dependent electron thermal conductivity, g is a coefficient describing the transfer of energy between the electrons and the lattice and S is the laser heating pulse source function. The z-axis is normal to the surface plane.

This formulation with two coupled parabolic partial differential equations is referred to as the parabolic two-step radiation heating model (PTS) in ref. [50] and referred to in this thesis as the PTS-TTM. The PTS-TTM is one of four formulations of macroscopic laser heating numerical methods described in ref. [50] with the conventional Fourier heating model with a laser source referred to as the parabolic one-step model.

The PTS-TTM of equation (2.4) is often attributed to Anisimov *et al.* [8] who used this model to demonstrate that the mechanism for the observed emission of electrons from a metal surface was dominated by the photoelectric effect over a small range of intensities. The model showed that above intensities of 10^{10} W/cm^2 for picosecond pulses the electron temperature, far out of equilibrium with the lattice, could approach the work function of a metal surface and the mechanism for electron emission would predominantly be that of thermionic emission.

The TTM assumes that the electron and lattice temperatures are out of equilibrium with each other due to the rapid heating of the electrons from interaction with an ultrashort laser pulse. The key concept in this model is the nonequilibrium temperature between the electron and lattice subsystems and the rate of energy transfer between the two subsystems. The energy transfer rate was developed by Kaganov *et al.* [51] to explain the deviation from Ohm's Law in the rapid heating of electrons in metals. Kaganov *et al.* formulated a rate equation to describe the amount of energy transferred to

the lattice subsystem from the heated electrons. The coefficient in the rate equation, $g(T_e - T_L)$, became known as the g-parameter and describes the rate of energy transfer to the lattice from the electrons.

2.2.2 *TTM parameters*

The first variable in the PTS-TTM is the electron heat capacity. This variable is often taken in the TTM to be linear in temperature [8]:

$$C_e = \gamma T_e \quad (\mathrm{J/[m^3 \cdot K]}) \tag{2.5}$$

where γ is the Sommerfeld parameter or the constant of electron heat capacity ($\mathrm{J/[m^3 \cdot K^2]}$), the former term is used to refer to this variable in this thesis.

This relationship was derived by assuming that the electrons form a degenerate non-interacting gas of free electron particles [19] that obey the Pauli exclusion principle. The Pauli exclusion principle allows only those electrons near the Fermi surface of a metal to gain energy by heating since the increase in energy requires a change in the density of states. Free states only exist above the Fermi level of any material and for an electron gas a small fraction of the electrons can participate in the heat capacity [22].

Equation (2.5) is only valid below the Fermi temperature, T_F, since the gas is assumed degenerate: two electrons can have the same orbital energy, but opposing spin states. The derivation on p.152 of ref. [22] gives a theoretical electron heat capacity of:

$$C_e = \left.\frac{dU}{dT}\right|_V = \frac{\pi^2}{2} N k_B \frac{T}{T_F} \tag{2.6}$$

where U is the kinetic energy of the system and the derivative is taken over a constant volume. The total number density of electrons is given by N [22].

The Sommerfeld parameter, usually associated with an experimentally measured heat capacity for a metal, does not agree completely with the constant terms in equation (2.6). The correction between the theoretical constant terms and the Sommerfeld parameter is done by giving the conduction band electrons in a metal a

thermal mass $m_{th} > m_e$. The increase in the effective mass of the electron is believed to be a result of interactions with the ion cores, phonon interaction and self-interaction in the gas, none of which have been accounted for in this model [22]. For the TTM, the experimentally derived Sommerfeld parameter is used in equation (2.5) and is considered valid as long as $T_e < T_F$.

In a metal, the electron thermal conductivity dominates over the lattice thermal conductivity. From the kinetic theory of gases, the thermal conductivity is:

$$\kappa = \tfrac{1}{3} C v l \tag{2.7}$$

where κ is the thermal conductivity, C is the heat capacity, v is the velocity of the particle and l is the mean free path. Using $T_F = \tfrac{1}{2}\, m v_F^2$ and substituting equation (2.6) for C, equation (2.7) becomes:

$$\kappa(T_e, T_L) = \frac{\pi^2 N k_B}{3 m_e} \tau_{coll}\, T_e = \kappa_0 \frac{T_e}{T_L} \quad \text{(W/[m·K])} \tag{2.8}$$

where τ_{coll} is an effective collision time provided $l = v_F \tau$ [22]. The collision time, taken as the collision between the electrons and ions, is assumed inversely proportional to the lattice temperature according to the Sommerfeld model for conductivity (p.18 in ref. [52]). This approximation leads to the common form of the electron thermal conductivity shown on the far right of equation (2.8), which I will refer to as the proportional electron thermal conductivity.

Equation (2.8) is valid for $T_e < T_F$ [22]; however, Anisimov *et al.* provided a more general solution for the electron thermal conductivity that they claimed was valid for all temperatures up to and above the Fermi temperature [53]:

$$\kappa(T_e, T_L) = \chi \frac{\left(\theta_e^2 + 0.16\right)^{5/4} \left(\theta_e^2 + 0.44\right) \theta_e}{\left(\theta_e^2 + 0.092\right)^{1/2} \left(\theta_e^2 + \eta \theta_L\right)} \quad \text{(W/[m·K])} \tag{2.9}$$

where $\theta_e = k_B T_e / U_F$ and $\theta_L = k_B T_L / U_F$, and χ and η are fitting parameters, which are 377 W/(m·K) and 0.139, respectively for copper [54]. When $\theta_e << 1$, $\kappa(T_e, T_L)$ takes on the form of equation (2.8). This equation will be referred to as the plasma electron thermal conductivity. This form of the electron conductivity with the hard constants 0.16, 0.44 and 0.092 is commonly used for metals in the TTM for femtosecond laser pulse ablation [33, 54, 55].

The evolution of the electron thermal conductivity with electron temperature, originally compared in ref. [55], is plotted for copper in Figure 2.3 and shows that the two models begin to differ when the electron temperature is only 2 % of the Fermi temperature (7.0 eV or 81 200 K for copper). The behaviour of the plasma electron thermal conductivity model conforms to the understanding that the electrons are sensitive to the lattice vibrations at low temperatures when the collisions are dominated by phonons [56] but as the temperature of the electron system increases, the effect of the phonons is diminished and the electron motion is dependent on electron-electron collisions. The shift in dependence is shown in Figure 2.3 when the electron thermal conductivity becomes independent of the lattice temperature at about 10 % of the Fermi temperature.

The next variable, the lattice heat capacity, is a constant in temperature for the PTS-TTM as predicted by the Debye model (Chapter 5 in ref. [22]). A constant lattice heat capacity is valid if the lattice temperature is above the Debye temperature, T_D, and this condition is satisfied for the noble metals, although the initial temperature of 300 K in the PTS-TTM is slightly below the Debye temperature for copper (Table 2.1). Closer inspection of the temperature dependence of the lattice heat capacity showed that as long as the lattice temperature of the metal is above approximately 0.7 T_D, the constant lattice heat capacity is still close to the asymptotic value (Figure 7 in Chapter 5 of ref. [22]). A temperature of 0.7 T_D is near 300 K for most of the metals in Table 2.1.

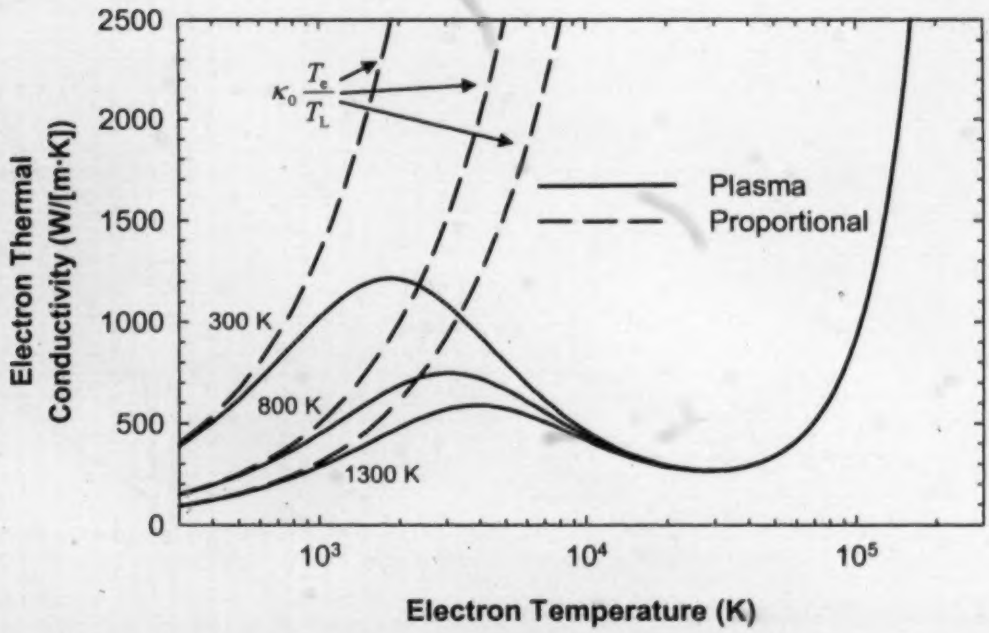

Figure 2.3: Electron thermal conductivity of copper calculated using the proportional and plasma electron thermal conductivity models [55].

To couple the energy deposited in the electron subsystem to the lattice subsystem requires electron-phonon coupling. The electron-phonon coupling coefficient was first derived to explain deviations observed in Ohm's Law [51], which Kaganov *et al.* [51] believed resulted from electrons having a higher equilibrated mean energy, out of thermal equilibrium with the lattice. Assuming that the electron subsystem was in thermal equilibrium and obeyed Fermi statistics, an energy coupling equation was derived by a phonon distribution function whose population was defined by electron state transitions. The general form of the energy coupled to the lattice per unit time per unit volume was:

$$\overline{U}(T_e, T_L) = \frac{2}{(2\pi)^3} \frac{m^2 C^2 (k_B T_D)^5}{\hbar^7 \rho s^4} \left\{ \left(\frac{T_e}{T_D} \right)^5 \int_0^{T_D/T_e} \frac{x^4 dx}{e^x - 1} - \left(\frac{T_L}{T_D} \right)^5 \int_0^{T_D/T_L} \frac{x^4 dx}{e^x - 1} \right\} \text{ (W/m}^3\text{)} \tag{2.10}$$

where m is the effective electron mass, ρ is the material density, s is the sound velocity and C is a constant describing the interaction between the electrons and the lattice.

The original derivation of energy coupling between electrons and phonons was stated in ref. [51] to have been derived in ref. [52]. In Chapter 9.3 of ref. [52], the coupling of the conduction band electron energy by a transition between states was derived by describing the coupling as a result of a displacement or dilation of the ion lattice resulting from longitudinal lattice vibrations (transverse lattice vibrations do not yield density fluctuations) [52]. The displacement potential resulting from longitudinal phonons scattered free electrons whose energy was taken up by the phonons. In this derivation, an energy function, C, appeared that was expected to have values between 1 eV and 10 eV that would not vary greatly over the scattering vectors. This function could be taken as constant for a particular material and for perfectly free electrons, an approximation made for the noble metals. The electrical conductivity was inversely proportional to C^2 allowing the constant to be measured experimentally. Experimentally measured values reported in ref. [52] are given in Table 2.5.

Kaganov *et al.* [51] provided several approximations to the general form of equation (2.10) depending upon the temperature range of interest. The best approximation for the TTM is equation (9) in ref. [51] assuming that T_e, $T_L >> T_D$:

$$\overline{U}(T_e, T_L) = \frac{1}{2(2\pi)^3} \frac{m^2 C^2 (k_B T_D)^5}{\hbar^7 \rho s^4 T_D} (T_e - T_L) \ \text{(W/m}^3\text{)} \tag{2.11}$$

The constant, C, is usually stated in units of eV since it is small, but is substituted into equation (2.11) in units of Joules. Anisimov *et al.* [8] took this equation as the energy coupling factor in the PTS-TTM, which is used written more familiarly as $g(T_e - T_L)$, where g is taken as a constant and from the approximation above is:

$$g = \frac{1}{2(2\pi)^3} \frac{m^2 C^2 (k_B T_D)^5}{\hbar^7 \rho s^4 T_D} \ \text{(W/[m}^3\cdot\text{K])} \tag{2.12}$$

Table 2.5: Experimentally derived and theoretically calculated electron-phonon coupling coefficients (*g*-parameter) for metals. The Exp. column are values obtained by comparing PTS-TTM calculations to measurements and the Calc. column are for values calculated using equation (2.12) with *C* given in the table. The electron thermal conductivity model used to predict the *g*-parameter is given in the κ Type column as either the proportional model or plasma model.

	g-parameter*		*C*	κ	
Metal	Exp.	Calc.	(eV)	Type	Refs.
Cu	10	2.48	6.2	prop.	[57]
Cu	1	2.48	6.2	prop.	[44]
Cu	(3.9 ± 0.5)	2.48	6.2	prop.	[58]
Cu	3	2.48	6.2	plasma	[59]
Ag	2.1	0.550	4.6	plasma	[55]
Au	(2.2 ± 0.3)	0.557	6.35	prop.	[25]
Au	1.1	0.557	6.35	prop.	[49]
Al	31	n/a	n/a	plasma	[55]
Cr	42	n/a	n/a	prop.	[60]
Co	93	n/a	n/a	prop.	[25]
Ni	36	n/a	n/a	prop.	[60]
Mo	13	n/a	n/a	prop.	[60]
Ru	110	n/a	n/a	prop.	[25]
Pt	25	n/a	n/a	prop.	[25]

* The *g*-parameter is given as (10^{16} W/[m^3·K])

Equation (2.11) plotted against equation (2.10) in Figure 2.4 shows that the approximation agrees with the general form of the electron-phonon energy coupling for a lattice temperature starting at room temperature (300 K) and progressing to melting temperatures above 1000 K for all electron temperatures below the Fermi temperature.

A summary of the previously reported *g*-parameters in the literature is also given in Table 2.5 including the form of the electron thermal conductivity used in the PTS-TTM to estimate *g*. Notice that except for the higher reported value in ref. [57], the *g*-parameter for the noble metals is nearly an order of magnitude lower than the transition metals, indicative of the different transport properties between these types of metals. The theoretical *g*-parameter values are calculated using the values for *C* (p.268 of ref. [52]).

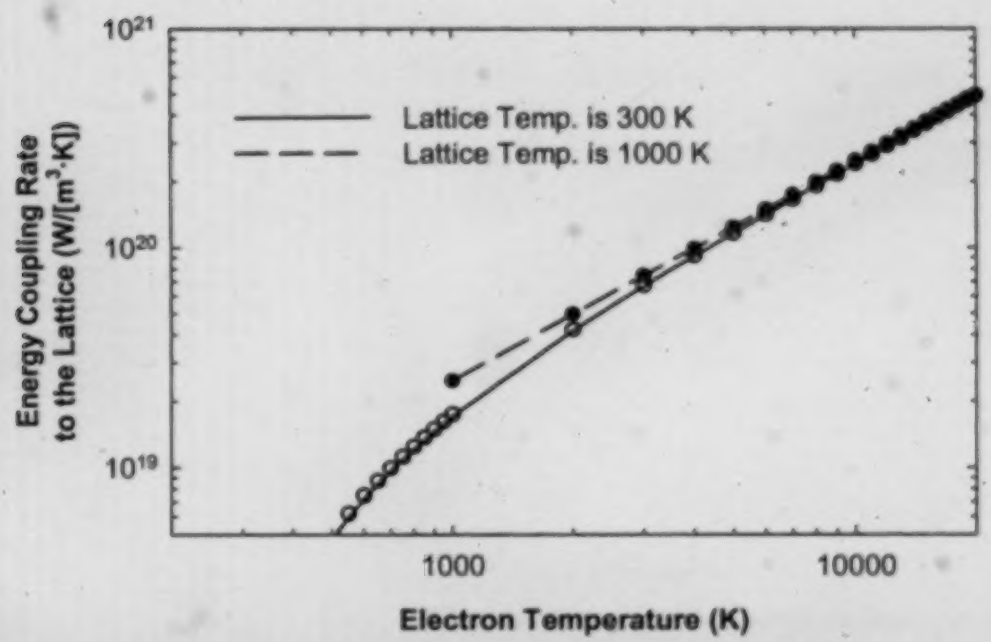

Figure 2.4: Comparison of the full equation and the approximation of the energy coupling equation in the TTM, derived in [51]. The lines are the general equation [equation (2.10)] and the points are the approximate solution of equation (2.11).

The definition of the sound velocity is important for calculating the *g*-parameter. The sound velocity used to calculate the *g*-parameter in Table 2.5 was the longitudinal velocity propagating in the [100] direction of a cubic crystal [22, 61]. This velocity was the smallest sound velocity as compared to longitudinal velocities in the [110] or [111] directions (see Section 3f in ref. [61]). The sound velocity varies significantly in different references. The calculated longitudinal sound velocity in the [100] direction for copper and silver, respectively, is 4345 m/s and 3436 m/s. The sound velocity tabulated in ref. [62] gives sound velocities with no direction or type as 3500 m/s for copper and 3650 m/s for silver and since the *g*-parameter varies as s^{-4}, small variations in the sound velocity affect the calculated values significantly.

The geometry of the region heated by the laser pulse may also affect the selection of the appropriate sound velocity. Extensional waves, measured for a cylinder with dimensions a fraction of the sound wavelength, have sound velocities of 3750 m/s for rolled copper, 2680 m/s in silver and 2030 m/s for hard-drawn gold [61] and would yield *g*-parameters of 4.45×10^{16} W/[m^3·K]), 1.49×10^{16} W/[m^3·K]) and $1.35 \times$

10^{16} W/[m^3·K]) for copper, silver and gold, respectively, closer to the experimental values reported in Table 2.5. The geometry of the ablation spots may play a role in the appropriate choice of the sound velocity when the ablation spots are smaller than the sound wavelengths, which is the criterion for using the extensional sound velocities rather than the longitudinal sound velocities. The *g*-parameter is inversely proportional to the electron-phonon coupling time. The noble metals, with a *g*-parameter of approximately 10^{16} W/(m^3·K), have an electron-phonon equilibration time of tens of picoseconds.

The final parameter in the PTS-TTM is the source term that describes the intensity change over the depth as:

$$S(z,t) = \frac{dI(z,t)}{dz} = \alpha(1-R)I(t)\exp(-\alpha z) \quad [\mathrm{W/m^3}] \tag{2.13}$$

This equation describes an incident 1D intensity distribution that is linearly absorbed in a Beer's Law profile at a constant rate, α, in the *z*-direction. This equation assumes that the depth of the material is long enough such that the portion of the intensity transmitted into the material, (1 - *R*), is completely absorbed. The temporal pulse shape, $I(t)$, depends on whether the pulse is shaped as a constant (Top Hat), Gaussian or hyperbolic secant squared distribution in time. The pulse shapes and their functional forms are discussed further in Section A.1 where the discretization of the PTS-TTM is developed.

A variation of the source term, particularly for noble metals, is the inclusion of the ballistic absorption depth. The ballistic absorption depth may be much larger than the optical penetration depth for a metal as shown in Table 2.3 and is added to the TTM source term as shown below [25, 26]:

$$S(z,t) = \frac{dI(z,t)}{dz} = \frac{(1-R)}{\delta+\delta_b} I(t)\exp\left(\frac{-z}{\delta+\delta_b}\right) \quad [\mathrm{W/m^3}] \tag{2.14}$$

where δ is α^{-1} and δ_b is given in Table 2.3.

The ballistic absorption depth was included in the TTM to explain deviations of transient reflectivities in thin gold films probed with a femtosecond laser pulse at 500 nm, a wavelength where the reflectivity is linearly related to the electron temperature [25]. The original PTS-TTM source equation overestimated the reflectivity (electron temperature) because of its shorter absorption depth. Ablation rate experiments show that the ablation rate is proportional to the *optical* penetration depth for the "gentle" regime and not the ballistic penetration depth. The optical penetration depth is used in the PTS-TTM in this thesis.

The TTM is a macroscopic model describing the collective behaviour of the electron and lattice subsystems. For the nanomilling ablation regime, peculiarities in each of the subsystems may be important and a microscopic model that describes the behaviour of individual particles is required. The MD simulation is a relatively new technique for describing the microscopic properties of a material under laser irradiation and is described in the following chapter.

2.3 Femtosecond laser pulse ablation of silicon

The understatement of the century is the importance of silicon to our technological progress. It is one of the most abundant materials on the planet, it is manufactured to high precision and its properties can be finely tuned [63]. The ability to finely tune the properties of a silicon crystal makes silicon an appropriate choice for controlled parameterized studies on femtosecond laser ablation and modeling of semiconductors.

What has emerged over the last two decades of research into silicon and its response to femtosecond laser pulse interaction is that there are two pathways of material response depending on the absorbed intensity. The first is a *thermal* pathway, where photon energy absorbed by the valence band electrons is sufficient to drive the temperature of the lattice to the melting temperature before returning to an amorphous or crystalline structure without ablation [64, 65]. The second pathway, the *non-thermal* pathway, excites enough valence band electrons into the conduction band to create a critical electron density for the incident wavelength, which destabilizes the lattice and

causes an abrupt expulsion of the energetic species into vacuum leaving behind a relatively cool substrate [66-68].

The thermal pathway defined by the melting threshold terminates with a surface that appears to be similar to the native sample showing no signs of laser interaction. The dynamics occur over several picoseconds and it usually reaches a steady-state in 5 ps [65]. The reflectivity of the surface shows a dip in the reflectivity as the conduction band electron density approaches the plasma resonance, where the real part of the dielectric constant is zero for the wavelength of interest [69]. After several picoseconds, the reflectivity slowly decays as a result of carrier diffusion into the bulk [65].

At approximately twice the single-shot melting threshold fluence, a non-thermal regime is encountered, which defines the single-shot ablation threshold fluence, $\phi_{th}(1)$. The dynamics of this energy density were originally seen as a sharp change in the reflectivity of the silicon surface that occurred in under a picosecond [65]. The surface examined under microscopy showed a crater in the irradiated region, indicating that a catastrophic breakdown was initiated as the energy density increased. For the 1 μm probe wavelength, most sensitive to free-carrier dynamics [70], as the excitation fluence was increased, the minimum reflectivity point appeared earlier in time that indicated that the resonant absorption peak was occurring sooner or that the free-carrier density was being generated at higher rates [65]. At four times the melting threshold, an abrupt change in the reflectivity curve occurs, likely because of material expulsion at approximately 600 fs after the laser pulse, demonstrating the rapid nature of this pathway.

Other groups have observed high conduction band electron densities in sub-picosecond time frames [67] but time-resolved optical reflectivity experiments indicated that significant material removal occurs after approximately 20 ps [66]. The material expansion in ref. [66] is indicated by the appearance of Newton rings due to the interference of the probe beam with itself as it reflects from the surface and the expanding interface of the ablation front.

Further studies into melting versus ablation have revealed that the final crystalline state of silicon surface will vary depending on the excitation fluence [71]. Crystalline silicon will relax to an amorphous state or crystalline state after heating depending on the maximum temperature that is reached. Raman spectroscopy images in the melting

fluence regime confirm that the silicon will remain amorphous, but at fluences above the ablation threshold, silicon will recrystallize to a single crystal [71].

Although a consistent qualitative picture of silicon ablation exists, variability in the excitation wavelength and mechanisms have led to variation in the reported ablation thresholds for silicon at femtosecond pulse widths. At 620 nm to 625 nm wavelength excitation, it is generally agreed that the threshold for the thermal pathway is in the range of 100 mJ/cm^2 to 170 mJ/cm^2 [64-66, 69, 72]. The angle of incidence (AOI) and polarization varies among these studies so there is still some ambiguity as to whether the threshold is the incident melting threshold for 0° AOI.

Table 2.6 shows the results in the literature for silicon ablation with pulse widths ranging from 5 fs to 1 ps in the visible to NIR wavelengths. This table shows that few publications of the single-shot silicon ablation threshold at femtosecond pulse widths report all the material parameters that may contribute to the variability in ablation thresholds for silicon, especially the variability in the single-shot ablation threshold at the frequently studied 100 fs pulse widths.

Table 2.6 also shows that experimental techniques can contribute to the variability since they vary in the measured dynamics and have inherent sensitivities. The GBLT, which analyzed the relationship between the ablation diameter and the incident Gaussian beam intensity distribution [38] (also see Appendix B), can vary in its accuracy by instrument error. In addition, multiple rings have been observed relating to different processes of amorphization, chemical reaction or ablation [71, 73] and a clear identification of the relevant processes is often not given. Diameters measured by AFM and SEM will be sensitive to different surface modifications and their overall accuracy is related to the feature sizes being measured. Large ablation spots made by long focal length lenses (> 20 cm) are less sensitive to instrument accuracy than small ablation spots made by microscope objectives [74].

Pump-probe reflectivity defines the ablation threshold as the fluence where the reflectivity reaches that of liquid silicon [69], but may suffer in accuracy due to spatial averaging, a problem overcome in time-resolved optical microscopy. Pump-probe reflectivity and time-resolved optical microscopy could potentially lead to thresholds smaller than those reported by the GBLT since the ablation spot may not be visible [65].

Table 2.6: Published, experimentally measured, incident single-shot ablation thresholds of silicon. The silicon conditions (cond.) are X: crystalline, I: intrinsic, N: n-type, P: p-type and SOS: silicon on sapphire; *T* is the material thickness; reported pulse width is Gaussian FWHM, italicized values have no reported pulse shape; bracketed value for ϕ_{th} is the reported error; reflectivity values in italics are assumed from other sources [23]. The focal spot diameter is given under *D*. Note the addition of the pump-probe (P-P) detector method to those listed in Table 2.4.

(cond.)	ρ (Ω-cm)	T (μm)	Env. (Torr)	λ (nm)	τ_p (fs)	R (%)	$\phi_{th}(1)$ (mJ/cm^2)	D (μm)	Det. Method	Ref
SOS(100)	n/a	0.50	Air	620	*90*	33.8	120(20)	90	R	[72]
I(111)-p	n/a	n/a	Air	620	*130*	*35.1**	150_{melt}	n/a	P-P	[66]
I(111)-p	n/a	n/a	Air	620	*130*	*35.1**	320_{abl}	n/a	P-P	[66]
I(100) (111)	n/a	n/a	10^{-10}	620	*100*	*22.6**	300	n/a	GBLT	[64]
I(111)	n/a	n/a	Air	620	*90*	*35.1*	100_{melt}	150	R	[65]
N(111)-p	n/a	n/a	10^{-4}	780	*5*	*33.1*	200	10's	OM-1	[73]
N(111)-p	n/a	n/a	10^{-4}	780	*25*	*33.1*	170(15)	n/a	OM-1	[75]
n/a	10-50	n/a	10^{-7}	780	*100*	*20.8**	150	316	TOF	[76]
n/a	10-50	n/a	10^{-7}	780	120	*33.1*	160_{fast}	160	TOF	[77]
n/a	10-50	n/a	10^{-7}	780	120	*33.1*	310_{slow}	160	TOF	[77]
N(111)-p	n/a	n/a	10^{-4}	780	*400*	*33.1*	280(30)	n/a	OM-1	[75]
N(n/a)	10-30	n/a	Air	786	*85*	*33.0*	158	20-120	AFM	[78]
N(n/a)	10-30	n/a	Air	786	*200*	*33.0*	238	20-120	AFM	[78]
N(n/a)	10-30	n/a	Air	786	*633*	*33.0*	240(40)	20-120	AFM	[78]
n/a	n/a	n/a	Air	786	*1000*	*33.0*	362	20-120	AFM	[78]
X(100)	n/a	n/a	10^{-1}	790	*130*	*33.0*	150-300	6.7	SEM-1	[74]
(100)	n/a	n/a	Air	800	83	*32.9*	458	2	AFM-2	[79]
X(100) (111)	n/a	n/a	Air	800	*120*	*32.9*	210(10)	8	SEM-1	[80]
X(100) (111)	n/a	n/a	Air	800	*120*	*32.9*	110(10)	24	SEM-1	[80]
N(111)-p	n/a	n/a	Air	800	*130*	*32.9*	260_{melt}	50	OM-1	[73]
N(111)	n/a	n/a	Air	800	*130*	*32.9*	550_{annul}	50	OM-1	[73]
N(111)	0.02	400	Air	800	*130*	*32.9*	270_{melt}	51	OM-1	[71]
N(111)	0.02	400	Air	800	*130*	*32.9*	410_{annul}	51	OM-1	[71]
N(111)	0.02	400	Air	800	*130*	*32.9*	580_{abl}	51	OM-1	[71]
N(n/a)	10-50	n/a	10^{-7}	1055	*900*	*19.4**	180	316	TOF	[76]
N(n/a)	10-30	n/a	Air	1060	*400*	*31.5*	56(53)	n/a	AFM	[78]
N(n/a)	10-30	n/a	Air	1060	*1000*	*31.5*	87(48)	n/a	AFM	[78]

* indicates that the experiment was not done at normal incidence

Techniques that define ablation by the "appearance" of ablation spots by SEM or AFM suffer from the depth resolution of the device. Large spots that are nanometers deep may not reliably appear in these techniques. This type of methodology would likely lead to higher threshold values since it would be the point where significant material removal occurred. Ablation rate thresholds from single-shot depths also have accuracy problems similar to GBLT where the instrument error and focusing condition would determine accuracy.

TOF techniques define ablation at the intercept of zero ion expulsion when analyzing the ion flux relationship with the incident fluence. The detector sensitivity would play a strong role in the extrapolation of the zero particle detection point if it takes a significant fraction of the material to generate a response. If the dynamics of ablation change because a new material response regime is entered, then the weaker low intensity response may be overshadowed by the stronger high intensity response, which when extrapolated will give a higher threshold. For example, the thermal pathway may not necessarily have significant ion expulsion in the nanosecond time frame and not be observed; however, very sensitive ion measurements can detect very small amounts of emitted material corresponding to nanometer removal depths, which other detection techniques may not observe.

The samples vary in initial conduction band electron density, apparent in Table 2.6, with samples ranging from intrinsic silicon to doped samples of n- or p-type. Resistivity and geometry with crystalline orientation is also not being reported consistently. Equating the results to models is especially difficult if one does not understand the nature of the experimental technique, its inherent errors and the original surface properties while optimizing the simulation to match the experimental values.

The initial carrier density in semiconductors is a possible variable in the determination of the femtosecond laser ablation threshold. Semiconductors and dielectrics usually have long linear absorption depths, α_0, when irradiated by photons in the NIR and visible spectrum. The ablation of semiconductors and dielectrics is expected to follow the creation of a critical density of electrons for the excitation wavelength since a highly absorbing phase exists just before the critical density is reached [69]. Silicon has an approximately 10 μm skin depth in the NIR but also has a strong two-photon

absorption (TPA) coefficient [72]. Silicon can also create high energy electrons through free-carrier absorption (FCA; also called electron-photon-phonon collision). This process generates higher energy electrons in the conduction band from photon absorption that can proceed to increase the electron density in the conduction band by collisions with the valence band electrons: impact ionization. Overall, the combination of these two processes is referred to as avalanche ionization.

The strength of FCA and impact ionization for the wavelength and material of interest should factor into the determination of the single-shot ablation threshold of silicon and the initial density of electrons may play a role. Intrinsic silicon with low initial conduction band electron densities of 10^{10} e^-/cm^3 may require TPA versus FCA in the initial interaction, modifying the observed single-shot ablation threshold as compared to an n-type silicon wafer with an initial conduction band electron density of 10^{18} e^-/cm^3. It is uncertain what role a high hole density with very few conduction band electrons may have on the single-shot ablation threshold as well.

2.4 Molecular dynamics modeling of femtosecond laser pulse ablation of silicon

Two of the most challenging questions in laser ablation studies indicated in the previous section is: "When does ablation occur and what dynamic pathways does it follow?" The challenge exists because experimentally we do not have the tools to view all contributions to the ablation process. The physics have to be reverse engineered from experimental information and from the available literature. The problem is compounded because the information collected experimentally is a convolution of collective behaviours of individual particle systems in a variety of states. For example, the collective behaviour of a large free electron density in a semiconductor can be an aggregate of electron-electron, electron-phonon and electron-hole interactions, each with their own properties. Conclusions drawn on the individual subsystem or particle behaviour is still an estimate from observed collective behaviour.

Theoretical investigations, including the TTM, also operate on collective behaviour at the macroscopic level on properties such as temperature and pressure, and do not provide insight into the particle dynamics. MD simulations are used to model individual particles and with the proper governing equations can begin to answer the

question: "When does ablation occur and what are the pathways to material removal?" The attractive feature of MD simulations is the ability to examine material subsystem particle dynamics (electrons, ions, neutrals and photons), an ability not available experimentally. Technically, MD has no limitations since it uses Newtonian mechanics to numerically solve the *N*-body problem and quantum effects can be included to simulate, for example, the density increase of water and silicon upon melting [81].

Our group has been improving an MD simulation of silicon that was originally developed by Dr. E.E.B. Campbell's group (herein called the original MD). Details of the original MD have been published previously [82, 83]. In summary, the original MD simulation used an empirical potential function derived by Stillinger and Weber [84] (SW potential) to create a tetrahedral lattice structure of silicon particles using 2- and 3-body potential functions. The 2-body potential gives the balance of attractive and repulsive forces to create a distribution of silicon particles with an interatomic distance of a = 2.35 Å; the 3-body potential distributes the particles into a tetrahedral structure. The 3-body potential is an example of a quantum effect included in the MD simulation. The 3-body potential governs the density increase of silicon upon melting [81]. Balamane *et al.* [85] modified the coefficients of the empirical SW potential to have the correct bulk cohesive bond energy since the SW potential was originally optimized to give the proper melting temperature [86]. Forces on the particles by neighbouring particles were calculated using Newtonian mechanics with temperature being simulated by the average energy of the particles. To increase the temperature, the kinetic energies of the particles are scaled by a constant given by the equipartition theorem.

The original MD had the photons interacting with the atoms rather than the electrons. To model ultrafast melting and laser absorption, the bonds simulated by the SW potential were removed according to the excitation level of an atom. Because the density of particles in each of the simulation cells could vary, the probability of an absorption event was calculated based on the Beer's Law absorption profile [87] rather than using a constant absorption value for each cell. Silicon is dominated by linear and TPA, so a linear absorption coefficient of α_0 = 803.49 cm^{-1} [88] and an instantaneous TPA coefficient of β = 55 cm/GW [67] were used for the 800 nm wavelength.

If a linear absorption event occurred for an atom, then a photon was removed from the simulation volume and a conduction band electron was "created" by randomly breaking the atom's bond with one of its neighbours. A broken bond was simulated by removing the attractive portion of the 2-body potential and the entire 3-body potential between the two atoms. Similarly, if a two-photon event occurred for an atom, two photons were removed and a conduction band electron with twice the photon energy was "created" by breaking two bonds in the same manner as before. When an atom lost a valence band electron to the conduction band, the simulation labelled this atom as "excited". If the atom was continually excited, without the electron relaxing back into the valence band and the total absorbed energy reached 4.85 eV (the work function of silicon [23]), then the electron became a free independent particle. This electron was labelled as "free" and was released halfway between the excited atom and one of its neighbours ($\frac{1}{2}a$ = 1.17 Å) in a random direction with the total absorbed energy minus the work function energy. The ion was simulated by putting the full SW potential back on to the atom and adding a Coulomb force with a cut-off distance of 20 Å. This cut-off distance was sufficient since there was no improvement going to greater distances [83] at a cost to computational time.

Three electron relaxation pathways were implemented. Conduction band electrons, represented as excited atoms through broken bonds, relaxed into the valence band 500 fs after excitation and transferred this energy to a nearby atom within a 3.8 Å distance to simulate optical phonon creation. This relaxation simulation is similar to a temperature increase by adding to the momentum of the nearby atom. The second relaxation mechanism had the free electrons, created when an atom reached an excitation energy higher than the work function, recombine non-radiatively if it passed within 1 Å of an ion and coupled this energy to the ion by adding to its momentum. The last relaxation mechanism had ions relaxing to neutral particles within 1 ps to simulate electron recombination from the bulk.

The original MD simulation was modified to include periodic boundary conditions, a heat flow model at the base of the simulation volume and was adapted to a parallel code to run on the Westgrid system at the University of Alberta (U of A) (herein labelled as the HF-MD). Periodic boundary conditions on the side walls of the

simulation and a 1-D heat flow simulation coupling the MD system to the heat bath at the base of the simulation using Langevin dynamics [86] improved the code by removing artificial dampening conditions that resulted in ablation thresholds that were an order of magnitude higher [83] than those reported experimentally. This improvement was the initial step in creating an MD simulation that began to report ablation thresholds of silicon from NIR, 100 fs laser pulse widths that matched results in the literature [86]. The results of the HF-MD simulation as compared to the experiments reported in the literature, as listed in Table 2.6, are shown in Figure 2.5 [86, 87].

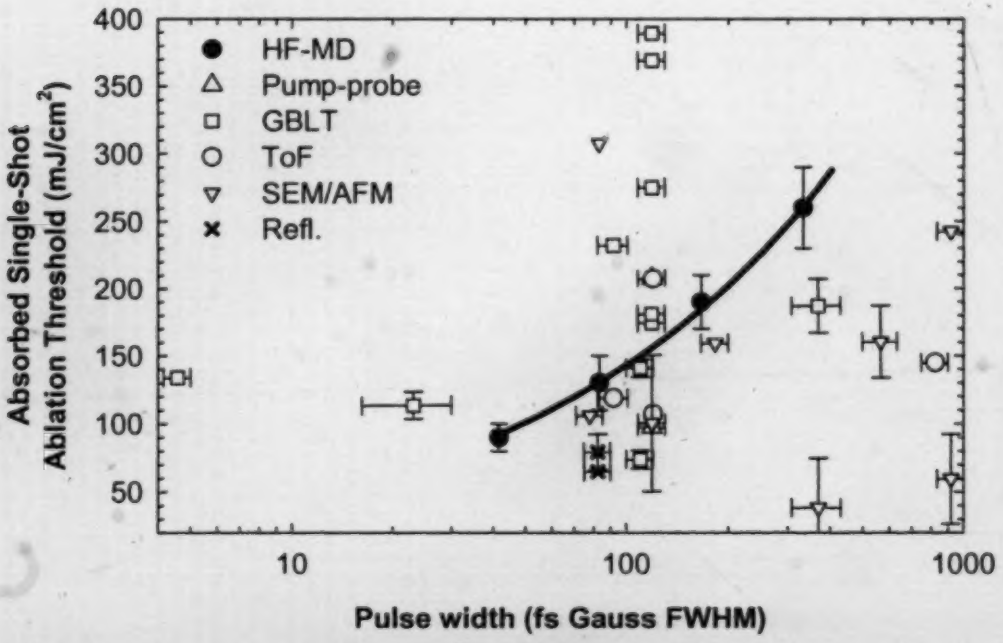

Figure 2.5: HF-MD simulation of the single-shot ablation threshold of silicon with 800 nm wavelength, femtosecond laser pulses as compared with experimental results reported in the literature. The literature values and references are listed in Table 2.6.

Comparing the HF-MD to the experimental results in the literature for the single-shot ablation threshold by assuming all values were reported as *incident* fluences shows a large spread in the data and a weak fit to the trend of the HF-MD with pulse width. The GBLT data has a large spread at 100 fs pulse widths confirming the earlier discussion that accuracy can be a weakness in the technique if the ablation spots become too small

or the outer edge of the spot is ambiguous. The "appearance" of the ablation spots by AFM/SEM also shows a spread. The TOF and pump-probe data is close to the HF-MD results at 100 fs and the TOF data, along with the AFM data, shows the ablation threshold to have a weak dependence on the pulse width, contrary to the HF-MD. For longer pulse widths, the energy deposition required may decrease for ablation as compared to the HF-MD with avalanche ionization energizing the electrons promoted by TPA to the conduction band. The HF-MD lacks this mechanism at this stage in its development.

In Table 2.7, results of other MD simulations and a 1-temperature heat flow model (1TM) are listed. The results of the original MD code at the 700 nm wavelength are shown where the simulation was done with a 25 Å diameter focal spot and absorption coefficients (α and β) set 2000× higher in order to get 90 % absorption of the pulse energy in 10 nm. The results from the HF-MD simulation as compared with other theoretical single-shot ablation thresholds are shown in Figure 2.6.

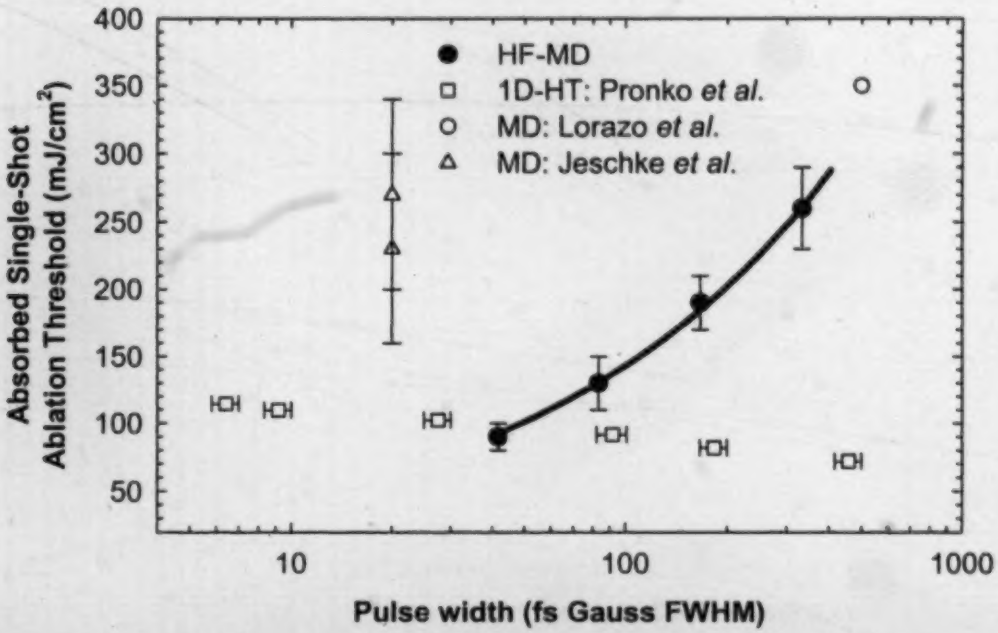

Figure 2.6: HF-MD simulation of the single-shot ablation threshold of silicon with 800 nm wavelength, femtosecond laser pulses as compared with theoretical results reported in the literature. The literature values at various wavelengths and references are listed in Table 2.7.

Table 2.7: Published, theoretically derived, absorbed single-shot ablation thresholds of silicon. The theoretical technique is given in the second last column

λ (nm)	τ_p (fs)	T (nm)	N (atoms)	$\phi_{th,abs}$ (mJ/cm^2)	Tech.	Ref
266	500	30	99 000	350	MD	[89]
308	*2.4*	n/a	n/a	115.6 (R=59 %)	1TM	[90]
308	*4*	n/a	n/a	114.0	1TM	[90]
308	*7*	n/a	n/a	114.8	1TM	[90]
308	*10*	n/a	n/a	110.0	1TM	[90]
308	*30*	n/a	n/a	102.5	1TM	[90]
308	*100*	n/a	n/a	91.8	1TM	[90]
308	*200*	n/a	n/a	82.0	1TM	[90]
308	*500*	n/a	n/a	72.2	1TM	[90]
700	*10*	10	23 000	3000(1000)	MD	[83]
700	*50*	10	23 000	4000(2000)	MD	[83]
700	*200*	10	23 000	6000(2000)	MD	[83]
700	*1000*	10	23 000	6000(2000)	MD	[83]
780	*20*	4.3	64	230(70)$_{melt}$ *	MD	[75]
780	*20*	4.3	64	270(70)$_{abl}$ *	MD	[75]
780	*500*	4.3	64	900(300)$_{melt}$ *	MD	[75]
780	*500*	4.3	64	960(300)$_{abl}$ *	MD	[75]

* originally reported in eV/atom and converted to absorbed fluence

The theoretical results, other than the 1D-HT of Pronko *et al.* [90], show an increase in energy deposition required for longer pulse widths. All of the MD models listed lack an avalanche model and generate electron densities through TPA. The experimental data in Figure 2.5 does not support this trend at the longer pulse widths.

Linear absorption and TPA are not the only means of electronic excitation in silicon [78, 91, 92]. Laser-induced breakdown of weakly absorbing to transparent solids, or simply solids having a energy band gap greater than the photon wavelength between the bound valence electrons and conduction band electrons, follows an additional process: avalanche ionization [56, 93]. This process, along with linear absorption and TPA, can generate a large enough electron density to make a highly absorbing surface layer with resistive metallic properties near the critical electron density for the photon

wavelength [94]. The strength of each process changes with the photon wavelength and field intensity. As the wavelength increases, from simple energetic calculations ignoring momentum conservation, linear absorption will no longer yield conduction band electrons. For silicon with a band gap of 1.11 eV [22], linear absorption no longer occurs at wavelengths greater than 1100 nm.

Increasing the wavelength beyond 2.23 μm (0.555 eV), TPA can no longer produce conduction band electrons and a larger number of simultaneous photons need to be absorbed to produce these electrons with each multiple having significantly lower rates. Avalanche ionization will eventually predominate at longer wavelengths and the two mechanisms that need to occur are FCA and impact ionization.

FCA is the absorption of photons by conduction band electrons. An electron in an oscillating field gains no energy, so a collision with an ion core or a lattice vibration is required to transfer the energy in the laser field to the electron (electron-photon-phonon collision). Carriers in the conduction band continually collide with electrons in the valence band; if the energy of an electron in the conduction band is greater than $2U_G$, then a collision with a valence band electron will yield two conduction band electrons with energies just above the band gap energy: this process is called impact ionization (electron-electron collision). The energizing of conduction band electrons and the collisions with the valence band electrons will exponentially increase the conduction band electron density leading to breakdown of the material.

Previous MD simulations of silicon have used photon energies (wavelengths) in the visible range where linear and two-photon processes dominate conduction band electron production leading to material breakdown. The avalanche ionization rate at these wavelengths is much smaller than the conduction band electron production rates of the other two processes and the addition of avalanche ionization would probably have little effect on the final results. The HF-MD simulation uses photon energies in the NIR (800 nm) and should include avalanche ionization with multiphoton absorption to be a complete model of NIR laser-silicon interaction.

To explore the modeling of avalanche ionization, first we explore a simplified calculation by some authors that lump FCA and impact ionization into one rate equation since calculation of all contributions to conduction band electron density requires solving

the Boltzmann transport equation [93]. In the papers of Bloembergen [93] and Du *et al.* [95], the avalanche ionization rate, $\eta(E)$, was dependent on the applied electric field strength and was derived using simplified electron multiplication by considering in the low frequency limit that:

$$\frac{dn_e(t)}{dt} = \eta(E)n_e(t) + \left(\frac{dn_e(t)}{dt}\right)_{generation} - \left(\frac{dn_e(t)}{dt}\right)_{losses} \tag{2.15}$$

where $n_e(t)$ is the number of conduction band electrons and $\eta(E)$ is the avalanche ionization rate. The second and third terms in equation (2.15) are the creation electrons by tunnelling or multiphoton ionization and the loss of electrons by recombination or electron capture at defect sites. Initial conduction band electrons required to start the process originate from [93]:

a) intrinsic thermal carrier densities
b) tunnelling (usually in the low frequency limit)
c) multiphoton ionization (usually in the high frequency limit)

To calculate the avalanche ionization rate, the initial thermally excited electron density was considered sufficient such that contributions by multiphoton ionization or tunnelling [95] were ignored. Losses were also neglected because the mean free path of the electrons was such that an insufficient number of electrons would leave the focal volume for $\tau_p < 10$ ns [93]. With the electron generation mechanism in the material dominated by avalanche ionization, the generation of free carriers was given by simple electron multiplication:

$$n_e(t) = n_0 \exp\left(\int_0^{\tau_p} \eta(E(t'))dt'\right) \quad (e^-/\text{cm}^{-3}) \tag{2.16}$$

where n_0 is the initial density of conduction band electrons (e^-/cm^{-3}).

By assuming a constant AC electric field in time, the integral in the exponent of equation (2.16) reduces to $\eta(E)\tau_p$. To calculate the avalanche ionization rate, a relationship with DC gas breakdown was made assuming the electron collision time was

smaller than the period of the AC field ($f\tau_p < 1$). The electrons gain energy through collisions in the presence of a laser pulse (Joule heating at low frequencies, inverse *bremsstrahlung* at high frequencies) [93]. With this assumption, the generation of carriers was compared to the DC breakdown of a gas experienced over a cathode-anode gap by the Townsend coefficient [93]:

$$\begin{aligned} \frac{dn_e}{dz} &= \alpha(E) n_e \\ \ln\left(\frac{n_{e_0}}{n_0}\right) &= \alpha(E) d \end{aligned} \tag{2.17}$$

where $\alpha(E)$ is the Townsend coefficient, d is the distance between the cathode and the anode. The logarithm of equation (2.16) with the constant AC electric field simplification is equivalent to equation (2.17) provided the losses were negligible in both cases giving:

$$\begin{aligned} \alpha(E) d &= \eta(E) \tau_p \\ \eta(E) &= \alpha(E) v_{drift} \end{aligned} \tag{2.18}$$

where v_{drift} is the drift velocity of the electrons in the cathode-anode gap and was considered to saturate at 2×10^7 cm/s in high electric fields (few MV/cm), especially those present in laser generated electric fields [95]. The Townsend coefficient is calculated using equation (2.3) in the paper by Thornber [96]:

$$\alpha(E) = \frac{eE}{U_1} \exp\left(\frac{-E_i}{E\left(1 + \frac{E}{E_p}\right) + E_{ir}} \right) \text{ (cm}^{-1}\text{)} \tag{2.19}$$

where U_1 is the electron ionization energy (J), E_i is the electric field necessary to overcome the decelerating effects of ionization (eV/cm equivalent to V/cm), E_p is the

electric field to overcome optical-phonon scattering (V/cm), E_{kT} is the electric-field strength to overcome thermal scattering (V/cm), e is the energy associated with 1 eV (J/V).

Substituting equation (2.19) into equation (2.18) gives the avalanche ionization rate $\eta(E)$ and using the values for silicon from Van Overstraeten and DeMan from Table I in the paper by Thornber [96] (U_I = 3.6 eV, E_i = 1.404 MeV/cm, E_p = 222.9 keV/cm, E_{kT} = 9.747 keV/cm), the avalanche ionization rate can be estimated for the electric field strength at the threshold intensity for silicon ablation. The incident threshold fluence for silicon ablation is approximately 300 mJ/cm^2 for a Gaussian laser pulse with a FWHM pulse width of 130 fs. Using equation (A.17), the peak intensity of this pulse is 2.2 × 10^{12} W/cm^2 and with a reflectivity of 33 % at 800 nm [23], the peak intensity in the silicon sample is 1.4 × 10^{12} W/cm^2. Using equation (B.2) to calculate the electric field in the medium from this intensity (repeated below):

$$I_{pk} = \frac{1}{2} c\varepsilon \left|E_{pk}\right|^2 = \frac{\left|E_{pk}\right|^2}{2\eta} = \frac{\sqrt{\varepsilon_{rel}}\left|E_{pk}\right|^2}{2\eta_0} \quad (\mathrm{W/m^2}) \tag{2.20}$$

assuming that μ_R = 1 in the material and with η_0 being the impedance of free space (377 Ω) with the relative permittivity ε_{rel} ~ 13.5 for silicon [88], the peak electric field inside the material at the surface at the threshold intensity is ~17 MV/cm. The avalanche ionization rate at this field strength is 9.4 × 10^{13} s^{-1}; a nearly sufficient rate to produce a critical density of electrons within a 130 fs FWHM Gaussian pulse width. The prediction for the pulse width scaling of fluence to maintain a fixed ionization rate for a Gaussian pulse shape in time, where the dominating mechanism is avalanche ionization, is a $\tau^{-½}$ scaling using equations (2.20) and (A.17) for the electric field and substituting this electric field equation into equation (2.19).

Breaking avalanche ionization down to its constituent components, FCA and impact ionization, requires the solution to the Boltzmann transport equation as mentioned earlier. The solution shows the generation of conduction band electrons from all mechanisms and determine the relative strengths of these mechanisms. Kaiser *et al.* [94] simulated 500 nm (2.48 eV), 50 fs to 200 fs pulse width laser interaction with SiO_2 (U_G =

9 eV) using the Boltzmann transport equation with collisional integrals for electron-electron collisions (electron thermal equilibration), electron-phonon collisions (lattice heating), electron-photon-phonon collisions (FCA), impact ionization and multiphoton ionization. The collisional integrals model the microscopic processes of energy and momentum transfer without using empirical models based on phenomenological data. They found that avalanche ionization was not linearly proportional to the rate of electron production for pulse widths less than 200 fs as shown in Figure 6 in ref. [94] and assumed in the previous discussion on avalanche rates. For pulse widths below 200 fs, the rate of electron generation was linearly proportional to the electron density after the electron density reached 6×10^{12} e^-/cm^3. In the paper of Kaiser *et al.*, they also demonstrated that as the band gap energy decreased to 6 eV from the 9 eV, used in their first set of calculations, the avalanche ionization rate did not contribute significantly over the multiphoton ionization rates for pulse widths below 200 fs, demonstrating the weak effect band gap has on changing the generation rates.

The weakness of the avalanche ionization rate at smaller pulse widths was already evident from the papers of Bloembergen [93] and Du *et al.* [95]; however Kaiser *et al.* [94] advocated the separation of the phenomenon into its distinct mechanisms of FCA and impact ionization because after the laser pulse valence electrons can be promoted to the lower end of the conduction band from collisions with electrons in the high energy tail of the conduction band electron distribution as shown in Figure 3 of ref. [94]. Impact ionization is also a relaxation mechanism for the conduction band electrons into the valence band when the laser pulse interaction has ended.

Simulation of the Boltzmann transport equation using the Fokker-Planck approximation to calculate the conduction band electron distribution function of silicon was made by Azzouz [91] for 800 nm, 100 fs laser pulses. The rate of conduction band electron generation from impact ionization was dependent on the electron energy not the electric field intensity. Conduction band electron generation was modeled as [97]:

$$\frac{\partial f(U,t)}{\partial t} = -\frac{\partial J(U,t)}{\partial t} + R_{\text{imp}}(U,t) + R_{\text{pi}}(U,t) \quad (e^-/[\text{cm}^3 \cdot \text{s}]) \tag{2.21}$$

where $f(U)$ is the distribution function of the conduction band electrons at energy U with $U = 0$ taken at the bottom of the conduction band, $J(U,t)$ is the loss of electrons due to Joule heating and energy diffusion and R_x represents the generation rate of conduction band electrons by impact ionization (imp) and photoionization (pi). Electrons generated by impact ionization by assuming equal sharing of the impacting electron energy between the impacting and generated electrons, an assumption that is not necessarily valid [98], were shown to have an overall rate of:

$$R_{imp}(U,t) = -\nu(U)f(U) + 4\nu(2U + U_G)f(2U + U_G) \quad (e^-/[cm^3 \cdot s]) \tag{2.22}$$

where $\nu(U)$ is the ionization rate from Keldysh theory and the factor of 4 is necessary to ensure that integration over energy gives $\partial n/\partial t = \int \nu(U)f(U)\,dU$. This equation shows that the rate at energy U referenced from the bottom of the conduction band increases with electrons having energy twice the energy U plus the additional band gap energy U_G since only these electrons have enough energy to remain in the conduction band after collision. The rate is reduced by the loss of electrons at energy U through collisions since those electrons do not have enough energy to remain in the conduction band.

The Keldysh-form of the ionization rate, $\nu(U)$, is:

$$\nu(U) = P\left(\frac{U}{U_{th}} - 1\right)^x \quad (s^{-1}) \tag{2.23}$$

where P is a constant used as a fitting parameter, U_{th} is a hard threshold for the initiation of the ionization usually taken to be U_G and x is the exponent for this model, which is equal to 2 for the Keldysh equation.

Azzouz [91], using $P = 20$ fs^{-1}, $U_{th} = 1.12$ eV and $x = 2$, showed that avalanche ionization can have an increasing role in the production of conduction band electrons as the band gap shrinks (for this paper, dielectrics had $h\nu < U_G$). Avalanche ionization still did not contribute greatly over multiphoton absorption to the production of conduction

band electrons until the pulse width of the laser was longer than 100 fs since the electrons did not have enough time to build up a sufficient density to cause material breakdown.

Several authors [98-100] have demonstrated that the impact ionization rate is a function of the electron energy as shown in equation (2.23); however, since silicon is an indirect band gap material with non-parabolic band structures, the direct substitution of the Keldysh form is questionable since it was originally derived for large direct band gap materials having parabolic band structures [98].

Cartier *et al.* [99] derived a three-level Keldysh impact ionization rate equation that fit the impact ionization data generated by measurements of soft x-ray photoemission and calculations with Monte Carlo methods based on realistic band structures for Si. Kamakura *et al.* [98] used a first-order perturbation theory to calculate an impact ionization rate for Monte Carlo simulations of silicon. The impact ionization rate with electron energy referenced to the bottom of the conduction band was determined to be:

$$\nu(U) = 10^{11}(U - 1.1)^{4.6} \quad (\mathrm{s}^{-1}) \tag{2.24}$$

The difference between equations (2.23) and (2.24) results from the different band structures used to derive the respective formulas. Sano *et al.* [100] indicated that forcing $x = 2$ for all materials results in a wide range of P values as fitting constants and, as shown in Cartier *et al.* [99], can require the summation of several Keldysh-type rates to fit the data. Sano *et al.* used a full collisional integral probability calculation for the impact ionization, but did not provide a final analytical formula. The results of these models are shown in Figure 2.7.

To demonstrate that a constant avalanche ionization rate overestimates the impact ionization rates of the electrons, the calculation of the avalanche rate with the Townsend coefficient at the ablation threshold as calculated earlier is also shown in Figure 2.7. The constant avalanche rate does not coincide with the collisional integral models until electron energies reach over 4 eV referenced to the bottom of the conduction band. An energy of 4 eV referenced to the bottom of the conduction band is greater than the conduction band energy of an electron created by TPA ($2\times1.55 - E_G = 1.98$ eV), and the

avalanche ionization rate overestimates the impact ionization rates of silicon as shown in Figure 2.7 at 1.98 eV.

The impact ionization rate of equation (2.24) by Kamakura *et al.* [98] will be used in the avalanche MD code since the full collisional integrals in Sano *et al.* [100] closely follow the rates calculated by Cartier *et al.* [99] and Kamakura *et al.* and the impact ionization rate in equation (2.24) is easily implemented in the MD simulation. The impact ionization rate using the Keldysh formula of equation (2.23) with the parameters from Azzouz [91] gives one to three orders of magnitude larger impact ionization rates in silicon than in the Kamakura model.

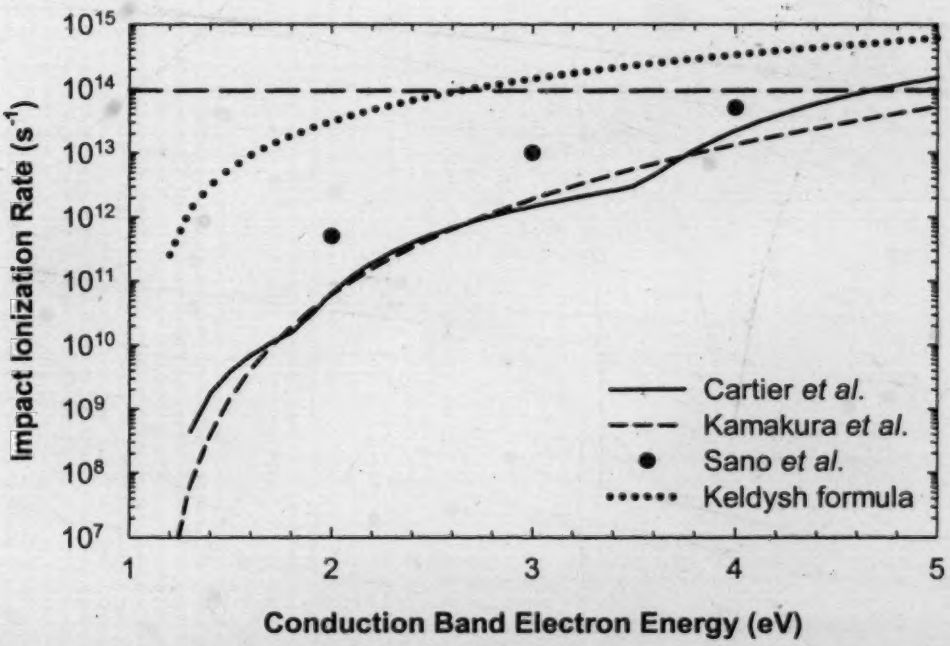

Figure 2.7: Impact ionization rate of conduction band electrons for silicon calculated using collisional integrals and the Keldysh ionization rate [98-100] using the parameters for silicon from ref. [91]. The upper line is the avalanche ionization rate of equation (2.18) calculated using the Townsend coefficient [93, 95] at the ablation threshold. The electron energy is referenced to the bottom of the conduction band.

Impact ionization cannot proceed in the MD simulation without the FCA mechanism to increase the electron energy in the conduction band. The maximum electron energy that can be created in the MD simulation, stated earlier, is from TPA

creating an electron with an energy of 1.98 eV referenced to the bottom of the conduction band. Linear and two-photon absorption only applies to valence band electrons. A correction needs to be made in the HF-MD model to include FCA to increase the conduction band electron energy and smooth out the distribution function in the conduction band as shown in Figure 3 in the paper of Kaiser *et al.* [94].

The standard method for calculating FCA is the model given in Schroder *et al.* [70] used to examine the photon absorption efficiency for photodetectors of n-type and p-type silicon with FCA being a detrimental mechanism. The equation is applicable at room temperature since intrinsic carrier density is dependent on the temperature of the semiconductor [101]. To eliminate the difficulties associated with carrier density changes with temperature, Schroder *et al.* made comparison experiments to the model with artificially doped silicon wafers to measure the effect of high concentrations of majority carriers on photon absorption. The absorption coefficient for FCA was:

$$\begin{aligned} \alpha_{\mathrm{FCA}}^{\mathrm{Schroder}} &= \frac{e^3 \lambda^2 n_e}{4\pi^2 \varepsilon_0 c^3 n m_{\mathrm{opt}}^2 \mu_e} \\ &= 1.964 \times 10^{-18} \lambda_{\mu m}^2 n_e \quad (\mathrm{cm}^{-1}) \\ &= 1.82 \times 10^{-10} \lambda^2 n_e \end{aligned} \tag{2.25}$$

where n_e is the density of the majority carrier, n is the refractive index and μ_c is the mobility of the majority carrier. The numerical value for α_{FCA} was obtained by substituting in the constants in MKS units and using $\mu_e = 0.100\ \mathrm{m}^2/(\mathrm{V \cdot s})$, $m_{\mathrm{opt}} = 0.28 m_e$ [70] and $n = 3.69$ [23].

There are two values listed in equation (2.25) because the first result was given in Schroder *et al.* [70] after substitution of the fundamental constants, the mobility and the effective electron mass shown above. This FCA coefficient was implemented in the MD code. The second value resulted from substitution of the fundamental constants from the NRL Plasma Formulary presented at the beginning of this thesis. The second result has a unitless coefficient and the units of α_{FCA} come from the units for λ and n_e. The second value will be used in future implementations of the MD simulation.

As a further note, a regression fit to the experimental data in Schroder *et al.* [70] gave $\alpha_{FCA} = 1\times10^{-18}\lambda^2 n_e$ cm^{-1}, half of the theoretical value, indicating the variability in the selection of α_{FCA} and the need for a sufficient parametric study in the MD simulation. Equation (2.25) is an approximation made to a more general form of the equation given by Schumann Jr. *et al.* [102] for free-carrier absorption in semiconductors. Equation (2.25) was approximated by assuming $\omega_L^2 \tau_{coll}^2 << 1$.

The addition of impact ionization and FCA to the HF-MD simulation should allow a better fit to the experimental data in Figure 2.5 as well as allow a comparison to reflectivity studies on silicon that correlate electron density generation with the optical properties of silicon.

Chapter 3

Materials and Methods*

Two general sets of experiments were conducted over the course of this thesis that can be categorized as femtosecond laser pulse experiments and CW laser experiments. The femtosecond laser pulse experiments comprised the single-shot ablation threshold and incubation measurement experiments, femtosecond nanomilling experiments and femtosecond laser pulse patterning of SAMs on gold-coated glass substrates experiments. The CW laser experiments were done in MecE using an Argon ion (Ar^+) laser to pattern SAMs on gold-coated substrates by thermal desorption. The thermal patterning of SAMs with the CW laser project was a collaboration with Dr. Alidad Amirfazli and M. Reza Shadnam (Ph.D. student) in MecE at the U of A. My role in this collaboration was to develop and characterize the experimental technique for controlled laser patterning of SAMs on gold-coated microscope slide substrates.

3.1 Experimental tools

3.1.1 Femtosecond nanomilling and ablation threshold experiments

For the femtosecond laser pulse experiments, a commercial regeneratively amplified femtosecond Ti:Sapphire laser system (Spectra-Physics Hurricane) [103] was

---

* Portions of this chapter were previously published in S. E. Kirkwood, M. R. Shadnam, R. Fedosejevs, and A. Amirfazli, "Direct writing of self-assembled monolayers on gold coated substrates using a CW Argon laser," *The International Conference on MEMS, NANO, and Smart Systems*, pp. 48-52, 2003.

used. This system was contained in a single chassis that allowed the user to select either amplified femtosecond pulses (nominal output of 700 μJ, 130 fs pulses at a maximum repetition rate of 1 kHz) at a 800 nm center wavelength with a 10 nm bandwidth as measured by a commercial fibre-coupled spectrometer [104], or femtosecond seed pulses from a mode-locked oscillator (Spectra-Physics Mai Tai) as shown in Figure 3.1. The oscillator had a nominal output of 7.5 nJ to 10 nJ energy, < 100 fs pulse duration at a repetition rate of 80 MHz and a selectable wavelength between 750 nm and 850 nm.

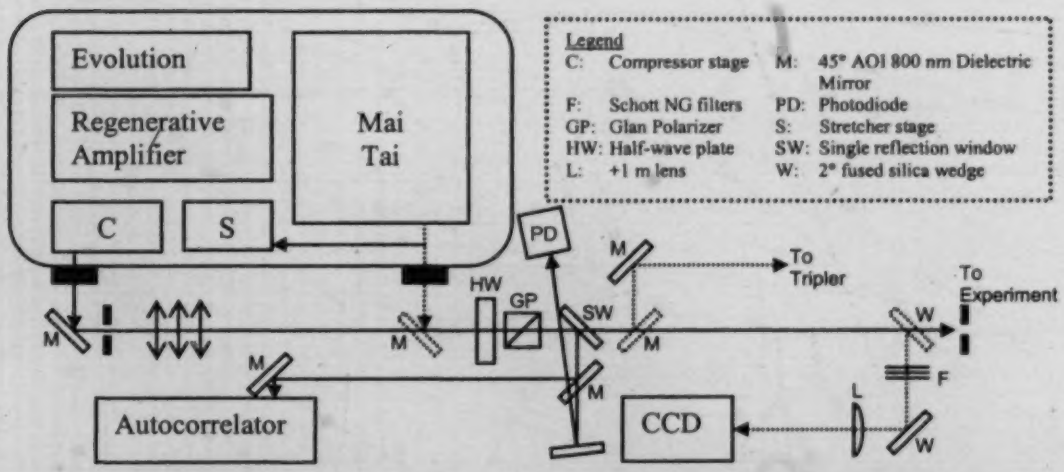

Figure 3.1: Block diagram of the femtosecond laser system with the energy selection optics, pulse width characterization and spatial characterization. The autocorrelator is a Positive Light SSA and the CCD camera is a Spiricon SP-980. The optics and beam lines indicated by dotted lines were optional beam lines steered by flip mirrors. The polarization of the main beam was parallel to the optics table as indicated after the first mirror in the diagram.

To amplify the Mai Tai seed pulses, the Hurricane used chirped pulse amplification. The seed pulses were spectrally stretched by a grating to nanosecond pulse durations and amplified in a Ti:Sapphire crystal pumped by a Q-switched Nd:YLF laser (Spectra-Physics Evolution) at 523.5 nm wavelength in the regenerative amplifier. A Pockels cell extracted seed pulses at a maximum 1 kHz repetition rate from the 80 MHz pulse train of the Mai Tai for injection into the regenerative amplifier and a second Pockels cell rotated the polarization of the amplified pulse after about 13 round trips in the cavity for coupling out of the amplifier by a thin film polarizer.

The pulse was recompressed in a gold grating compressor giving final pulse energies between 400 μJ and 600 μJ per pulse. Adjustment of the distance between the retro-reflector and the compressor grating could be used to tune the amplified pulse widths from 120 fs to 800 fs FWHM assuming a Gaussian temporal profile. Dispersion compensation for the optics to the final experimental setup could be achieved by chirping the pulse so that the blue component was at the leading edge of the pulse.

A commercial single-shot autocorrelator (Positive Light SSA) [105] with 20 fs resolution was used to measure the pulse width of the amplified pulses at the output of the laser system. This autocorrelator was a background-free detection system that split the input beams into two non-collinear beams that overlapped in a KDP crystal. The second harmonic light was imaged onto a linear charge-coupled detector (CCD) array after a blue filter so that only the autocorrelation beam (second harmonic) was recorded. The output of the CCD array was viewed on a Tektronix TDS360 oscilloscope at 5 ms full sweep time where the FWHM of the output pulse was measured.

To calibrate the autocorrelator, a micrometer, which controlled the position of the retro-reflecting mirror, was adjusted (x_{space}) and the movement in time of a reference point on the oscilloscope (for example: the peak of the pulse) was recorded (t_{opt}). The calibration of the autocorrelator was $2x_{space}/(c_0\, t_{opt})$ in fs/μs (the distance was doubled since the micrometer was mounted on a retro-reflector stage). Multiple calibrations yielded (0.455 ± 0.01) fs/μs. To determine the FWHM of the original pulse, we first assumed that the incoming laser pulse was Gaussian in time, which requires that the autocorrelation FWHM (in fs) be divided by the square root of 2. Overall these two calibration values were equivalent to multiplying the autocorrelator FWHM (in μs) by 0.32 to get the FWHM of the Gaussian pulse in femtoseconds.

A commercial imaging system (Spiricon SP-980 CCD camera [106] and LBA-PC software [107]) was used to characterize the focal spot quality of the femtosecond pulses defined by a 100 cm lens (herein referred to as the equivalent focal plane system). The beam was picked off by a 0.5° fused silica wedge, propagated through a set of NG Schott glass filters, reflected off a 2° fused silica wedge and was focused onto a Spiricon SP-980 linear CCD array by a 100 cm focal length UV-Grade Synthetic Fused Silica (UVGSFS) lens. Any distortions due to misalignment in the regenerative amplifier were corrected to

obtain a high quality Gaussian beam spot. Slight ellipticity of the beam was acceptable as shown in Figure 3.2.

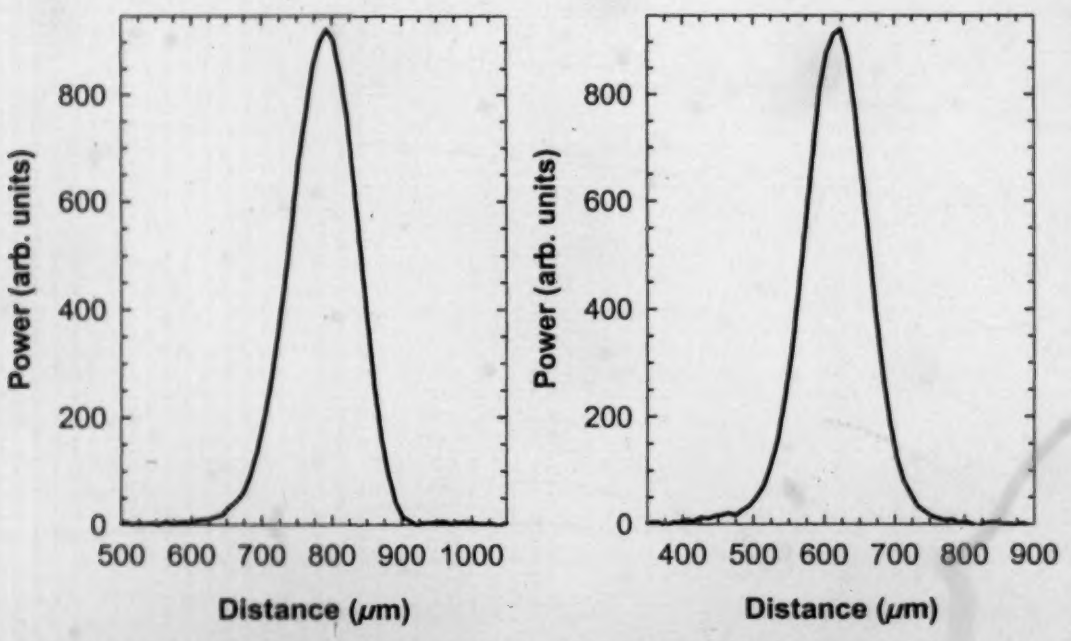

Figure 3.2: Example of the beam profile measured on the SP-980 CCD camera in the equivalent focal plane system. The major axis of the beam profile is on the left and the minor axis is on the right.

Two power meters were used for energy calibrations: a Spectra-Physics Model 407A power meter with the 407 thermocouple head and a Gentec TPM-300CE power meter with the PS-310WB thermocouple head [108]. The Spectra-Physics Model 407A was used for the femtosecond laser ablation experiments. The Gentec power meter was used mainly for the CW laser patterning of self-assembled monolayers experiments with the Ar^+ laser and in the femtosecond laser experiments when the Spectra-Physics 407A was not available due to repairs.

In the femtosecond laser experiments, the power meters were used to calibrate FND-100 ultrafast silicon photodiodes [109] at the 800 nm wavelength that monitored the pulse energy in each shot. The photodiodes were mounted in Hammond Series 1411 aluminum enclosures [110] with an approximately 2" hole cut into the front face. Two UVGSFS diffuser plates were mounted over the opening to scatter the input laser

radiation, making the devices insensitive to beam steering (the entire assembly is referred to herein as a photodiode). The photodiodes were biased at 90 V DC and mounted on Dylux rods that were held in anodized aluminum post tubes to eliminate ground loops. The calibration of the photodiodes was done before every experiment so their absolute calibrations and sensitivities to each incident wavelength were never required (see Appendix C.3 for an example of an energy calibration).

The circuit diagram of the photodiode detectors built by Blair Harwood (our lab technician) is shown in Figure 3.3.

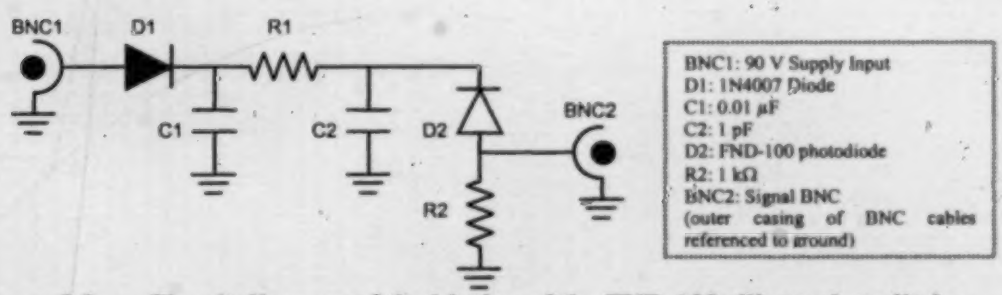

Figure 3.3: Circuit diagram of the biasing of the FND-100 silicon photodiodes.

The nanomilling samples were mounted on a computer controlled 3-dimensional Melles Griot Nanomover I system [111] that was capable of 50 nm position resolution. The positioning stage had an extra kinematic mount on the front face to allow the experimenter to fine tune the alignment of the target to 0° AOI. This mount was built by the Department of Electrical and Computer Engineering (ECE) Machine Shop.

For experiments performed under vacuum, a chamber that could accommodate the Nanomover was used. This chamber was also built by the ECE Machine Shop. The diffusion-pumped vacuum chamber was 60 cm in diameter and 50 cm high (141 L volume) and was capable of base pressures of 10^{-5} Torr under ideal conditions. A 3" diameter CaF_2 window for coupling the laser into the chamber was mounted at a slight angle of inclination to keep retro-reflections from focusing into the optic.

To measure singly-excited copper atoms removed from the copper thin film substrate during nanomilling, a Hamamatsu R7518 photomultiplier tube (PMT) [112] was used. A 1" interference filter with a centre wavelength of 326.1 nm and a 10 nm

bandwidth (CVI F10-326.1-3 [113]) and a 12 % transmissivity was mounted to the front of the detector to measure photons emitted at the copper emission lines of 325 nm and 327 nm. To define the observation angle precisely, an 11 mm diameter aperture was placed before the interference filter. The PMT was calibrated using a diffuse scattering barium sulfate plate irradiated with calibrated laser pulses to provide a known intensity source (W/Sr) with an absolute error of ±15 %. This calibration was done by Michael Taschuk (Ph.D. student) and details can be found in his thesis [114]. For these experiments, the PMT was biased from 700 V to 1200 V, which corresponded to gains between 10^5 and 10^7 and the response was linear for incident photon numbers of less than 10^4.

Offline diagnostic tools were used to measure the resultant ablation spots and SAM line widths. A Philips FEI LaB6 Environmental Scanning Electron Microscope (ESEM) in the Advanced Microscopy Facility in the Department of Biological Sciences at the U of A and a LEO 1430 Scanning Electron Microscope (SEM) with a tungsten filament as an electron source in the Nanofabrication Facility (NanoFab) in ECE were used to measure the ablation diameters of metal samples and the line widths of patterned SAM substrates. A Zygo New View 5000 white light interferometer (WLI) [115] was used as a profilometer to measure ablation depths of samples and the ablation diameters of silicon since the silicon samples did not form adequate images on the SEM even with a thin gold conductive film added to the surface. It is not clear as to why an image of a gold-coated silicon surface was not possible; however, diameters were measured as accurately as possible with the profilometer.

3.1.2 CW laser patterning of self-assembled monolayers

For direct writing of SAMs on gold-coated glass substrates, a CW Coherent Innova 70 Ar^+ laser [116] was used. The Innova 70 is a discharge pumped laser that lases in wavelengths ranging from 457 nm to 529 nm depending on the cavity configuration with a maximum output power of 700 mW in a single-line mode at 488 nm. For these experiments, the flat high reflector was used and the wavelength was tuned to 488 nm with the cavity aperture set to 4 to get the best spatial quality as defined by imaging the Ar^+ laser with the Spiricon imaging system. The laser was operated in Low Light power

regulation mode (2 W maximum) with the tube current monitored and recorded each time it was turned on. The laser usually required a 15 minute warm-up time.

A half-wave plate and Glan polarizer combination was used for energy selection in these experiments. An Industrial Fibre Optics photometer (IF-PM) [117] was used as an energy diagnostic tool and was calibrated for each experiment by a calibrated standard. The calibrated standard was a Newport 1815-C power meter with the setup DIP switch set to 1010 corresponding to a "Low Power with Attenuator" Mode with an OD 3.0 (Model 883-SL) filtered semiconductor detector head (Model 818-SL) [118] with the CAL set to 4.52 for 488 nm.

The thin gold film microscope slides required special handling to ensure the surface was not contaminated. A special mount was made in the MecE Machine Shop that clamped down on the slide to hold it during laser processing with contact parts made of PTFE as shown in Figure 3.4.

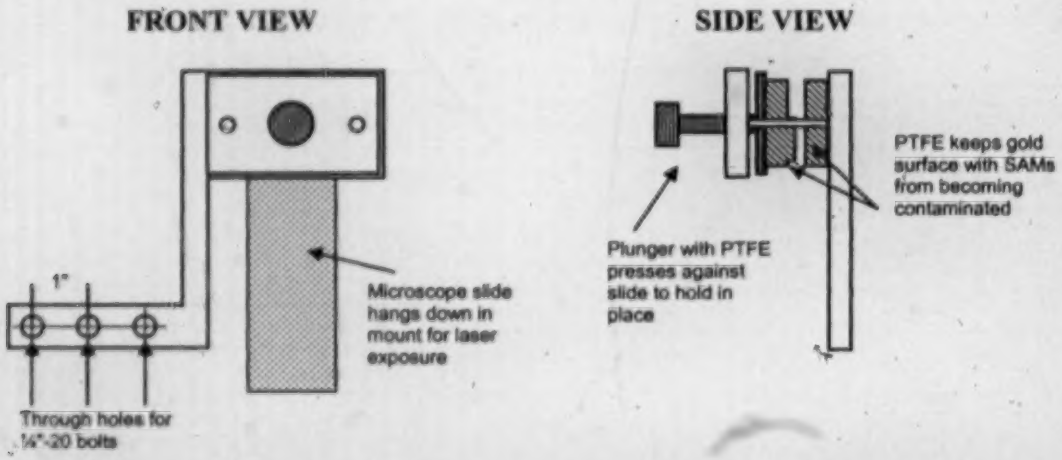
FRONT VIEW
SIDE VIEW
1"
Microscope slide hangs down in mount for laser exposure
Through holes for ¼"-20 bolts
PTFE keeps gold surface with SAMs from becoming contaminated
Plunger with PTFE presses against slide to hold in place

Figure 3.4: Schematic of the SAM microscope slide mount. The front perspective on the left shows the through holes designed for mounting on the front of the Oriel stage and the orientation of the holder during experimentation with details of the PTFE shown on the right.

Samples were mounted on 2D Oriel stages that translated perpendicularly to the optic axis with Oriel motorized micrometers controlled by the Triple Controller, Model 18010 (now part of Newport [118]). The Oriel mounts were attached to a magnetic base.

The focusing optic (10 cm or 25 cm focal length lens) was mounted on a third Oriel stage for translation along the optical axis.

An Environmental Process Control (EPC) Chamber was built in the MecE Machine Shop. The chamber was made of Plexiglas with an inlet for nitrogen gas and an air outlet at the base that allowed for the Encoder Mike wire to feed through and for the expulsion of the ambient atmosphere. One side of the chamber was attached by screws and had a rubber seal to allow for sample loading, and a 1/16" thick BK7 window was mounted on one face for laser coupling into the chamber. A small steel plate was recessed in the base of the chamber to mount the translation stages with a magnetic base in the chamber. The MecE Machine Shop tested the chamber and showed that the atmosphere was 97 % nitrogen after 7 minutes of flushing.

The SAM lines were imaged using either the ESEM or SEM as described in Section 3.1.1. The line widths were measured by size of the dark region in the image that resulted from the brightness differences between the two SAMs [119].

3.2 Materials

3.2.1 Target samples and substrates

The single-shot ablation threshold and incubation coefficient were measured for both bulk and thin film samples of copper and gold, and bulk samples of silicon. For the experiments with copper, a sample of commercial high purity polycrystalline copper foil 25 μm thick [1] was used with a specified purity of 99.9 % and an average roughness R_a of (280 ± 80) nm as measured by white light interferometry in a 120 μm field of view. The foil was stored tightly wrapped and showed no visual signs of aging or discoloration.

The thin metal films were prepared in the NanoFab by sputtering the films onto silicon substrates in a Kurt J. Lesker CMS Series deposition system [120] that used magnetron sputtering with sputter targets supplied by the NanoFab. The silicon substrates used for deposition of the films were cleaned by Piranha etch in the clean room facilities before sputtering. The quality of the thin film samples varied since thin films were made by various users and stored in a variety of conditions over the years. The copper thin film samples prepared for the nanomilling and threshold determination project were 250 nm thin films sputtered onto a silicon substrate with a 250 nm

chromium adhesion layer between the copper and silicon layers. The film was visually smooth with an R_a of (0.6 ± 0.2) nm measured by the white light interferometer in a 120 μm field of view. The 250 nm copper thin film sample was stored in a nitrogen environment to minimize oxidation of the surface.

Other copper thin film samples were used to explore the sensitivity of the ablation threshold to sample variations. The single-shot ablation threshold was measured for a 500 nm copper thin film that had been exposed to ambient air for one year and showed visible signs of oxidation (the surface was mottled with brown patches indicative of oxidation). Copper samples of varying thicknesses were prepared for other depth profiling experiments using Laser-Induced Breakdown Spectroscopy. The films had copper thicknesses varying from 100 nm to 300 nm with chromium adhesion layers varying from 50 nm to 300 nm. The reflectivity of the thin film samples was measured as a calibration step.

Gold thin films were sputtered onto microscope slides for the SAM patterning projects. The microscope slides were made of soda lime glass [121] and purchased through Fisher Scientific as Premium microscope slides (catalogue number 12-544-1). The glass slides were not cleaned before sputtering since the slides were purchased pre-cleaned and wrapped in cellophane to eliminate debris and to keep them clean.

Two types of silicon substrates were used to measure the single-shot ablation threshold. The first was purchased through the NanoFab. The silicon was p-type silicon, Boron doped, with a <100> orientation and a resistivity of 1-30 Ω-cm [122]. The second sample was high-resistivity (5000 Ω-cm to 7000 Ω-cm) intrinsic silicon with a (100) orientation [123]. Both samples were single-side polished.

3.2.2 SAM deposition chemicals

For the patterning of SAMs on gold-coated glass substrates, gold thin film samples were prepared as indicated in the previous section and then stored in a clean glass microscope slide holder filled with 200-proof denatured ethanol [124]. Two SAM chemicals were used to achieve either a hydrophobic or a hydrophilic region. The hydrophobic monolayer was Fluka 1-hexadecanethiol (95 % purum, 100 mL) purchased from Sigma-Aldrich (catalogue number 52270) [125]. The hydrophilic monolayer was

16-mercaptohexadecanoic acid (90 % pure, 1 g) purchased from Sigma-Aldrich (catalogue number 448303-1G). SAM surface patterning will be described in Section 3.5.

3.3 Femtosecond laser experiment techniques

3.3.1 Preliminary notes on Ti:Sapphire laser performance

The Ti:Sapphire laser system was arranged on the optics table when the lab was built so that the output passed through the two apertures indicated in Figure 3.1. The first aperture alignment was made using the last mirror inside the Hurricane chassis. The alignment through the first aperture was always verified but rarely adjusted. The output beam was reflected at 90° by a dielectric mirror through the first aperture, as shown in the figure, to an aperture at the far end of the table. Alignment through the second aperture was made using a diffraction pattern formed by closing down the first aperture. The second aperture was imaged by a CCD camera and viewed on a television screen so the alignment could be optimized. This was a necessary step since all the experiments in the lab were built based on this starting alignment.

Energy selection was made by a combination half-wave plate and Glan polarizer. The Glan polarizer was oriented to maintain the horizontal polarization state of the laser (parallel to the optics table). The output of the Ti:Sapphire had a pre-pulse that occurred 8 ns before the main pulse. This pre-pulse resulted from leakage out of the regenerative amplifier resulting in a pulse about 1000× smaller in energy occurring one round-trip (8 ns) before the main pulse.

The pre-pulse was measured using a FND-100 ultrafast silicon photodiode, labelled PD in Figure 3.1, optimized for faster transients and limited stored energy by changing the circuit in Figure 3.3 to C1 = 1 μF, C2 = 1.5 pF and R2 = 50 Ω (referred to as the pre-pulse photodiode). The pulse train was measured on a Tektronix TDS360 scope with a 50 Ω terminator. This configuration caused the pre-pulse photodiode to saturate at approximately 200 mV peak voltage when the main pulse arrived, so Schott NG glass filters were used to reduce the input beam energy as required. The transmissivity of the filters was calibrated in another experiment and these values were used to correct the main pulse and pre-pulse measurements to calculate the contrast ratio.

The polarization of the main pulse and the pre-pulse from the output of the Ti:Sapphire was measured by removing the half-wave plate and rotating the Glan polarizer. The peaks of the main pulse and the pre-pulse were measured as stated above using NG Schott glass filters and correcting for transmissivity. The polarization of the pre-pulse was shifted approximately 15° from the main pulse as shown in Figure 3.5.

The offset in the pre-pulse polarization from the main pulse forced energy selections to be kept between 0° and 30° on the half-wave plate (45° theoretically giving zero energy). If the half-wave plate was turned beyond 30°, then the contrast ratio would drop giving a pre-pulse of significant energy compared to the main pulse interacting with the sample. Another undesired effect was polarization mixing. The polarization of the main pulse was 1000:1, so angles beyond 30° also led to a mixed polarization that was undesired since these would affect laser-induced periodic surface structuring, which was investigated along with the single-shot ablation threshold. The measurement of the contrast ratio against the half-wave plate angle is shown in Figure 3.6.

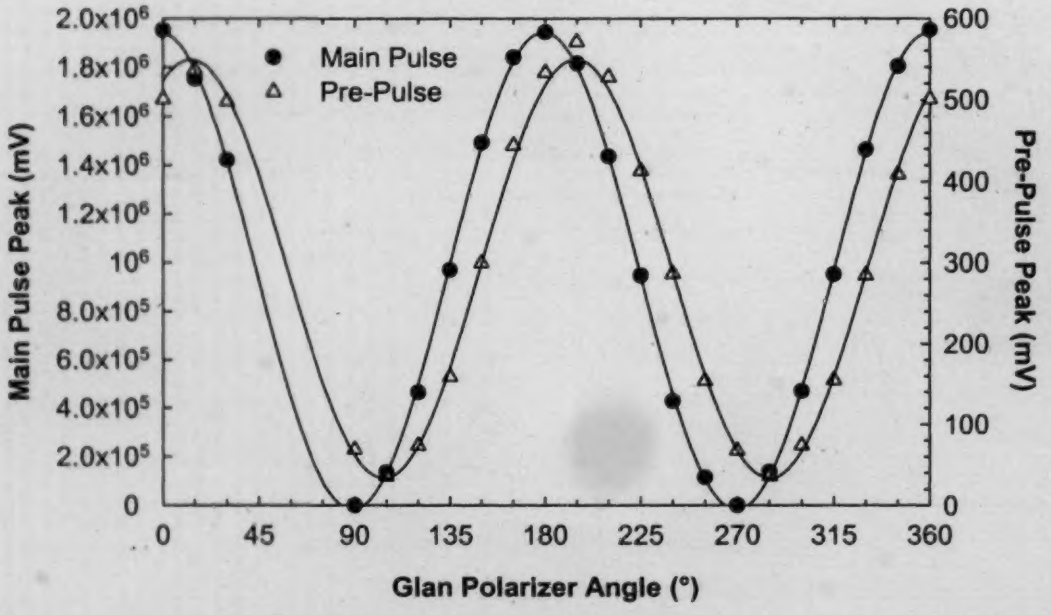

Figure 3.5: Polarization of the main pulse and the pre-pulse from the output of the Ti:Sapphire laser. The minimum in the main pulse at 90° and 270° is actually 484 mV and 598 mV, respectively.

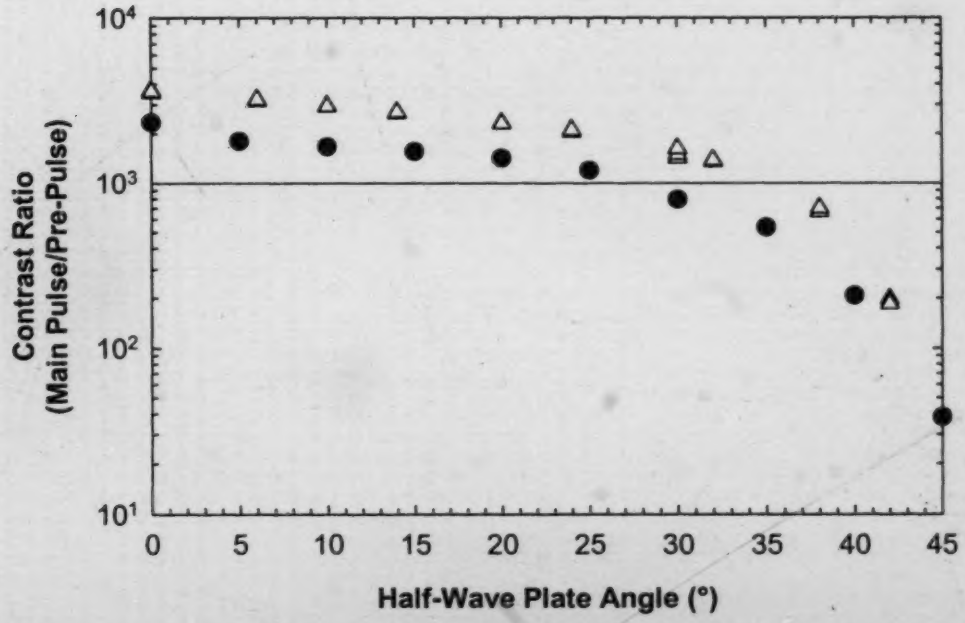

Figure 3.6: Contrast ratio of the Ti:Sapphire laser after the half-wave plate and Glan polarizer. The reference line shows the desired 1000:1 contrast ratio for the experiments. Two measurements were made as shown by the two data sets.

Energy selection was made between 0° and 30° on the half-wave plate as stated earlier and further reductions in energy were achieved using NG Schott glass filters in the main beam path.

The optical components were mounted in kinematic mounts with anodized aluminum bases and post holders, and brass posts. Anodized aluminum collars were on the brass posts to allow adjustment of the AOI on an optic after the height of the optic was defined. Most of the optics mounts were built in the ECE Machine Shop.

3.3.2 Initial steps in the femtosecond laser experiments

Femtosecond laser-material interaction studies were carried out in several setups over several years. The setup shown in Figure 3.7 was used for the majority of the results reported in this thesis and represents the generic setup for ablation experiments. When the nanomilling experiment was built initially, the laser beam was centered on the apertures shown in Figure 3.7. The lens was placed into the beam path and its alignment

was adjusted such that the diffracted 4 % retro-reflection from each face was aligned on the second aperture as it was closed. When the two retro-reflections aligned, this indicated that the lens was square to the beam (0° AOI) and the optic axis went through the centre of the lens. This procedure minimizes ellipticity and asymmetry in the focal spot. The lens was oriented with the curved surface towards the Ti:Sapphire output to minimize 3rd order aberrations and to allow the focal spot to approach the diffraction limit. A collar on the brass post maintained the height alignment of the optic so it could be removed from the setup during experimental alignment.

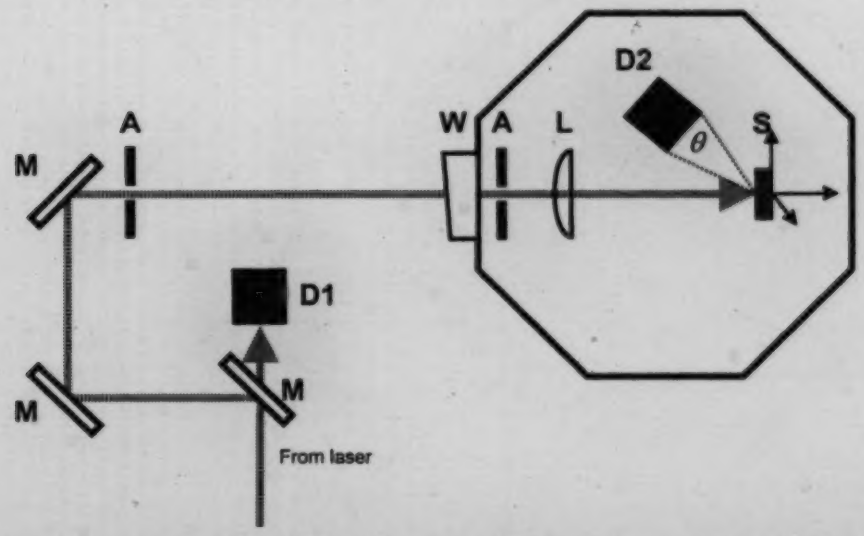

Figure 3.7: Experimental setup for nanomilling and femtosecond SAM laser patterning. The labels in the diagram correspond to: M, 45° AOI 800 nm centre wavelength dielectric mirrors; A, apertures; W, CaF_2 window mounted at an angle; L, focusing lens; D1, FND-100 photodiode assembly; D2, PMT; S, substrate and motion stage.

At the start of each experiment, a beam block was placed after the first aperture in the nanomilling setup, the lens was removed from the setup and the sample was mounted on the Nanomover before the aperture on the Ti:Sapphire chassis was opened. The Ti:Sapphire was aligned along the table as indicated in the previous section.

Preliminary calibrations of the laser were made by measuring the autocorrelation FWHM on the Tektronix TDS360, the contrast ratio on the pre-pulse photodiode at 0° on the half-wave plate, the spatial profile on the equivalent focal plane camera system, and

the output energy on the Spectra-Physics power meter at 1 kHz. If the contrast ratio was above 1000, the equivalent focal plane spatial profile was Gaussian with a FWHM of approximately $(100 \pm 20)\ \mu m$, the pulse width was less than 450 μs FWHM (143 fs FWHM Gaussian), and the output power above 400 mW, then the experiment continued. If any of these conditions were not met, I realigned the Ti:Sapphire system and the extent of this realignment depended on the degree of non-conformity.

If the experiment continued, then the laser beam was steered towards the experimental setup by dielectric mirrors at a 45° AOI. Since the laser was horizontally polarized, it was p-polarized on the mirrors and provided sufficient leakage light to measure the pulse energy with the photodiode. The laser was directed to the experimental setup though two final alignment apertures, shown in Figure 3.7, to square the beam along the pre-defined experimental path.

The beam block was placed between the sample location and the lens location and the laser was aligned through the apertures using two steering mirrors. Once the beam was centered on both apertures, the beam block was removed and the reflective sample was aligned using the kinematic mount on the Melles Griot to 0° AOI with the main laser by aligning the reflected light from the sample to the first aperture. The beam block was replaced between the lens and sample location and the lens was replaced into its holder. The AOI of the lens was adjusted (yaw adjustment) until the two diffracted retro-reflections from the surface of each face overlapped on the back of the second aperture and the brass post was secured.

The energy reference plane was defined as after the lens, so energy calibrations were made by placing the power meter (Spectra-Physics or Gentec) after the focusing optic. The focal lengths of the lenses were greater than +20 cm so the intensity was still well below the damage threshold for the power meter in the first few centimeters.

The output of the photodiode was measured on a Tektronix TDS 210/220 digital oscilloscope with either a 1 MΩ or 50 Ω termination. Care was taken to make sure the peak voltage did not exceed 10 V. A 1 MΩ termination was the input impedance of the oscilloscope and the femtosecond pulse caused a rapid nanosecond rise followed by a slow decay at the RC time constant defined by 1 MΩ input impedance and the RG-58 BNC cable capacitance of ~30 pF/ft. The measurement of the photodiode signal was

made at 100 μs after the very fast rise of the signal since the oscilloscope tended to have noise fluctuations at the peak. The point 100 μs from the peak was a clean, well-defined point in the curve. The pulse energy was defined as the difference in the voltage from the baseline to the voltage 100 μs after the peak. If the cables were longer than 6 ft, then the *RC* time-constant was such that the signal would not relax to zero before the rise of the next pulse at the 1 kHz repetition rate. It was imperative that each pulse in the calibration reached the baseline before the next pulse or else the calibration was distorted for experiments done in single-shot mode or at repetition rates of less than 1 kHz. For longer cable lengths, a 50 Ω terminator gave pulse-like signals in a 5 ns time scale and the peak of the pulse referenced to the baseline was used as the photodiode signal.

Random triplicates of 6 to 8 energy values were made when calibrating the photodiode with the power meter. This test verified whether any systematic errors were present during calibration such as warming of the sensor head over time that could lead to changing energy measurements over time. The power meter was zeroed at the start of every calibration to compensate for any temperature changes.

The photodiode and power meter measurements were plotted in an Excel spreadsheet and a linear regression of the data determined the calibration in V/J. The intercept was examined for a significant offset (95 % confidence interval) that indicated bias in the calibration (see Appendix C.3).

3.3.3 Focal spot calibration

Two focal spot positioning techniques were used to define the position of the target with respect to the focal plane. The first technique used a diode laser focused on the target by a 20 cm lens at an angle from the optical axis. The reflected light from the target was defocused by another 20 cm lens to propagate several meters to a sheet of graph paper with 1/2 cm square divisions on a wall. To determine the focal plane position on the graph paper, a reflective target such as silicon with a low damage threshold was mounted on the Nanomover, as indicated in Section 3.3.2, and the target was moved along the optical axis, through the focal region, with a single shot taken every Δz (usually with a 100 μm step size) on a fresh spot. The sample was removed and the spots examined by optical microscopy.

The position on the Nanomover corresponding to the location of the minimum spot size was noted and the sample was remounted on the Nanomover and aligned for 0° AOI to the Ti:Sapphire beam, as discussed in the previous section, to ensure that the diode laser returned to the same spot on the wall. The sample was translated to the focal spot position and a mark was made at the diode laser position on the graph paper. For every new experiment with a specularly reflective sample and the Ti:Sapphire at 0° AOI, the position of the diode spot on the wall indicated that the sample was at the focal spot to within 20 μm. Backlash is an inherent mechanical error in all motion stages, but it was not compensated for in this calibration technique either since it represented very little error in the Nanomover positioning.

If the focal spot measurements in the optical microscope were inconclusive, for example, the step size passed through the focal region too quickly and smaller steps were required, the calibration was repeated until a satisfactory focal plane was determined. The smallest Rayleigh range for these experiments was approximately 400 μm with a 10 μm 2 e-folding beam radius, making this technique sufficiently accurate.

The second focal spot positioning technique was introduced later in the experiments. A CCD camera on a periscope with a 10× microscope objective was mounted off the optical axis in the chamber and a pin was placed in the exact center of the chamber as defined by HeNe lasers that criss-crossed through alignment decals mounted on the window ports of the chamber. This reference point was imaged by the CCD camera while the pin was illuminated by the HeNe lasers. Once the image was formed, the HeNe lasers were removed and the diode laser was focused onto the pin and adjusted until the illumination was seen on the CCD camera.

The nanomilling lens was mounted on a translation stage that had a mechanical micrometer adjustment and was aligned to be square with the Ti:Sapphire beam path as described in Section 3.3.2. A reflective sample was mounted on the Nanomover target positioning stage and an ablation spot was made with a single shot to provide a scattering point for the diode laser. The sample was moved towards the reference plane in the centre of the chamber, as defined when an image formed on the CCD camera. The image indicated the sample was at the centre of the chamber and now the lens position needed to be calibrated so that the Ti:Sapphire focal spot was also at the reference plane.

The focal plane was defined in the same manner as the first calibration technique by taking single shots at fresh spots on the sample, except the *lens* was moved towards the sample with each shot and the position of the lens recorded. In the end, the lens was translated to the lens position where the minimum spot size was located as measured by optical microscopy. At the end of each experiment, the Nanomover target positioning stage was parked in the same position, out of the focal plane.

Each fresh sample for subsequent experiments was mounted on the positioning stage and an ablation spot made at the edge of the target by a single-shot of the Ti:Sapphire laser. This spot was imaged onto the CCD camera using the diode laser as an illumination source indicating that the sample was at the reference plane, which now coincided with the focal plane of the nanomilling lens.

A microscope objective could have been used as a machining lens and would have made a practical imaging system, except that the ablation spots would have been too small and the errors too large in calibrating the single-shot ablation threshold and incubation coefficient of a material.

3.3.4 Femtosecond laser ablation threshold and incubation experiments

After the initial setup, the Ti:Sapphire was switched to single-shot mode and the power meter was removed from the chamber. If the experiment required a vacuum, then the chamber was pumped down at this stage; otherwise the chamber was sealed and left at atmospheric pressure. The sample was moved to the image plane as defined by one of the focal spot positioning techniques given in Section 3.3.3.

Random triplicates of ablation shots were made with N shots incident on each spot. Measurements were usually made of the 1, 5, 10, 100 and 1000 shot ablation thresholds. A typical N-shot ablation threshold experiment would start with a marker of several shots at the beginning of a column to help identify the zero position and each data point was separated by approximately 100 μm so smaller spots could be found later in the offline measurement device.

After an ablation series was completed for a sample, the sample was removed from the Nanomover and imaged by the offline techniques described in Section 3.1.1. A MATLAB script program was written to measure the ablation diameters measured by the

ESEM/SEM. Using the Image Processing Toolbox, the images were loaded individually into the program and the user evaluated the images by defining the centre of the ablation spot and then the edges that determined the extremities of the major and minor axis of the ellipse (or circle). An ellipse was drawn over the ablation spot and if the user accepted the ellipse as representative of the ablation crater and orientation, the calibration of pixels/μm (collected in Microsoft Photo Editor using the scale bar on each image) was entered into the program and the new image saved with a new file extension. A new file extension allowed the user to keep the original image while maintaining a record of the measurement.

If the ellipse did not adequately represent the ablation spot, then the user clicked outside the image frame and repeated the process until an ellipse that represented the ablation crater was determined. The program repeated until all the ablation spots for an *N*-shot data series were measured and the results were written to a text file with two columns for the ellipse axes in μm and two columns for the axes measurements in pixels. The data were analyzed with the technique presented in Section 4.1 of the next chapter. Ablation spots were made in random triplicates so that ablation spot measurement error statistics could be collected and used in calculating the overall error in the reported ablation threshold (see Appendix C).

3.3.5 Femtosecond laser pulse nanomilling

Initial steps and focal plane calibrations were the same as outlined in Sections 3.3.2 and 3.3.3.

The PMT was placed as shown in Figure 3.7, 12 cm from the target sample and the observation solid angle was $\sim 6 \times 10^{-3}$ Sr. The PMT output was attached to a Tektronix TDS360 scope set to 25 ns/div and 200 mV/div using a 50 Ω terminator. The laser was triggered by computer and the oscilloscope was triggered by the synchronization pulses sent by the delay generator used to control the timing of the Ti:Sapphire regenerative amplifier. Synchronization forced the PMT signals from the copper emission to occur at the same point in the scope trace, essential for data post-processing. Further background optical noise reduction was accomplished by covering the chamber with black cloth and turning off the room lights during experimentation.

Incident fluences were chosen near the ablation threshold for multiple pulses as demonstrated in Figure 2.2 and experiments were performed at atmospheric pressures. The nanomilled depths were measured offline using white light interferometry.

The PMT trace generated by each laser shot was captured through the GPIB port of the oscilloscope to a computer running LabVIEW. The incident photon number was calculated by integrating the area over a 25 ns window providing a value in V·ns that was directly proportional to the number of incident photons. At these low photon rates, the interference filter acts like a "probability filter" instead of an intensity attenuator so the peak detection was not reduced by 12 % in the final calculations. Using the absolute calibrations, the photons incident on the PMT were plotted for each shot number.

3.3.6 Femtosecond laser pulse patterning of SAMs

Initial steps were the same as outlined in Section 3.3.2 and we assume that the focal plane was calibrated for this procedure. A mechanical beam block was used to initiate and terminate exposure of the sample to the laser beam running at 1 kHz. Chemical preparation is described in Section 3.5.2.

The thin gold film microscope slide coated with the hydrophobic monolayer was mounted using a variation of the mount shown in Figure 3.4. The new mount did not have an arm that offset the sample to hang next to the translation stage; instead the through holes were underneath the sample holder system so that the sample was centered on the Nanomover in the vacuum chamber. The sample holder was attached to the Nanomover before mounting the SAM-coated samples.

Samples were removed from the hydrophobic monolayer solution with PTFE tweezers while wearing powder-free gloves and gripped on the sides of the slide by gloved hands. Samples were blown dry using nitrogen gas from the ECE building supply at 8 psig and care was taken to make sure both sides of the sample were dry.

The slide was placed into the sample holder and was translated to the focal plane. The chamber was closed and the sample was exposed to the focused Ti:Sapphire beam while moving at a predetermined speed with incident fluences above and below the multiple shot ablation threshold. The scanning speed was determined by the repetition rate of the laser and estimated beam spot as follows:

$$v = \frac{2w_0}{N} R \quad (\mu m/s) \tag{3.1}$$

where $2w_0$ is the 2 e-folding intensity beam diameter in μm, N is the number of incident pulses desired for the irradiation and R is the repetition rate of the laser.

After scanning all the lines on the target, the sample was removed while wearing gloves and immersed in the hydrophilic monolayer solution for approximately five minutes. Afterwards it was rinsed with ethanol, blown dry with nitrogen and stored in the nitrogen gas filled storage chamber to keep the sample from oxidation by ozone. Offline measurements were made with ESEM/SEM to measure the hydrophilic line widths and the white light interferometer measured the resultant surface features.

3.3.7 Reflectivity calibrations

To measure the variability in the reflectivity of the thin film samples, the specular reflectivity was measured in the setup shown in Figure 3.8.

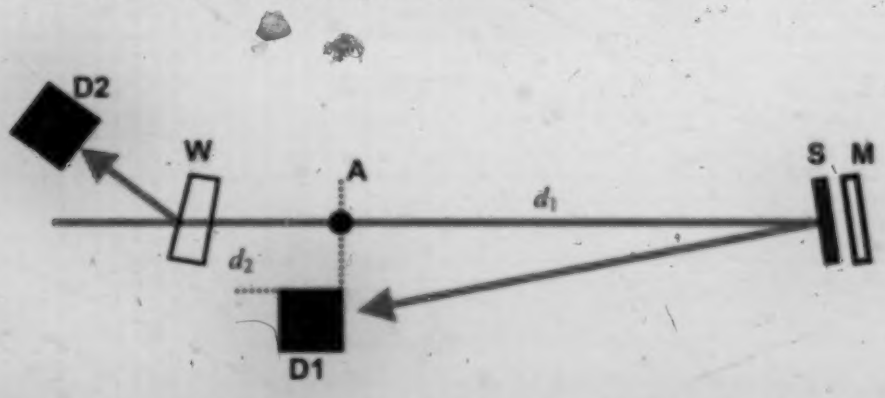

Figure 3.8: General experimental setup for measuring the specular reflectivity. The labels in the diagram correspond to: M, 0° AOI 800 nm centre wavelength dielectric mirror; W, BK7 window; S, substrate under test; D1, power meter or photodiode; D2, photodiode.

The reflectivity of the samples was measured at the 800 nm wavelength using the amplified pulses from the Ti:Sapphire as the illumination source. A 0° AOI 800 nm dielectric mirror was the reflection standard and the reflectivity was also measured using

the Spectra-Physics power meter at position A in Figure 3.8 to measure the incident pulse energy and in the D1 position to measure the reflected pulse energy.

A calibration curve of the standard was generated between the reflected energy detector (D1) and the incident energy detector (D2) in random triplicates at select energies by rotation of the half-wave plate between angles of 0° and 30°. The standard reflector was replaced by the sample under test and the same curve was generated between the reflected and incident energy detectors. The reflectivity was calculated as:

$$R = \left(\frac{D2}{D1}\right)_{standard}\left(\frac{D1}{D2}\right)_{sample} R_{corr} \equiv \frac{D1_{sample}}{D1_{standard}} R_{corr} \tag{3.2}$$

where R_{corr} is the corrected reflectivity if the standard was not measured as 100 %.

Variations of this technique have been used. Specular reflectivity could be measured, for example, by placing the power meter at positions A and D1 to measure the standard and this procedure can be repeated for the sample.

The reflectivity of rough samples requires an integrating sphere to collect all the light scattered on the surface. An in-house integrating sphere coated with barium sulfate paint with photodiode detectors was used. The photodiodes were mounted on the periphery with baffles in front of each of the detectors to block from direct illumination. The reflectivity was measured using a 20 mW CW Melles Griot diode laser operating at 790 nm wavelength [111]. The diode laser was part of an assembly that included a Diode Driver and Thermoelectric Cooler; the current was set to 73 mA and the temperature to 20.2°C. The alignment is shown in Figure 3.9.

The chopper was set to ~360 Hz to generate a time-varying signal on the photodiodes where the peak-to-peak (pk-pk) values of the two photodiodes were measured on a Tektronix 210 scope. Samples in the sphere were mounted off from normal incidence. The pk-pk values of the samples under test were compared to the pk-pk values of the diffuse scatter standard to calculate the reflectivity of the sample.

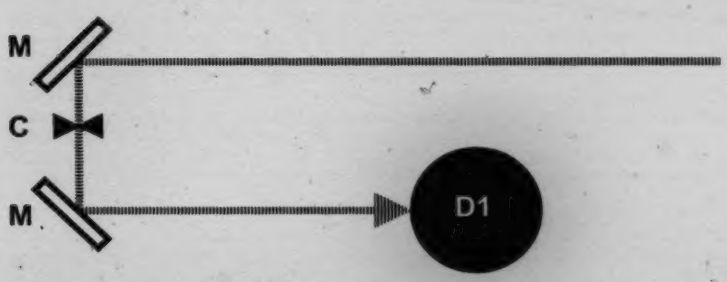

Figure 3.9: Setup for measuring the diffuse reflectivity. The labels in the diagram correspond to: M, 45° AOI 800 nm centre wavelength dielectric mirrors; C, beam chopper; D1, integrating sphere.

3.3.8 Transient reflection dynamics of incident femtosecond laser pulses

The experimental setup was built in the configuration shown in Figure 3.10. The configuration was based on the desire to collect the incident and reflected amplitude and spectrum of the ablation laser pulse to measure the transient changes in the sample reflectivity. The incident and reflected spectra were similar so the spectrometers were removed from the setup, but the configuration was maintained.

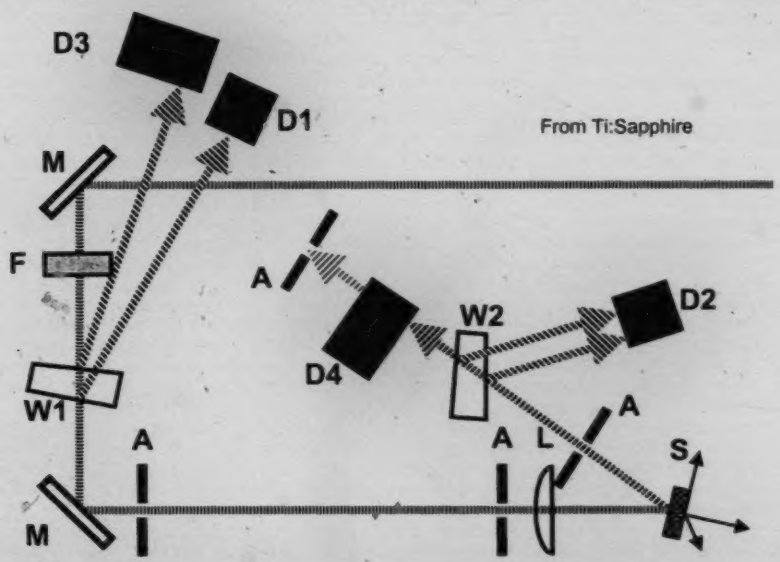

Figure 3.10: Experimental setup measuring the transient reflectivity of a laser pulse incident on a target with a specular reflective surface. The labels in the diagram correspond to: M, aluminum mirrors; F, NG Schott glass filters; A, apertures; W1, 2° UVGSFS wedge; W2, Dynasil 4000 window; L, 15 cm BK7 plano-convex lens; S, specularly reflective sample on Oriel stage; D1 and D2, photodiodes; D3 and D4, Ocean Optics spectrometers (removed, see text).

The focal plane position from the lens was approximated from the focal length specifications of the lens since exact positioning of the sample at the focal plane was not absolutely necessary. The ablation diameters were used to calculate the beam waist (see Section 4.1). A standard reflector was placed in the sample position, S in Figure 3.10, at the approximate focal plane with the Ti:Sapphire at very low intensities and the apertures for the reflected laser beam were installed to define this reference point. After calibration of the standard reflector, the sample under test was mounted in the modified SAM sample slide holder, described in Section 3.3.6, and placed in the reference position, which would cause the reflected beam to pass through the apertures.

To start each experiment, the laser energy, the autocorrelation pulse width, the focal spot spatial quality and the contrast ratio were measured after the laser beam was aligned down the optical table as indicated previously. A beam block was placed in front of the wedge, W1, and the lens was removed from the setup. A standard reflector (0° AOI 800 nm dielectric mirror) was placed in the sample focal plane and the laser was aligned through the first two apertures and the beam block was placed between the lens and the sample. The lens was replaced into the beam line and the angle and centering of the lens was adjusted until the two retro-reflections from the surface of each face overlapped on the back of the second aperture. The brass post for the lens was secured.

Calibration of photodiode D1 attached to a Tektronix TDS210/220 oscilloscope with a 1 MΩ termination was made by measuring the voltage signal 100 μs after the peak voltage rise from the laser pulse. The voltage readings were calibrated against the Spectra-Physics power meter using the same technique described in Section 3.3.2. The incident energy was attenuated a couple of orders of magnitude below the ablation threshold of the mirror (assumed to be 1 J/cm^2) using Schott NG absorbing filters and the standard reflector in the sample position was aligned so the laser beam propagated through the final two apertures. Photodiode D2 was attached to another Tektronix TDS210/220 oscilloscope and measured the same as D1, and was calibrated against the incident photodiode D1 with the same technique as above.

After cross-calibration of the two photodiodes, the beam was blocked, the 100 % reflection standard removed and the Oriel stage with the sample moved into the focal

plane. The attenuated beam hit the sample and an IR camera (Find-R-Scope [126]) was used to verify the alignment through the reflection apertures.

The repetition rate of the Ti:Sapphire was reduced to single shot mode and a fresh spot on the sample was irradiated with fluences that ranged above and below the ablation threshold. Incident fluences a couple of orders below the ablation threshold were used to verify the baseline reflectivity of the sample since they were previously measured using the technique described in Section 3.3.7.

The photodiode responses were recorded for each shot to calculate the reflectivity and the fluence was calibrated by measuring the ablation spot diameters and calculating the beam waist with the analysis technique described in Section 4.1.

3.4 Patterning SAMs with the Argon ion laser

Gold thin film substrates were prepared in the NanoFab as described in Section 3.2.1 and deposition of the hydrophobic monolayers will be discussed in Section 3.5. The experimental setup was built in Dr. Wilson's laboratory on the fifth floor of MecE at the U of A. This setup is shown in Figure 3.11.

Two focusing optics were used to assess the variation in the resultant SAM line widths due to variations in intensity and beam size. The distance from the optic to the sample was calculated using Gaussian beam ray matrix calculations assuming a collimated beam input to the BK7 plano-convex lens. The distance from the lens mount to the BK7 window was calculated and the position of the Environmental Process Control (EPC) Chamber defined for experiments involving either lens. An outline was drawn on the steel plate to make sure the magnetic base, which held the target positioning stage, was returned to the same spot each time. The confocal range of the 10 cm lens was calculated to be 10 mm, and the 25 cm lens to be 66 mm (for the 514.5 nm line). To ensure that the smallest focal spot was incident on the sample, the lens was scanned along the optical axis for the 10 cm lens and left stationary for the 25 cm lens, since the maximum range of the Oriel stages was 25 mm.

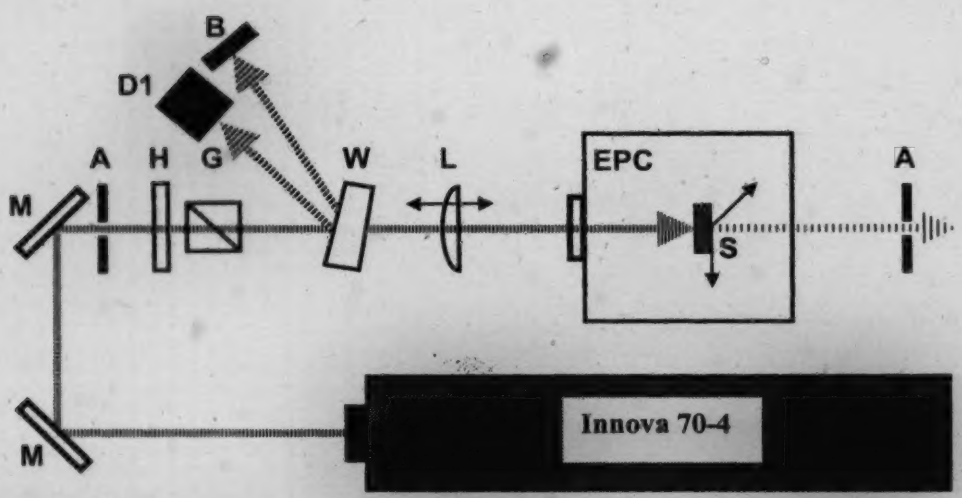

Figure 3.11: Experimental setup for the CW Ar^+ direct laser writing of SAMs. The labels in the diagram correspond to: M, aluminum mirrors; A, apertures; H, half-wave plate; G, Glan polarizer; W, 2° UVGSFS wedge; D1, Industrial Fibre Optics photometer; L, 10 cm or 25 cm BK7 plano-convex lens; EPC, environmental process control chamber; S, substrate and motion stage, the angled arrow indicating translation along the y-axis (out of the page). The Gentec TPM-300 power meter with the PS-310WB head was used as the calibration standard.

Before the experiment, the laser was aligned through the two apertures using the aluminum mirrors with the EPC Chamber and lens removed from the optical path. After alignment, the photometer was calibrated against the calibration standard power meter placed after the 2° wedge quartz plate. The small change due to the lens and entrance window to the sample in the Environmental Chamber was calibrated by separate measurements and used to calculate the actual power at the sample position.

After calibration, the focusing lens was aligned in the system by examining the transmitted beam on the second aperture and the two reflected beams on the first aperture. The EPC Chamber was placed in the optical path and the back reflection of the coupling window was aligned with the first aperture. A gold-coated slide without an SAM surface was mounted in the slide holder with the power set to a minimum and the slide tilt was adjusted such that the back reflection was centered on the first aperture and the magnetic base was secured.

After the complete alignment, the hydrophobic SAM-coated sample was mounted in the PTFE holder. The EPC Chamber was sealed and the nitrogen flow started. After 7

minutes, patterning of the SAM surface began. Incident powers were within a range delimited by gold film damage and the threshold for monolayer desorption. Incident powers ranged from 50 mW to 150 mW for the 10 cm lens, and 100 mW to 250 mW for the 25 cm lens.

The procedure for patterning the SAM substrates involved random triplicates of incident power values to minimize systematic errors and examine experimental error. To create the lines, the focused beam was scanned at 200 μm/s to draw 6 mm long lines. The incident power was monitored before and after each scan since the power of the Ar^+ laser could drift during a run. The resultant widths were correlated to the measured incident power.

After completing the scan sequence for each slide, the chamber was opened and the processed hydrophobic SAM-coated microscope slide was dipped in the hydrophilic solution. After a two minute immersion, the sample was removed, blown dry with nitrogen, and placed in a fresh container with absolute ethanol for storage.

3.5 SAM substrate preparation

3.5.1 Patterning of SAMs with the Argon Ion laser

Sample preparation was done by M.R. Shadnam for this portion of the project. The substrates were prepared by cleaning 1 mm thick soda-lime glass microscope slides (Erie Electroverre Glass) for 2 hours in chromic acid and subsequent rinsing with distilled water. The slides were sonicated in acetone for 10 minutes, rinsed in distilled water, blown dry with nitrogen and stored in 200-proof denatured ethanol [124]. This procedure ensured the surface cleanliness before forming the gold surface layer by sputtering a 50 Å titanium adhesion layer and a 300 Å gold film layer in an ultra-high vacuum chamber in the NanoFab. After removal from the chamber, the slides were immediately transferred to a 1 mmol/L ethanolic solution of 1-hexadecanethiol for 2 hours, rinsed with and stored in ethanol.

The hydrophilic solution, prepared on the day of the experiment, was a 1 mmol/L ethanolic solution of 16-mercaptohexadecanoic acid. After preparation, the solution was further filtered by a PTFE filter (~1-3 μm pore size).

3.5.2 Patterning of SAMs with femtosecond laser pulses

When the femtosecond patterning project started, I bought chemicals and developed my own SAM deposition technique based on the literature review of SAMs on metal surfaces in Section 5.1. The following procedure assumes that the 30 nm to 50 nm gold thin film substrates were prepared, stored in ethanol and available for deposition of the SAM preceding this procedure. Powder-free gloves were worn always.

The glassware was cleaned using a 10:1 solution of deionized (DI) water (available in all ECE laboratories) and Versa-Clean liquid (Fisher Scientific catalogue number 04-342) measured in a graduated cylinder and poured into a 600 mL beaker. *Versa-Clean is a non-toxic alternative to chromic acid for cleaning glassware.* A 100 mL volumetric flask, a 150 mL beaker, a PTFE-coated spatula, PTFE tweezers, staining dishes and a glass funnel were cleaned with a lint-free towel (Kim-Wipes) soaked in the cleaning solution and rinsed with DI water. The glassware was dried for 10 minutes on a Versa-Dry pad in a fume-hood under a heat lamp.

The hydrophobic monolayer solution was made by drawing from an amber bottle used to store a small 5 mL to 10 mL sub-sample of the chemical to keep from contaminating the original sample. A weighing boat was placed in the leveled analytic scale (Denver Instruments APX-60) and zeroed. The hydrophobic chemical was extracted using a Pasteur pipette and disposable bulb and was measured to 25.8 mg. The pipette was disposed in the glass disposal and the bulb thrown in the regular trash.

The contents of the weighing boat were poured into the 100 mL volumetric flask and the boat rinsed with a squeeze bottle filled with denatured alcohol (85 % ethanol, 15 % methanol) to ensure all the liquid was poured into the flask. The flask was topped to 100 mL and then poured into the staining dish. The staining dish was a square glass jar that kept microscope slide surfaces separated while immersed in a liquid. A stainless steel 6" 20-gauge sparging needle, used for aerating liquids, was attached to an argon tank and the needle was put into the 1 mmol/L hydrophobic monolayer solution. Argon flowed at 5 psig for 10 minutes after the gold-coated slides were immersed in the hydrophobic solution [127]. The gas flow was turned off, the needle was removed slowly and the dish covered with aluminum foil as to not disturb the argon gas-filled head space. The slides were stored for 24 hours in this solution.

The hydrophilic solution was made on the day of the experiment (next day from making the hydrophobic SAM slides). A fresh weighing boat was placed in the analytic balance and the balance was zeroed. A sample of 28.8 mg of the hydrophilic compound was extracted using a PTFE-coated spatula and the contents of the weighing boat were rinsed into a clean 100 mL volumetric flask with an ethanol-filled squeeze bottle. The flask was filled to 100 mL as measured by the bottom of the meniscus. The flask was placed in a sonicator filled with water for several minutes until the large pieces of the solute were broken down and dissolved. The solution was poured into a 150 mL beaker and covered with aluminum foil.

Chapter 4

Femtosecond laser pulse nanomilling of metal surfaces*

4.1 Determining the single-shot ablation threshold for a material using Gaussian spatially-shaped laser pulses

A frequently used technique for determining the ablation threshold was developed by Liu to measure the diameter of a Gaussian laser beam by examining the ablation diameters on a material surface at various laser energies [38]. To evaluate the ablation threshold for copper, the dependence of the ablation spot size on the ablation threshold fluence and peak incident laser fluence for a Gaussian profile beam is given by:

$$D^2 = 2w_0^2 \ln\left(\frac{\phi_{pk}}{\phi_{th}}\right) \ (\mathrm{m}^2) \qquad (4.1)$$

---

* Portions of this chapter were previously published in: S.E. Kirkwood, A.C. van Popta, Y.Y. Tsui, and R. Fedosejevs, "Single and multiple shot near-infrared femtosecond laser pulse ablation thresholds of copper," *Appl. Phys. A*, vol. 81, pp. 729-735, 2005; S.E. Kirkwood, M.T. Taschuk, Y.Y. Tsui, and R. Fedosejevs, "Nanomilling surfaces using near-threshold femtosecond laser pulses," *J. Phys. Conf. Ser.* (accepted May 9, 2006).

where D is the diameter of the ablation spot, w_0 is the e-folding electric field amplitude beam radius (or 2 e-folding intensity radius) for a Gaussian beam spot, ϕ_{pk} is the peak energy density (fluence) and ϕ_{th} is the threshold fluence for observable damage. We have called this technique the Gaussian beam limiting technique (GBLT).

The ablation threshold was measured for different numbers of laser shots, N. In each experiment where the sample surface was irradiated with N pulses at each sample point, eight to ten different pulse energies that extended over a range of approximately $0.5\phi_{th}(N)$ to $20\phi_{th}(N)$ were measured. These energies were repeated in triplicate to evaluate the experimental error. The major and minor diameters of the ablation spots were measured by scanning electron microscopy, since a small amount of ellipticity was often observed in the ablation spots, and the squares of these diameters were plotted against the logarithm of the incident pulse energy to give two curves for each experiment:

$$D_i^2 = 2w_i^2 \ln\left(\frac{E_{pulse}}{E_{th}}\right) \quad (m^2) \tag{4.2}$$

where i represents either the major or minor axis, w_i is the 2 e-folding intensity beam radius and the ratio of pulse energies replaces the ratio of fluences in equation (4.1). A linear regression fit of the data provided a slope that gave the major and minor beam radii, and an intercept for each line at $D^2 = 0$ to get E_{th}. The weighted average [128] of the energy threshold from each line at the $D^2 = 0$ intercept was converted into the threshold fluence, ϕ_{th}, for ablation using:

$$\phi_{th} = \frac{2E_{th}}{\pi w_{major} w_{minor}} \quad (J/cm^2) \tag{4.3}$$

Increased precision in the measurement of the ablation threshold was achieved from repeated experiments (see Appendix C.3). The errors in the ablation threshold and beam radius were calculated from the standard deviation in the linear regression fits of equation (4.2) [128]. The error in the energy was a combination of the accuracy of the energy monitor and the precision in the calibration against the photodiode. All error

values were calculated as the first standard deviation assuming a random, normally distributed error.

To evaluate the incubation coefficient, a weighted least squares fit of all the N-pulse ablation thresholds for a sample was made to the linearized form of equation (2.3) (p.201 of ref. [128])

$$\ln[\phi_{th}(N)] = (\xi - 1)\ln(N) + \ln[\phi_{th}(1)] \qquad (4.4)$$

The slope of the fit returns the incubation coefficient and the intercept provides the single-shot ablation threshold. The single-shot ablation threshold was a free variable in the least squares fit and was compared with that from equation (4.3) for consistency within the error bars of the measurements.

For each measurement of spot diameters from N incident pulses, repetition of an experimental data set on different days did not always yield equivalent beam radii (w_i) due to variations in the beam spots from day-to-day fluctuations in the laser operating conditions. Normalization of the data set with respect to the beam waist allowed for combining experimental data points graphically to demonstrate the consistency of the measurements. Normalization was done in terms of a relative diameter squared, D_{Rsq}, where the diameters were normalized to the respective Gaussian beam diameters determined from each individual experiment as given by:

$$D_{Rsq} = \frac{D_{minor} D_{major}}{4 w_{major} w_{minor}} = \frac{1}{2}\ln\left(\frac{\phi_{pk}}{\phi_{th}}\right) \text{ (unitless)} \qquad (4.5)$$

where D_{major} and D_{minor} are the diameters of the individual ablation spots measured with the MATLAB program and w_{major} and w_{minor} is the extrapolated beam waist from equation (4.2). This normalization is a post-processing normalization that has also been used by Lenzner *et al.* [129].

4.2 Femtosecond laser pulse ablation threshold and incubation of copper

Measurements of the single-shot and multiple-shot ablation thresholds are reported and the reduction of the ablation threshold with the number of shots can be quantified in terms of an incubation coefficient for fs NIR laser interaction. The only previously reported measurement of an incubation parameter for copper is that of Jee *et al.* [39] who used 1064 nm, 10 ns Nd:YAG laser pulses on nearly surface-defect-free copper samples of different crystal orientations. Three different copper samples were used in this chapter to study the variation in the ablation threshold for samples with different surface reflectivities: GF copper foil and two thin films of copper with thicknesses of 250 nm and 500 nm. Often in practical laser ablation applications, metal surfaces have been exposed to air for a long period of time and may have modified surface reflectivities. The effects of surface quality will be shown.

The ablation threshold for the GF copper foil was evaluated using the method described in Section 4.1 for $N = 1$, 2, 5, 10, 100 and 1000 pulses. Examples of scanning electron microscope (SEM) images of ablation spots are shown in Figure 4.1.

The ablation diameters were measured at the outer boundary of the ripple zone as shown in Figure 4.1. Such rippling is often observed on metal surfaces [15, 39, 130] and are not a major focus of the current investigation. The 1000-pulse ablation spots were slightly more difficult to ascertain since the rippling boundary crossed into a region containing debris. An annular region immediately surrounding the rippled ablation region was nearly free of debris indicative of some cleaning from the blast wave produced by the ablation plasma expanding outwards after each laser shot. This surrounding region was not measured as an ablated zone. An example of 1 and 10 shot data from one experiment (limited to these data sets for clarity of plot) is shown in Figure 4.2. A plot of the full experimental results for $N = 1$, 10 and 100 pulses is shown in the upper graph of Figure 4.3. The average single-shot ablation threshold from all the experiments on the copper foil sample was determined to be $\phi_{th}(1) = (1.06 \pm 0.12)$ J/cm^2.

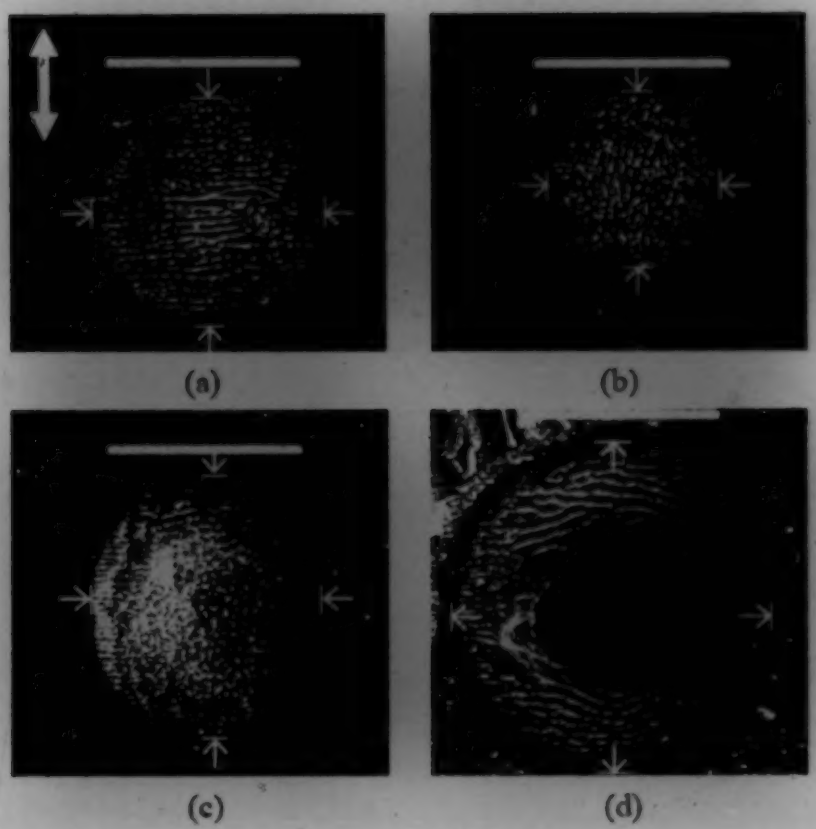

Figure 4.1: SEM images of GF copper foil ablation spots. The incident peak fluence and elliptical diameters measured were (a) 1 shot, 6.1 J/cm^2, 23.7 μm × 23.5 μm (b) 10 shot, 1.1 J/cm^2, 18.3 μm × 17.1 μm (c) 100 shots, 1.4 J/cm^2, 27.4 μm × 23.1 μm, (d) 1000 shots, 1.9 J/cm^2, 34.3 μm × 32.1 μm. The scale bars are 20 μm long and the small arrows indicate the measured diameter extremities. The electric field polarization for all spots is indicated in the top left image.

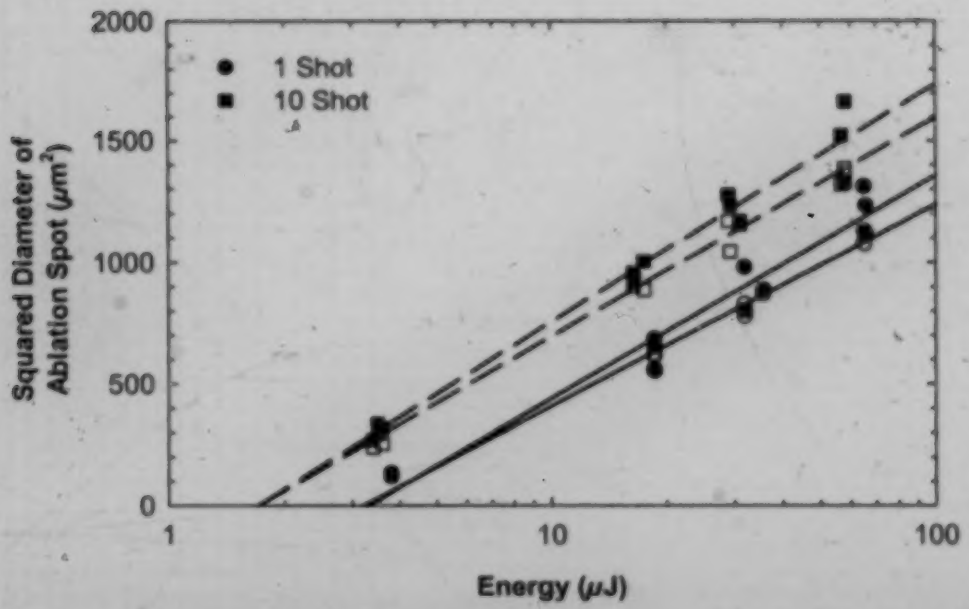

Figure 4.2: An example of the determination of the major and minor axes diameter and energy ablation threshold of GF copper foil for 1- and 10-shot ablation spots measured by SEM. The closed symbols represent the major axis data, and the open symbols, the minor axis. The lines are equation (4.2) with the major axis having values $w = 14.1\ \mu m$, and $E_{th} = 3.3\ \mu J$, and the minor axis having values $w = 13.4\ \mu m$ and $E_{th} = 3.2\ \mu J$ for the 1-shot data. For the 10-shot data, the major axis has values $w = 14.6\ \mu m$, and $E_{th} = 1.7\ \mu J$, and the minor axis has values $w = 14.0\ \mu m$ and $E_{th} = 1.7\ \mu J$.

Strong incubation of damage was observed for multiple shot data as shown in the upper graph of Figure 4.3. The ablation thresholds measured in each individual experiment were plotted versus the number of shots on a log-log plot in the lower graph of Figure 4.3 in order to visualize the incubation effect. The incubation coefficient determined by a least squares fit using equation (4.4) was evaluated as $\xi = 0.76 \pm 0.02$.

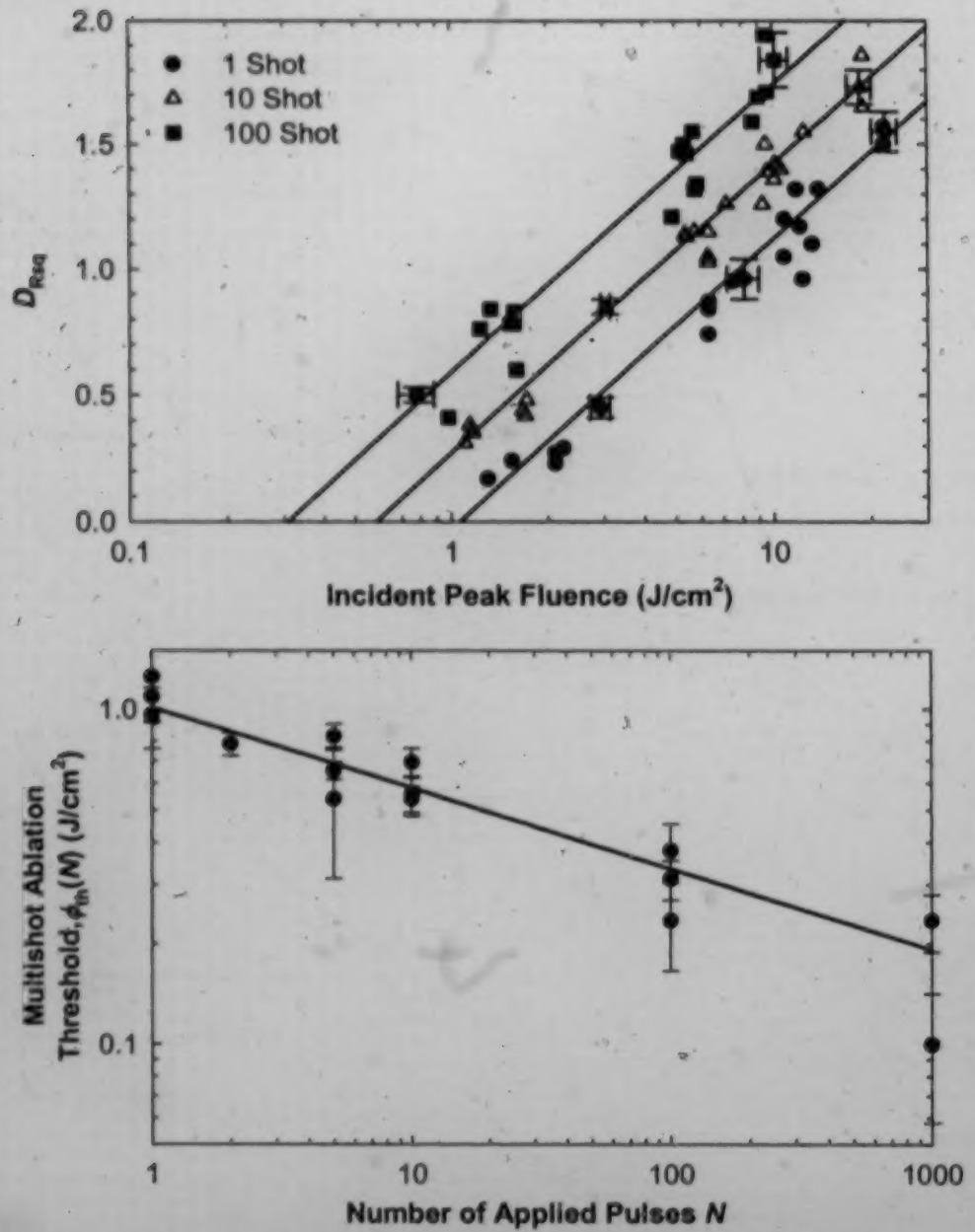

Figure 4.3: Determination of the ablation threshold of GF copper foil for 1, 10 and 100 shot ablation measured by SEM for three sets of experimental data (Upper). The lines are equation (4.5) with $\phi_{th}(1) = 1.06$ J/cm^2, $\phi_{th}(10) = 0.581$ J/cm^2 and $\phi_{th}(100) = 0.307$ J/cm^2. (Lower) Plot of the multishot ablation threshold versus number of shots for copper. The line is equation (2.3) with $\phi_{th}(1) = 1.01$ J/cm^2 and $\xi = 0.76$.

For comparison between different copper samples, independent experiments with a highly reflective 250 nm copper thin film and a more absorbing 500 nm copper thin film were carried out. For the 250 nm copper thin film the normalized beam diameters for the ablation experiment measured by an SEM are plotted in Figure 4.4 versus the incident fluence. From these data, a measured single-shot ablation threshold of (1.10 ± 0.11) J/cm^2 and an incubation coefficient of 0.76 ± 0.06 were determined which were consistent with the copper foil results.

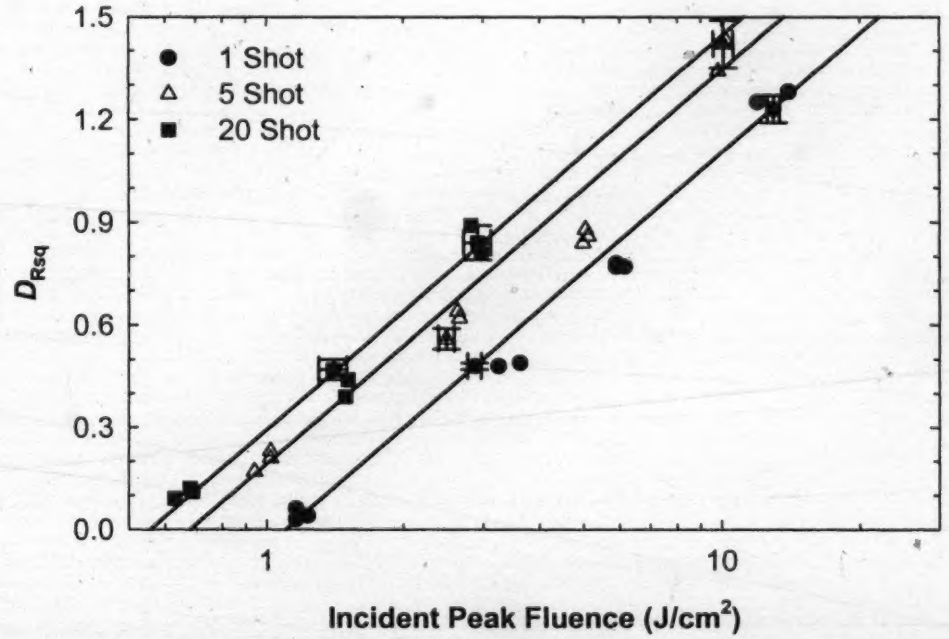

Figure 4.4: Determination of the ablation threshold for the 250 nm copper thin film for 1, 5 and 20 shots measured by SEM. The line is equation (4.5) with $\phi_{th}(1) = 1.10$ J/cm^2, $\phi_{th}(5) = 0.680$ J/cm^2 and $\phi_{th}(20) = 0.557$ J/cm^2.

The ablation threshold was expected to depend significantly on the absorption coefficient for the sample. In a separate experimental investigation, a 500 nm copper thin film, which had been exposed to ambient air for over a year, was also used in ablation studies using single-shot femtosecond pulses. The 500 nm copper thin film exhibited obvious evidence of surface contamination since reddish and brownish coloured regions were visible on the surface. A single-shot ablation threshold experiment with this sample

yielded $\phi_{th}(1) = (0.272 \pm 0.084)$ J/cm^2. This value is significantly below the value for the above samples; however, the reflectivity of this sample was visually less than that of the above samples and a measurement of surface absorptance at 800 nm of the various samples was carried out.

Measurements of the specular reflectivity of each film were made by firing the unfocused femtosecond laser beam onto the sample and collecting the reflected energy at a repetition rate of 1 kHz with the power meter placed approximately 48 cm, distance d_1 in Figure 3.8. from the sample. The sample was placed at a 4° AOI and the reflected power within a 2° cone angle was measured and compared to that of a high-reflectivity normal incidence dielectric mirror. The mirror had a measured reflectance of greater than 0.997 ± 0.002 at this angle and wavelength.

The 250 nm copper thin film gave a measured reflectance (primarily specular) of 0.940 ± 0.019. Since no additional scattered radiation was observed, this reflectivity gave an absorptance of 0.06 ± 0.019 for the 250 nm thin copper film sample and an absorbed single-shot ablation threshold of (66 ± 21) mJ/cm^2 relative to the measured incident single-shot ablation threshold of (1.10 ± 0.11) J/cm^2. The 500 nm thin copper film had a reflectance of 0.774 ± 0.031, which gave an absorptance of 0.226 ± 0.031 and an absorbed single-shot ablation threshold fluence of (61 ± 19) mJ/cm^2 from the measured incident threshold fluence of (272 ± 84) mJ/cm^2.

Since the copper foil was not optically smooth and some scattered reflectance could be observed from the sample, integrating spheres were used to measure the total reflectivity in two separate experiments as discussed in Section 3.3.7. The results gave a reflectance of 0.948 ± 0.012 for the copper foil. This yielded an absorbed single-shot ablation threshold fluence of (55 ± 13) mJ/cm^2. Note that the theoretical reflectance of a fresh copper surface at 800 nm (1.55 eV) is 0.961 [23].

4.3 Nanomilling copper surfaces

After establishing the single-shot ablation threshold and the incubation coefficient for a clean copper surface with 130 fs laser pulse widths in the NIR, nanomilling experiments were performed for different incident pulse numbers near the multiple-shot ablation threshold line as illustrated in Figure 2.2.

To quantify the nanomilling results, optically smooth surfaces were required. Two copper thin film samples sputtered onto silicon wafers were used with thicknesses of 100 nm and 300 nm. For each sample, the single-shot ablation threshold, the incubation coefficient and reflectivity were measured, as described in Section 3.3.4 and Section 3.3.7. The single-shot ablation threshold for the 100 nm and 300 nm copper thin film samples were measured to be (890 ± 40) mJ/cm^2 with a reflectivity of (97 ± 1) % and (896 ± 80) mJ/cm^2 with (83 ± 1) % reflectivity at the 800 nm wavelength, respectively. Both thresholds deviated from the single-shot ablation threshold previously reported for both bulk copper samples and a thin copper film with a 250 nm thickness where the reflectivity was approximately 95 %. The single-shot ablation threshold for thin films of metals has been reported to decrease as the film thickness approaches the characteristic length for electron diffusion [26, 44, 49]; the lower single-shot ablation threshold for the 100 nm copper film is within expectation. The single-shot ablation threshold for the 300 nm thin copper film was anomalous, but given the low reflectivity it possibly had an altered crystal structure from pure polycrystalline copper as a result of the deposition conditions employed for fabrication.

Despite the discrepancy in the single-shot ablation threshold for the 300 nm thin copper film, the incubation coefficient of this sample agreed with the value previously reported in Section 4.2. The average incubation coefficient for both samples was measured to be 0.77 ± 0.01 making the 300 nm sample an interesting comparison to our well-controlled thin copper film samples. The incident fluence for each experiment was established using the GBLT by measuring the diameters created by the single-shot ablation craters versus energy and extracting the slope for each experiment as described Section 4.1.

Optical profilometry scans [115] of the nanomilled surfaces established that nanomilling did occur near the ablation threshold for copper. Figure 4.5 shows nanostructured profiles for copper thin film surfaces as they occurred with respect to the ablation threshold and incident pulse number.

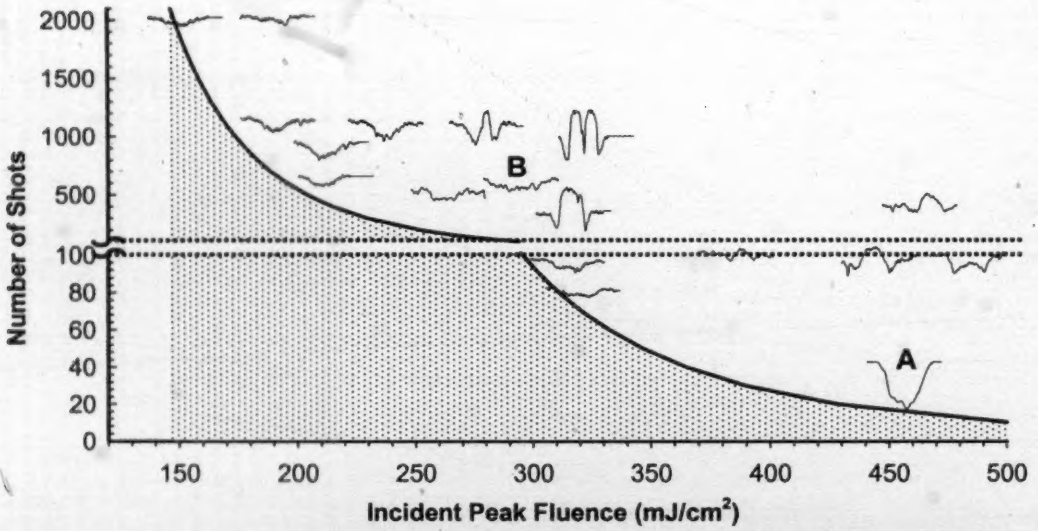

Figure 4.5: Nanostructured surface profiles measured by optical interferometric profilometry. The scan length in each profile is 30 μm across and all aspect ratios are equivalent at 3000:1 and directly comparable, except for the profile labeled A. This profile is discussed in the text. The shaded region defines where nanomilling should not occur with the solid line representing the multiple-shot ablation threshold defined in equation (2.3). The profile labeled B will be discussed further in the text.

All profiles were plotted with the same aspect ratio of 30 μm:10 nm (3000:1) making all data directly comparable except for that labelled A, which is the 83 % reflective sample. Using $\phi_{th}(1) = 852$ mJ/cm^2 and $\xi = 0.77$, a line was drawn in Figure 4.5 to differentiate between the regions expected to show material removal and the region where no ablation was expected, similar to Figure 2.2.

The crater profiles in Figure 4.5 were less than 10 nm deep with the exception of the profile labelled A (83 % reflective sample). Those structures produced near the nanomilling threshold were not perfectly Gaussian in shape and may indicate a nonlinear enhancement of minor irregularities in the beam. Incident energy densities further above the multiple-shot ablation threshold line resulted in surface structures with bumps in the centre of the laser interaction region rising to less than 10 nm heights. Although surface nanostructuring may be of interest, it was our goal to avoid such structures. These nanostructures may be void formation within the sample or between the film and the substrate.

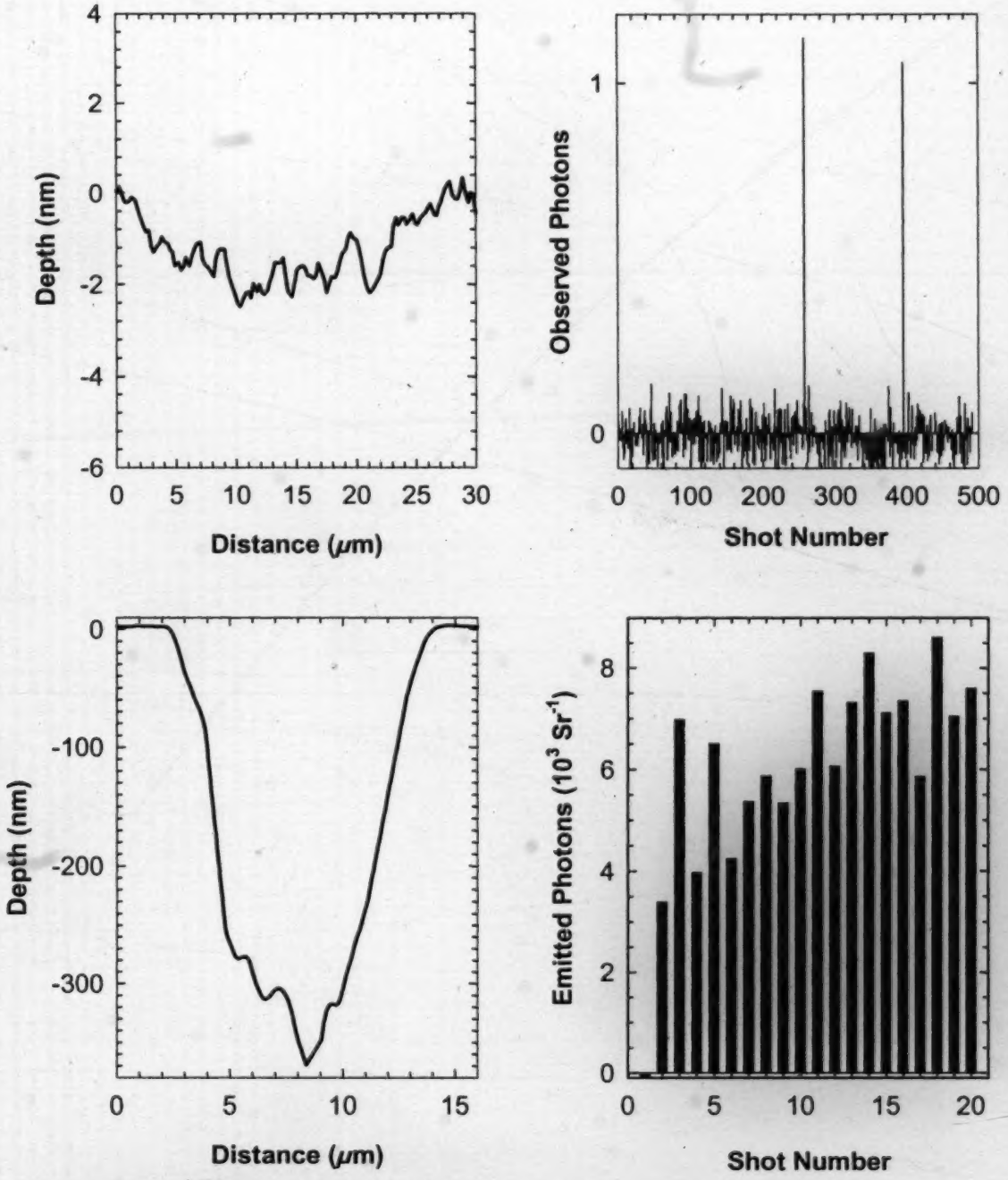

Figure 4.6: White light interferometric profilometry measurement and PMT traces of nanomilled results. (top left) 97 % reflective sample nanomilled at ϕ_{pk} = 290 mJ/cm^2 and PMT trace (top right) and the 83 % reflective sample nanomilled at ϕ_{pk} = 458 mJ/cm^2 (bottom left) and PMT trace (bottom right).

Reflectivity played a significant role in the nanomilling results in the multiple-shot regime as well as the single-shot. The nanomilled shot indicated by A in Figure 4.5 showed a hole 371 nm deep milled by illuminating the 300 nm sample with a reflectivity of 83 % with 20 pulses having a peak incident fluence of 458 mJ/cm^2. The enhanced drilling rate is not surprising if the incident energy is scaled with reflectivity, however *a priori* knowledge of reflectivity may not be available when operating on specific device under tests, making online monitoring a key component in nanomilling.

To establish a simple real time monitor of the nanomilling process, a PMT was used to detect optical emission from ejected species during the ablation process as described in Section 3.3.5. The bottom right of Figure 4.6 shows an example of the PMT trace measured for the sample irradiation leading to profile A in Figure 4.5. In contrast, irradiation of the sample with 97 % reflectivity illuminated with 500 pulses having a ϕ_{pk} of 290 mJ/cm^2 yielded a crater of 1.9 nm depth and PMT signals as shown at the top right of Figure 4.6. For the 371 nm hole, the PMT measured many photons emitted at every shot while for the 1.9 nm hole, two spikes of approximately the same integrated values were measured. These spikes at the top right of Figure 4.6 corresponded to single photon detection events. The probability of observing a single false positive event in 1000 laser pulses was estimated as less than 1 % making the observation of two photons emitted in a run of 500 shots statistically very significant.

4.4 Two-temperature modeling of femtosecond laser pulse interaction with metals

The PTS-TTM is a one-dimensional (space) numerical model that gives the temperature profile into the metal ignoring lateral heat diffusion, which is acceptable for comparison to experiments with focal diameters much larger than the optical skin depth and the heat penetration depth [131, 132].

The TTM has been used to predict the ablation threshold of metals [44], electron emission from a metal [8, 133], thermo-modulation [25, 57, 131] and ultrafast heat transport [24] by assuming that the melting temperature was an appropriate metric. The basic model assumes that the melting temperature is reached isometrically and isobarically, an assumption that will not be challenged in this thesis; however, combined PTS-TTM and MD modeling shows pressure changes of approximately 5 GPa

(compressive and tensile) in a 50 nm film nearly 1 ps after interaction with a 200 fs at 430 mJ/cm^2 absorbed fluence [134]. Pressure changes would affect the transport properties of the material.

4.4.1 Discretization of the TTM

Figure 4.7 illustrates the concept of the PTS-TTM that will be modeled in this thesis. The focused laser pulse interacts with a small lateral section of the metal surface. Ignoring the lateral diffusion of energy in the material (x-axis direction), the region outside the dashed lines in Figure 4.7 represents the assumption of the hard energy density threshold nature of ultrashort laser ablation with no HAZ. If the heat is not considered to diffuse laterally and if the surface does not reach the melting temperature at that point in the x-axis, then no ablation will occur.

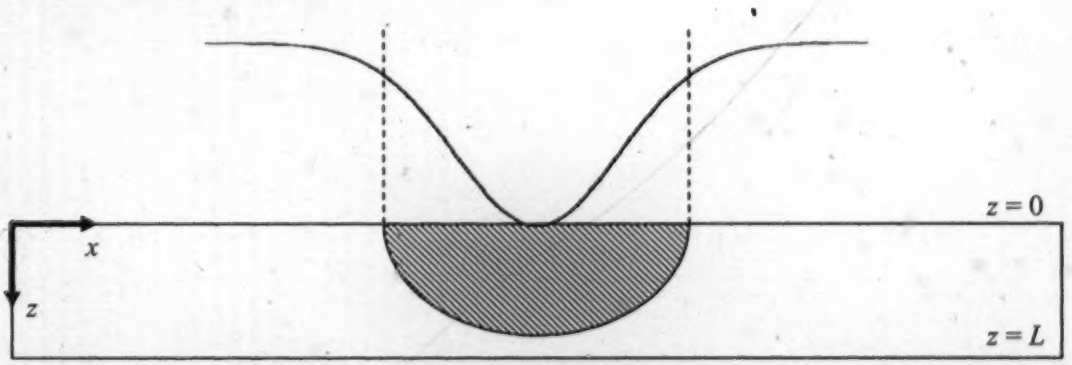

Figure 4.7: Illustration of the heated region by an ultrashort laser pulse modeled by the TTM. The heated region is shown as the hatched region. The Cartesian co-ordinate system for the simulation is shown on the top left of the material schematic. The dashed lines at the edge of the heated region demonstrate the hard threshold nature of the heating process in the TTM for a metal. The Gaussian-shaped curve represents the spatial extent of the laser pulse. The length-to-depth aspect ratio is approximately 150:1.

The PTS-TTM, equation (2.4), was solved using a one-dimensional finite-difference time-domain numerical scheme in the z-axis. Both of these equations are first-order derivatives in time and second-order derivatives in space. To evaluate the PTS-TTM, T_e, T_L, Q and κ represent functions $f(z,t)$ that are at least twice differentiable

in both space and time. These functions can also be approximated on a uniform grid of space and time divided up into steps Δz and Δt, respectively, as shown in Figure 4.8.

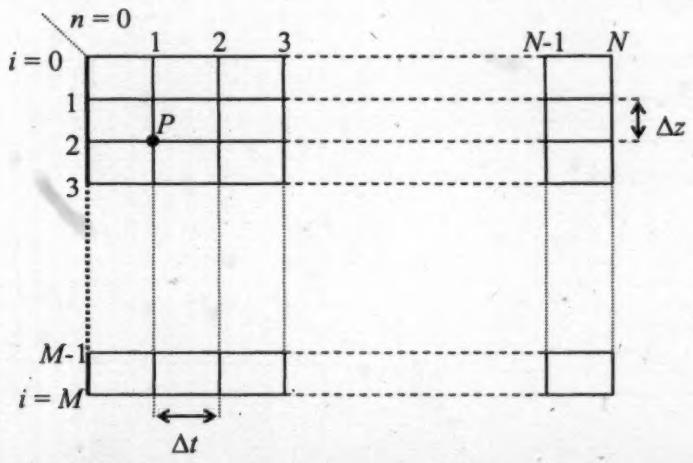

Figure 4.8: Discretization of the one-dimensional TTM in space and time. The dark line on the left indicates the infinitesimal slice of material at the initial time step before it propagates in time from left to right. A position *P* of the function is defined by its index location *P*(*i*,*n*); here *P*(2,1). The discrete function only exists on the intersecting points.

The value of the function $f(z,t)$ at a point P at node (i,n) can be written as:

$$f(z,t)\big|_P = f(i\Delta z, n\Delta t) = f(z_i, t_n) = f(i,n) = f_i^n \tag{4.6}$$

where i and n are integers. The last term in equation (4.6) will indicate the value of the discrete function at node (i,n). To avoid confusion between the notation f_i^n for the discrete function at node (i,n) and the derivatives of the function $f(z,t)$, written as $f_{zz}(z,t)$ for the second-order partial derivative of the continuous function in the z-axis or $f_t(i,n)$ for the first-order partial derivative in time evaluated at the node (i,n), the function and its derivatives will include (z,t) or (i,n).

For the time derivative, the first-order accurate forward-difference equation is:

$$f_t(z,t) = f_t(i,n) = \frac{f_i^{n+1} - f_i^n}{\Delta t} + O(\Delta t) \tag{4.7}$$

For the spatial derivative, the second-order accurate central-difference equation is:

$$f_{zz}(z,t) = f_{zz}(i,n) = \frac{f_{i+1}^n - 2f_i^n + f_{i-1}^n}{\Delta z^2} + O(\Delta z^2) \tag{4.8}$$

These discrete equations are an explicit time-marching formulation of the PTS-TTM with associated stability requirements. An implicit scheme could be used to create an unconditionally stable discrete model; however, since the PTS-TTM was a set of nonlinear coupled partial differential equations, an explicit scheme was easier to implement provided the stability criterion was met.

This scheme was an initial-value problem with insulated boundary conditions:

$$T(z,0) = U(z,0) = T_0 \ \text{(K)} \tag{4.9}$$

$$\frac{d}{dz}T(0,t) = \frac{d}{dz}T(L,t) = 0 \tag{4.10}$$

$$\frac{d}{dz}U(0,t) = \frac{d}{dz}U(L,t) = 0 \tag{4.11}$$

where T is the electron temperature, U is the lattice temperature and L is the length of the simulation.

The stability of the PTS-TTM should be evaluated using Maximum Analysis [135] since it was a nonlinear partial differential equation. The PTS-TTM with the proportional electron thermal conductivity, equation (2.8), was evaluated by examining the more rapidly evolving electron temperature equation using von Neumann analysis. This analysis technique replaces the temperature, T, with an error function $\alpha^n \exp(j\beta x)$. To perform von Neumann analysis on the PTS-TTM, U was set to 300 K, the g-parameter and source term were ignored, and the electron temperature equation was

solved for $|\alpha| < 1$. This technique provided a sufficiently stringent stability requirement for the model. The complete discretization of the TTM and the stability requirement is derived in Appendix A.

4.4.2 TTM results for the ablation threshold and nanomilling of copper

The melting temperature of copper, 1357.8 K [23], was taken as the predictor for the single-shot ablation threshold. Using the thermophysical parameters from Table 2.1, the peak absorbed fluence for the ablation of copper was calculated to be 93.5 mJ/cm^2 with a g-parameter of 10×10^{16} W/(m^3·K) for a Gaussian pulse having a FWHM of 130 fs at 800 nm. The sample thickness was 800 nm in the simulation and the grid step size, Δz, was 1.6 nm. The temporal dynamics of the electron and lattice temperatures and the spatial profile of the temperatures at their peak values are plotted in Figure 4.9.

At the single-shot ablation threshold predicted by the PTS-TTM with the proportional electron thermal conductivity, the peak electron temperature reached 18 200 K (1.6 eV), well below the Fermi temperature. At this peak temperature, the thermophysical parameters described in Section 2.2.2 were still valid. The rear surface of the material for both the electron and lattice temperatures did not heat up, indicating that the length of the simulation was adequate to avoid artificial heat trapping.

To determine the sensitivity of the predicted ablation threshold to the thermophysical parameters, each of the parameters were tuned ±10 % and the ablation threshold varied as follows: C_L, 12 %; γ, 2 %; κ_0, 4 %, showing that the ablation threshold was most sensitive to the lattice heat capacity, which is expected since the melting temperature was the predictor.

The prediction of the ablation threshold was also examined as a function of the simulation grid parameters. For simulation lengths greater than 600 nm, the ablation threshold was the same. If the simulation length dropped to 400 nm, then the predicted ablation threshold dropped to 92.3 mJ/cm^2 (1.3 %) due to artificial heat trapping in the simulation volume. Simulation step sizes of less than 2 nm had the same predicted ablation thresholds.

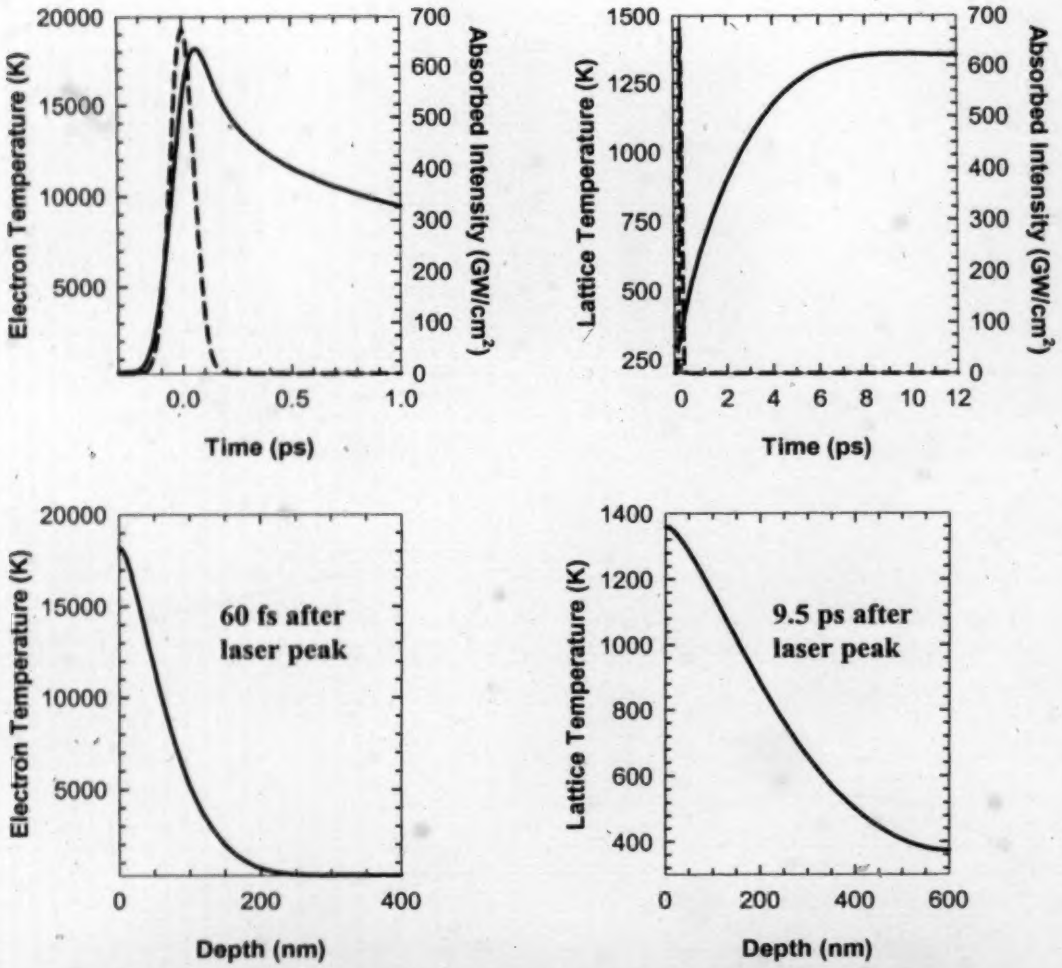

Figure 4.9: TTM results for copper using the proportional electron thermal conductivity heated by a 800 nm, 130 fs FWHM Gaussian-shaped laser pulse at 93.54 mJ/cm^2 (absorbed) with $g = 10 \times 10^{16}$ W/(m^3·K). (upper left) The electron temperature over time showing the peak electron temperature is 18 200 K. (upper right) The lattice temperature over time showing the peak lattice temperature is 1358.9 K (slightly above the melting temperature). The peak electron temperature was reached 60 fs after the peak of the laser and the lattice temperature peak was reached 9.5 ps after the laser peak. (lower left) The electron temperature through the sample at the time of peak temperature showing no artificial heat trapping. (lower right) The lattice temperature through the substrate at the time of the peak temperature also shows no artificial heat trapping.

The absorbed single-shot ablation threshold of 93.5 mJ/cm^2 was up to 1.5× higher than the absorbed threshold fluences measured in Section 4.2. Increasing the *g*-parameter to 15×10^{16} W/(m^3·K) and 20×10^{16} W/(m^3·K), decreased the predicted absorbed single-shot ablation threshold to 76 mJ/cm^2 and 65 mJ/cm^2, respectively, approaching the experimental absorbed single-shot ablation threshold determined in Section 4.2. Increasing the *g*-parameter to larger values in the 10^{17} W/(m^3·K) range to fit the single-shot ablation threshold raised a question: if the noble metals have similar properties and are themselves different than the other transition metals (Table 2.1), then why does the *g*-parameter of copper differ from silver and gold and approach values of the transition metals (Table 2.5) [136]?

The PTS-TTM predicted that the peak electron temperature of copper from interaction with a 130 fs Gaussian FWHM pulse width at 800 nm was 18 200 K when melted at 93.5 mJ/cm^2. This peak temperature was 22 % of the Fermi temperature and from Figure 2.3, a large discrepancy between the two models for the electron thermal conductivity can be seen. Changing the electron thermal conductivity to the plasma model of equation (2.9) and using the parameters 377 W/(m·K) and 0.139 for copper [54], the predicted absorbed single-shot ablation threshold for a 800 nm, 130 fs pulse was 60.7 mJ/cm^2 with a *g*-parameter of 3×10^{16} W/(m^3·K), within the bounds of the experimentally observed single-shot ablation threshold in Section 4.2 and the *g*-parameters measured and calculated for the noble metals as reported in Table 2.5. This result is shown in Figure 4.10. A *g*-parameter of 3×10^{16} W/(m^3·K) gave an absorbed single-shot ablation threshold of 172 mJ/cm^2 for the proportional electron thermal conductivity of equation (2.8).

Using the plasma electron thermal conductivity in the TTM, the absorbed single-shot ablation threshold at 800 nm was predicted for a range of Gaussian pulse widths as shown in Figure 4.11. The simulation length varied from 600 nm to 800 nm and the mesh sizes varied from 1 nm to 5 nm spatial step sizes. The spatial step was increased to accommodate longer simulation times for longer pulse widths. A comparison was made to the ablation threshold variation with pulse width predicted by the proportional electron thermal conductivity with a *g*-parameter of 10×10^{16} W/(m^3·K).

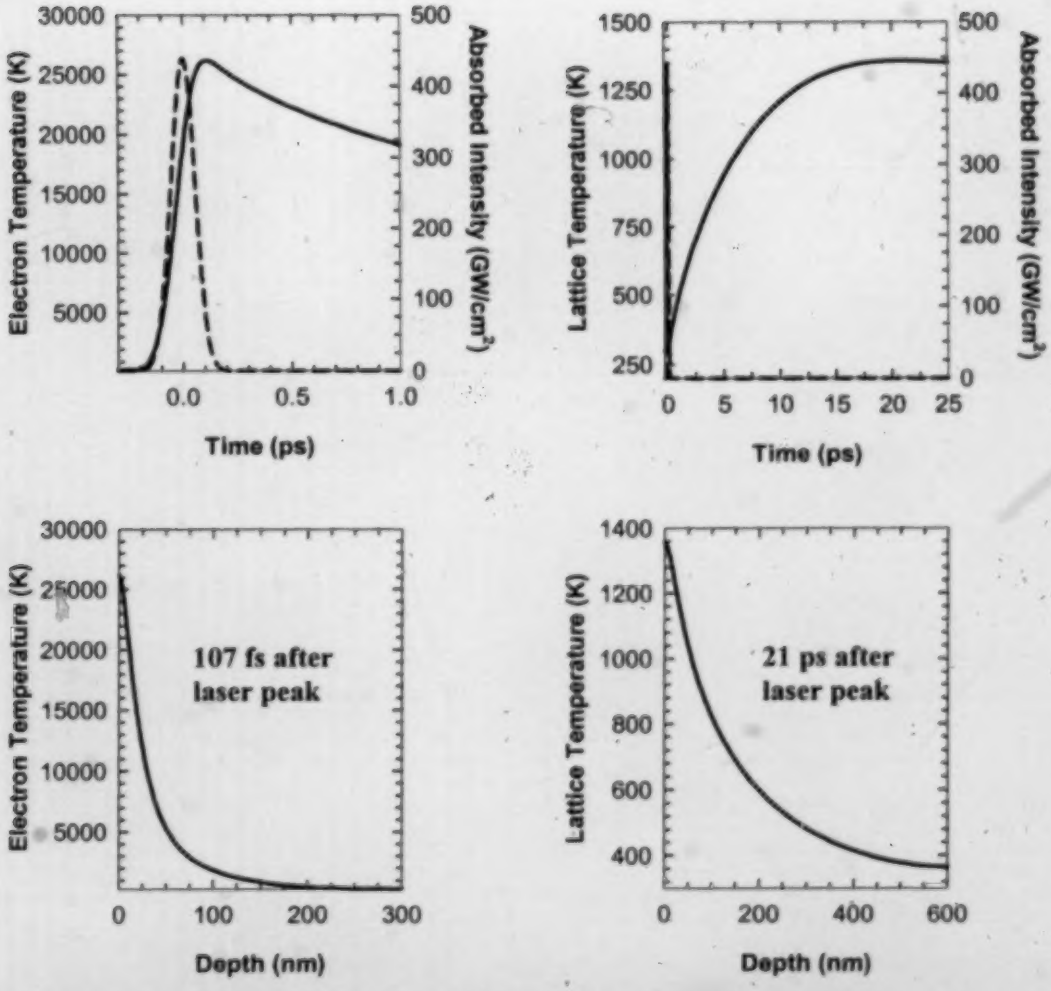

Figure 4.10: TTM results for copper using the plasma electron thermal conductivity for copper heated by a 800 nm, 130 fs FWHM Gaussian-shaped laser pulse at 60.7 mJ/cm^2 (absorbed) with $g = 3 \times 10^{16}$ W/(m^3·K). (upper left) The electron temperature over time showing the peak electron temperature is 26 200 K. (upper right) The lattice temperature over time showing the peak lattice temperature is 1357.8 K (slightly above the melting temperature). The peak electron temperature was reached 107 fs after the peak of the laser and the lattice temperature peak was reached 20.8 ps after the laser peak. (lower left) The electron temperature through the sample at the time of peak temperature. (lower right) The lattice temperature through the substrate at the time of the peak temperature.

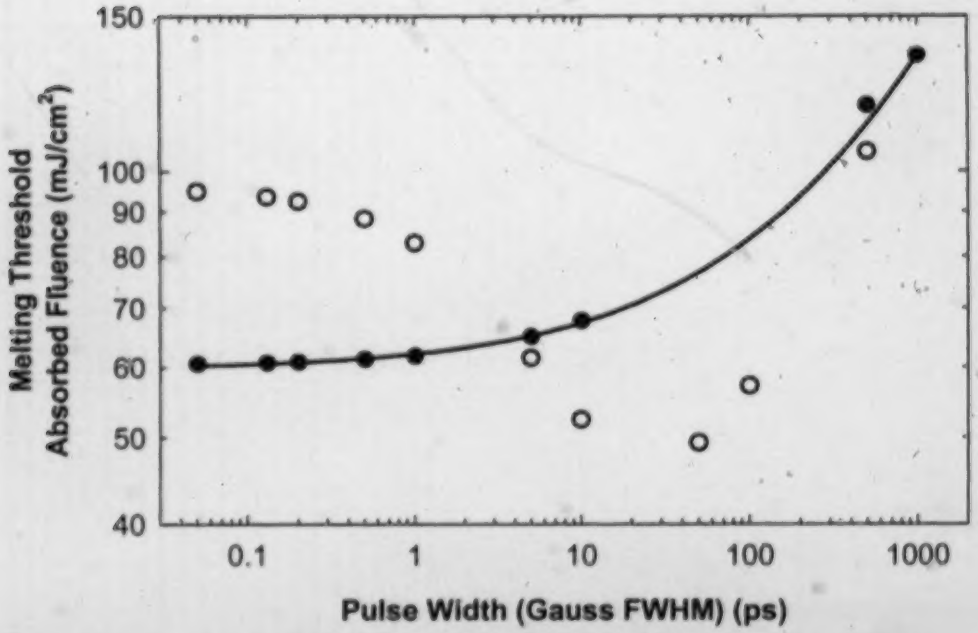

Figure 4.11: Prediction of the absorbed single-shot ablation threshold for copper using the PTS-TTM with the plasma electron thermal conductivity at the 800 nm wavelength (filled circles) and a comparison to the PTS-TTM with the proportional electron thermal conductivity (open circles). The line is a guide for the eye.

The temperature dynamics were simulated using the PTS-TTM for a few of the nanomilling laser fluences presented in Figure 4.5. A 300 nm slab was simulated at three absorbed fluences of 4.4 mJ/cm^2, 8.7 mJ/cm^2 and 13.5 mJ/cm^2, corresponding to incident peak fluences of 88 mJ/cm^2, 170 mJ/cm^2 and 290 mJ/cm^2 at 95 % reflectivity. The peak lattice temperature reached 367 K, 435 K and 515 K, for each case respectively, and the peak electron temperature was 5 000 K, 8 000 K and 10 600 K, respectively. The lattice temperatures are below melting, as expected, but the heating rates are 4×10^{13} K/s, a rate that may be significant in the incubation of damage as will be discussed in Chapter 7.

4.5 Discussion

From the measurements in Section 4.2, the incubation of damage is an important factor in multiple-shot measurements of the ablation threshold. Only one measurement of incubation for copper had been reported giving a typical value of 0.92 [39]. In that work, 10 ns, 1064 nm pulses were used and incubation of multiple-pulse damage was

attributed to the accumulation of to a slip-line defect formation below the observable onset of laser damage. The slip-line defect accumulation was based on a thermal cycling model and was consistent with metal fatigue studies and parameters. No scaling law exists for mapping incubation data from the nanosecond to the femtosecond regime, but a possibility will be discussed in Chapter 7. The result of the present measurement indicates that the incubation coefficient may decrease (increased effect of multiple pulse damage incubation) from nanosecond to femtosecond pulse widths for NIR pulse laser irradiation of copper surfaces. This decrease may result from the much more rapid thermal cycling of the temperature profile of the copper on a picosecond time scale with femtosecond irradiation, leading to larger stresses than the slower, gentler cycling on a nanosecond time scale with nanosecond pulses. The incubation phenomenon might depend on the final preparation of the sample surface, but for the two different samples measured here, a foil surface and a thin film surface, the results were similar.

A number of previous reports of the ablation threshold for copper give values in the range of hundreds of mJ/cm^2 for 800 nm, 100 fs to 200 fs laser interaction [30, 31, 33]. These reports on ablation thresholds were from drilling experiments on metal surfaces where hundreds of shots were used to determine the drill depth and the results were extrapolated to find the minimum fluence at which damage occurred. The drill rate was usually fit to equation (2.2).

This ablation rate technique is often used to evaluate ablation thresholds of materials [29, 31-33, 43]. These threshold values are characteristic of surface machining with hundreds or thousands of pulses and are appropriate for a surface with a significantly altered morphology and reflectance for each pulse compared to a clean surface, and that has internal stress damage from the HAZ from previous laser shots. Thresholds deduced from ablation rate studies would be significantly lower than those for single shots on clean surfaces. In addition, there is often a weak and strong ablation regime that is observed, leading to two threshold values, as mentioned in Section 2.1.

In the NIR, Nolte and Momma *et al.* [30, 31] have reported the weak and strong ablation thresholds as 0.14 J/cm^2 and 0.46 J/cm^2, respectively. Furusawa *et al.* [33] also reported the strong ablation threshold as 0.43 J/cm^2 for 120 fs to 150 fs pulses. These thresholds are considerably lower than our single-shot threshold value for clean copper

samples. Confirmation that a large part of this threshold reduction may be due to increased effective absorption from the roughened and damaged surface can be seen when the weak ablation threshold from UV femtosecond pulses is examined. Preuss *et al.* [29] and Li *et al.* [34] reported values for the weak ablation threshold of copper of 0.17 J/cm^2 and 0.16 J/cm^2, respectively, using 500 fs, 250 nm pulses. For pure copper, the expected absorption for 250 nm radiation is 63.4 %. The absorbed energy fluences at these threshold values would be in the range of 0.101 J/cm^2 to 0.108 J/cm^2. Previously reported measurements for 248 nm, 250 fs pulses [137] for copper targets indicate a reflectivity value that increases by about 13 % when the intensity increases from 10^{12} W/cm^2 to 10^{13} W/cm^2 and the absorbed fluences may be lower than these estimates and close to the values reported here. The fact that the reported UV threshold values are close to the 0.14 J/cm^2 threshold value reported at 780 nm by Nolte *et al.* [31] indicates the likelihood of equivalent strong absorption occurring for the 800 nm measurements in this multiple-shot ablating regime.

Ablation thresholds have also been measured by single-shot TOF measurements of electrons and ions liberated from the surface. Amoruso *et al.* [36, 37] gave a weak ablation threshold of 0.54 J/cm^2 for p-polarized light and ~1.5 J/cm^2 for s-polarized light at 50° AOI on solid copper targets for 120 fs, 780 nm laser pulses. In those experiments, the authors report cleaning the target with low power laser shots prior to the main shot, which based on our incubation results above, may have incurred some degree of incubation damage. The expected absorptances for pure copper surfaces at 0° AOI, 50° p-polarized AOI and 50° s-polarized AOI are 3.6 %, 6.3 % and 2.7 %, respectively. If one uses the ratio of these expected absorptances to scale the results of Amoruso *et al.* to 0° AOI, then the reported thresholds would correspond to 0.945 J/cm^2 and 1.13 J/cm^2 from the p- and s-polarized thresholds, respectively. While the real absorptances of the copper samples used in those experiments are expected to be somewhat higher than the theoretical values for pure copper (as with our experiments), the s- and p-polarized reflectivity curves are expected to behave in a similar manner to the pure copper. The predicted scaling to 0° AOI is expected to remain approximately valid. The resultant scaled threshold values are similar to our threshold value reported here.

A few previous single-shot thresholds have been reported in the nanosecond pulse regime. The nanosecond pulse interaction is dominated by classical heat diffusion scaling and cannot be related directly to the femtosecond measurements. The damage fluences should be higher, scaling as $\tau^{1/2}$ in this regime. The previously reported single-shot thresholds range from 1.8 J/cm^2 for 23 ns, 248 nm pulses measured by an electric plasma probe [35] to 10.5 J/cm^2 for 10 ns, 1064 nm pulses measured by 200× Nomarski OM and SEM imaging [39] of the surface damage. Given the expected 63.4 % absorption for 248 nm pulses and approximately similar absorption for 1064 nm pulses versus our 800 nm pulses, these results are consistent with the expected large increase in the absorbed threshold fluence for nanosecond pulses versus our 130 fs pulses.

One can estimate the expected ablation threshold based on the simple theoretical model of the two-temperature model of ablation, as was done when the study on the single-shot ablation threshold and incubation coefficient for copper was originally published [13]. Corkum *et al.* [44] presented a model for melting thresholds of metals for the case of ultrafast laser interaction where the pulse width of the laser used was shorter than a critical time parameter defined as the time where significant heat transfer to the lattice occurs. Based on the PTS-TTM for the electrons and lattice, they examined coupling of the electron energy to the lattice subsystem. An electron thermal diffusion depth, at which point the energy couples to the lattice, was calculated as:

$$z_R = \left(\frac{128}{\pi}\right)^{\frac{1}{8}} \left(\frac{\kappa_0^2 C_L}{\Delta T_{im} g^2 \gamma}\right)^{\frac{1}{4}} \text{ (m)} \qquad (4.12)$$

where κ_0 is the lattice thermal conductivity, C_L is the lattice volumetric heat capacity, ΔT_{im} is the difference between the melting temperature and initial temperature, γ is the Sommerfeld parameter, and g is the electron-lattice coupling coefficient. For example, in [13], we substituted in the material parameter values from standard reference handbooks [23, 138], κ_0 = 4.01 W/(cm·K), C_L = 3.4 J/(cm^3·K), ΔT_{im} = (1360.8 – 298) K, and γ = 97 J/(m^3·K^2) and selected an electron-lattice coupling coefficient as $g = 10^{17}$ W/(m^3·K).

An electron penetration depth (z_R) of 240 nm was calculated. The absorbed melting threshold $\phi_{th,a}^{melt}$ was estimated as [44]:

$$\phi_{th,a}^{melt} = C_L \Delta T_{im} z_R \quad (J/cm^2) \qquad (4.13)$$

Substituting the lattice volumetric heat capacity, the temperature differential and the derived penetration depth yielded an absorbed melting threshold of 87 mJ/cm^2. Corkum *et al.* [44] calculated an absorbed threshold of ~60 mJ/cm^2 with numerical integration of the detailed coupling equations for a picosecond pulse with $g = 10^{17}$ W/(m^3·K) using the proportional electron thermal conductivity model of equation (2.8). If the electron-lattice coupling coefficient is changed to their reported value of 10^{16} W/(m^3·K), then the electron penetration depth would reach 760 nm with an estimated absorbed melting threshold of 280 mJ/cm^2. The more widely reported value of 10^{17} W/(m^3·K) was consistent with the damage thresholds reported in ref. [13]. Noble metals typically have similar thermophysical properties and since the *g*-parameter can be derived using these parameters [51], the *g*-parameters should be similar for all the noble metals near a value of 3×10^{16} W/(m^3·K) shown in this work and given in other references [58, 59].

The PTS-TTM model of Corkum *et al.* [44] used the proportional electron thermal conductivity equation to predict the ablation threshold for copper. Numerical simulations with this model yield a melting threshold of 93.5 mJ/cm^2, close to the 87 mJ/cm^2 above. The PTS-TTM calculations in Figure 4.11 show two problems with the proportional electron thermal conductivity: the predicted ablation thresholds are much higher than found experimentally and the thermal conductivity becomes quite high at 2 % of the Fermi temperature. The deviation from the $\tau^{1/2}$ dependence of the ablation threshold should lead to a pulse width independent regime as shown in the experimental results of Corkum *et al.* [44]. The PTS-TTM with the proportional electron thermal conductivity shows an increase of the single-shot ablation threshold between 10 ps and 50 ps pulse widths when the peak electron temperature during laser interaction increases from 1700 K from a 50 ps laser pulse to 3900 K from 10 ps laser pulse width interaction. This electron temperature range occurs in the regime where the two electron thermal

conductivity models deviate in Figure 2.3. The proportional electron thermal conductivity increases significantly, requiring more energy to drive the metal to the melting temperature. Since publishing our work in the single-shot ablation threshold and incubation coefficient on clean copper surfaces [13], a change in the PTS-TTM when examining the models of the electron thermal conductivity and the plasma electron thermal conductivity has become apparent with a *g*-parameter of 3×10^{16} W/(m^3·K) a more appropriate choice for modeling femtosecond laser heating of copper surfaces.

The morphology of the resultant copper foil surfaces is also of interest in nanomilling materials. In the SEM images of Figure 4.1, rippling was observed on the copper foil surfaces. According to Young *et al.* [130], rippling occurs on metals with a period equal to the incident wavelength of light and is oriented perpendicular to the electric field polarization. By orientation, the authors refer to the "ripple line" direction. The appearance of ripples in this manner was also observed by Jee *et al.* [39]. Further discussion of rippling can be found in ref. [15] and references therein. As can be seen in Figure 4.1, we observed similar rippling patterns in the irradiation of copper with single-shot and multi-shot ablation measurements. The absence of ripples on the 250 nm copper thin film sample is also of interest. This was consistent with the observations of Young *et al.* [130] that rippling would only occur on a metal due to wave scattering from defects, especially scratches. The foil sample in Figure 4.1 had considerable surface roughness and structure to begin with, making the starting roughness or pre-existing features important in the seeding of such ripples in applications of nanomilling.

To avoid the rippling morphology in the nanomilling results, thin optically-smooth copper thin films were used. The nanomilling results, especially the result at the top left of Figure 4.6, show that irradiation at the low fluence of 290 mJ/cm^2 leads to very gentle ablation with little excitation of the copper atoms. The average material removal rate corresponded to a few isolated atoms in each laser pulse, a process observed in MD simulations [86, 87]. The excitation of copper atoms is expected to be a stochastic event that occurs with a probability that increases with the absorbed fluence. The number of emissions observed could be used as a diagnostic for the rate of the nanomilling process.

The bump formation in the nanomilling results is a peculiarity with thin films below the ablation threshold. Models of nanojet formation using single-shot femtosecond

laser pulses have shown that thin 60 nm metal films with a high plastic deformation potential, in particular copper, silver and gold, are prone to the development of bumps and jets when irradiated at fluences near the ablation threshold [139]. The metal does not reach the melting temperature and the momentum gained through excitation forces the film off of the substrate. When the melting temperature is reached, further structuring to a hollow nanojet may be formed with the metal stretching out; the ultimate size limited by surface-tension forces. At higher fluences, these structures would be destroyed. These structures are expected to vanish if nanomilling on optically smooth *bulk* copper samples were used to characterize the nanomilling process.

Two hypotheses on nanomilling dynamics currently exist and are the subjects of future investigations. Nanomilling could be occurring in bursts after a certain amount of energy has been stored over many sub-single-shot ablation threshold shots. Such dynamics would be consistent with the isolated photon emission events shown in upper right graph of Figure 4.6. The other possibility is that the material is being removed continually in small random amounts with detectable amounts occurring at random.

One publication has previously reported nanometer-scale depth removal using 70 fs, 800 nm laser pulses on copper surfaces with an ablation rate of 3-10 pm/pulse [42]. In that work, three multiple-shot ablation thresholds were observed at 18 mJ/cm^2, 220 mJ/cm^2 and 1 J/cm^2, where the last two thresholds were attributed to the gentle and strong ablation regimes, and the third at 18 mJ/cm^2 was attributed to a multiphoton absorption process similar to that seen in the ablation of transparent polymers with 248 nm, 500 fs laser pulses. The multiphoton absorption fit to the data shows a comparable trend to the crater depths observed for incident pulse numbers greater than 10^5 at incident fluences below 220 mJ/cm^2, but the physics are not clear as yet.

The ablation rate of 3-10 pm/pulse is an interesting result since it is similar to the ablation rates observed in this work with a minimum ablation rate of approximately 0.7 pm/pulse (~1.4 nm/2000 shots) seen in Figure 4.5 to 4 pm/pulse (~2 nm/500 shots) shown at the top left of Figure 4.6. Atoms have sizes of approximately 220-250 pm [140], so these ablation rates would indicate sub-atomic machining on a continual basis. Details of the individual constituents in an ablation plume at these low incident fluences can be revealed using TOF particle diagnostics and MD simulations. Further

investigations, both experimental and theoretical, will be required to establish the true nature of this low fluence regime.

The nanomilling mechanism would be revealed when the incubation mechanism for femtosecond pulse widths is understood. Two competing theories exist to explain incubation: the first is that the sub-threshold pulses lead to energy stored in the material by permanently disordering the crystalline structure, and the second is that repetitive thermal cycling leads to material fatigue. The difference between these hypotheses is that incubation would not be observed in a truly amorphous material such as quartz with the first hypothesis. The second hypothesis would show incubation in all materials and would be dependent on the macroscopic material properties.

4.6 Engineering application: Smart micromachining

Excited particle emission during nanomilling allows the user to precisely control the amount of material removed and the quality of the nanomilling process. The PMT monitors the progress of nanomilling. If too many photons are emitted for any one shot, as shown in the bottom right graph of Figure 4.6, nanomilling can be shut off before catastrophic drilling occurs, improving the quality of the process. This monitoring technique is useful in industrial applications where the reflectivity, an important parameter in laser-matter interactions [13], is not necessarily known and the process can be terminated if the device could be destroyed.

A logical extension would be to controllably drill layered substrates where the detection of the second or any subsequent layer indicates termination of the nanomilling process. This end-point micromachining [136] technique could be applied in circuit board repair or SAW trimming where the appearance of the dielectric layer in the PMT signal would indicate the complete removal of the metal layer and the termination of the nanomilling process.

Chapter 5

Laser patterning of metal surfaces with self-assembled monolayers*

SAM systems are of interest for their application to wetting, electrochemical, microcrystal and microfluidic studies. Technologically, we are interested in SAM systems for their potential in the development of bio-sensors and barrier-free microfluidic lab-on-chips. Nanoscale engineering of metal surfaces can be extended from applications requiring nanomilling of the *native* substrate to applications that operate on the *adsorption layers*, made controllably through self-assembly, as shown in this chapter. Two techniques will be described: the first is a thermal technique that desorbs the SAM from the substrate within a heated region created by scanning a CW laser focal spot; the other technique exploits nanomilling to minimally remove a metal surface and the SAM through ablation. The contrast between the thermal desorption and ablative removal of SAMs is important since the SAMs are also shown to prove that the nanomilling technique is ablative.

---

* Portions of this chapter were previously published in: S.E. Kirkwood, M.R. Shadnam, R. Fedosejevs, and A. Amirfazli, "Direct writing of self-assembled monolayers on gold coated substrates using a CW Argon laser," *The International Conference on MEMS, NANO, and Smart Systems*, pp. 48-52, 2003; M.R. Shadnam, S.E. Kirkwood, R. Fedosejevs, and A. Amirfazli, "Direct patterning of self-assembled monolayers on gold using a laser beam," *Langmuir*, vol. 20, pp. 2667-2676, 2004; S.E. Kirkwood, M.R. Shadnam, A. Amirfazli, and R. Fedosejevs, "Mechanism for femtosecond laser pulse patterning of self-assembled monolayers on gold-coated substrates," *Journal of Physics: Conference Series*, 2006 (Accepted October 20, 2005).

5.1 Self-assembled monolayers of alkanethiols on metal surfaces

Nanoscale engineering of material surfaces can be accomplished by manipulating the adsorption layer. Monolayers of hydrocarbons and water vapour always coat the surface of materials in air, but selected molecules could be chosen to adhere to surfaces to tune their behaviour. Fatty acids are hydrophobic molecules, they do not mix with water, and smearing fatty acids onto metal surfaces, which are naturally hydrophilic, changes the metal surface to hydrophobic: water will bead on the metal rather than spread out as a film. This technique was used in the 1930s in steam condenser plants where heat transfer from steam to cooling water was required to be rapid and efficient [141]. Keeping the water on the cool metal plates as droplets increased the surface area of the water compared to a uniform film, increasing the efficiency of the plant. Fatty acids were smeared on the plates to make the water vapour condense as droplets, but the water vapour eventually reverted back to a film as the fatty acids were washed away.

Blackman *et al.* [141] hypothesized that since sulfur had an affinity to noble metals, a hydrocarbon or fatty acid with a sulfur head would likely bind to the plates and keep the hydrocarbons from washing away. They noticed that the molecules could adsorb from the gas phase as well as from solution, so adding these molecules to the water vapour made the water form as droplets on the plates as they adsorbed onto the surface and increased the efficiency of the plates by over 200 % due to the increased surface area presented by droplet formation.

The work of Blackman *et al.* [141] on molecules that adsorb readily and behave collectively on a material surface demonstrated what is now referred to as SAMs. SAMs are monolayer systems that form spontaneously when a substrate is immersed in a solution of the desired monolayer and the affinity of the head group to the substrate is sufficient to promote chemical bonding [142]. An example of the 1-hexadecanethiol SAM coating used in this thesis is shown in Figure 5.1.

We worked with 16-carbon alkanethiols (alkane for single bonded carbon atoms, thiol is the sulfur-hydrogen combination) where the gold surface and the thiol (HS) head group have a strong interaction potential and have been shown to create stable, ordered structures on gold surfaces [143]. The surface characteristics can be manipulated by

changing the terminal (or tail) group or the alkane chain length to create a surface with different properties in neighbouring regions.

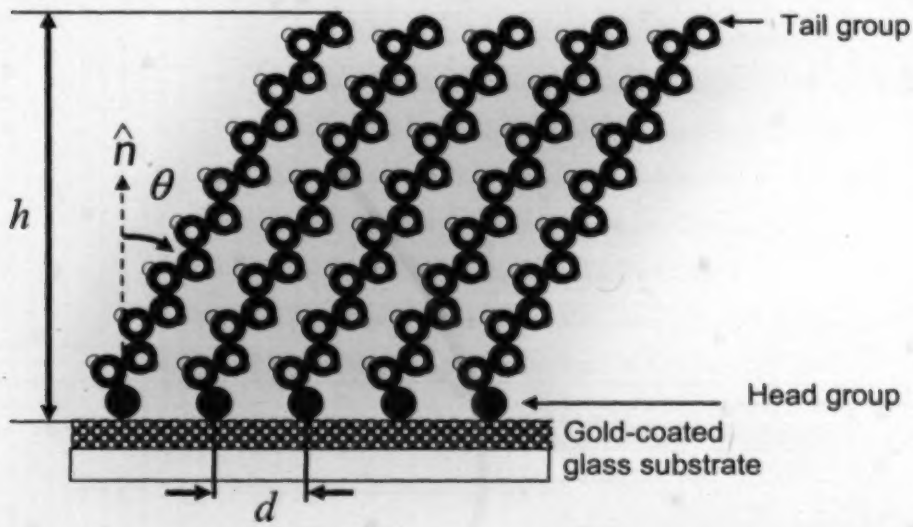

Figure 5.1: Schematic representation of a 1-hexadecanethiol monolayer coating on a thin gold film surface. The height of the monolayer (h) is 21 Å, the tilt angle (θ) is approximately 30° and the distance between sulfur atoms (d) is 4.95 Å.

From ellipsometry and IR studies, the 16-carbon alkanethiol SAMs were shown to be 21 Å thick [144, 145] and tilted at an angle of approximately 30° [144-147]. This angle is necessary because the van der Waals interactions optimize the steric (packing) properties by having the carbons of the molecules entering the kinks in the chain like a ratchet. Blackman *et al.* [141] hypothesized that van der Waals interactions would preferentially lead to erect molecules on the surface, not a "lying-down" format. The strength of the Van der Waals interaction is dependent on the chain length since alkanethiol SAMs with fewer than eight carbons remain disordered and fail to reach a "standing-up" stable phase [143]. Scanning tunnel microscopy (STM) and e^- diffraction studies showed that the molecules have a crystalline orientation with a sulfur atom spacing of 4.995 Å (see, for example, Figure 9 in ref. [147] or Figure 1C in ref. [148]).

SAMs of *n*-alkanethiols (a general term with *n* representing the number of carbon atoms in the chain [149]) were used since the head group (thiol) had an affinity for the gold substrate and the tail group tuned the metal between hydrophobic and hydrophilic,

depending on the molecule. A methyl group (-CH_3, this group is represented in Figure 5.1) gives a metal surface hydrophobic qualities and a carboxylic acid group (-COOH) gives the metal a hydrophilic quality. Another example of an SAM is a carboxylate head group (-COO^-) with an 11 carbon chain that has an affinity to alumina glass surfaces and its organization also comes from van der Waals interactions with the carbon groups in the all-*trans* configuration [142]. The terms *cis* and *trans* are configuration terms with *trans* referring to the isomer configuration of versus *cis* with the configuration of [17]. The use of *trans* in describing the saturated hydrocarbons in the SAMs indicates that the freely rotating molecules have adopted a similar configuration since it is the only configuration to allow for tight packing of the carbon molecules and high van der Waals interaction. A molecule like undecanoic acid could give a glass surface hydrophobic properties or di(ethyl perfluoroctanoate) disulfide would give a metal surface a PTFE-like behaviour (that could prevent bio-fouling in microfluidic systems [147, 150]).

Homogeneous systems in general are not very interesting in the application of SAMs. More complex systems may require spatial variation of the tail groups, depending on the application. For example, tail groups could have complex protein adsorption properties to study DNA activity [151] in a specific region on a lab-on-chip assembly and be protein resistant in other regions [152], making patterning of SAMs an important engineering endeavour.

In this work, SAMs of 1-hexadecanethiol [$HS(CH_2)_{15}CH_3$, hydrophobic] and 16-mercaptohexadecanoic acid [$HS(CH_2)_{15}COOH$, hydrophilic] were deposited from solution to pattern gold thin film substrates. These are *n*-alkanethiols and have been extensively studied over 20 years starting from work by George Whitesides' group at Harvard University [119, 143, 153, 154]. The dynamics of SAM formation and stability have also been extensively studied with significant contributions by G. Poirier at NIST using STM [148, 155-157].

Poirier studied gas-phase molecular adsorption of *n*-alkanethiols using STM to show that self-assembly occurred in two stages [148]. The first stage was rapid, occurring over seconds to minutes. It started with the sulfur binding to free surface sites on the gold with the molecule in a lying-down phase (see Figure 8 in ref. [148]) until the

concentration on the surface was nearly 90 %. The second stage started with the molecules nucleating in a standing-up phase over several hours. Macroscopically, at 90 % adsorption (in the lying down phase) the surface would have the wetting properties expected of the system; however, it would still not be very stable because the van der Waals interactions necessary for a stable SAM occur in the standing-up phase. The second phase is an important step in the formation of the SAMs.

These growth phases were observed using surface plasmon resonance spectroscopy (SPRS) [158]. SPRS can monitor film thickness and optical properties similar to ellipsometry and in particular can measure the dynamics of film formation by coupling the evanescent field of a laser through a prism into a surface plasmon and equating the incident angle for minimum reflectivity with the dielectric constant of the film. In the work of Peterlinz *et al.* [158], the formation dynamics of several *n*-alkanethiols differing in solution concentration were measured. The first stage was rapid as indicated by Poirier [148] and followed first-order Langmuir adsorption isotherm kinetics; a function of the available sites for adsorption [158, 159]. The second ordering stage was longer and took 24 hours before the 21 Å height was achieved for the 16-carbon alkanethiols. The standing-up phase was only observed for solution concentrations of 0.1 mmol/L to 1 mmol/L showing that SAM formation was especially sensitive to solution concentration. At concentrations below 1 μmol/L, the SAM formation was incomplete.

Three complications affect the stability of *n*-alkanethiol SAMs on noble metal surfaces over the long term and affect the applicability of *n*-alkanethiol SAMs in practical systems. The first complication is film quality. SAMs of *n*-alkanethiol have been observed restructuring the gold surface to minimize stresses [156], which results in void formation [148]. Thin gold films made by evaporation (a common technique) can have a high density of grain boundaries on the surface at evaporation rates of ~0.5 Å/s and develop a (100) structure that limits the extent of van der Waals interactions and leads to weaker monolayer films if the gold films were made at fast deposition rates (~1.5 Å/s) [160]. Sulfur atoms at grain boundaries or void locations are susceptible to chemical reactions or higher desorption rates [148, 161].

Sulfur oxidation is the second complication since it oxidizes easily in the presence of ozone [127, 157, 162]. Sulfur atoms exposed at grain boundaries and vacancies from film restructuring are no longer protected by the barrier created by the carbon chains as shown in Figure 5.1. Oxidized sulfur (sulfinate and sulfonate) is weakly bound to a gold substrate and can be rinsed off easily with ethanol [127]. Ozone was shown to be very destructive at partial pressures in the atmosphere (10^{-7} Torr) by STM, where oxidation was nucleated at the vacancy islands, and the ozone completely removed the molecules from the gold surface in 33 minutes [157].

Long term storage is the third complication with *n*-alkanethiol SAMs on noble metal surfaces. SAM coated substrates cannot be left in ambient conditions since it is susceptible to oxidation by atmospheric ozone. Storage in solution also poses a problem for two reasons. First, atmospheric gases are present in liquids and special precautions are required to remove the gas from the solution. More advanced storage techniques include bubbling argon gas into the ethanol or solution to remove the ambient air before sealing it [127]. Photo-oxidation in the presence of O_2 and UV light is also an oxidation pathway since O_2 does not oxidize sulfur directly [162]. Second, SAMs exist in equilibrium with the monolayer solution and are subject to reversible dynamics. An octadecanethiol SAM with radiolabeled ^{35}S was observed to desorb from a surface after removal from the 1 mmol/L solution and submersion into a pure solvent. Over a couple of days, the SAM surface coverage equilibrated to 80 % coverage when stored in water and 50 % coverage in ethanol [163]. Water did not degrade the SAM completely due to its limited solubility with hydrocarbons. A 5 % solution of dimethyl sulfoxide (DMSO) in pure water kept an alkanethiol SAM surface stable for upwards of 550 days [164].

An advantage to *n*-alkanethiol SAMs is that they displace surface contaminants at the expense of formation time. Chlorine is a typical contaminant of high-purity gold and it was displaced through self-assembly [165]. Intentionally placed propanethiols (3 carbons) were displaced by octadecanethiol, but increased the formation time, though forming a stable structure in the end [143].

SAMs are used frequently in biological studies of protein or DNA activity towards desired markers. Two types of SAMs are required, one with the marker at the tail group and another to prevent biofouling, the adsorption of undesired proteins on a

surface, since the response is measured as an increase in film thickness in surface plasmon resonance experiments. The use of poly- or oligo(ethyl glycol) groups were the most useful to prevent biofouling. The protein or DNA that shows activity towards a marker binds to the surface, but other proteins that do not show activity don't accidentally stick to the gold surface, confusing the results [151].

SAMs are also useful for nonlinear optics with some tail groups showing second harmonic generation and electro-optic switching [147]. MEMS devices with cantilevers made of metal tend to show static friction (stiction) effects as they are pulling away from the substrate and SAMs adsorbed to the cantilevers eliminate the stiction effect and allow for free oscillatory movement of the cantilever [166].

Many SAM patterning techniques have been developed over 20 years and a review on the topic can be found in ref. [149]. In summary, two types of patterning techniques are used: serial and parallel. Parallel processing refers to techniques that can pattern the entire substrate in one application. Microcontact printing (μCP) is the most popular since it can create features of less than 100 nm and the fabrication of the stamp is simple. An elastomer stamp is fabricated from a polymer such as PDMS and the SAM is the ink that is transferred to the head group compatible substrate. This technique is considered rapid because it can pattern an entire surface; however, it is only fast if you ignore the pre-processing overhead, and it is inflexible to change, requiring a new stamp with every variation.

Parallel processing by lithography techniques refer to photo-desorption of SAMs without removal of the underlying substrate using an exposure mask pattern. SAM lithography relies on direct desorption of the *n*-alkanethiolate negative ion (RS^-, R representing the carbon chain molecule) at 193 nm [167] or by photo-oxidation of the sulfur atom by illuminating the substrate through a mask with UV light, for example an Hg lamp, in the presence of oxygen [167, 168]. The resolution of this technique is limited to the illumination wavelength and imaging techniques. The disadvantages of lithography are similar to μCP with pre-processing overhead and new masks required for each variation.

Serial direct writing techniques based on nanotechnology tools have reduced the feature sizes to 10 nm [149]. Dip-pen techniques that drag a small volume of liquid

between the tip and substrate to deposit the SAM and AFM/STM techniques to remove SAMs in the vicinity of the tip are extremely slow techniques. The advantage to these serial techniques is their patterning flexibility.

A fast and flexible technique is required that fills the gap between the rather inflexible parallel techniques and the flexible but slow serial techniques. Laser patterning meets both requirements, though a thorough study is required to determine the resolution limitations of the technique. In this thesis, the methodology and proof-of-concept results of a novel technique for complex SAM pattern formation is developed.

Nanoscale engineering of SAM surfaces with lasers is a relatively new technique and using SAMs as etch resists, serial patterning of substrates using femtosecond pulses could lead to rapid prototyping of micropatterns to avoid the expense of photolithography masks until the final mass production stage.

5.2 Patterning metal surfaces with self-assembled monolayers by thermally-induced desorption

For this work, direct writing occurs by scanning a CW laser focal spot to remove SAMs from gold-coated microscope slides and depositing new SAMs into the irradiated regions to create specific surface properties. The direct laser writing of *n*-alkanethiol SAMs was developed to compete with current patterning systems in speed, flexibility and resolution, especially since many offer nanometer-scale resolutions. One of our goals in demonstrating this technique was creating barrier-free microfluidic channels on the gold substrate by controlling the surface hydrophobicity and hydrophilicity through SAM patterning. An example is a hydrophilic channel made of carboxylic acid-terminated molecules in a methyl-terminated matrix. The $-CH_3$ matrix is created by a hydrophobic monolayer of 1-hexadecanethiol and the hydrophilic channels by a -COOH terminated 16-mercaptohexadecanoic acid monolayer. After thermally desorbing the hydrophobic monolayer from the surface with a laser, the cleared regions are replaced with the hydrophilic monolayers. This process is depicted in Figure 5.2

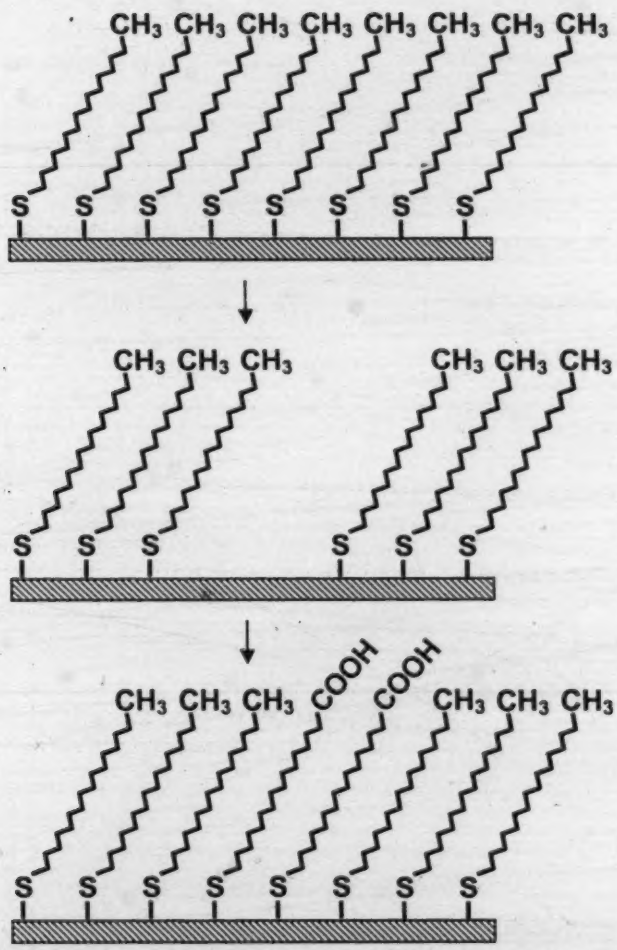

Figure 5.2: The SAM system with the thiol chemically bound to a gold-coated glass substrate. (a) Homogeneous hydrophobic monolayer surface (b) Surface after localized exposure to laser (c) Surface after replacement with the hydrophilic monolayer.

SAMs were desorbed thermally with laser powers between 50 mW and 150 mW using a +10 cm focal length lens, and between 100 mW and 250 mW using a +25 cm focal length lens using the experimental procedure in Section 3.4. The two focal lengths yielded different spots sizes and intensities for the previously mentioned power ranges. The necessity of heating the SAM to a temperature at which desorption would occur limited the minimum power. The damage threshold of the gold film limited the maximum power in the experiment. If the laser intensity exceeded the damage threshold of the gold film, then damage was seen on the gold surface as shown in Figure 5.3.

Figure 5.3: An OM image of gold film damage by overheating the glass slide. The scale bar is 50 μm.

Establishing the threshold for monolayer desorption involved gradually reducing the incident powers from the damage threshold of the gold film until no desorption occurred. The SAM patterned gold surfaces were examined by SEM and these results were used to determine the threshold for SAM desorption. Figure 5.4 shows a successful and unsuccessful creation of a hydrophilic SAM line. The dark region is the hydrophilic monolayer and the bright region is the hydrophobic monolayer [119].

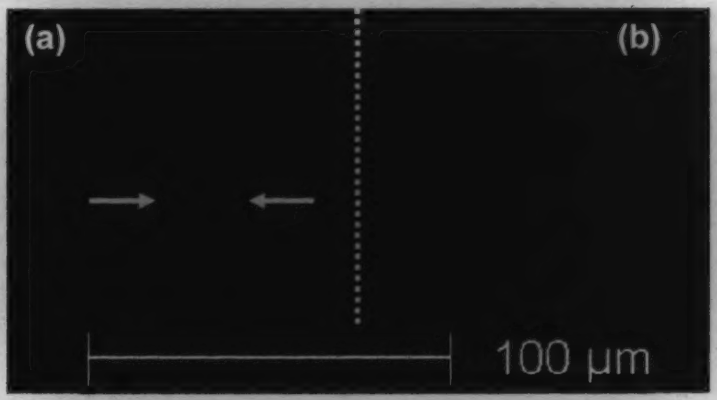

Figure 5.4: SEM images of two regions scanned with a +10 cm lens. (a) 30 mW incident power was used in the region between the arrows and did not yield hydrophobic monolayer desorption. (b) 50 mW incident power was used and the hydrophobic monolayer was desorbed and replaced by the hydrophilic monolayer.

The slides were imaged by OM within one day of the writing. Placing a small drop of tridecane from a syringe, and drawing the drop along the hydrophilic lines created barrier-free microfluidic lines that could be measured by OM as shown in Figure 5.5. The line widths reduced in size with a reduction in incident laser intensity, but the line widths were always greater than the focal spot size measured using the Spiricon camera system. The 2 e–folding intensity focal beam radius for the 10 cm lens was 22.6 μm and for the 25 cm lens was 52.5 μm. The line widths, as they scale with incident power for both lenses, are shown in Figure 5.6. The line widths ranged from 30 μm to 100 μm in the +10 cm lens experiments and 90 μm to 200 μm in the +25 cm lens experiments.

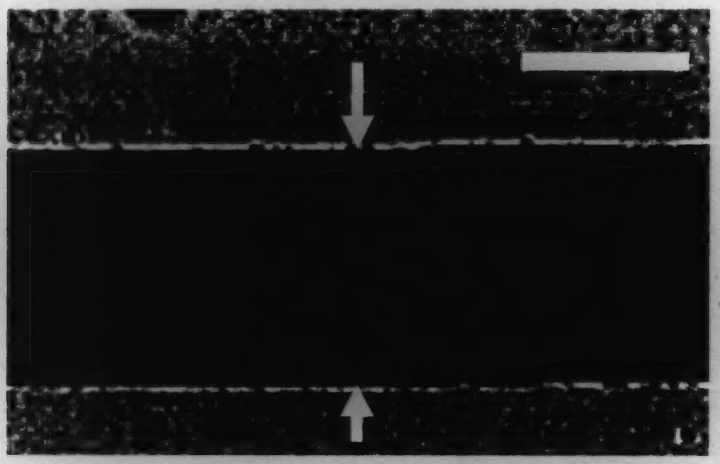

Figure 5.5: An OM image of a 70 μm wide hydrophilic line written with a 90 mW Ar^+ beam focused by a +10 cm BK7 plano-convex lens, delimited by arrows. The image results from tridecane bound within the hydrophilic region of the surface. The white scale bar is 50 μm long.

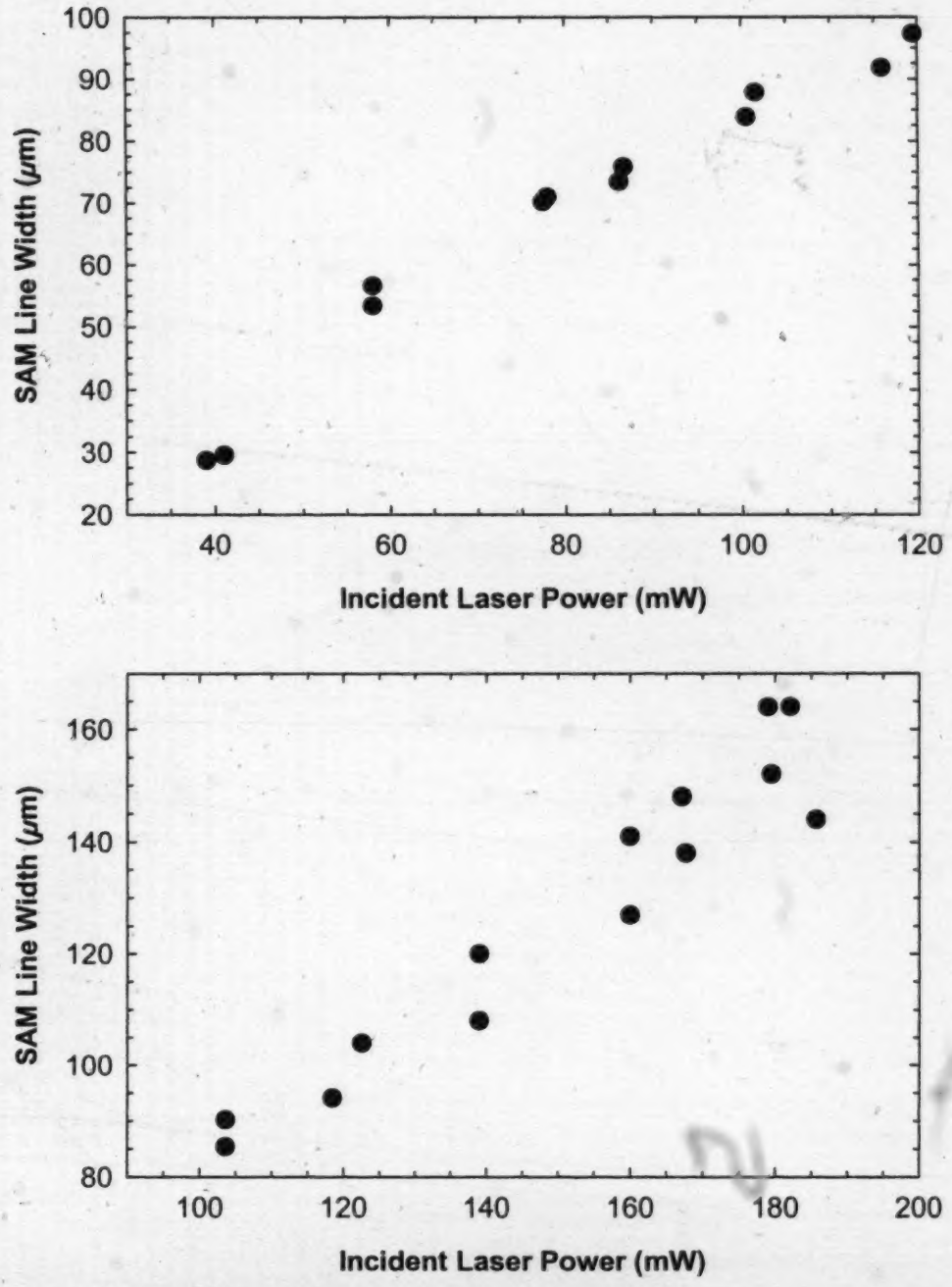

Figure 5.6: SAM line widths created by scanning the focal spot of a CW Ar^+ laser at 200 μm/s to induce thermal desorption. (upper) The lines created with the 10 cm lens and (lower) SAM lines created with the 25 cm lens.

5.3 Modeling thermally induced self-assembled monolayer desorption from thin gold film surfaces

As part of our collaboration, M.R. Shadnam, a Ph.D. student in the Surface Engineering and Instrumentation Laboratory under Dr. Alidad Amirfazli, developed a thermal model to predict expected monolayer line widths from scanning a focused CW Ar^+ laser under different focusing conditions. The main variables involved in producing these lines and accurately modeling the process were the incident power, 2 e-fold intensity beam diameter, surface absorption, scan speed, thermal conductivity and thermal diffusivity.

The model was based on Fourier's law with temperature-dependent thermal properties and a laser heat source modeled as:

$$S(x,y,z,t) = \frac{2PA(T)}{\pi w_0^2} \exp\left(-\frac{2\left([x-vt]^2 + y^2\right)}{w_0^2}\right)\delta(z) \tag{5.1}$$

where P is the laser power, A is the absorbed percentage, w_0 is the 2 e-folding beam waist and v is the laser scanning speed. The delta function in the z-axis is used since the beam waist is much smaller than the absorption depth [11].

The thermal properties of the system were governed by the soda lime glass slide for a focused CW laser spot [169] and the thermal diffusivity of 3.3×10^{-7} m^2/s and thermal conductivity of 0.872 W/(m·K) for the soda lime glass were taken from the manufacturer's data [121]. The thermal conductivity was temperature dependent and using data from the literature as well as the manufacturer's data, a 6.8×10^{-4} $W/(m \cdot K^2)$ slope was determined [11].

Two approaches can be taken to solve for the SAM desorption width observed experimentally. A 2D time-dependent temperature distribution requires a Green's function [170] and the steady-state solution with a temperature-dependent thermal conductivity and temperature-independent thermal diffusivity requires a Kirchoff transformation [171, 172]. Analysis of the two approaches yielded the same lateral features with the time-dependent solution giving the asymmetry in the temperature distribution along the scanning direction [11]. The steady-state solution was equivalent

to the time-dependent Green's function results since the scanning velocity was smaller than $0.3D/w_0$, where D is the diffusivity [169], which results in a maximum scanning velocity of 2 mm/s for the 25 cm focal length lens where $w_0 = 52.5\ \mu m$.

The steady-state analytical solution was used in ref. [11] with the SAMs line widths considered to be 100 % desorbed after the gold surface reached a temperature between 470 K and 490 K [173, 174]. Thermal desorption of radiolabeled sulfur in octadecanethiol molecules in an oven showed complete removal of the SAMs at temperatures over 490 K [163]. An error analysis was performed to examine the appropriate selection of the beam waist, temperature-dependent thermal conductivity and desorption temperature, and in this work, Shadnam *et al.* [11] found that the temperature-dependent thermal conductivity of 6.8×10^{-4} W/(m·K^2) and desorption temperature of 485 K were the best predictors for the SAM line width. The beam waist was also optimized to get a better fit and the results are shown in Figure 5.7.

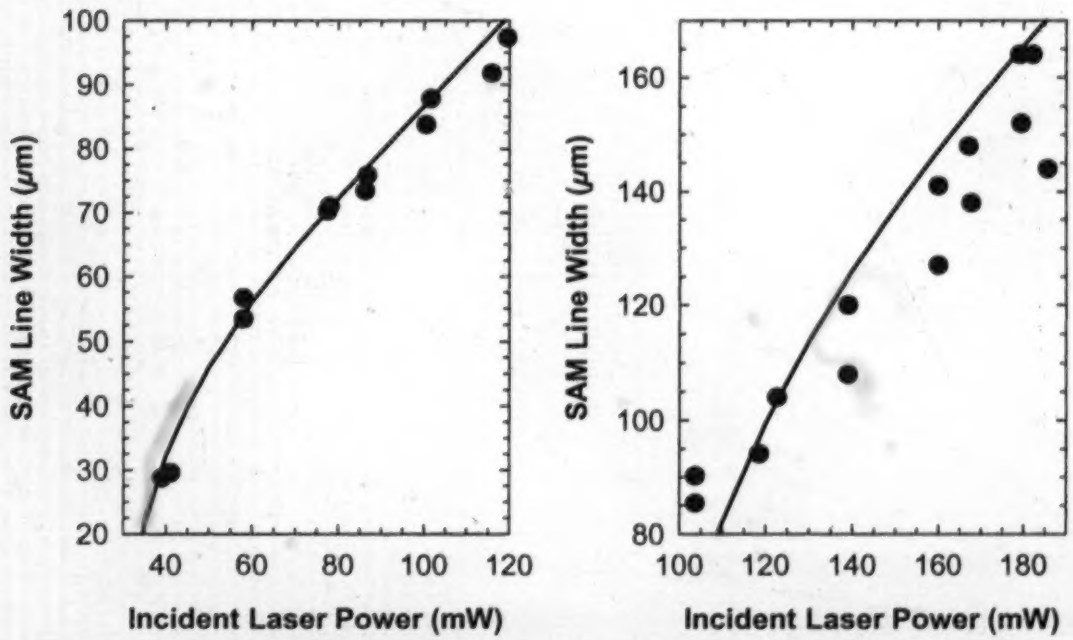

Figure 5.7: SAM line widths created by scanning the focal spot of a CW Ar^+ laser at 200 μm/s compared to the steady-state thermal model. (left) The lines created with the 10 cm lens, (right) SAM lines created with the 25 cm lens.

The model assumes that the absorption of the laser and the diffusivity were constant in temperature. Changing the temperature-dependent thermal conductivity and the diffusivity by 10 % yielded the same trend lines as shown in Figure 5.7. Changes in the absorption coefficient from 44 % [11] by 10 % shifted the lines, but did not alter their slopes. The beam waist was the most sensitive parameter, changing the slopes of the lines. For the 25 cm lens data on the right in Figure 5.7, changing the absorption coefficient rotated the line about the point near 170 mW, with the smaller beam waists giving a closer fit to the data at 100 mW. The optimization of the parameters in ref. [11] already gave 2 e-folding beam radii for the 10 cm and 25 cm lenses of 15.5 μm and 44.5 μm, respectively, both smaller than the experimentally measured beam waists of 22.6 μm and 52.5 μm, respectively.

5.4 Patterning metal surfaces with self-assembled monolayers by femtosecond laser pulse nanomilling of thin gold film surfaces

Thermal desorption of SAMs limited lateral feature sizes to the micrometer-scale with the minimum line width reached to date of 4 μm with a 10× objective [175]. To reach the nanometer-scale, non-thermal pathways to SAM removal are required, and nanomilling is an ideal mechanism in the NIR since removal of less than 10 nm in depth would not disturb the surface morphology to affect the behaviour of the barrier-free microfluidic channels. To clarify the definition of the mechanisms involved in each of the techniques, a schematic defining desorption versus ablation is shown in Figure 5.8.

The CW laser methodology has been extended to femtosecond laser pulses to perform sub-diffraction limited patterning of SAMs of 1-hexadecanethiol (hydrophobic) on a 30 nm gold thin film substrate using fluences below the single-shot ablation threshold. The remaining bare region can be etched to create patterns similar to lithographic techniques or backfilled with 16-mercaptohexadecanoic acid (hydrophilic) as done in our work to tune the surface energy. The patterning technique for CW laser interaction was shown to be thermal, but thermal patterning was not expected to be valid for femtosecond laser pulses. To predict the patterning pathway, we assumed at first that the process was photolytic.

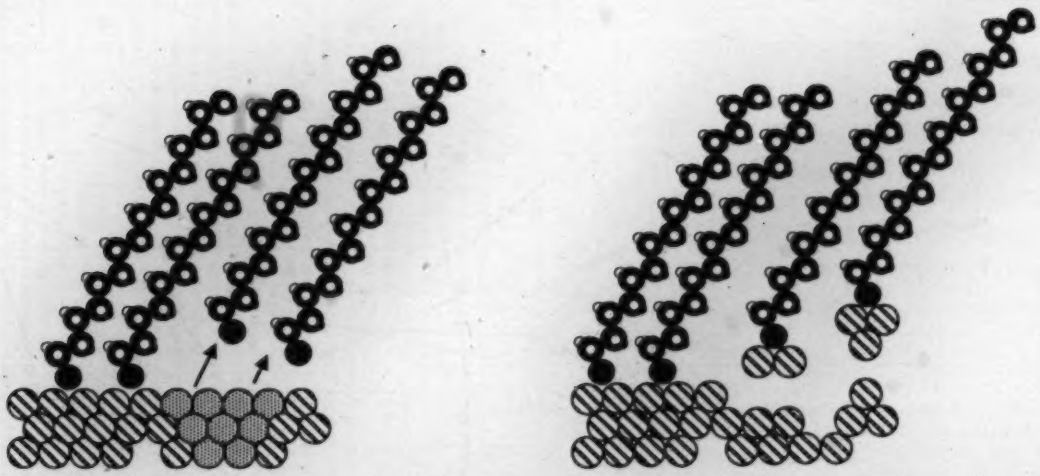

Figure 5.8: Schematic of the mechanism differences between the two SAM laser patterning techniques. (Left) The SAM is thermally *desorbed* when the gold atoms heat up to the desorption temperature (dotted fill) and break the thiolate bond. (Right) The SAM is removed with the few gold atoms removed by *nanomilling* the surface.

The sulfur-gold bond dissociation energy at room temperature is (253 ± 14.6) kJ/mol [23]. Converting the dissociation energy into bond energy gives 2.63 eV/bond and this energy is equivalent to a photon at a wavelength of 472 nm. If the SAMs are removed by a photolytic reaction and the energy is dominated by the thiolate bond, then 2-photon absorption of 800 nm photons would remove the SAMs. Van der Waals interactions are necessary for the stability of the SAM (see Section 5.1) so more energy may be necessary to remove the SAMs.

Experiments for determining the nature of the *n*-alkanethiol bond strength on the gold surface using laser desorption Fourier transform mass spectrometry (LD-FTMS) [176], showed that 193 nm wavelengths produced the negative ion of the *n*-alkanethiol molecule. LD-FTMS is a technique where the focal spot of an ArF laser beam is used to remove organic molecules from a metal surface without decomposing the molecule. In Brewer *et al.* [177], they showed that the removal pathway at 254 nm is oxidation with ozone and would also occur if oxygen was present in the molecule, like 16-mercaptohexadeanoic acid (-COOH terminal group). We are patterning the methyl group terminated SAM, so with no oxygen present, 193 nm wavelengths would be required to remove the SAM from the gold. This evidence formed the hypothesis that the

femtosecond removal mechanism was ablative rather than photolytic since multiphoton absorption probability increases with I^n and the intensity would be in the nanomilling regime before it was high enough to allow for 5-photon photolytic bond cleavage.

The first step was to measure the single-shot ablation threshold and incubation coefficient of the bulk and the 30 nm thin gold films (Sections 3.3.2 to 3.3.4) to determine whether patterning was occurring in the nanomilling regime. The ablation threshold and incubation coefficient of a clean *bulk* gold sample represented the expected values for any gold substrate under femtosecond laser pulse interaction. From these expected values, differences in $\phi_{th}(1)$ and ξ may then be related to film thickness [26], reflectivity/absorption changes from the deposition technique [13] or the presence of an SAM. The bulk gold ϕ_{th} and ξ values are shown in Figure 5.9. The single-shot ablation threshold and incubation coefficient measured for a 30 nm thin gold film with a SAM coating is shown in Figure 5.10.

Line scans for laser patterning were made in the nanomilling fluence regime at 50 μm/s with the Ti:Sapphire running at a 1 kHz repetition rate after calibrating the single-shot ablation threshold and incubation coefficient for the sample. The incident beam waist on the sample was extracted from the calibration by equation (4.1) so that the effective number of pulses could be calculated by equation (3.1).

SEM images of the thin gold film substrates after laser scanning showed the removal of the hydrophobic SAM in the focal region of the laser and the deposition of the hydrophilic SAM as in Figure 5.11. The line width of the patterned region was approximately 6 μm, while the smallest line width observed was approximately 4 μm wide. Compared to the intensity diameter of the laser (24.8 μm or 20.6 μm FWHM), the minimum value indicates a five times reduction from the FWHM focal spot size of the laser to the resulting line width demonstrating the ability of femtosecond laser pulses to pattern SAMs on gold-coated substrates below the diffraction-limited spot size.

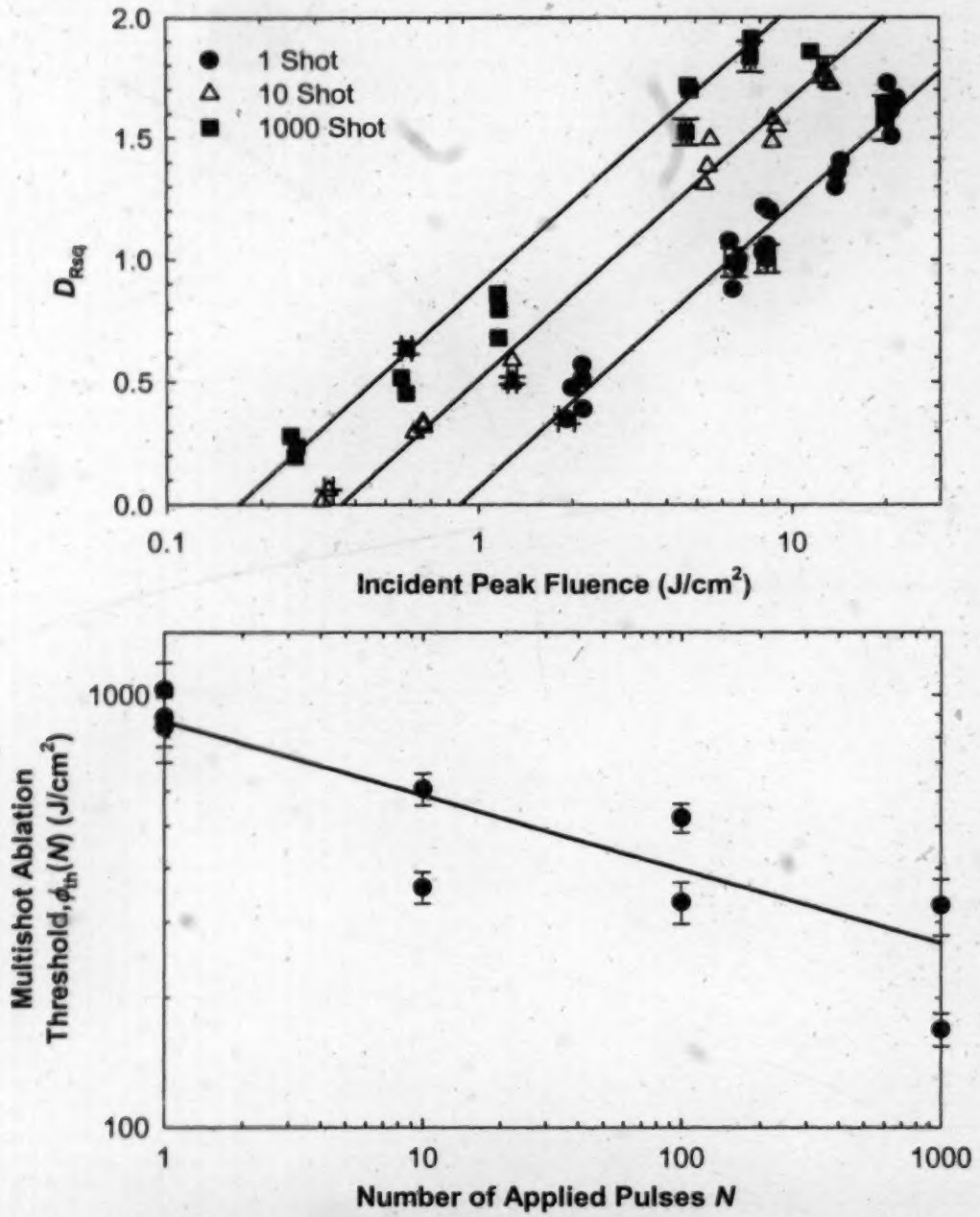

Figure 5.9: Determination of the ablation threshold of GF gold foil for 1, 10 and 1000 shot ablation measured by SEM (Upper). The lines are equation (4.5) with $\phi_{th}(1) = 833$ mJ/cm^2, $\phi_{th}(10) = 361$ mJ/cm^2 and $\phi_{th}(1000) = 169$ mJ/cm^2. (Lower) Plot of the multishot ablation threshold versus number of shots for gold. The line is equation (2.3) with $\phi_{th}(1) = 868$ mJ/cm^2 and $\xi = 0.83$.

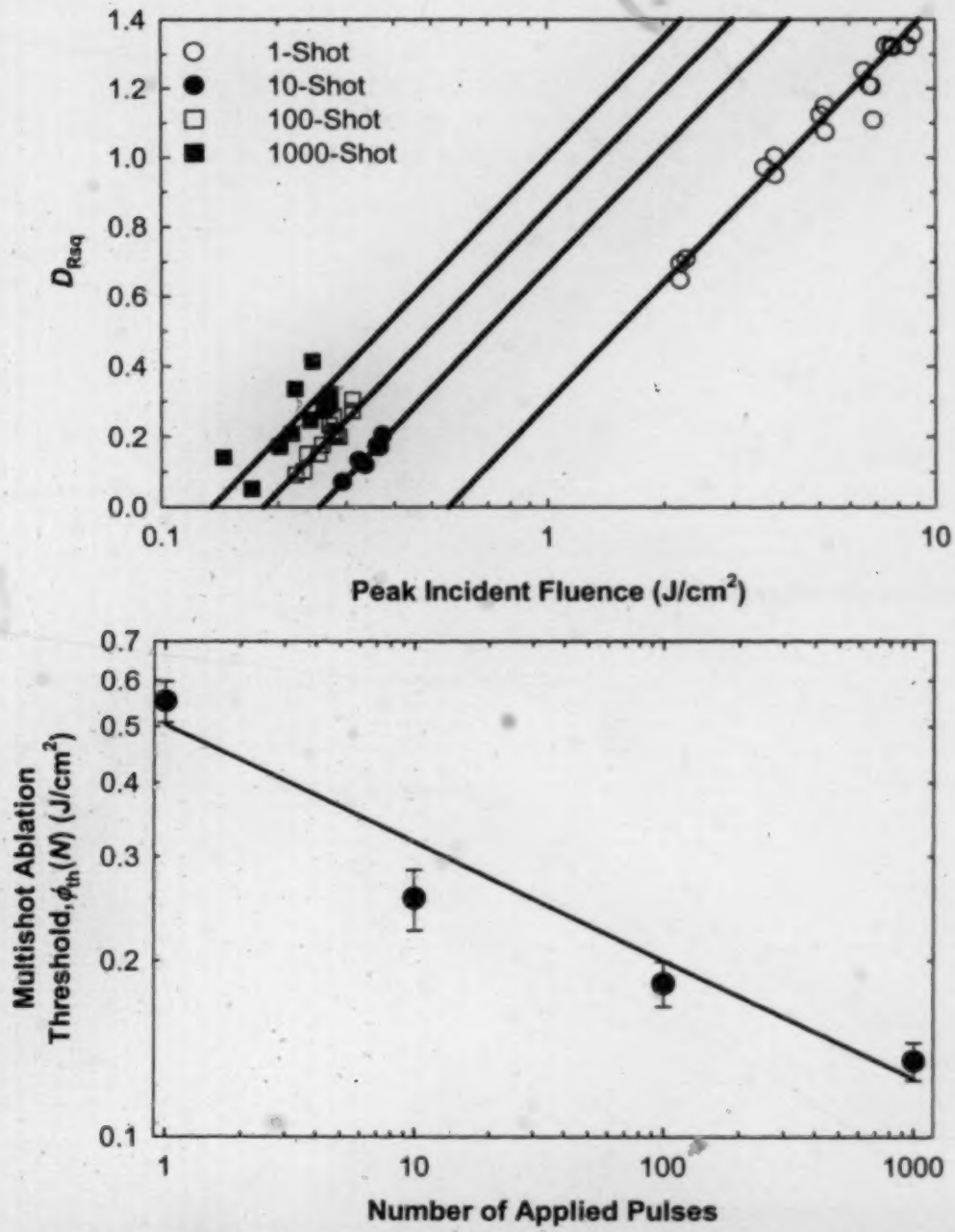

Figure 5.10: Determination of the ablation threshold of a 30 nm thin gold film with the hydrophobic monolayer surface for 1, 10, 100 and 1000 shot ablation measured by SEM (Upper). The lines are equation (4.5) with $\phi_{th}(1) = 553$ mJ/cm^2, $\phi_{th}(10) = 255$ mJ/cm^2, $\phi_{th}(100) = 183$ mJ/cm^2 and $\phi_{th}(1000) = 135$ mJ/cm^2. (Lower) Multishot ablation threshold versus number of shots for gold. The line is equation (2.3) with $\phi_{th}(1) = 553$ mJ/cm^2 and $\xi = 0.80$.

Figure 5.11: SEM image of a region on the gold-coated substrate scanned with an incident peak fluence of 150 mJ/cm^2, a repetition rate of 1 kHz and a scanning speed of 50 μm/s. With the incident elliptical Gaussian intensity beam radius of 14.0 μm by 12.4 μm and the major axis parallel to the scan direction, the overlap of the pulses gives an effective incident pulse number of 560 pulses for the line scan.

To prove that nanometer-scale lateral feature sizes were possible, smaller line widths were drawn with a 40× microscope objective. The objective replaced the 15 cm lens in the transient reflectivity experimental setup of Section 3.3.8. An aluminum mirror was placed between the two apertures before the objective in Figure 3.10 to image the substrate with a CCD camera placed next to detector D1. The Oriel stages were mounted at 0° AOI and the focal plane was defined as the position in the z-axis from the image plane where the minimum spot size was seen by optical microscopy.

Two lenses were placed in the main beam path before the experimental setup to reduce the spot size such that the two e-folding beam waist was smaller than the input aperture of the objective to achieve a Gaussian focal spot rather than an Airy spot. A 100 cm lens was placed 56 cm before a -50 cm lens in the beam line to collimate the divergent laser beam; the filter holder was moved before the Galilean telescope to avoid nonlinear absorption effects in the filters. The telescope reduced the incident 2 e-folding elliptical intensity beam waist of 3.5 mm × 3.4 mm with respective full angle divergences of 360 μrad and 250 μrad by a factor of two to avoid any clipping while entering the 8.9 mm microscope objective entrance aperture. The transmissivity of the objective was

calibrated in this configuration to be (45.1 ± 1.5) %. The single-shot ablation threshold and the focal plane beam waist were measured using the GBLT and yielded (112 ± 19) mJ/cm^2 and 1.80 μm × 1.76 μm, respectively. Sub-diffraction limited line widths are shown in Figure 5.12.

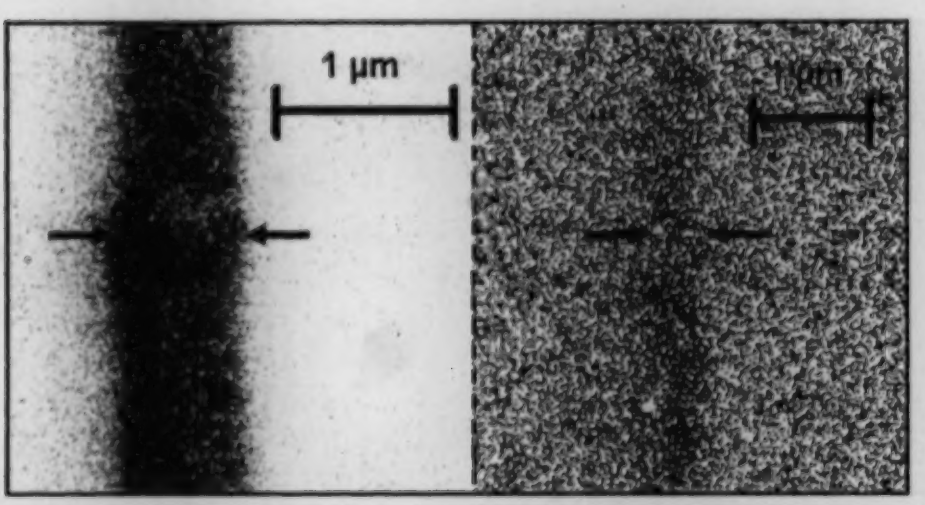

Figure 5.12: Sub-micrometer line widths of SAMs on gold-coated substrate using NIR femtosecond laser pulse nanomilling. Lines were scanned at 1 kHz repetition rate at a speed of 3.7 μm/s (959 pulses) with an incident peak fluence of (left) 37 mJ/cm^2 and (right) 26 mJ/cm^2. The contrast and brightness for the image on the right has been exaggerated to emphasize the SAM line.

Sub-diffraction limited SAM line widths of (750 ± 50) nm for incident laser fluences of 37 mJ/cm^2 and (375 ± 25) nm for 26 mJ/cm^2 were near the 959-pulse ablation threshold of the film of approximately (28.5 ± 4.9) mJ/cm^2 assuming an incubation coefficient of 0.8. White light interferometry profiles of the nanomilled region showed that the lines had a bumped morphology in portions of the scanned line of less than 10 nm, similar to the regions seen in Figure 4.5 and within expectation of recent results modeling nanojet and bump formations on noble metals [139].

5.5 Discussion

For the *thermal* patterning of the SAM surface, evidence of patterning was indicated by the wetting properties and the SEM images of the surface. These indicators proved that the reaction was desorption, as compared to incomplete reactions (decomposition) such as carbon bond cleavage or R-sulfur cleavage, with R representing the carbon chain. Carbon-bond cleavage would leave a methyl terminated group with the same hydrophobic properties as the background on the surface and would not show differential wetting. R-sulfur atom cleavage would leave no free gold atoms for hydrophilic SAM bonding and the hydrophilic monolayers would at most physisorb to the surface; however, physisorbed SAMs are easily rinsed away [162, 178]. Contact angle measurements performed in Dr. Amirfazli's lab independently confirmed that our channels had the appropriate wetting angle consistent with -COOH terminated molecular groups chemically bound to the gold film surface.

To model the CW desorption system, we needed to know whether we have a thermal or photolytic reaction. If we are breaking a bond that is sensitive to a particular wavelength (photolytic), then no incident power dependence would be observed. At the sensitive wavelength, an on/off behaviour will occur as opposed to a substrate-dependent reaction where increasing reactions occur for increasing powers. Figure 5.6 showed a substrate-dependent reaction because the line widths of the SAMs are increasing as the power increases at the edges demonstrating that a thermal model was required.

The feature sizes, which were governed by the thermal parameters of the substrate and whose results were not sensitive to changes in these parameters, could not be reduced unless faster scan rates or smaller beam waists were used. The smallest beam waists from a 10× microscope objective result in 4 μm feature sizes, but are still larger than a well-focused beam spot. We showed that by using a non-thermal pathway for SAMs, nanomilling of the substrate, sub-diffraction limited feature sizes could be achieved.

TTM modeling of copper nanomilling showed that the temperature on the surface rose to 500 K in a picosecond with relaxation beginning soon afterwards. The heating time would be several picoseconds and too fast for a reaction governed by slow reaction rates. The reaction rate dependence can be illustrated by examining a kinetic equation:

$$\frac{d\theta}{dt} = \theta(t)^n \nu \exp\left(-\frac{E_a}{k_B T}\right) \tag{5.2}$$

where $\theta(t)$is the fraction of surface coverage, n is the order of the reaction (considered first order here: dependent on available reaction sites), ν is the frequency factor or a co-factor dependent on the heating rate and E_a is the activation energy [179]. The frequency factor describes the reaction frequency and how often it "notices" the change in energetics. A low frequency factor, on the order of 10^8, responds to slow rates, such as conventional heating. If the heating rate is too rapid, then other less energetically favourable reactions (with activation energies E_a that are higher than the low frequency reaction), may occur if the frequency factor of that reaction is much higher, say 10^{14}.

The mechanism for the patterning of the SAMs using femtosecond laser pulses was found to be ablative, defined as removal of the SAMs along with at least a few gold atoms. Reducing the peak incident fluence from above the ablation threshold showed that removal of monolayers occurred at the periphery of the visibly damaged gold spots and continued to occur even when visible damage to the film was not seen by SEM, as in Figure 5.11 and Figure 5.12. With continued reduction of ϕ_{pk}, the removal of the monolayers stopped. To determine whether the removal regime was ablative, measurements of $\phi_{th}(1)$ and ξ were made as shown in Figure 5.10. Measuring ξ required additional measurements of the multiple-shot ablation threshold for $N = 10$, 100 and 1000, with the measured $\phi_{th}(N)$ for the 30 nm gold thin film coated with the hydrophobic monolayer as (553 ± 45) mJ/cm^2 for $N = 1$, (255 ± 30) mJ/cm^2 for $N = 10$, (183 ± 16) mJ/cm^2 for $N = 100$ and (135 ± 10) mJ/cm^2 for $N = 1000$. This gave an incubation coefficient of 0.80 ± 0.01.

The presence of the hydrophobic monolayer on the thin gold film was not expected to perturb the ablation mechanism and alter the thresholds when compared to a clean gold thin film. Published values for the single-shot ablation threshold confirmed this hypothesis. Amoruso *et al.* [36] used 780 nm, 120 fs pulses at a 50° AOI to measure the electrons and ions removed from the surface of bulk gold (99.99 % purity). Scaling the ablation threshold of the vapourization regime of 460 mJ/cm^2 using tables for the complex index of refraction for gold at 800 nm [180] in the p-polarized state yielded

700 mJ/cm^2 for the single-shot ablation threshold. This threshold is higher than the value measured here; however, it has been established that the ablation threshold will decrease as the thickness of a metal decreases below the electron diffusion length with a critical thickness of ~443 nm for gold [26, 49]. Quartz crystal microbalance (QCM) measurements of the single-shot ablation threshold at 850 nm for a 250 nm thick gold electrode resulted in a value between 350 mJ/cm^2 and 450 mJ/cm^2 [181]. This agrees with our measured single-shot ablation thresholds being between our values for bulk gold and a 30 nm thin film.

To our knowledge only one report on the incubation coefficient of gold exists: a value of 0.922 for gold films with thicknesses varying from 90 nm to 1500 nm [49] for $N > 10^4$ shots with 200 fs laser pulse widths. These measurements were made at the 400 nm wavelength, which is above the resonant *d*-shell absorption line for gold [45] and it is uncertain how this affects the incubation coefficient when scaling to 800 nm.

The fluence range for patterning was 90 mJ/cm^2 to 190 mJ/cm^2 for line scans made at 50 μm/s at a 1 kHz repetition rate, which corresponded to irradiances of 510 to 560 pulses for any one spot. Above 190 mJ/cm^2, visible ablation damage was observed in the centre of the patterning region. The damage threshold for this pulse range varies from 134 mJ/cm^2 to 183 mJ/cm^2 using the multiple shot ablation threshold scaling equation with the incubation coefficient, equation (2.3), including the errors. This places the patterning regime into the near-threshold ablation region, where nanomilling was measured in thin copper films just above the multishot ablation threshold as in Figure 4.5.

Chang *et al.* [182] showed NIR femtosecond pulse SAM patterning on gold films and proposed that SAM removal was due to photo-oxidation of the gold-sulfur bond; however, no substantial argument or control experiment was presented. To determine whether photo-oxidation was required for patterning in the femtosecond regime, we performed O_2 dilution experiments. By pumping down the vacuum chamber to ~100 mTorr and refilling to 633 Torr with $N_{2(g)}$ from the blow-off of a liquid nitrogen tank sequentially three times, a ratio of one oxygen molecule in the chamber per 10 million sulfur atoms on the monolayer surface was achieved. This assumed a (5 Å)^2 area per sulfur atom on the gold thin film surface and an initial 21 % molar concentration of oxygen at atmospheric pressure. Line scans were made at 50 μm/s between

130 mJ/cm^2 and 190 mJ/cm^2 and no measurable change in the contrast ratio or the line widths was detected by SEM for experiments done in an oxygen deprived atmosphere and in ambient air.

Considering the above discussion, the previously proposed mechanism for femtosecond laser patterning (800 nm, 220 fs) of SAMs on gold thin films as photo-oxidation [182] is not plausible. The peak incident fluence for the study in [182] would be ~ 1 J/cm^2 with 5 pulses overlapping (using their theoretical focal spot size of 1.6 μm and scanning conditions of 70 mm/s, 5.5 mW and 100 kHz). This fluence, well above $\phi_{th}(1)$ here, would lead to ablation of the sample as the dominant patterning mechanism and since no control experiment as described above was performed, the photo-oxidation proposal cannot be substantiated.

The advantage of the laser patterning procedure is its flexibility to produce complex patterns with a variety of SAMs differing in chain length and functional group, allowing for modulation of the surface properties. Introduction of pattern changes is easy since this is a simple three-step procedure. The mechanism for patterning allows for erasing and re-writing any pattern. Computer-aided motion and control can optimize processing time and pattern control and allow for repeatable and precise chips built in an assembly-line format.

Laser removal of SAMs is not unique since it has been observed using LD-FTMS [176]. Mixed SAM surfaces were made using laser desorption by Takehara *et al.* [183] who used a pulsed laser and single shot exposure with a focused beam and ten-shot exposure with an unfocused beam to desorb monolayers in a single location from a gold electrode surface. In Takehara *et al.* [183], the mechanism for desorption or bond breaking was not indicated.

5.6 Engineering application: Self-assembled monolayer patterning of glass substrates with femtosecond laser pulses

The main focus of the thesis was to determine the mechanisms for SAM patterning with CW and femtosecond pulse width laser systems. In the CW regime, a thermal mechanism caused desorption of the molecules from the gold substrate. For the femtosecond laser pulses, an ablative regime was required since the heating rates were

too fast for the molecules to respond to the change. The applicability of SAMs on noble metal substrates is limited due to the stability issues outlined in Section 5.1. Siloxane-terminated SAMs are stable SAMs on glass substrates [152] and with the limited surface etching of nanomilling, femtosecond laser pulses can be used to pattern microfluidic substrates to create complex heterogeneous substrates for diagnostic methods. Biofouling may also be an issue in certain regions of a substrate and selective deposition and patterning of PTFE-terminated SAMs can also be used.

Multiphoton absorption at the SAM bonding site could also be a patterning pathway for glass substrates using femtosecond laser pulses since the ablation threshold of dielectrics are typically 10 to 100 times higher than for metal surfaces. The strongest bond strength known is that of the carbon-carbon bond at 700 kJ/mol [23], which is equivalently 7.25 eV/bond, making any bond energies between an SAM and a glass substrate less than this maximum value and accessible to direct photon desorption, especially with the availability of third harmonic (4.66 eV/photon) femtosecond laser pulses.

This work has shown that nanomilling of metal surfaces is a fast, flexible and corrective SAM patterning technique that can be a competitive methodology to many of the available patterning techniques. This technique can also be applied in a complementary fashion as a prototyping tool for more expensive lithographic techniques.

Chapter 6

Femtosecond laser pulse ablation of silicon

Predicting the possible mechanisms of nanomilling, and especially incubation, requires a model that provides details into the microscopic properties of materials under femtosecond laser pulse interaction. The TTM is a macroscopic model that yields thermal properties of the material and can only predict the single-shot ablation threshold of a metal provided melting is an adequate predictor and the material reaches melting isobarically and isometrically. A microscopic model is still required to give a more detailed picture of the non-equilibrium interaction and to distinguish between ion expulsion and free electron generation at low incident laser fluences as responsible for the incubation phenomenon or a thermal cycling phenomenon, presented in Chapter 7. Furthermore, a microscopic model would also provide insight into the pm/pulse ablation rates reported in Hashida *et al.* [42] and in Chapter 4 of this thesis on nanomilling.

Jee *et al.* [39] demonstrated that incubation was similar to a metal moving through a fatigue stress-strain cycle. If a metal is approaching the melting temperature when irradiated by laser pulses below the single-shot ablation threshold, then it may be possible to explain the incubation phenomenon at femtosecond pulse widths using the thermal stress-cycling model presented by Jee *et al.* and discussed as a future experimental direction in Section 7.2.

Before doing thermal stress-cycling analysis and modeling, a microscopic model to predict the ablation threshold adequately for metals requires avalanche ionization to

explore the microscopic properties under femtosecond pulse interaction. Our group has been working on an MD simulation for silicon that can be used to predict the single-shot ablation threshold of silicon by 800 nm, 100 fs Gaussian FWHM laser pulses. The HF-MD simulation did not have an independent electron subsystem and it lacked an avalanche ionization mechanism. To adapt the code for metal ablation, an electron subsystem needed to be added. Predicting the scaling of the single-shot ablation threshold of silicon over a range of pulse widths would indicate the success of the new model making it amenable for laser-semiconductor and eventually laser-metal dynamics.

The MD simulation of the single-shot ablation threshold of silicon is still an open issue since the fit with the experimental data over pulse width is not complete. Open questions remain in modeling the fundamental processes for laser absorption by the conduction band electrons and coupling of this absorbed energy to the lattice in the MD simulation. This section gives the results of adding avalanche ionization to the HF-MD simulation (herein called the avalanche MD)*.

6.1 Pulse dependent single-shot ablation threshold of silicon

The single-shot ablation threshold of silicon was measured using the experimental technique described in Section 3.3. Images of the spots were made using the WLI and the single-shot ablation threshold was analyzed using the Gaussian beam limiting technique described in Section 4.1. Examples of WLI images are shown in Figure 6.1 with an enhanced image in Figure 6.2 highlighting the 1 nm deep ring around the crater.

The ablation spots had a protrusion of about 4 nm around the edge of the ablation hole. At higher incident fluences, the height of this protrusion remained approximately constant and as the hole depth increased, it was clear that the lip of the ablation spot occurred further out from the centre of the spot than this protrusion; therefore, all ablation spot measurements were made to the outside edge of the protrusion indicated by the arrow labelled A in Figure 6.1 for low fluences ($\phi_{pk} < 1$ J/cm^2) and out to the shoulder of

---

* The update to the HF-MD simulation was written by Nelson Young, B.Sc. (Physics, University of Alberta), an undergraduate 4th year electrical engineering student. I managed the project by participating in the examination of the literature and guiding the direction of the project with N. Young and performing single-shot ablation threshold experiments on silicon substrates. Code writing, compilation and testing presented in this thesis was performed by N. Young.

the crater for high incident fluences. An example of a crater made at low incident fluence imaged along the dotted line in Figure 6.1(a) is shown in Figure 6.3.

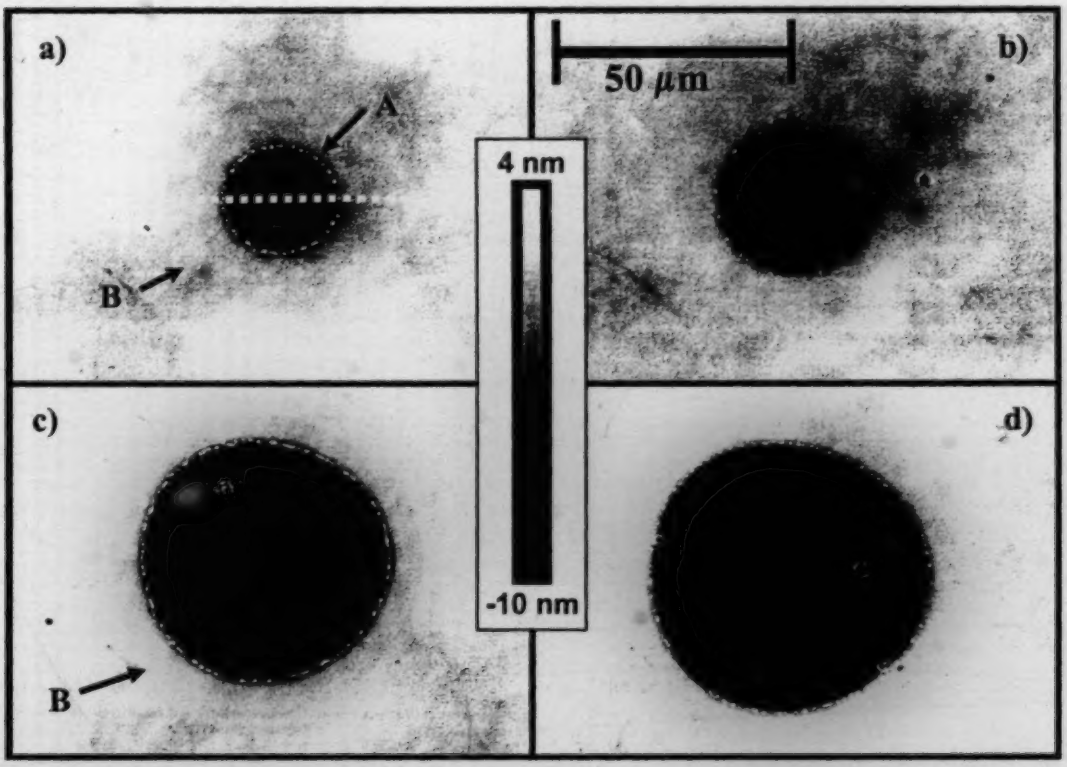

Figure 6.1: WLI images of intrinsic silicon ablation spots. The images on the left (a and c) are intrinsic silicon with a native oxide and on the right (b and d) intrinsic silicon with no native oxide. The incident peak fluence and elliptical diameters measured were (a) 310 mJ/cm^2, 26.9 μm × 26.4 μm, (b) 340 mJ/cm^2, 35.7 μm × 34.7 μm, (c) 450 mJ/cm^2, 53.1 μm × 52.8 μm, (d) 500 mJ/cm^2, 60.8 μm × 59.8 μm. The dotted line in (a) is an example line out discussed in the text. The arrows indicate two regions on the silicon with a native oxide after ablation. The region labelled A indicates the outer edge of the protrusion at low incident laser fluences. The region labelled B shows the region that was etched to ~1 nm, consistent with the thickness of a native silicon oxide layer.

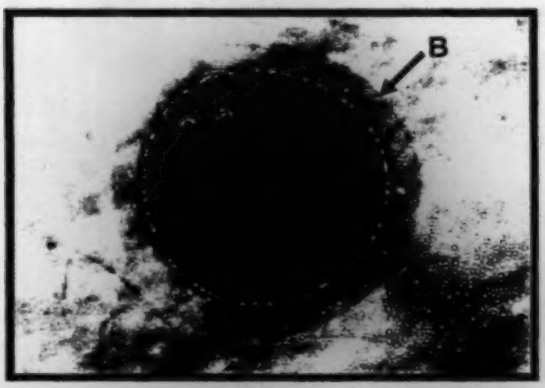

Figure 6.2: Enhancement of the WLI image of Figure 6.1(c) to expose the region on the native oxide silicon sample labeled as B in Figure 6.1(a and c).

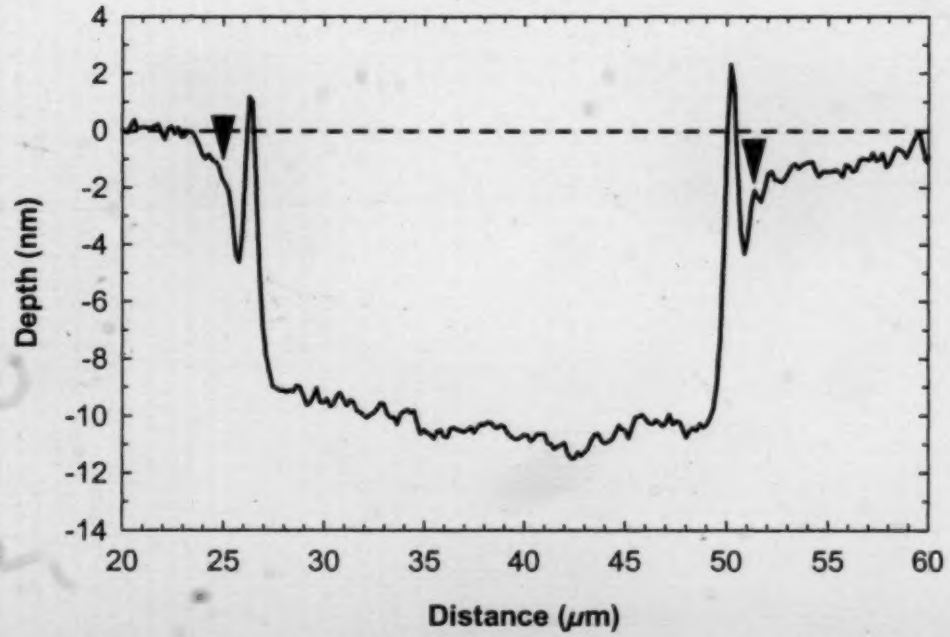

Figure 6.3: Line out of an ablation spot made on the intrinsic silicon with a native oxide measured using the WLI. The incident peak fluence was 310 mJ/cm^2 and the measured diameter was 26.9 μm. The dotted line is a guide for the eye showing the 0 nm level and the arrows indicate the measured points for evaluating the ablation threshold.

The single-shot ablation threshold for silicon was evaluated using the diameters as indicated in Figure 6.3. The spikes in the ablation spots were only visible for low incident fluences. At higher incident peak fluences ($\phi_{0x} > 1.5$ J/cm^2), the protrusions were clearly *inside* the crater. The ablation threshold was also calculated using the protrusions as the edge of the crater for the low fluence crater diameters to see the error that would be produced if they were used as an edge feature and the single-shot ablation threshold varied by approximately 4 %, within the error of the reported ablation thresholds.

The outer rim defined in Figure 6.1 by the arrow labelled B is a region that was only visible on the silicon sample with a native oxide. It was approximately 1 nm to 2 nm deep and is shown in close up in Figure 6.4. This region is interesting because it appears to be as deep as the expected native oxide depth of approximately 3 nm for a silicon sample [71].

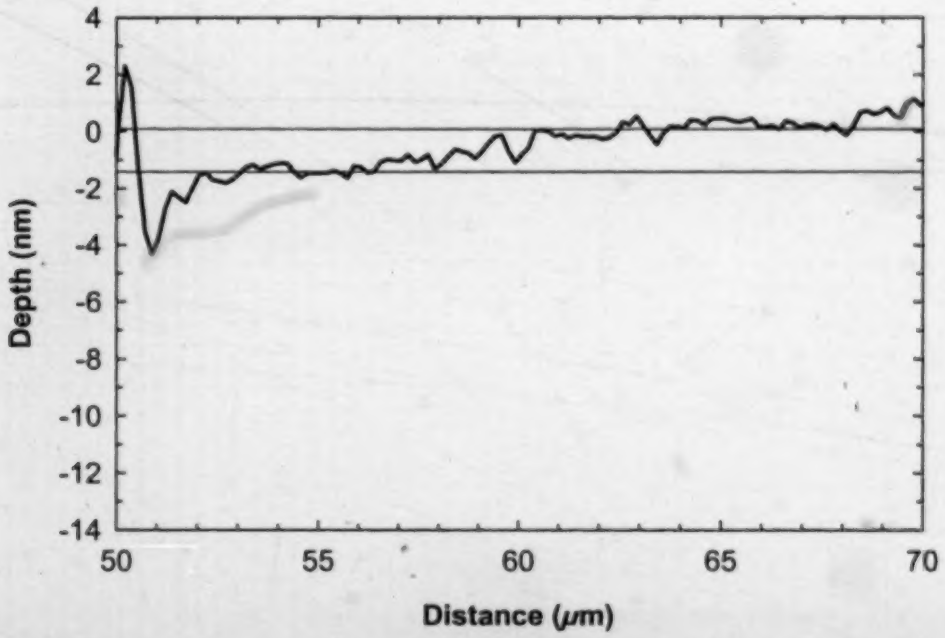

Figure 6.4: Close up of the rim of the ablation spot made on the intrinsic silicon with a native oxide measured using the WLI in Figure 6.3. The lines on the graph are guides for the eye showing that the surface has dropped a couple of nanometers before reaching the edge of the crater and then the spike. The incident peak fluence was 310 mJ/cm^2.

A plot of the incident single-shot ablation threshold is shown in Figure 6.5. The incident $\phi_{th}(1)$ with respect to pulse width was also measured for a p-type silicon substrate doped with boron as supplied by the NanoFab. Experiments for each pulse width were done in random triplicates and the error bars represent the first standard deviation from the diameter measurements, and the slope and intercept regressions (see Appendix C). The experiments done with the intrinsic silicon samples were done in vacuum to closely match the conditions of the MD simulation where no pressure above the simulation particles exists. The experiments done with the p-type silicon were done in ambient atmospheric conditions.

The reflectivity is an important parameter, as shown in Section 4.2 with copper, since it can result in large variations in the incident single-shot ablation threshold making the report of the *absorbed* single-shot ablation threshold more important. The reflectivity of the silicon samples was measured to verify that the reflectivity did not vary among samples. Reflectivities of the p-type silicon samples were measured as (32.7 ± 0.8) % using the specular reflectivity technique described in Section 3.3. The reflectivity of the intrinsic silicon sample with the native oxide removed with a buffered oxide etch (BOE) was measured using the transient reflectivity experimental setup at low incident fluences. The reflectivity of the BOE intrinsic silicon sample was measured as (34.4 ± 0.1) % from the weighted average of multiple measurements over random triplicates of incident fluences. The expected reflectivity of single crystal silicon at 800 nm from standard reference material was 32.9 % [23]. The reflectivity of the intrinsic silicon sample before the BOE was not measured, but from the results in Figure 6.5 and the small variation between the p-type and BOE silicon sample and their proximities to the expected value, the intrinsic silicon reflectivity is likely close to the reflectivity of the BOE silicon.

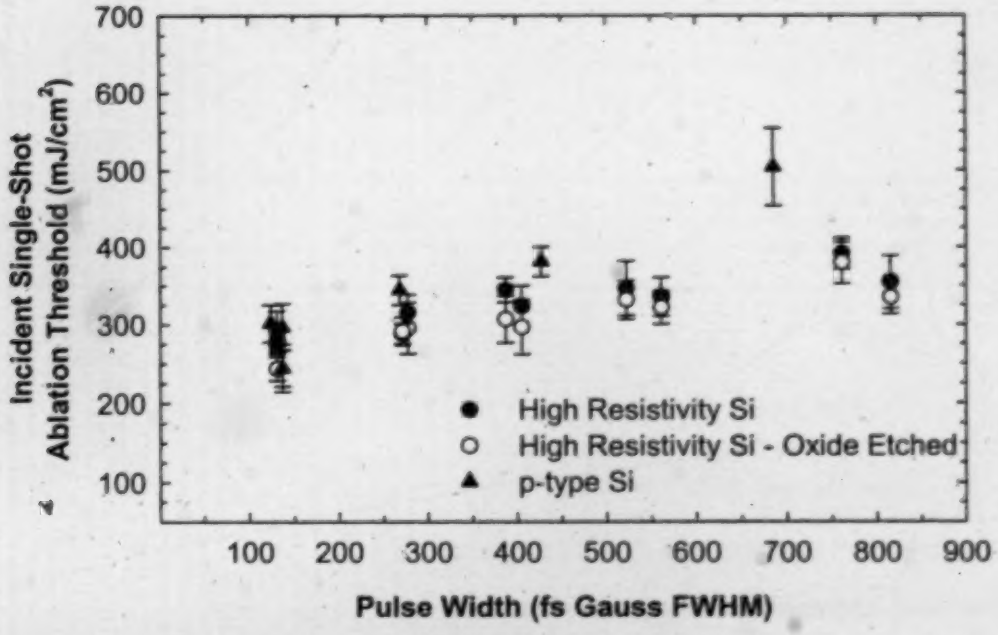

Figure 6.5: Determination of the single-shot ablation threshold for intrinsic and p-type silicon with femtosecond pulse widths at 800 nm.

6.2 Modeling femtosecond laser pulse ablation of silicon with molecular dynamics

6.2.1 Modeling avalanche ionization

The original MD code accounted for electron excitation by breaking the SW potential between neighbouring atoms; this simulated ultrafast melting. If one-photon absorption occurred, then one SW potential was modified: one bond was broken. If TPA occurred, then two bonds were broken. The probabilities were calculated as [87]:

$$P_{1\hbar\nu} = 1 - \exp\left(-\frac{\alpha_0 M_{Si}}{\rho A}\right) \text{ (unitless)} \tag{6.1}$$

$$P_{2\hbar\nu} = 1 - \exp\left(-\frac{\beta M_{Si}}{\rho A}\frac{N_{ph}(z)E_{ph}}{A}\right) \text{ (unitless)} \tag{6.2}$$

where M_{Si} is the atomic mass of Si (28.0855 g/mol) [23], ρ is the density of silicon (2.329 g/cm^3) [23], A is the cross-sectional area (3.8 Å)^2, $N_{ph}(z)$ is the number of photons entering the cell at a depth z from the surface and E_{ph} is the photon energy (1.55 eV).

In the HF-MD, probabilities were used to model absorption since the density of atoms in the simulation cell could fluctuate. The probabilities were compared to a random number generated at the start of each loop with the loop repeated for the number of atoms that were in the simulation cell at a given time step.

To change the HF-MD to operate with an electron subsystem, the first change was to reduce the probabilities of the one- and two-photon absorption probabilities by four. These absorption events operate on valence electrons and since there are four valence electrons in silicon, the loop needed to be increased by a factor of four. As valence electrons were promoted to the conduction band, the number of loops reduced.

The probability of FCA was calculated similar to the linear absorption probability:

$$P_{FCA} = 1 - \exp\left(-\frac{\alpha_{FCA} M_{Si}}{\rho A}\right) \text{ (unitless)} \tag{6.3}$$

The FCA coefficient, α_{FCA}, in the simulation was $1.964 \times 10^{-10} \times (800 \times 10^{-7}\ \text{cm})^2 n_{CB}\ (\text{cm}^{-1}) = 1.26 \times 10^{-18} n_{CB}\ (\text{cm}^{-1})$ using the coefficient in ref. [70]. The carrier density was constant at one electron in each simulation cell ($1.8 \times 10^{22}\ e^-/\text{cm}^3$) and the loop repeated for every conduction band electron in the simulation cell. The initial conduction band electron density was zero, so the above conduction band electron density in the probability was an adequate value for the MD.

To complete the avalanche MD model, the energy of each electron needed to be tracked because the impact ionization, equation (2.24), depends on the energy of each electron in the conduction band.

To track the conduction band electron energy for the impact ionization model, the avalanche MD code was modified to break only one SW potential for any absorption event and track the conduction band electron energy referenced to the top of valence band. If a one-photon event occurred, the energy of the electron in the conduction band

was $h\nu$ and if a TPA event occurred, the electron energy was $2h\nu$. In this accounting system, in subsequent interactions the conduction band electrons could also:

a) increase in energy from FCA

b) couple back to the parent atom and release its energy by recombination simulated by an increase in the atom's kinetic energy

c) impact ionize another valence band electron and share the energy equally between the pair of electrons

d) become a free electron if the electron energy reached the work function (4.85 eV) of silicon and become subjected to Coulomb forces

To track the conduction band electron energies, each atom in the simulation had four floating-point numbers whose values were the energies of the individual electrons in the conduction band. A value of zero indicated an electron bound to its parent atom in the valence band. At this stage in the development of the model, the avalanche MD code does not distinguish between a direct or indirect band gap semiconductor. Effectively, the code models silicon as a direct band gap semiconductor with a 1.12 eV band gap energy and a continuous conduction band structure (i.e.: no exclusion rules on electron occupation and phonon coupling to conserve momentum transfer) except that it uses experimental values that are relevant for the indirect band structure of silicon.

To model impact ionization, the simulation would determine whether any conduction band electrons surrounded the parent atom. If those electrons had energy of at least $2E_G$ but less than 4.85 eV, then an impact probability was calculated using the impact ionization rate multiplied by the time step of 0.5 fs. The impact ionization rate of equation (2.24) had to be shifted in energy since the electron energies in the MD simulation were referenced from the top of the valence band. The probability of an impact ionization event was the multiplication of this shifted rate with the MD time step:

$$P_{v(U)} = 1.9\times10^{11}\left(U-2U_0\right)^4\Delta t \tag{6.4}$$

The avalanche MD simulation was done in a $10\times10\times120$ cell volume, which described a simulation volume of 3.8 nm × 3.8 nm × 45.6 nm. Ablation was defined as the removal of 2 nm layer (2949 particles), a depth that could be measured

experimentally using advanced imaging systems such as an AFM or an interferometric depth profiler. The simulation times were long (upwards of 9 days) and convergence to a simulation that gave an absorbed fluence with an exact removal of 2949 particles was difficult. The reported MD single-shot ablation thresholds are averages of two simulations with values that span through 2949 particles.

A comparison of the avalanche MD to the experimental measurements for the intrinsic silicon single-shot ablation threshold carried out in vacuum and the p-type silicon wafer carried out in air is shown in Figure 6.6.

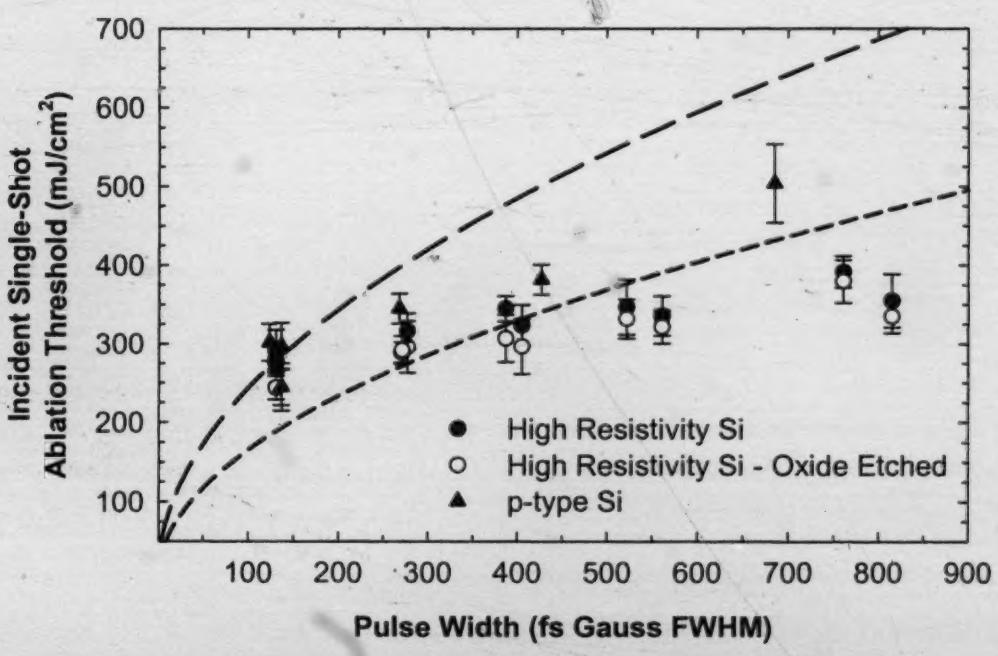

Figure 6.6: Plot of the avalanche MD simulation with the experimental single-shot ablation thresholds for different silicon wafers. The upper line is the avalanche MD with an FCA coefficient as given in equation (6.3) and the lower is 10× this value. The avalanche MD simulation results were scaled by the 32.9 % reflectivity of silicon to be an incident single-shot ablation threshold.

6.2.2 Dynamics of conduction band electron generation in the avalanche MD simulation

The avalanche MD simulation results in Figure 6.6 showed that the single-shot ablation threshold depended strongly on the TPA coefficient since at smaller pulse widths

the $\phi_{th}(1)$ continued to decrease at a $\tau^{1/2}$ rate. Exploiting the advantage of MD to access material subsystems, the electron generation mechanisms were plotted for fluences at the ablation threshold at several pulse widths. In Figure 6.7, the number of occurrences of each of the four mechanisms shows that TPA was the dominant mechanism for pulse widths between 41 fs and 333 fs FWHM.

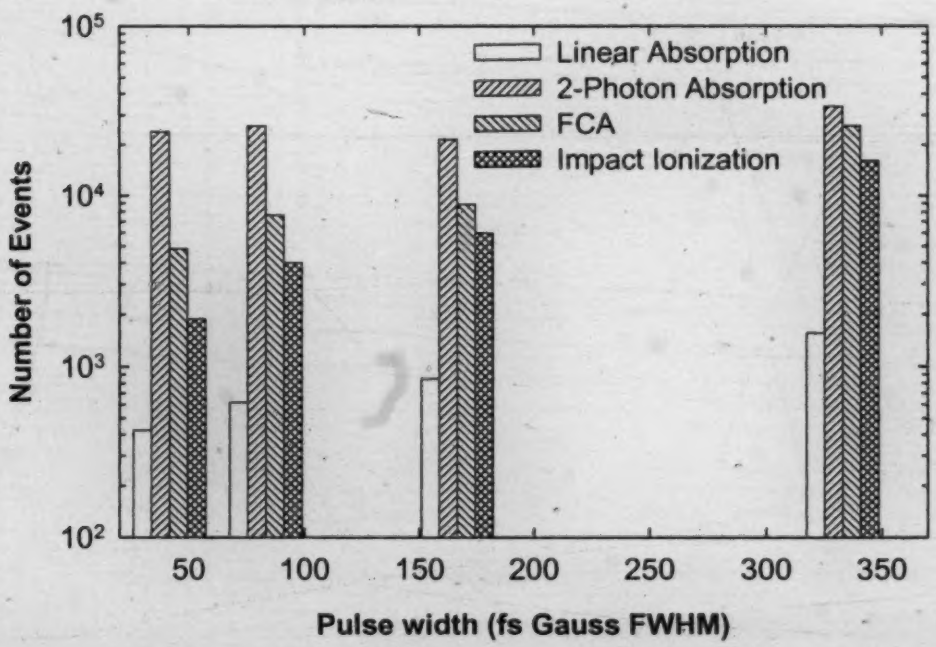

Figure 6.7: Strength of the conduction band electron generation mechanisms during the laser pulse in the avalanche MD simulation near the single-shot ablation threshold at 41 fs, 83 fs, 166 fs and 333 fs Gaussian FWHM pulse widths. The first set of bars has an absorbed fluence of 100 mJ/cm^2 (41.6 fs), the second set of bars has an absorbed fluence of 140 mJ/cm^2 (83.6 fs), the third set has an absorbed fluence of 180 mJ/cm^2 (166.5 fs) and the last set has an absorbed fluence of 330 mJ/cm^2 (333 fs).

The dynamics of conduction band electron generation was plotted over the pulse width to examine the final density of the electrons in the conduction band and to determine when the maximum density was reached. The critical density for 800 nm was calculated for the free-electron mass of m_e (a maximum value) and the electron-hole plasma effective mass in silicon of $0.18m_e$ [69] (a minimum value) to be 1.74×10^{21} cm^{-3} and 3.14×10^{20} cm^{-3}, respectively.

There are several electron effective masses in silicon, which depend on the process being considered. The fundamental effective masses are the longitudinal and transverse with values of $0.92m_e$ and $0.19m_e$, respectively (p. 216 in ref. [22]). There exists a conduction band or thermal velocity effective mass of $0.28m_e$ [184, 185] and a density-of-states effective mass [185] that are functions of the fundamental effective masses. All of these effective masses are used in the description of room-temperature silicon. At elevated temperatures and conduction-band electron densities, an electron-hole plasma is formed where the optically probed effective mass can be as low as $0.15m_e$ to $0.18m_e$ [186]. Schroder *et al.* [70] used $m_{opt} = 0.28m_e$, for heavily-doped Si in equation (2.25) in Section 2.4, in line with the conduction band electron effective mass for room-temperature silicon. A comparison of FCA with the Drude model will follow where the electron-hole plasma effective mass of $0.18m_e$ is used in the description of the dielectric function.

In Figure 6.8, the number of electrons promoted from the valence band to the conduction band over the time of the pulse is shown for a 41.6 fs Gaussian FWHM pulse. The maximum electron density was reached at the end of the pulse since impact ionization can continue after the pulse if there are excited electrons in the conduction band. Impact ionization is one of three relaxation mechanisms for silicon, the other two relaxation mechanisms are Auger recombination and diffusion into the bulk, both of which tend to occur at time scales greater than 1 ps [65].

In Figure 6.9, the number of electrons promoted over a 333 fs FWHM Gaussian pulse width is shown. The maximum electron density was reached near end of the pulse as with the 41.6 fs pulse. In both cases, the critical density of electrons for the 800 nm wavelength was exceeded before the laser pulse reached its peak. For the 41.6 fs laser pulse, the critical density was reached between 15 fs and 25 fs before the peak, and for the 333 fs laser pulse the critical density was reached 122 fs to 172 fs before the peak of the pulse. Up to the point in the kink in the conduction band electron density in Figure 6.9, linear absorption was the dominant conduction band electron generation mechanism until the intensity was sufficient for TPA to dominate; once again demonstrating the potential of MD simulations to examine the microscopic dynamics in laser ablation.

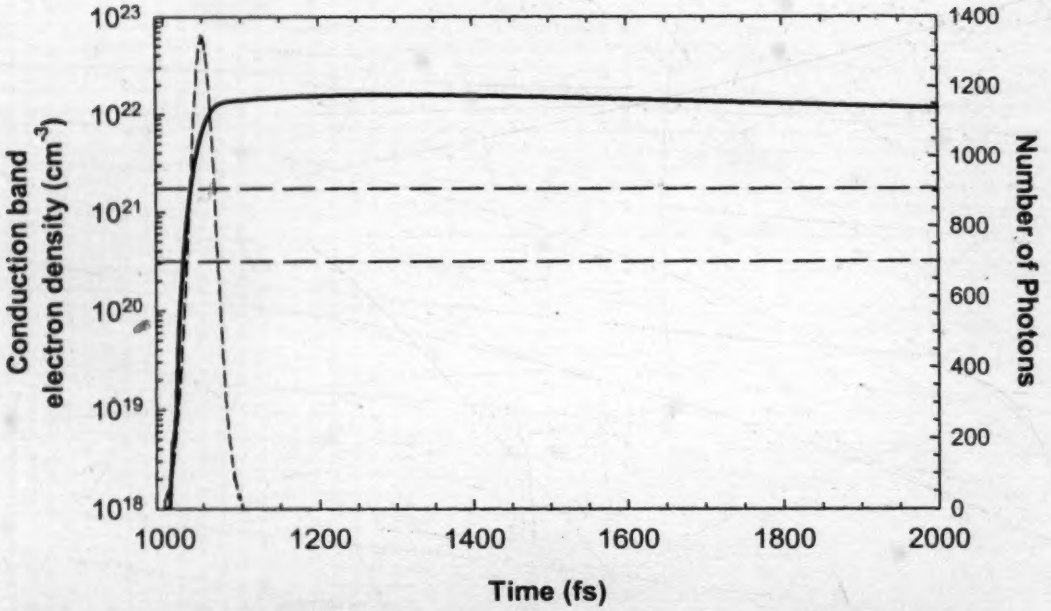

Figure 6.8: Conduction band electron density in the avalanche MD simulation volume for a 41.6 fs Gaussian FWHM pulse with an absorbed fluence of 100 mJ/cm^2. The upper line is the critical density for 800 nm wavelength with $m_{opt} = m_e$ and the lower line is the critical density for $m_{opt} = 0.18m_e$. The dashed line is the incident number of photons at the surface entering the simulation per time step.

As the electron density approaches the critical density for a particular frequency, a thin, highly-absorbing skin layer is created that is eventually followed by an approximately 50 % reflective interface that reflects a large part of the incident electromagnetic field [137]. If the critical density is reached within the lifetime of the pulse, then an experimenter would see an increase in the sample reflectivity during the pulse lifetime as they approached the single-shot ablation threshold. The avalanche MD simulation suggests that if the electron generation is as strong as shown, a dramatic change in the reflectivity would be evident at fluences near the ablation threshold.

An experiment measuring the reflectivity of the main pulse from silicon with increased fluence would be a direct challenge on the electron generation dynamics in the MD at this stage in the simulation development. The transient reflectivity of intrinsic silicon and p-type (Boron doped) was investigated using the experimental setup described in Section 3.3 and the results of the experiment are shown in Figure 6.10.

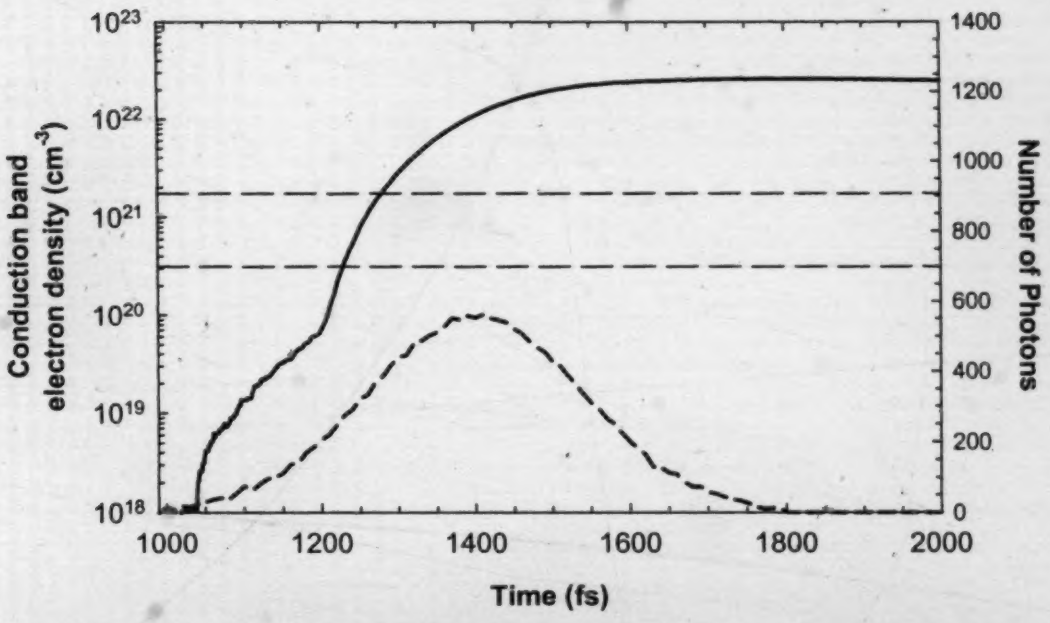

Figure 6.9: Conduction band electron density in the avalanche MD simulation volume for a 333 fs Gaussian FWHM pulse with an absorbed fluence of 330 mJ/cm^2. The upper dashed line is the critical density for 800 nm wavelength with $m_{opt} = m_e$ and the lower dashed line is the critical density for $m_{opt} = 0.18m_e$. The dashed line is the incident number of photons at the surface entering the simulation per time step.

6.3 Discussion

The avalanche MD simulation of the single-shot ablation threshold was dependent predominantly on TPA. Figure 6.7, Figure 6.8 and Figure 6.9 show that the conduction band electron density was generated mostly by TPA and that the density exceeded the critical density by two orders of magnitude for 800 nm excitation. This density exceeds first-order expectations that the critical density can only be exceeded by a factor of four if you assume that: the electromagnetic field could no longer couple to the conduction band electrons due to plasma shielding, impact ionization caused equal sharing of the conduction band electron energy and all electrons in the conduction band were at an energy just shy of the work function of silicon (4.85 eV).

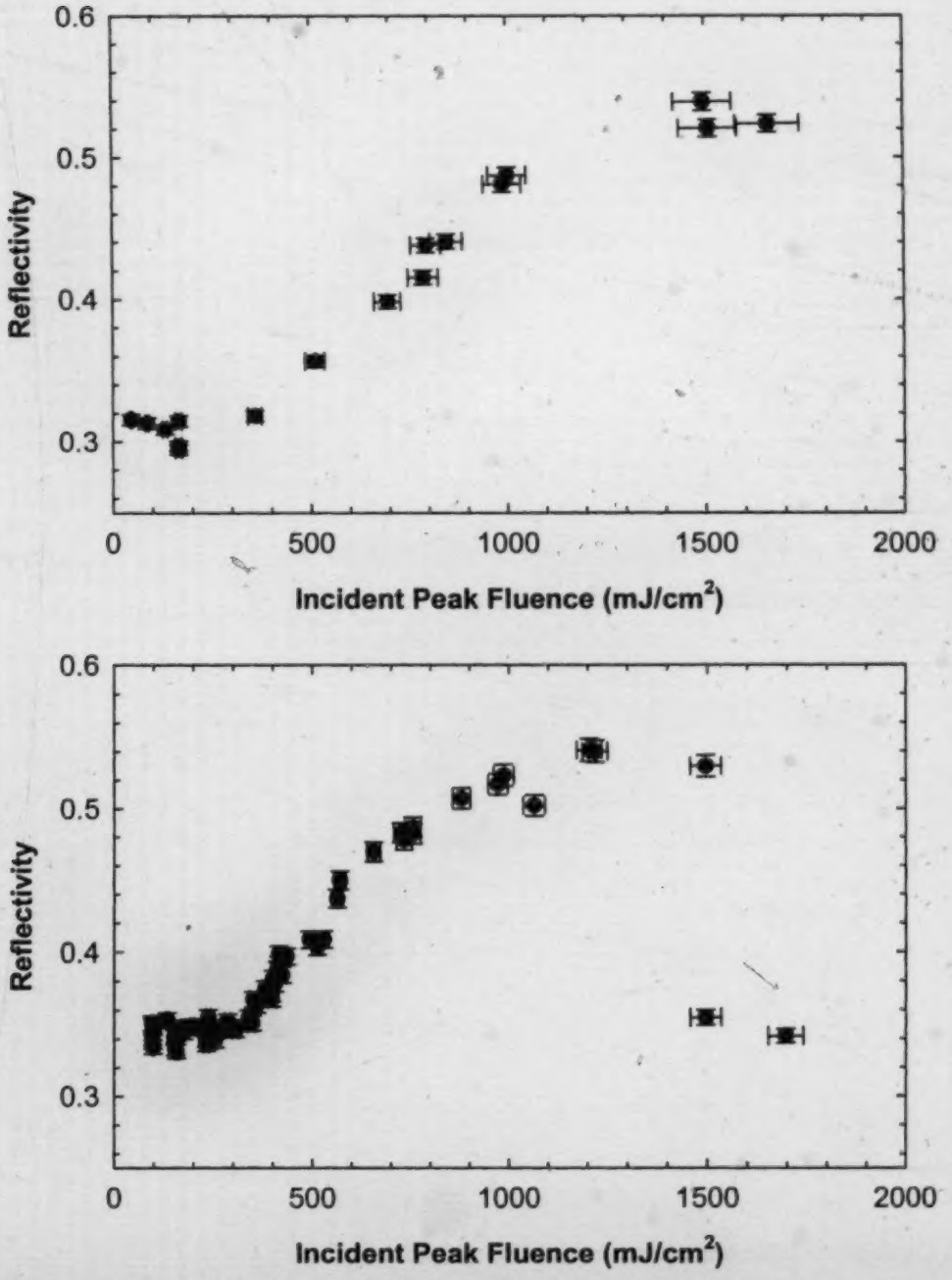

Figure 6.10: Transient reflectivity of the 800 nm, 140 fs to 150 fs FWHM Gaussian main pulse from silicon measured over a range of incident peak fluences for (upper graph) p-type silicon and (lower) BOE etched intrinsic silicon. The single-shot ablation threshold of silicon at this pulse width is between 200 mJ/cm^2 and 300 mJ/cm^2.

The reflectivity of a plasma at critical density is not 100 % [69], so the electromagnetic field could continue to interact with the plasma in a thin layer, heating up conduction band electrons and could continue to promote impact ionization of the valence band electrons at later times in the pulse. The reflectivity would reach nearly 70 % and at the ablation threshold the sample would be highly reflective during a portion of the laser pulse interaction when measuring the transient reflectivity.

Measurement of the transient reflectivity in Figure 6.10 showed that the reflectivity did not increase significantly (~40 %) above the small-signal reflectivity (32.9 %) until *two to three times* the ablation threshold, an indication that the conduction band electron density has not reached the critical density within the lifetime of the pulse, countering the results shown in Figure 6.8 and Figure 6.9. There are two possible explanations for the contrasting results; one is that the transient reflectivity experiments represent a spatial integration of the conduction band electron density of a spatially varying fluence and that at the ablation threshold; only a fraction of the laser pulse is generating a large conduction band electron density.

The second possibility is that the MD simulation operates on a reduced volume from the calculated optical absorption depth. If all the absorption contributions were additive and the 130 fs laser pulse fluence was near the absorbed single-shot ablation threshold measured experimentally, assuming a 33 % reflectivity [23], then the total absorption depth with a linear absorption of 803 cm^{-1}, a two-photon contribution at $\beta =$ 55 cm/GW of 60 000 cm^{-1} and $\alpha_{FCA} = 2260\ cm^{-1}$ gives an overall absorption depth of 160 nm, three times higher than the MD simulation volume. If any of these values are slightly weaker, for example, tuning the TPA to lower values as in the discussion above, then the overall absorption depth would be longer such that the densities reported in the MD would be near critical density. This result would confirm the experimental results on transient reflectivity.

At fluences nearly an order of magnitude above the single-shot ablation threshold in Figure 6.10, there is an abrupt drop in the reflectivity. This may be due to the rapidly expanding material where the density is changing over the lifetime of the pulse as seen in ref. [65] where the reflectivity of silicon changes dramatically in less than 1 ps when irradiated by a 1 μm, 90 fs pulse.

The original MD simulation was developed with a TPA coefficient of 55 cm/GW as given in ref. [67]. In the work of Sokolowski-Tinten *et al.* [67], the single-shot ablation threshold of silicon coincided with the measured single-shot ablation threshold of gallium arsenide. The authors stated that since the ablation thresholds were comparable, the absorption depths must be comparable. The linear absorption coefficient of gallium arsenide was an order of magnitude larger than silicon, so TPA was assumed to be the mechanism in silicon that would create an absorption depth similar to GaAs, and a value of 55 cm/GW was derived for the 625 nm wavelength. The effects of FCA did not enter into the comparison work, so it is possible that the authors overestimated the value. Recently, the authors have added some uncertainty to this value and adjusted their prediction to (50 ± 10) cm/GW [69] from new measurements putting it in line with work done at a similar wavelength [72].

In the work of Reitze *et al.* [72], the TPA coefficient was measured to be 34.6 cm/GW for 620 nm excitation with femtosecond laser pulses, similar in wavelength to the work in ref. [67] at 625 nm. Examining the band structure of silicon shows that the TPA coefficient should change significantly when measured with an incident photon above or below 1.71 eV since silicon has a direct absorption band gap at $\vec{k} = 0$ of 3.43 eV. Calculations of the band structure of silicon show that the direct band gap is between 3.3 eV and 3.8 eV [187]. A TPA event with an incident photon of energy less than 1.71 eV would need to be indirect.

From the literature, it appears that β_{direct} is greater than 20 cm/GW and that an indirect, phonon-assisted TPA coefficient, $\beta_{indirect}$, is a few cm/GW. Two measurements of $\beta_{indirect}$ for crystalline silicon when measured with picosecond laser pulses at 1060 nm (1.17 eV) that gave 1.5 cm/GW [188] and (1.5 ± 1) cm/GW [189]. In the work of Reintjes *et al.* [188], they stated that two indirect TPA events occurred, instantaneous and stepwise. Stepwise absorption occurred when an electron was promoted by linear absorption to the conduction band and was then promoted further into the conduction band making for an overall nonlinear process. Cooling the silicon samples to 20 K, they measured the strength of the stepwise and the instantaneous TPA events. The stepwise TPA should scale with temperature as phonon-assisted linear absorption would increase. At low temperatures, the stepwise and linear absorption effects were negligible and

instantaneous TPA could be measured directly. They showed that stepwise TPA was minimal in silicon and that the instantaneous TPA was not significantly changed with temperature.

In the work of Boggess Jr. *et al.* [189], the room-temperature instantaneous TPA coefficient was measured as (1.5 ± 1) cm/GW and the stepwise effect attributed to FCA, which is the appropriate mechanism since the promotion of the valence electron to the conduction band and the subsequent absorption of photon energy by a conduction band electrons are known to be separate processes as described in Section 2.4.

A significant decrease in the TPA coefficient would result in fewer generated electrons and a significant increase in the FCA coefficient or the impact ionization mechanisms would be necessary to generate a higher density of conduction band electrons if a TPA coefficient of 1.5 cm/GW was appropriate. The impact ionization model has been discussed throughout the literature and it appears as though the model of Kamakura *et al.* [98] was representative of the expected dynamics in silicon. The other mechanism that may be altered would be FCA.

In Figure 6.6, the more absorbed energy required for the avalanche MD to ablate the silicon is clear when compared to the experimental results. The avalanche ionization process in the MD simulation is expected to decrease the single-shot ablation threshold of silicon from that predicted by the HF-MD significantly because the avalanche ionization process would have sufficient time to exponentially increase the electron density to offset the decrease in the effect of the TPA process at longer pulse widths.

The FCA model of Schroder *et al.* has been the standard model used for some time, but a recent publication by Isenberg *et al.* [190] has brought the results of this study to question. Isenberg *et al.* contended that the surface resistivity predicted by Schroder *et al.* [70] did not conform to recent four-point probe measurements. They returned to the original publication on FCA of heavily doped silicon [102] and they argued that the more general form of the equation was required to model the absorption coefficient and index of refraction changes in silicon due to dopants. They evaluated the original equations and then proposed an empirical fit to the data:

$$\alpha_{FCA} = c_{FCA}(\lambda) n_e \lambda^2 \left[1 + A\left(1 + \mathrm{erf}\left\{ m \log\left({}^{n_e}\!/_{n_{ref}} \right) \right\} \right) \right] \ (\mathrm{m}^{-1}) \tag{6.5}$$

where the fitting parameters c_{FCA} is 4.45×10^{-11}, A is 5.75, and m is 0.67 with n_{ref} of 6.3×10^{11} carriers/cm^3 for n-type silicon at $\lambda = 1200$ nm. Fitting parameters for λ of 5 μm and 8 μm was provided as well for p-type silicon for all three wavelengths. At 1200 nm, equation (6.5) increases the FCA coefficient by a factor of three at electron densities approaching the critical density for 800 nm, 130 fs laser ablation (3.14×10^{20} e^-/cm^3 to 1.73×10^{21} e^-/cm^3 for m_{opt} between $0.18m_e$ and m_e, respectively).

Another method of modeling FCA in silicon and a means of comparing the results of both Schroder *et al.* [70] and Isenberg *et al.* [190] is to modify the dielectric constant with the addition of the Drude model [69, 191]. The Drude model is typically used in metals to describe the resistance of the electrons in the conduction band to the application of an external field where the collisions lead to Joule heating [19]. In laser-silicon interaction near the ablation threshold, the conduction band electron density can reach densities similar to that of room temperature metals and some authors suggest that this can be modeled by adding the Drude model to the intrinsic complex dielectric constant.

The absorption coefficient is related to the dielectric constant by [192]:

$$\alpha = 2\frac{\omega_L}{c_0} \mathrm{Im}(\hat{n}) = 2\frac{\omega_L}{c_0} \mathrm{Im}\left(\sqrt{\hat{\varepsilon}}\right) \ (\mathrm{m}^{-1}) \tag{6.6}$$

One transformation of the complex dielectric constant is from Hulin *et al.* [191]:

$$\hat{\varepsilon}_{\mathrm{Hulin}} = \varepsilon_R \left(1 - \frac{n_e}{N_{crit}\left(1 + j/\omega_L \tau_D\right)} \right) + j\varepsilon_I \tag{6.7}$$

where ε_R and ε_I are the real and imaginary parts of the complex dielectric constant from standard reference material (at 800 nm, $\varepsilon_R = 13.65$ and $\varepsilon_I = 0.048$ [23]). An alternative equation was given by Sokolowski-Tinten *et al.* [69]:

$$\hat{\varepsilon}_{S\text{-}T} = \hat{\varepsilon}_i + \Delta\varepsilon_{FCA}$$
$$= \hat{\varepsilon}_i - \frac{n_e e^2}{\varepsilon_0 m_{opt} \omega_L^2} \frac{1}{(1 + j/\omega_L \tau_D)} \tag{6.8}$$

where $\hat{\varepsilon}_i = \varepsilon_R + j\varepsilon_I$. The only difference between the two equations is that the Drude model operates on the complex form of the dielectric function in equation (6.8) as opposed to just the real part, ε_R, in equation (6.7). The Drude dampening time is τ_D, which is the collision time of the electrons with the ion cores or the phonons. The classic Drude dampening time is derived for metals at 10 fs [19].

The Drude dampening time depends on the lattice conditions [56, 69]; at low electron densities, the dampening time is dominated by electron-phonon collisions with lifetimes of the order of 100 fs. As the electron carrier density increases, the lattice becomes ionized and the dampening time decreases due to Coulomb attraction approaching values of approximately 1 fs. In some approximations, the inverse of the electron plasma frequency is used [56], which in this case would have $\tau_D = 56$ fs for $n = 10^{17}$ e^-/cm^3, reaching 1 fs for $N_{crit} = 3.14 \times 10^{20}$ e^-/cm^3 (critical density for the 800 nm wavelength and for $m_{opt} = 0.18 m_e$) and 0.4 fs for $N_{crit} = 1.73 \times 10^{21}$ e^-/cm^3 ($m_{opt} = m_e$). In the paper of Sokolowski-Tinten *et al.* [69], they found a Drude dampening time of 0.5 fs at 625 nm and in Hulin *et al.* [191], they found a Drude dampening time of 0.3 fs for 620 nm. For $\tau_D = 0.5$ fs, $\omega_L^2 \tau_{coll}^2 \sim 1$ and increases with increasing τ_D showing that the approximation in the paper by Schroder *et al.* is valid for a large range of carrier densities in this work. A comparison of all four absorption coefficients, with τ_D of 1 fs (where applicable) and the empirical formula of equation (6.5) with the fitting parameters for 1200 nm, is shown in Figure 6.11.

A couple of interesting features can be seen in Figure 6.11. The first is that both approximations to FCA have lower predicted coefficients than the complex dielectric constant modified by the Drude model. The second feature is that both approximations to the FCA would not be significant until 10^{21} cm^{-3} since the linear absorption coefficient, α_0, predicted by the linear dielectric function in equations (6.7) and (6.8) is not altered by the FCA until it reaches this density.

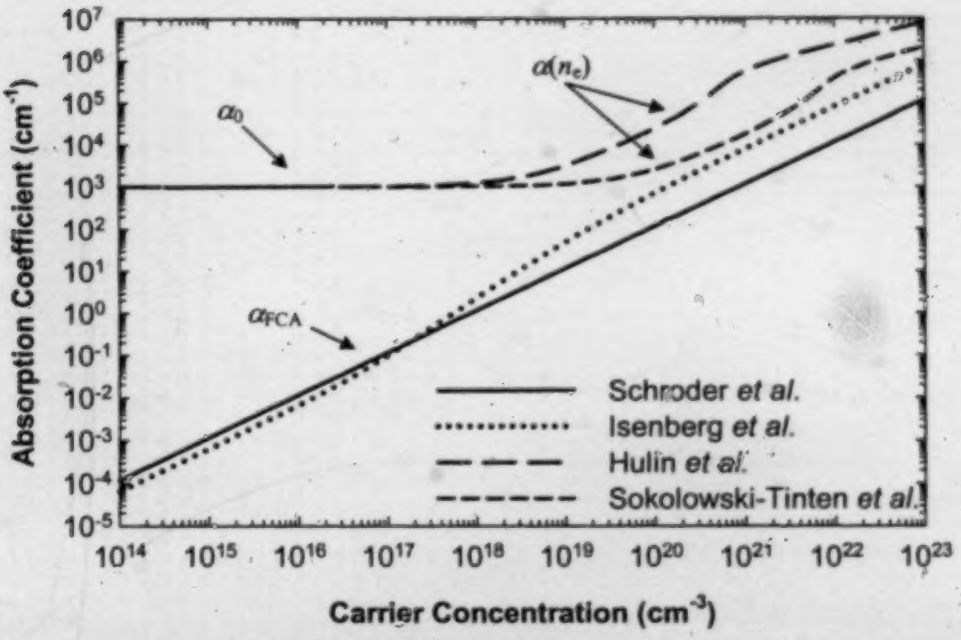

Figure 6.11: Absorption coefficient of silicon from the Drude model modified dielectric constants with a Drude dampening time of 1 fs and the approximation of the FCA contribution from the two approximations at the 800 nm wavelength.

The full absorption mechanism (linear absorption plus FCA) defined by the complex dielectric function gives a constant absorption coefficient of approximately 1000 cm^{-1}. In Figure 6.11, the FCA coefficient approximated by Schroder *et al.* does not have as much strength as the FCA coefficient approximated by the dielectric function with the Drude modifications. The absorption coefficient at the $0.18m_e$ critical density carrier concentration has a Schroder approximation of α_{FCA} at 350 cm^{-1}, an Isenberg approximation of 2 600 cm^{-1}, a Hulin approximation of 100 000 cm^{-1} and Sokolowski-Tinten approximation of 5 600 cm^{-1} showing a maximum discrepancy of nearly three orders of magnitude between extremes. Note that the Drude dampening time, as discussed above, can be a dynamic quantity [56] and a proper selection and comparison is still necessary for choosing the appropriate FCA coefficient.

By increasing the FCA coefficient in the MD simulation, the model in Figure 6.6 began to approximate the trend in the ablation threshold for pulse widths longer than 300 fs, although it still diverged from the experimental single-shot ablation thresholds at pulse widths shorter than 150 fs. The increase in the FCA coefficient is justified by the

above discussion and Figure 6.11, but a full parametric study of the TPA, FCA and impact ionization mechanisms is necessary to examine the predictions on the single-shot ablation threshold.

A reduction in the TPA coefficient would increase the single-shot ablation threshold over the pulse widths of interest since the efficiency of electron promotion to the conduction band would be reduced. To reach critical density, more energy would need to be deposited to the conduction band electrons through FCA to promote impact ionization. The single-shot ablation threshold would increase as the pulse width increased since the intensity necessary for TPA is inversely proportional to the pulse width. An increase in the FCA coefficient with a TPA coefficient of 55 cm/GW was already shown in Figure 6.6 to decrease the energy required, especially at longer pulse widths where the longer interaction time with the conduction band electrons required less peak energy. As the TPA coefficient decreases and the FCA coefficient is increased, a point can be reached where the conduction band electrons are energized into free electrons and escape the simulation volume and consequently increase the single-shot ablation threshold. Careful tuning of the parameters would be required.

Chapter 7

General Discussion

In this chapter, I will discuss the possible nanomilling mechanism based on the evidence presented in the previous chapters and the extension of this work to new studies. In particular, I will discuss the thermomechanical mechanism of cyclical stress involved in incubation as presented by Jee *et al.* [39] and examine methods for determining the scaling of this mechanism to the femtosecond pulse width regime. The scaling study is very important for femtosecond laser pulse interactions with surfaces since it is not fully understood what microscopic processes are involved in repetitive pulse interactions on a material surface when the incident fluence is below the single-shot ablation threshold.

7.1 The nanomilling mechanism

There are two possible pathways for NIR femtosecond laser pulse nanomilling: the removal of the atoms in bursts when a sufficient amount of energy has accumulated in the lattice or continual removal of atoms where small amounts of material are being ejected with each shot.

From the TTM, calculations of the peak temperature at the surface of copper at incident fluences of 170 mJ/cm^2 to 270 mJ/cm^2 with a 95 % reflectivity give temperature rises of 130 K to 200 K. With the peak temperature below the melting temperature, other

effects like amorphization of the metal in the interaction region are likely, as seen in gold when measured with X-ray diffraction (XRD) [193].

Hirayama *et al.* [193] measured the ablation threshold of gold with an average of 300 shots and examined the bottom of the ablation spot for the effects of residual heating on the crystallinity of the sample. The XRD data showed that the native sample gave strong peaks that indicated the crystallinity of the gold, and these peaks nearly vanished when the sample was irradiated at an incident fluence of 62 mJ/cm^2 with multiple pulses. The estimated temperature rise using the TTM and the plasma electron thermal conductivity model with a reflectivity of gold at 800 nm of 98 % [23] is 38 K at this incident fluence, indicating that structural deformation is possible at fluences well below the single-shot ablation threshold and possibly could lead to energy accumulation and expulsion of material in bursts.

The PMT measurements of the excited neutrals removed from the surface during nanomilling indicates that the altered lattice may be removed in bursts. To estimate the expected photon yield in either burst mode or continual ablation mode, the available emission efficiency of silicon using 800 nm, 130 fs pulses from studies in our lab are used. The ablation efficiency is defined as the number of photons emitted per ablated atom [114, 194]. This experiment was used to estimate the applicability of plasma emission as an adequate μLIBS source and it showed that the emission efficiency of silicon ranged from 10^{-3} to 10^{-5} as the incident laser energy decreased. In the low energy nanomilling regime, an emission efficiency of 10^{-5} would require 100 000 atoms for a single photon to be emitted. The PMT observed a solid angle of ~6×10^{-3} Sr and with a 12 % filter in front of the PMT (see Section 3.3.5) and assuming an isotropic expansion of the ablated atoms over 2π Sr (hemisphere), approximately 10^9 atoms would be required in a single shot for the PMT to detect a single photon.

The nanomilled crater in the upper left of Figure 4.6 had an approximate depth of 2 nm and an approximate radius of 15 μm. Using the thermophysical properties in Table 2.1, the number of copper atoms in the crater by assuming a disk with these dimensions is approximately 10^{11} atoms and if each of the 500 laser shots removed the same number of atoms, each shot would remove 2×10^8 atoms and the PMT would rarely detect any photons. On average, approximately ten photons should be randomly

observed over the 500 shots and since only two photons were observed, it could be that the emission efficiency is lower than that of silicon reported in refs. [114, 194]. If the nanomilling occurred in two bursts as suggested by the upper right graph of Figure 4.6, then 5×10^{10} atoms would be removed in each of the bursts and approximately 50 photons would be detected. Since only a single photon was detected each time an event occurred, it cannot be concluded from this data as to whether a burst mode mechanism prevails.

Although the evidence for the burst-mode nanomilling pathway is not yet proven, the experiments with SAMs on metal surfaces patterned with femtosecond laser pulses proved that material was removed from the surface and that the effective change in the surface profile was not, for example, pressure causing the surface in the laser focal spot to recede or expand. Femtosecond patterning of gold surfaces with SAMs further proves that the gold atoms are removed at incident fluences in the nanomilling regime as shown in Section 5.4, even though the surface shows bulging similar to that shown for copper in Figure 4.5 and attributed to the thermo-elastic effect of thin films [139]. The transient heating of the substrate is too fast for thermal bond breaking of the gold-sulfur (thiolate) bond to occur, which further supports the hypothesis that the patterning technique is ablative. The appearance of a contrast difference in the SEM images of Figure 5.11 and Figure 5.12 shows that the deposition region was bare for the second hydrophilic SAM, illustrating nanomilling.

At low fluences below the single-shot ablation threshold, MD simulations of 800 nm, 120 fs Gaussian FWHM on silicon show the removal of isolated atoms but that the material melts within the first 15 nm of the surface during 30 ps following the laser heating [87], confirming the results presented in ref. [195] that at these fluences changes in the intrinsic material structure can occur, but significant material is not removed, which may support the burst-mode hypothesis.

7.2 Incubation and fatigue

All solids experience strain, ε, under the application of stress, σ (force per unit area), by the displacement of atoms from their equilibrium position, $\varepsilon = \Delta L/L$ [140]. The amount of strain a solid experiences is linearly proportional to the amount of stress

applied and the constant of proportionality is Young's modulus, Y. A solid will displace linearly in the direction of a stress force until the stress reaches the yield point, σ_Y, where the material will experience additional strain with little additional stress: this is also called the *slip* point where the atomic bonds have been overcome [140] or called the plastic deformation point when materials do not return to their original position after the stress is removed [140].

After the stress yield point the solid will not return to its equilibrium position. If more stress is applied, then an ultimate strength point is reached where the solid will break with variable amounts of additional strain, depending on the material. The melting temperature of metals can be ranked in the same order as their respective Young's modulus [140].

This description is the expectation for a solid when stress has been applied for one cycle. Repeated cycling of stress on a solid leads to fatigue, where the ultimate breaking stress of the material after repeated cycles changes [196, 197]. In discussing fatigue, stress-cycling will be used to describe repeated applications of the same amount of stress and strain-cycling will be used to describe the displacement of the material by the same distance in each cycle.

In strain-cycling, a material can experience strain-hardening where a material on the first cycle follows the stress-strain curve seen in most texts, also called the *static* stress-strain curve, but on subsequent cycles the material requires more stress to reach the same amount of strain, eventually approaching the point of "saturation hardening" [196]. In contrast, strain softening occurs when subsequent cycles require less stress to achieve the same amount of strain. In each case, the amount of stress required asymptotically approaches a fundamental value after which continued cycling of the stress eventually leads to material failure.

There is evidence that every material has an endurance-limit strain, a minimum displacement below which repeated strain-cycling will not change the material permanently, making the lifetime of the material infinite [196]. This limit may be of importance when examining laser-induced incubation at very low incident fluences.

In the original paper dealing with the incubation of laser damage in metal surfaces, Jee *et al.* [39], stated the stress required to reach the yield stress point where

slip-line defect formation occurs in stress-cycling by laser pulse interaction with a metal surface was given by:

$$\sigma = \sigma_F N^b \tag{7.1}$$

where σ_F is the fatigue-strength coefficient, b is the fatigue-strength exponent and N is the number of cycles. If b is greater than zero, the material will build up stress from repeated cycles until it reaches the plastic yield point and fails. Equating the stress-cycling equation (7.1) with the incubation equation (2.3), $b = \xi - 1$ and if ξ is less than one, then repeated laser cycling reduces the ablation threshold.

To get the fatigue-strength coefficient, they defined the stress applied to a metal surface by the action of an NIR nanosecond laser pulse as a thermal stress:

$$\sigma = Y\varepsilon = \frac{-Y\alpha}{(1-\nu)} dT \tag{7.2}$$

where σ is the thermal stress in Pa, ε is the strain, Y is Young's modulus in Pa, α is the thermal expansion coefficient in K^{-1} (16.5×10^{-6}/K for copper [23]) and ν is Poisson's ratio (around 0.37 for copper, p.3-88 in ref. [61]). For a spatially uniform rectangular pulse shape in time, the temperature change at the surface, dT, was given as:

$$dT = \frac{2A}{\sqrt{\pi \kappa C_L \tau_P}} \phi \tag{7.3}$$

where A is the optical absorption and ϕ is the laser fluence giving a fatigue-strength coefficient of:

$$\sigma_F = \frac{-Y\alpha}{(1-\nu)} \frac{2A}{\sqrt{\pi \kappa C_L \tau_P}} \phi \tag{7.4}$$

From the above model, the incubation coefficient would change depending on the peak temperature reached in the material. Both nanosecond laser pulses and femtosecond laser pulses can achieve temperatures up to the melting temperature, yet the incubation coefficient has been observed to change from 0.92 for nanosecond pulse widths [39] to 0.76 ± 0.02 for femtosecond pulse widths [13]. The difference between the two laser interactions is the heating rates. In the nanosecond laser pulse regime, the heating rates are about 10^9 K/s [26] and in the femtosecond pulse regime they can reach 10^{13} K/s.

Three possibilities exist for scaling the incubation coefficient from the nanosecond to femtosecond laser pulse regime. This first possibility is that the heating *rate* changes the fatigue-strength coefficient. For the same number of nanosecond and femtosecond pulses incident on the surface of a metal, if the fatigue-strength coefficient varies because of the heating rate, then the change in the incubation coefficient is:

$$\xi_{fs} = \xi_{ns} + \log\left(\frac{\sigma_F^{ns}}{\sigma_F^{fs}}\right) \tag{7.5}$$

where the fatigue-strength coefficient for femtosecond pulses, σ_F^{fs}, must be greater than that for nanosecond laser pulses. The second possibility is that the heating rates have an effect on the fatigue-strength *exponent*.

Both of these possibilities would validate that incubation is a purely thermomechanical phenomenon if the change in the incubation coefficient saturates at a pulse width where the lattice response is independent of the incident laser pulse width. The lattice temperature equilibrates with the electron temperature at times greater than 1 ps, where the single-shot ablation threshold starts to become independent to the change in pulse width shown in Figure 4.11. Pulse widths below 1 ps would heat the lattice subsystem at the same rate and the incubation coefficient would remain unchanged, whether it was affected by the fatigue-strength coefficient or the fatigue-strength exponent. For low-cycle fatigue interactions where the effects of stress/strain-cycling are equivalent, the effects of softening/hardening is expected to saturate, where this saturation is expressed as minimum value of the incubation coefficient for metals around 0.80 [39].

The third possibility is that the different heating rates may activate different fatigue *modes* in the metal. Fatigue is a complex subject [196] and there is evidence that even lower heating rates, 1000 K/s, can affect the mechanical properties of a metal where a non-uniform temperature distribution can change the microstructure by dislocations, through recrystallization or the growth of grains and grain boundaries [198]. As discussed in Chapter 5 with the desorption of SAMs on metal surfaces, heating rates may change the nature of the pathway by activating processes that have higher activation energies because of the frequency of interaction as shown in the equation for reaction kinetics in equation (5.2).

At nanosecond pulse widths, the slower heating rates may induce a fatigue mode that has a lower activation energy, E_a. If this fatigue mode has a slow response frequency, ν, then a heating rate that is faster than ν, for example with a femtosecond laser pulse, would activate a different fatigue mode with a higher activation energy and faster response frequency because the original fatigue mode would not notice the rapid change. This may be visible experimentally with a sudden change in the incubation coefficient at a specific pulse width where the change between fatigue modes occurs. If the latter is true, then microstructural analysis may reveal the existence of different fatigue modes.

7.3 Future experimental directions in nanomilling, incubation and fatigue

To ascertain whether the nanomilling pathway for femtosecond pulses is burst-mode as opposed to a continual process, a quartz crystal microbalance (QCM) system can monitor the removal of nanometer layers. A QCM is a piezo-element with electrodes that create an oscillation in the crystal due to a driving AC voltage. The oscillation frequency is monitored and frequency changes as little as 0.1 Hz can be measured with commercial devices [199]. The sensitivity of a QCM varies as a Gaussian function over its active surface area, which is usually about a 3 mm radius with its peak value at the centre [48], and the frequency change depends on the amount of material removed/added over the surface area. Although the sensitivity of the mass loading is dependent on the position of the point mass addition or removal, a first-order estimate using a uniform sensitivity, C_f, of a commercial 5 MHz AT-cut QCM of 5.7 MHz·m^2/kg

[200] will measure a frequency change Δf given as $C_f \rho V / A_{QCM}$, where V is the volume of the removed electrode, ρ is the density and A_{QCM} is the active area of the QCM.

A nanomilled hole in gold as shown in the upper left graph of Figure 4.6 assuming an ablated disk with a 2 nm depth and 15 μm radius would have a frequency change of 5.5×10^{-3} Hz, below the detection limit of the QCM. Increasing the focal spot to an interaction radius of 1.5 mm (nearly the entire active region) would be necessary to differentiate between burst and continual removal. If nanomilling occurs in bursts, then the QCM would measure increases in the frequency as jumps. If nanomilling occurs steadily, then the resultant frequency changes would be continual with incident pulses.

Detection of the ablated species as a diagnostic of nanomilling would require additional ionization of the ablated materials. The electron temperatures predicted by the TTM model reach about 1 eV, insufficient for overcoming the work function of a copper surface (~4.75 eV on average [23]) so there is unlikely to be any charged particles removed from the surface. Using a delayed femtosecond laser pulse as an ionizing pulse, the timing of the ablation with respect to the pump pulse can be measured as well as the particle density assuming that the pulse is sufficient to ionize most of the ejected species. Available third harmonic pulses of a few hundred femtosecond pulse widths would be sufficient for ionization of the ablation plume species.

Once the pathway is determined for femtosecond pulse widths, the scaling of the incubation coefficient would need to be determined up to the nanosecond pulse regime. The scaling of the incubation coefficient by pulse width has already been suggested to result from one of three possible pathways and that experimentally measuring the incubation coefficient for different pulse widths at NIR laser wavelengths, in conjunction with the TTM, may reveal which of the three pathways occur. The NIR wavelength is necessary to ensure that the heating is collisional with the electron subsystem and that no other resonant behaviour occurs to confound the scaling data.

To provide further evidence of the fatigue mode and the dynamics involved in incubation and the nanomilling of metals requires imaging the microstructure of the material. If grain boundaries, grain boundary migration, recrystallization, dislocations or cracks appear or change, then these can be imaged by TEM [196] since the edges in these fatigue modes diffract the electron beam to reveal the structure. If the dynamics of

fatigue propagation is of interest, then X-rays are also capable of imaging microstructural defects [196] in a metal and a thin sample irradiated with a laser pulse can be probed by femtosecond X-ray pulses that probe the thin metal film to reveal the changes in the microstructure with an X-ray CCD camera.

A final comment on fatigue cycling is the endurance-limit strain. If the endurance-limit strain is indicative of an incubation coefficient of one, then it may be that very low fluence laser interactions will eventually cease to show multiple pulse damage. This would result in a change in the incubation coefficient as the number of pulses increased for a particular laser wavelength and pulse width on a surface and may need to be investigated to determine whether the concept of a constant incubation coefficient for a particular pulse width, independent of the incident number of pulses, is valid for high-cycle fatigue. Reports on high-cycle fatigue show that the relationships between stress and strain eventually break down [197] leading to this hypothesis about the limited validity range of the incubation coefficient and its effect on nanomilling. Endurance-limit strain may also explain the results in Hashida *et al.* [42], where the threshold of the pm/pulse ablation rate was an abrupt transition from machining to no visible ablation with incident pulse numbers exceeding 10^5.

Nanomilling is dependent on the incubation phenomenon and the mechanism of incubation of damage in a metal by multiple pulse interaction with femtosecond laser pulses is an important contributor to this phenomenon. The experiments in this thesis raise the hypothesis that incubation may occur as discrete events in a burst-mode, which may be verified through future experiments investigating stress-strain cycling and fatigue in metals.

Chapter 8

Conclusion

NIR femtosecond laser pulses can nanomill metal surfaces to depths smaller than the optical penetration depth. The shallowest depth of ~2 nm has been achieved on a thin copper film surface using several thousand laser pulses at incident fluences well below the single-shot ablation threshold. Material removal was evident from the craters measured by WLI, the emission of singly-excited copper atoms measured by a PMT, and the patterning of SAMs in the nanomilled region. WLI scans of femtosecond laser pulse patterning of SAMs confirmed material removal with a morphology similar to that seen in nanomilling at fluences slightly more intense than the near-threshold regime.

TTM, with the melting threshold of the metal used as the predictor for ablation, showed that the nanomilled region had peak lattice temperatures below the melting temperature. The maximum temperature of a few hundred Kelvin occurred a few picoseconds after the peak of the laser pulse. The *g*-parameter, which describes the energy coupling of the electron and lattice subsystem for femtosecond laser pulse heating, converged for the noble metals when the electron thermal conductivity model was changed from the traditionally used Sommerfeld approximation (proportional model) to the plasma model. The TTM also showed heating rates of 10^{13} K/s, four orders of magnitude higher than rates using nanosecond laser pulses. These heating rates may alter the thermal-fatigue cycling in the metal, creating a stronger incubation effect where

damage is more readily stored in the material. Limited heat deposition may also result in material removal in a burst-mode and is the subject of further investigation.

NIR femtosecond laser pulse ablation of metal surfaces was found to be strongly dependent on: the single-shot ablation threshold, the incubation coefficient and the reflectivity. Careful study of this parameter space has led to the understanding of the discrepancies in the reported values for the ablation threshold for copper surfaces, and these parameters play a significant role in nanomilling. The reflectivity of a metal surface may not be known in many engineering applications and the use of a detector has been shown to be able to monitor the nanomilling process to achieve the desired nanomilling accuracy.

Surfaces were shown to be nanomilled both thermally and ablatively by operating on molecular adsorbates. SAMs with a 2 nm thickness chemisorbed on a gold surface can be patterned by scanning a CW laser beam on the surface. The CW laser created a temperature rise whose lateral extent and peak temperature were dependent on the thermal properties of the substrate and the laser scanning speed. Ultimate lateral feature sizes were limited to micrometers. Femtosecond laser pulses, whose removal mechanism was ablative, produced lateral feature sizes that were below the diffraction limit of the focusing conditions resulting in ultimate line widths of several hundred nanometers.

Extension of the modeling of ablation to explore the microscopic dynamics of the ablation process was achieved using an MD simulation of silicon. A version of the MD simulation that was capable of predicting the single-shot ablation threshold of silicon from 800 nm, 100 fs laser pulses was modified to include avalanche ionization. The original code was strongly dependent on the TPA coefficient for pulse width scaling of the single-shot ablation threshold. A strong FCA and impact ionization mechanism, both of which model avalanche ionization, showed that the MD simulation of silicon can start to predict the scaling of the single-shot ablation threshold at longer pulse widths. Future work includes using the code to model the ablation dynamics in metals since the separate electron subsystem can be examined in detail.

Overall the thesis has advanced the understanding of ablation at intensities around the single and multiple shot ablation thresholds showing the control of ablation processes to nanometer precision is possible.

References

[1] Goodfellow Cambridge Limited, Ermine Business Park, Huntingdon, Cambridgeshire, England, PE29 6WR

[2] Schott North America Inc., 555 Taxter Rd., Elmsford, NY, USA, 10523

[3] J. D. Huba, *NRL Plasma Formulary*. Washington: Naval Research Laboratory, 2002.

[4] B. N. Chichkov, C. Momma, S. Nolte, F. von Alvensleben, and A. Tünnermann, "Femtosecond, picosecond and nanosecond laser ablation of solids," *Appl. Phys. A: Mater. Sci. Process.*, vol. 63, pp. 109-115, 1996.

[5] P. Simon and J. Ihlemann, "Ablation of submicron structures on metals and semiconductors by femtosecond UV-laser pulses," *Appl. Surf. Sci.*, vol. 109-110, pp. 25-29, 1997.

[6] F. Korte, S. Nolte, B. N. Chichkov, T. Bauer, G. Kamlage, T. Wagner, C. Fallnich, and H. Welling, "Far-field and near-field material processing with femtosecond laser pulses," *Appl. Phys. A: Mater. Sci. Process.*, vol. 69, pp. S7-S11, 1999.

[7] B. N. Chichkov, F. Korte, J. Koch, S. Nolte, and A. Ostendorf, "Femtosecond laser ablation and nanostructuring," *Proc. SPIE*, vol. 4760, pp. 19-24, 2002.

[8] S. I. Anisimov, B. L. Kapeliovich, and T. L. Perel'man, "Electron emission from metal surfaces exposed to ultrashort laser pulses," *Sov. Phys. JETP*, vol. 39, pp. 375-377, 1974.

[9] S. E. Kirkwood, M. T. Taschuk, Y. Y. Tsui, and R. Fedosejevs, "Nanomilling surfaces using near-threshold femtosecond laser pulses," *J. Phys. Conf. Ser.*, (Accepted May 9, 2006).

[10] S. E. Kirkwood, M. R. Shadnam, R. Fedosejevs, and A. Amirfazli, "Direct writing of self-assembled monolayers on gold coated substrates using a CW Argon laser," presented at The International Conference on MEMS, NANO, and Smart Systems, Banff, Alberta, Canada, 2003.

[11] M. R. Shadnam, S. E. Kirkwood, R. Fedosejevs, and A. Amirfazli, "Direct patterning of self-assembled monolayers on gold using a laser beam," *Langmuir*, vol. 20, pp. 2667-2676, 2004.

[12] M. R. Shadnam, S. E. Kirkwood, R. Fedosejevs, and A. Amirfazli, "Thermo-kinetics study of laser induced desorption of self assembled monolayer from gold: Case of laser micropatterning," *J. Phys. Chem. B*, vol. 109, pp. 11996-12002, 2005.

[13] S. E. Kirkwood, A. C. van Popta, Y. Y. Tsui, and R. Fedosejevs, "Single and multiple shot near-infrared femtosecond laser pulse ablation thresholds of copper," *Appl. Phys. A: Mater. Sci. Process.*, vol. 81, pp. 729-735, 2005.

[14] S. E. Kirkwood, M. R. Shadnam, A. Amirfazli, and R. Fedosejevs, "Mechanism for femtosecond laser pulse patterning of self-assembled monolayers on gold-coated substrates," *J. Phys. Conf. Ser.*, (Accepted October 20, 2005).

[15] D. Bäuerle, *Laser Processing and Chemistry*, 3rd ed. Berlin: Springer, 2000.

[16] M. von Allmen and A. Blatter, *Laser-Beam Interactions with Materials*, 2nd ed. Berlin: Springer-Verlag, 1995.

[17] J. C. Kotz and K. F. Purcell, *Chemistry and Chemical Reactivity*, 2nd ed. Philadelphia: Saunders College Publishing, 1991.

[18] B. Hammer and J. K. Nørskov, "Why gold is the noblest of all the metals," *Nature*, vol. 376, pp. 238-240, 1995.

[19] M. P. Marder, *Condensed Matter Physics*. New York: John Wiley & Sons, 2000.

[20] T. Q. Qiu and C. L. Tien, "Femtosecond laser heating of multi-layer metals-I. Analysis," *Int. J. Heat Mass Transfer* vol. 37, pp. 2789-2797, 1994.

[21] K. C. Rustagi, "Bilinear optical polarizability of silver," *Il Nuovo Cimento*, vol. 53, pp. 346-362, 1968.

[22] C. Kittel, *Introduction to Solid State Physics*, 7th ed. Hoboken: John Wiley & Sons, 1996.

[23] D. R. Lide, "CRC Handbook of Chemistry and Physics, Internet Version 2007," 87th ed. Boca Raton, FL: Taylor & Francis, 2007.

[24] S. D. Brorson, J. G. Fujimoto, and E. P. Ippen, "Femtosecond electronic heat-transport dynamics in thin gold films," *Phys. Rev. Lett.*, vol. 59, pp. 1962-1965, 1987.

[25] J. Hohlfeld, S. S. Wellershoff, J. Güdde, U. Conrad, V. Jahnke, and E. Matthias, "Electron and lattice dynamics following optical excitation of metals," *Chem. Phys.*, vol. 251, pp. 237-258, 2000.

[26] S. S. Wellershoff, J. Hohlfeld, J. Güdde, and E. Matthias, "The role of electron–phonon coupling in femtosecond laser damage of metals," *Appl. Phys. A: Mater. Sci. Process.*, vol. 69, pp. S99-S107, 1999.

[27] T. Juhasz, H. E. Elsayed-Ali, G. O. Smith, C. Suárez, and W. E. Bron, "Direct measurement of the transport of nonequilibrium electrons in gold films with different crystal structures," *Phys. Rev. B*, vol. 48, pp. 15488-15491, 1993.

[28] J. Hohlfeld, J. G. Müller, S. S. Wellershoff, and E. Matthias, "Time-resolved thermoreflectivity of thin gold films and its dependence on film thickness," *Appl. Phys. B: Lasers Opt.*, vol. 64, pp. 387-390, 1997.

[29] S. Preuss, A. Demchuk, and M. Stuke, "Sub-picosecond UV laser ablation of metals," *Appl. Phys. A: Mater. Sci. Process.*, vol. 61, pp. 33-37, 1995.

[30] C. Momma, S. Nolte, B. N. Chichkov, F. von Alvensleben, and A. Tünnermann, "Precise laser ablation with ultrashort pulses," *Appl. Surf. Sci.*, vol. 109/110, pp. 15-19, 1997.

[31] S. Nolte, C. Momma, H. Jacobs, A. Tünnermann, B. N. Chichkov, B. Wellegehausen, and H. Welling, "Ablation of metals by ultrashort laser pulses," *J. Opt. Soc. Am. B*, vol. 14, pp. 2716-2722, 1997.

[32] M.-H. Hong, Y.-F. Lu, W. D. Song, D. M. Liu, and T.-S. Low, "Audible acoustic wave real-time monitoring in laser processing of microelectronic materials," *Proc. SPIE*, vol. 3184, pp. 148-157, 1997.

[33] K. Furusawa, K. Takahashi, H. Kumagai, K. Midorikawa, and M. Obara, "Ablation characteristics of Au, Ag, and Cu metals using a femtosecond Ti:sapphire laser," *Appl. Phys. A: Mater. Sci. Process.*, vol. 69, pp. S359-S366, 1999.

[34] C. Li, M. Argument, Y. Y. Tsui, and R. Fedosejevs, "Micromachining with femtosecond 250-nm laser pulses," *Proc. SPIE*, vol. 4087, pp. 1194-1200, 2000.

[35] Y.-F. Lu and M.-H. Hong, "Electric signal detection at the early stage of laser ablation in air," *J. Appl. Phys.*, vol. 86, pp. 2812-2817, 1999.

[36] S. Amoruso, X. Wang, C. Altucci, C. de Lisio, M. Armenante, R. Bruzzese, N. Spinelli, and R. Velotta, "Double-peak distribution of electron and ion emission profile during femtosecond laser ablation of metals," *Appl. Surf. Sci.*, vol. 186, pp. 358-363, 2002.

[37] S. Amoruso, X. Wang, C. Altucci, C. de Lisio, M. Armenante, R. Bruzzese, and R. Velotta, "Thermal and nonthermal ion emission during high-fluence femtosecond laser ablation of metallic targets," *Appl. Phys. Lett.*, vol. 77, pp. 3728-3730, 2000.

[38] J. M. Liu, "Simple technique for measurements of pulsed Gaussian-beam spot sizes," *Opt. Lett.*, vol. 7, pp. 196-198, 1982.

[39] Y. Jee, M. F. Becker, and R. M. Walser, "Laser-induced damage on single-crystal metal-surfaces," *J. Opt. Soc. Am. B*, vol. 5, pp. 648-659, 1988.

[40] J. Krüger and W. Kautek, "Femtosecond-pulse laser processing of metallic and semiconducting thin films," *Proc. SPIE*, vol. 2403, pp. 436-448, 1995.

[41] P. T. Mannion, J. Magee, E. Coyne, G. M. O.Connor, and T. J. Glynn, "The effect of damage accumulation behaviour on ablation thresholds and damage morphology in ultrafast laser micro-machining of common metals in air," *Appl. Surf. Sci.*, vol. 233, pp. 275-287, 2004.

[42] M. Hashida, A. F. Semerok, O. Gobert, G. Petite, Y. Izawa, and J. F. Wagner, "Ablation threshold dependence on pulse duration for copper," *Appl. Surf. Sci.*, vol. 197-198, pp. 862-867, 2002.

[43] J. Jandeleit, G. Urbasch, H. D. Hoffmann, H.-G. Treusch, and E. W. Kreutz, "Picosecond laser ablation of thin copper films," *Appl. Phys. A: Mater. Sci. Process.*, vol. 63, pp. 117-121, 1996.

[44] P. B. Corkum, F. Brunel, N. K. Sherman, and T. Srinivasan-Rao, "Thermal response of metals to ultrashort-pulse laser excitation," *Phys. Rev. Lett.*, vol. 61, pp. 2886-2889, 1988.

[45] C. Guo and A. J. Taylor, "Ultrafast electronic disorder in heat-induced structural deformations and phase transitions in metals," *Phys. Rev. B*, vol. 62, pp. 5382-5386, 2000.

[46] X. Zhang, S. S. Chu, J. R. Ho, and C. P. Grigoropoulos, "Excimer laser ablation of thin gold films on a quartz crystal microbalance at various argon background pressures," *Appl. Phys. A: Mater. Sci. Process.*, vol. 64, pp. 545-552, 1997.

[47] J. Békési, R. Vajtal, P. Simon, and L. B. Kiss, "Subpicosecond excimer laser ablation of thick gold films of ultra-fine particles generated by a gas desorption technique," *Appl. Phys. A: Mater. Sci. Process.*, vol. 69, pp. S385-S387, 1999.

[48] J. Pérez and B. R. Weiner, "The laser ablation of gold films at the electrode surface of a Quartz Crystal Microbalance," *Appl. Surf. Sci.*, vol. 62, pp. 281-285, 1992.

[49] J. Güdde, J. Hohlfeld, J. G. Muller, and E. Matthias, "Damage threshold dependence on electron–phonon coupling in Au and Ni films," *Appl. Surf. Sci.*, vol. 127-129, pp. 40-45, 1998.

[50] T. Q. Qiu and C. L. Tien, "Heat transfer mechanisms during short-pulse laser heating of metals," *J. Heat Transfer*, vol. 115, pp. 835-841, 1993.

[51] M. I. Kaganov, I. M. Lifshitz, and L. V. Tanatarov, "Relaxation between electrons and the crystalline lattice," *Sov. Phys. JETP*, vol. 4, pp. 173-178, 1957.

[52] A. H. Wilson, *The Theory of Metals*, 2nd ed. Cambridge: University Press, 1954.

[53] S. I. Anisimov and B. Rethfeld, "On the theory of ultrashort laser pulse interaction with a metal," *Proc. SPIE*, vol. 3093, pp. 192-203, 1997.

[54] C. Schäfer, H. M. Urbassek, and L. V. Zhigilei, "Metal ablation by picosecond laser pulses: A hybrid simulation," *Phys. Rev. B*, vol. 66, pp. 115404, 2002.

[55] V. Schmidt, W. Husinsky, and G. Betz, "Ultrashort laser ablation of metals: pump–probe experiments, the role of ballistic electrons and the two-temperature model," *Appl. Surf. Sci.*, vol. 197-198, pp. 145-155, 2002.

[56] E. G. Gamaly, A. V. Rode, B. Luther-Davies, and V. T. Tikhonchuk, "Ablation of solids by femtosecond lasers: Ablation mechanism and ablation thresholds for metals and dielectrics," *Phys. Plasmas*, vol. 9, pp. 949-957, 2002.

[57] H. E. Elsayed-Ali, T. B. Norris, M. A. Pessot, and G. A. Mourou, "Time-resolved observation of electron-phonon relaxation in copper," *Phys. Rev. Lett.*, vol. 58, pp. 1212-1215, 1987.

[58] S. D. Brorson, A. Kazeroonian, J. S. Moodera, D. W. Face, T. K. Cheng, E. P. Ippen, M. S. Dresselhaus, and G. Dresselhaus, "Femtosecond room-temperature measurement of the electron-phonon coupling constant λ in metallic superconductors," *Phys. Rev. Lett.*, vol. 64, pp. 2172-2175, 1990.

[59] J. P. Colombier, P. Combis, F. Bonneau, R. Le Harzic, and E. Audouard, "Hydrodynamic simulations of metal ablation by femtosecond laser irradiation," *Phys. Rev. B*, vol. 71, pp. 165406, 2005.

[60] S. S. Wellershoff, J. Güdde, J. Hohlfeld, J. G. Müller, and E. Matthias, "The role of electron-phonon coupling in femtosecond laser damage of metals," *Proc. SPIE*, vol. 3343, pp. 378-387, 1998.

[61] D. E. Gray, *American Institute of Physics Handbook*, 2nd ed. New York: McGraw-Hill, 1963.

[62] W. Benenson, J. W. Harris, H. Stocker, and H. Lutz, *Handbook of Physics*. New York: American Institute of Physics, 2002.

[63] Silicon Valley Microelectronics, "Silicon Wafer Product Services Silicon Wafers Lifecycle Education Resources US Europe Asia," October 31, 2006, http://www.svmi.com/education/siliconwafers.shtml

[64] A. Cavalleri, K. Sokolowski-Tinten, J. Bialkowski, M. Schreiner, and D. von der Linde, "Femtosecond melting and ablation of semiconductors studied with time of flight mass spectroscopy," *J. Appl. Phys.*, vol. 85, pp. 3301-3309, 1999.

[65] C. V. Shank, R. Yen, and C. Hirlimann, "Time-resolved reflectivity measurements of femtosecond-optical-pulse-induced phase transitions in silicon," *Phys. Rev. Lett.*, vol. 50, pp. 454-457, 1983.

[66] D. von der Linde, K. Sokolowski-Tinten, and J. Bialkowski, "Laser-solid interaction in the femtosecond time regime," *Appl. Surf. Sci.*, vol. 109-110, pp. 1-10, 1997.

[67] K. Sokolowski-Tinten, J. Bialkowski, and D. von der Linde, "Ultrafast laser-induced order-disorder transitions in semiconductors," *Phys. Rev. B*, vol. 51, pp. 14186-14198, 1995.

[68] K. Sokolowski-Tinten, A. Cavalleri, and D. von der Linde, "Single-pulse time- and fluence-resolved optical measurements at femtosecond excited surfaces," *Appl. Phys. A: Mater. Sci. Process.*, vol. 69, pp. 577-579, 1999.

[69] K. Sokolowski-Tinten and D. von der Linde, "Generation of dense electron-hole plasmas in silicon," *Phys. Rev. B*, vol. 61, pp. 2643-2650, 2000.

[70] D. K. Schroder, R. N. Thomas, and J. C. Swartz, "Free carrier absorption in silicon," *IEEE Trans. Electron Dev.*, vol. ED-25, pp. 254-261, 1978.

[71] J. Bonse, K.-W. Brzezinka, and A. J. Meixner, "Modifying single-crystalline silicon by femtosecond laser pulses: an analysis by micro Raman spectroscopy, scanning laser microscopy and atomic force microscopy," *Appl. Surf. Sci.*, vol. 221, pp. 215-230, 2004.

[72] D. H. Reitze, T. R. Zhang, W. M. Wood, and M. C. Downer, "Two-photon spectroscopy of silicon using femtosecond pulses at above-gap frequencies," *J. Opt. Soc. Am. B*, vol. 7, pp. 84-89, 1990.

[73] J. Bonse, S. Baudach, J. Krüger, W. Kautek, and M. Lenzner, "Femtosecond laser ablation of silicon-modification thresholds and morphology," *Appl. Phys. A: Mater. Sci. Process.*, vol. 74, pp. 19-25, 2002.

[74] A. Borowiec, M. MacKenzie, G. C. Weatherly, and H. K. Haugen, "Transmission and scanning electron microscopy studies of single femtosecond-laser-pulse ablation of silicon," *Appl. Phys. A: Mater. Sci. Process.*, vol. 76, pp. 201-207, 2003.

[75] H. O. Jeschke, M. E. Garcia, M. Lenzner, J. Bonse, J. Krüger, and W. Kautek, "Laser ablation thresholds of silicon for different pulse durations: theory and experiment," *Appl. Surf. Sci.*, vol. 197-198, pp. 839-844, 2002.

[76] S. Amoruso, G. Ausanio, R. Bruzzese, L. Gragnanieloo, L. Lanotte, M. Vitiello, and X. Wang, "Characterization of laser ablation of solid targets with near-infrared laser pulses of 100 fs and 1 ps durations," *Appl. Surf. Sci.*, vol. 252, pp. 4863-4870, 2006.

[77] S. Amoruso, C. Altucci, R. Bruzzese, C. de Lisio, N. Spinelli, R. Velotta, M. Vitiello, and X. Wang, "Study of the plasma plume generated during near IR

femtosecond laser irradiation of silicon targets," *Appl. Phys. A: Mater. Sci. Process.*, vol. 79, pp. 1377-1380, 2004.

[78] P. P. Pronko, P. A. van Rompay, C. Horvath, F. H. Loesel, T. Juhasz, X. Liu, and G. A. Mourou, "Avalanche ionization and dielectric breakdown in silicon with ultrafast laser pulses," *Phys. Rev. B*, vol. 58, pp. 2387-2390, 1998.

[79] D. J. Hwang, C. P. Grigoropoulos, and T. Y. Choi, "Efficiency of silicon micromachining by femtosecond laser pulses in ambient air," *J. Appl. Phys.*, vol. 99, pp. 083101, 2006.

[80] M. Meunier, B. Fisette, A. Houle, A. V. Kabashin, S. V. Broude, and P. Miller, "Processing of metals and semiconductors by a femtosecond laser-based microfabrication system," *Proc. SPIE*, vol. 4978, pp. 169-179, 2003.

[81] D. C. Rapaport, *The Art of Molecular Dynamics*. Cambridge: Cambridge University Press, 1995.

[82] R. F. W. Herrmann, J. Gerlach, and E. E. B. Campbell, "Molecular dynamics simulation of laser ablation of silicon," *Nucl. Instrum. Methods Phys. Res., Sect. B*, vol. 122, pp. 401-404, 1997.

[83] R. F. W. Herrmann, J. Gerlach, and E. E. B. Campbell, "Ultrashort pulse laser ablation of silicon: an MD simulation study," *Appl. Phys. A: Mater. Sci. Process.*, vol. 66, pp. 35-42, 1998.

[84] F. H. Stillinger and T. A. Weber, "Computer simulation of local order in condensed phases of silicon," *Phys. Rev. B*, vol. 31, pp. 5262-5271, 1985.

[85] H. Balamane, T. Halicioglu, and W. A. Tiller, "Comparative study of silicon empirical interatomic potentials," *Phys. Rev. B*, vol. 46, pp. 2250-2279, 1992.

[86] R. Holenstein, S. E. Kirkwood, R. Fedosejevs, and Y. Y. Tsui, "Simulation of femtosecond laser ablation of silicon," *Proc. SPIE*, vol. 5579, pp. 688-695, 2004.

[87] R. Holenstein, "Molecular Dynamics Simulation of Silicon", M.Sc. Thesis, Department of Electrical and Computer Engineering, University of Alberta, Edmonton, AB, Canada, 2004

[88] D. E. Aspnes and A. A. Studna, "Dielectric functions and optical parameters of Si, Ge, GaP, GaAs, GaSb, InP, InAs, and InSb from 1.5 to 6.0 eV," *Phys. Rev. B*, vol. 27, pp. 985-1009, 1983.

[89] P. Lorazo, L. J. Lewis, and M. Meunier, "Short-pulse laser ablation of solids: From phase explosion to fragmentation," *Phys. Rev. Lett.*, vol. 91, pp. 225502, 2003.

[90] P. P. Pronko, S. K. Dutta, D. Du, and R. K. Singh, "Thermophysical effects in laser processing of materials with picosecond and femtosecond pulses," *J. Appl. Phys.*, vol. 78, pp. 6233-6241, 1995.

[91] I. M. Azzouz, "Investigation of photoionization processes in ultrashort laser induced damage in optical materials," *J. Phys. B: At. Mol. Opt. Phys.*, vol. 37, pp. 3259-3264, 2004.

[92] K. Yeom, H. Jiang, and J. Singh, "High power laser semiconductor interactions: A Monte Carlo study for silicon," *J. Appl. Phys.*, vol. 81, pp. 1807-1812, 1997.

[93] N. Bloembergen, "Laser-induced electric breakdown in solids," *IEEE J. Quantum Electron.*, vol. QE-10, pp. 375-386, 1974.

[94] A. Kaiser, B. Rethfeld, M. Vicanek, and G. Simon, "Microscopic processes in dielectrics under irradiation by subpicosecond laser pulses," *Phys. Rev. B*, vol. 61, pp. 11437-11450, 2000.

[95] D. Du, X. Liu, G. Korn, J. A. Squier, and G. A. Mourou, "Laser-induced breakdown by impact ionization in SiO_2 with pulse widths from 7 ns to 150 fs," *Appl. Phys. Lett.*, vol. 64, pp. 3071-3073, 1994.

[96] K. K. Thornber, "Applications of scaling to problems in high-field electronic transport," *J. Appl. Phys.*, vol. 52, pp. 279-290, 1981.

[97] B. C. Stuart, M. D. Feit, S. Herman, A. M. Rubenchik, B. W. Shore, and M. D. Perry, "Nanosecond-to-femtosecond laser-induced breakdown in dielectrics," *Phys. Rev. B*, vol. 53, pp. 1749-1761, 1996.

[98] Y. Kamakura, H. Mizuno, M. Yamaji, M. Morifuji, K. Taniguchi, C. Hamaguchi, T. Kunikiyo, and M. Takenaka, "Impact ionization model for full band Monte Carlo simulation," *J. Appl. Phys.*, vol. 75, pp. 3500-3506, 1994.

[99] E. Cartier, M. V. Fischetti, E. A. Eklund, and F. R. McFeely, "Impact ionization in silicon," *Appl. Phys. Lett.*, vol. 62, pp. 3339-3341, 1993.

[100] N. Sano and A. Yoshii, "Impact-ionization model consistent with the band structure of semiconductors," *J. Appl. Phys.*, vol. 77, pp. 2020-2025, 1995.

[101] A. S. Sedra and K. C. Smith, *Microelectronic Circuits*, 4th ed. New York: Oxford University Press, 1998.

[102] P. A. Schumann Jr. and R. P. Phillips, "Comparison of classical approximations to free carrier absorption in semiconductors," *Solid State Electron.*, vol. 10, pp. 943-948, 1967.

[103] Spectra-Physics, Inc., 1335 Terra Bella Ave., Mountain View, CA, USA, 94039

[104] Ocean Optics, Inc., 830 Douglas Ave., Dunedin, FL, USA, 34698

[105] Positive Light, Inc., 101 Cooper Ct., Los Gatos, CA, USA, 95032

[106] Optikon Corporation Ltd., 1099 Guelph St., Kitchener, ON, Canada, N2B 2E4

[107] Spiricon, Inc., 2600 North Main, Logan, Utah, USA, 84341

[108] Gentec Inc. (Electro-Optics Division), 2625 Rue Dalton, Sainte-Foy, QC, Canada, G1P 3S9

[109] EG&G Electro-Optics, 35 Congress Street, Salem, MA, USA, 01970

[110] Hammond Manufacturing (Electronics Group), 475 Cayuga Road #100, Cheektowaga, NY, USA, 14225-1309

[111] Melles Griot, Inc., 2051 Palomar Airport Rd., 200, Carlsbad, CA, USA, 92009

[112] Hamamatsu Corporation, 360 Foothill Rd., Bridgewater, NJ, USA, 08807

[113] CVI Laser, LLC, 200 Dorado Place SE, Albuquerque, NM, USA, 87123

[114] M. T. Taschuk, "Quantification of laser-induced breakdown spectroscopy at low energies", Ph.D. Dissertation, Electrical and Computer Engineering, University of Alberta, Edmonton, 2006

[115] Zygo Corporation, Laurel Brook Rd., Middlefield, CT, USA, 06455-0448

[116] Coherent, Inc., 5100 Patrick Henry Dr., Santa Clara, CA, USA, 95054

[117] Industrial Fiber Optics, 627 South 48th Street, Suite 100, Tempe, AZ, USA, 85281

[118] Newport Corporation, 1791 Deere Avenue, Irvine, CA, USA, 92606

[119] G. P. López, H. A. Biebuyck, and G. M. Whitesides, "Scanning electron microscopy can form images of patterns in self-assembled monolayers," *Langmuir*, vol. 9, pp. 1513-1516, 1993.

[120] Kurt. J. Lesker Company, P.O. Box 10, 1925 Route 51, Clairton, PA, USA, 15025-2700

[121] Erie Scientific Company, 20 Post Road, Portsmouth, NH, USA, 03801

[122] Silicon Valley Microelectronics, Inc., 2985 Kifer Road, Santa Clara, CA, USA, 95051

[123] Silicon, Inc., P.O. Box 190335, Boise, ID, USA, 83719

[124] Brenntag Canada, Inc., 43 Jutland Rd., Toronto, Ont., Canada, M8Z 2G6

[125] Sigma-Aldrich Canada Ltd., 2149 Winston Park Dr., Oakville, ON, Canada, L6H 6J8

[126] FJW Optical Systems Inc., 322 Woodwork Lane, Palatine, IL, USA, 60067-4933

[127] J. R. Scott, L. S. Baker, W. R. Everett, C. L. Wilkins, and I. Fritsch, "Laser desorption Fourier transform mass spectrometry exchange studies in air-oxidized alkanethiol self-assembled monolayers on gold," *Anal. Chem.*, vol. 69, pp. 2636-2639, 1997.

[128] J. R. Taylor, *An Introduction to Error Analysis: The Study of Uncertainties in Physical Measurements*, 2nd ed. Sausalito: University Science Books, 1997.

[129] M. Lenzner, F. Krausz, J. Krüger, and W. Kautek, "Photoablation with sub-10 fs laser pulses," *Appl. Surf. Sci.*, vol. 154-155, pp. 11-16, 2000.

[130] J. F. Young, J. S. Preston, H. M. van Driel, and J. E. Sipe, "Laser-induced periodic surface structure. II. Experiments on Ge, Si, Al, and brass," *Phys. Rev. B*, vol. 27, pp. 1155-1172, 1983.

[131] G. L. Eesley, "Generation of nonequilibrium electron and lattice temperatures in copper by picosecond laser pulses," *Phys. Rev. B*, vol. 33, pp. 2144-2152, 1986.

[132] T. Q. Qiu and C. L. Tien, "Short-pulse laser heating on metals," *Int. J. Heat Mass Transfer* vol. 35, pp. 719-726, 1992.

[133] W. S. Fann, R. Storz, H. W. K. Tom, and J. Bokor, "Direct measurement of nonequilibrium electron-energy distributions in subpicosecond laser-heated gold films," *Phys. Rev. Lett.*, vol. 68, pp. 2834-2837, 1992.

[134] D. S. Ivanov and L. V. Zhigilei, "Combined atomistic-continuum modeling of short-pulse laser melting and disintegration of metal films," *Phys. Rev. B*, vol. 68, pp. 064114, 2003.

[135] V. Van, Private Communication, 2006

[136] R. Fedosejevs, Private Communication, 2006

[137] R. Fedosejevs, R. Ottmann, R. Sigel, G. Kühnle, S. Szatmári, and F. P. Schäfer, "Absorption of subpicosecond ultraviolet laser pulses in high-density plasma," *Appl. Phys. B: Lasers Opt.*, vol. 50, pp. 79-99, 1990.

[138] D. E. Gray, *American Institute of Physics Handbook*, 3rd ed. New York: McGraw-Hill, 1972.

[139] Y. P. Meshcheryakov and N. M. Bulgakova, "Thermoelastic modeling of microbump and nanojet formation on nanosize gold films under femtosecond laser irradiation," *Appl. Phys. A: Mater. Sci. Process.*, vol. 82, pp. 363-368, 2006.

[140] E. Hecht, *Physics: Algebra/Trig*, 3rd ed. Pacific Grove: Brooks/Cole-Thomson Learning, 2003.

[141] L. C. F. Blackman and M. J. S. Dewar, "Promoters for the dropwise condensation of steam. Part IV. Discussion of dropwise condensation and testing of compounds," *J. Chem. Soc.*, pp. 171-176, 1957.

[142] H. O. Finklea, "Electrochemistry of Organized Monolayers of Thiols and Related Molecules on Electrodes," in *Electroanalytical Chemistry: A Series of Advances*, vol. 19, A. J. Bard and I. Rubinstein, Eds. New York: Marcel Dekker, Inc., 1996, pp. 110-335.

[143] C. D. Bain, E. B. Troughton, Y.-T. Tao, J. Evall, G. M. Whitesides, and R. G. Nuzzo, "Formation of monolayer films by spontaneous assembly of organic thiols from solution onto gold," *J. Am. Chem. Soc.*, vol. 111, pp. 321-335, 1989.

[144] L. H. Dubois, B. R. Zegarski, and R. G. Nuzzo, "Fundamental studies of the interactions of adsorbates on organic surfaces," *Proc. Natl. Acad. Sci.*, vol. 84, pp. 4739-4742, 1987.

[145] F. Schreiber, "Structure and growth of self-assembled monolayers," *Prog. Surf. Sci.*, vol. 65, pp. 151-256, 2000.

[146] A. Ulman, J. E. Eilers, and N. Tillman, "Packing and molecular orientation of alkanethiol monolayers on gold surfaces," *Langmuir*, vol. 5, pp. 1147-1152, 1989.

[147] A. Ulman, "Formation and structure of self-assembled monolayers," *Chem. Rev.*, vol. 96, pp. 1533-1554, 1996.

[148] G. E. Poirier, "Characterization of organosulfur molecular monolayers on Au(111) using scanning tunneling microscopy," *Chem. Rev.*, vol. 97, pp. 1117-1127, 1997.

[149] R. K. Smith, P. A. Lewis, and P. S. Weiss, "Patterning of self-assembled monolayers," *Prog. Surf. Sci.*, vol. 75, pp. 1-68, 2004.

[150] R. Vaidya, L. M. Tender, G. Bradley, M. J. O'Brien II, M. Cone, and G. P. López, "Computer-controlled laser ablation: A convenient and versatile tool for micropatterning biofunctional synthetic surfaces for applications in biosensing and tissue engineering," *Biotechnol. Prog.*, vol. 14, pp. 371-377, 1998.

[151] G. B. Sigal, C. Bamdad, A. Barberis, J. Strominger, and G. M. Whitesides, "A self-assembled monolayer for the binding and study of histidine-tagged proteins by surface plasmon resonance," *Anal. Chem.*, vol. 68, pp. 490-497, 1996.

[152] M. Mrksich and G. M. Whitesides, "Using self-assembled monolayers to understand the interactions of man-made surfaces with proteins and cells," *Annu. Rev. Biophys. Biomol. Struct.*, vol. 25, pp. 55-78, 1996.

[153] C. D. Bain, J. Evall, and G. M. Whitesides, "Formation of monolayers by the coadsorption of thiols on gold: Variation in the head group, tail group, and solvent," *J. Am. Chem. Soc.*, vol. 111, pp. 7155-7164, 1989.

[154] C. D. Bain and G. M. Whitesides, "Formation of monolayers by the coadsorption of thiols on gold: Variation in the length of the alkyl chain," *J. Am. Chem. Soc.*, vol. 111, pp. 7164-7175, 1989.

[155] G. E. Poirier and M. J. Tarlov, "The c(4×2) superlattice of n-alkanethiol monolayers self-assembled on Au(111)," *Langmuir*, vol. 10, pp. 2853-2856, 1994.

[156] G. E. Poirier, "Mechanisms of formation of Au vacancy islands on alkanethiol monolayers on Au(111)," *Langmuir*, vol. 13, pp. 2019-2026, 1997.

[157] G. E. Poirier, T. M. Herne, C. C. Miller, and M. J. Tarlov, "Molecular-scale characterization of the reaction of ozone with decanethiol monolayers on Au(111)," *J. Am. Chem. Soc.*, vol. 121, pp. 9703-9711, 1999.

[158] K. A. Peterlinz and R. Georgiadis, "In situ kinetics of self-assembly by surface plasmon resonance spectroscopy," *Langmuir*, vol. 12, pp. 4731-4740, 1996.

[159] D. S. Karpovich and G. J. Blanchard, "Direct measurement of the adsorption kinetics of alkanethiolate self-assembled monolayers on a microcrystalline gold surface," *Langmuir*, vol. 10, pp. 3315-3322, 1994.

[160] M.-T. Lee, C.-C. Hsueh, M. S. Freund, and G. S. Ferguson, "Air oxidation of self-assembled monolayers on polycrystalline gold: The role of the gold substrate," *Langmuir*, vol. 14, pp. 6419-6423, 1998.

[161] E. Cooper and G. J. Leggett, "Static secondary ion mass spectrometry studies of self-assembled monolayers: Influence of adsorbate chain length and terminal functional group on rates of photooxidation of alkanethiols on gold," *Langmuir*, vol. 14, pp. 4795-4801, 1998.

[162] M. H. Schoenfisch and J. E. Pemberton, "Air stability of alkanethiol self-assembled monolayers on silver and gold surfaces," *J. Am. Chem. Soc.*, vol. 120, pp. 4502-4513, 1998.

[163] J. B. Schlenoff, M. Li, and H. Ly, "Stability and self-exchange in alkanethiol monolayers," *J. Am. Chem. Soc.*, vol. 117, pp. 12528-12536, 1995.

[164] G. Yang, N. A. Amro, Z. B. Starkewolfe, and G.-y. Liu, "Molecular-level approach to inhibit degradations of alkanethiol self-assembled monolayers in aqueous media," *Langmuir*, vol. 20, pp. 3995-4003, 2004.

[165] M. J. Tarlov and J. G. Newman, "Static secondary ion mass spectrometry of self-assembled alkanethiol monolayers on gold," *Langmuir*, vol. 8, pp. 1398-1405, 1992.

[166] J.-M. Kim, C.-W. Baek, J.-H. Park, D.-S. Shin, Y.-S. Lee, and Y.-K. Kim, "Continuous anti-stiction coatings using self-assembled monolayers for gold microstructures," *J. Micromech. Microeng.*, vol. 12, pp. 688-695, 2002.

[167] J. Huang and J. C. Hemminger, "Photooxidation of thiols in self-assembled monolayers on gold," *J. Am. Chem. Soc.*, vol. 115, pp. 3342-3343, 1993.

[168] S. Sun, K. S. L. Chong, and G. J. Leggett, "Nanoscale molecular patterns fabricated by using scanning near-field optical lithography," *J. Am. Chem. Soc.*, vol. 124, pp. 2414-2415, 2002.

[169] M. L. Burgener and R. E. Reedy, "Temperature distributions produced in a two-layer structure by a scanning cw laser or electron beam," *J. Appl. Phys.*, vol. 53, pp. 4357-4363, 1982.

[170] F. Ferrieu and G. Auvert, "Temperature evolutions in silicon induced by a scanning cw laser, pulsed laser, or electron beam," *J. Appl. Phys.*, vol. 54, pp. 2646-2649, 1983.

[171] M. Lax, "Temperature rise induced by a laser beam II. The nonlinear case," *Appl. Phys. Lett.*, vol. 33, pp. 786-788, 1978.

[172] J. E. Moody and R. H. Hendel, "Temperature profiles induced by a scanning cw laser beam," *J. Appl. Phys.*, vol. 53, pp. 4364-4371, 1982.

[173] R. G. Nuzzo, F. A. Fusco, and D. L. Allara, "Spontaneously organized molecular assemblies. 3. Preparation and properties of solution adsorbed monolayers of organic disulfides on gold surfaces," *J. Am. Chem. Soc.*, vol. 109, pp. 2358-2368, 1987.

[174] M. Venkataramanan and T. Pradeep, "A method to study the phase transition and desorption of self-assembled monolayers on planar gold surfaces," *Anal. Chem.*, vol. 72, pp. 5852-5856, 2000.

[175] M. R. Shadnam, A. Luu, S. E. Kirkwood, R. Fedosejevs, and A. Amirfazli, "Mechanism for femtosecond laser pulse patterning of self-assembled monolayers," presented at The 230th American Chemical Society National Meeting, Washington, DC, 2005.

[176] Y. Li, J. Huang, R. T. McIver Jr., and J. C. Hemminger, "Characterization of thiol self-assembled films by laser desorption Fourier transform mass spectrometry," *J. Am. Chem. Soc.*, vol. 114, pp. 2428-2432, 1992.

[177] N. J. Brewer, R. E. Rawsterne, S. Kothari, and G. J. Leggett, "Oxidation of self-assembled monolayers by UV light with a wavelength of 254 nm," *J. Am. Chem. Soc.*, vol. 123, pp. 4089-4090, 2001.

[178] A. B. Horn, D. A. Russell, L. J. Shorthouse, and T. R. E. Simpson, "Ageing of alkanethiol self-assembled monolayers," *J. Am. Chem. Soc., Faraday Trans.*, vol. 92, pp. 4759-4762, 1996.

[179] R. B. Hall, "Pulsed-laser-induced desorption studies of the kinetics of surface reactions," *J. Phys. Chem.*, vol. 91, pp. 1007-1015, 1987.

[180] J. Bass and K. H. Fischer, *Landolt-Börnstein Numerical Data and Functional Relationships in Science and Technology*, vol. 15. Berlin-Heidelberg: Springer-Verlag, 1982.

[181] O. Andrusyak, M. Bubelnik, J. Mares, T. McGovern, and C. W. Siders, "Single-pulse and burst-mode ablation of gold films measured by quartz crystal microbalance," *Proc. SPIE*, vol. 5647, pp. 61-71, 2004.

[182] W. Chang, M. Choi, J. Kim, S. Cho, and K. Whang, "Sub-micron scale patterning using femtosecond laser and self-assembled monolayers interaction," *Appl. Surf. Sci.*, vol. 240, pp. 296-304, 2005.

[183] K. Takehara, S. Yamada, and Y. Ide, "Use of the laser-desorption technique for the preparation of a mixed-thiol monolayer on a gold electrode," *J. Electroanal. Chem.*, vol. 333, pp. 339-344, 1992.

[184] A. K. Walton and P. L. Reimann, "Conduction band effective mass in N-type silicon," *J. Phys. C: Solid State Phys.*, vol. 3, pp. 1410-1416, 1970.

[185] M. E. Green, "Intrinsic concentration, effective densities of states, and effective mass in silicon," *J. Appl. Phys.*, vol. 67, pp. 2944-2954, 1990.

[186] L.-A. Lompré, J. M. Liu, H. Kurz, and N. Bloembergen, "Optical heating of electron-hole plasma in silicon by picosecond pulses," *Appl. Phys. Lett.*, vol. 44, pp. 3-5, 1984.

[187] E. O. Kane, "Band structure of silicon from an adjusted Heine-Abarenkov calculation," *Phys. Rev.*, vol. 146, pp. 558-567, 1966.

[188] J. F. Reintjes and J. C. McGroddy, "Indirect two-photon transitions in Si at 1.06 μm," *Phys. Rev. Lett.*, vol. 30, pp. 901-903, 1973.

[189] T. F. Boggess Jr., K. M. Bohnert, K. Mansour, S. C. Moss, I. W. Boyd, and A. L. Smirl, "Simultaneous measurement of the two-photon coefficient and the free-carrier cross section above the bandgap of crystalline silicon," *IEEE J. Quantum Electron.*, vol. 22, pp. 360-368, 1986.

[190] J. Isenberg and W. Warta, "Free carrier absorption in heavily doped silicon layers," *Appl. Phys. Lett.*, vol. 84, pp. 2265-2267, 2004.

[191] D. Hulin, M. Combescot, J. Bok, A. Migus, J. Y. Vinet, and A. Antonetti, "Energy transfer during silicon irradiation by femtosecond laser pulse," *Phys. Rev. Lett.*, vol. 52, pp. 1998-2001, 1984.

[192] M. Born and E. Wolf, *Principles of Optics*, 7th ed. Cambridge: Cambridge University Press, 1999.

[193] Y. Hirayama and M. Obara, "Heat effects of metals ablated with femtosecond laser pulses," *Appl. Surf. Sci.*, vol. 197-198, pp. 741-745, 2002.

[194] M. T. Taschuk, S. E. Kirkwood, Y. Y. Tsui, and R. Fedosejevs, "Quantitative emission from femtosecond microplasmas for laser-induced breakdown spectroscopy," *J. Phys. Conf. Ser.*, (Accepted January 31, 2006).

[195] D. S. Ivanov and L. V. Zhigilei, "Effect of pressure relaxation on the mechanisms of short-pulse laser melting," *Phys. Rev. Lett.*, vol. 91, pp. 105701, 2003.

[196] S. S. Manson, "Fatigue: A complex subject-some simple approximations," *Exp. Mech.*, vol. 5, pp. 193-226, 1965.

[197] P. Lukás, M. Klesnil, and J. Polák, "High cycle fatigue life of metals," *Mater. Sci. Eng.*, vol. 15, pp. 239-245, 1974.

[198] X. Peng, J. Fan, Y. Yang, Y. Chen, and Y. Yin, "Investigations to the effect of heating-rate on the mechanical properties of aluminum alloy LY12," *Int. J. Struct.*, vol. 40, pp. 7385-7397, 2003.

[199] Maxtek Inc., 5980 Lakeshore Dr., Cypress, CA, USA, 90630-3371

[200] P. J. Cumpson and M. P. Seah, "The quartz crystal microbalance: radial/polar dependence of mass sensitivity both on and off electrodes," *Meas. Sci. Technol.*, vol. 1, pp. 544-555, 1990.

[201] J. E. Marsden, *Introduction to Partial Differential Equations*. New York: Springer, 1998.

[202] M. R. Spiegal and J. Liu, *Schaum's Mathematical Handbook of Formulas and Tables*, 2nd ed. New York: McGraw-Hill, 1999.

[203] J. T. Verdeyen, *Laser Electronics*, 2nd ed. Englewood Cliffs: Prentice-Hall, 1989.

A. Discretization of the TTM

A.1 Formula development

The most commonly used TTM in the literature was the PTS-TTM with a spatially-independent thermal conductivity as given in equation (2.8). The TTM to be discretized is:

$$\begin{aligned} C_e \frac{\partial T_e}{\partial t} &= \kappa_0 \frac{T_e}{T_L} \frac{\partial^2 T_e}{\partial z^2} - g(T_e - T_L) + S(z,t) \\ C_L \frac{\partial T_L}{\partial t} &= g(T_e - T_L) \end{aligned} \tag{A.1}$$

The discretization of the PTS-TTM in equation (2.4) with a constant thermal conductivity proceeds by replacing all the derivatives with their respective discrete equations (4.7) and (4.8) to get:

$$\begin{aligned} \gamma T_i^n \frac{T_i^{n+1} - T_i^n}{\Delta t} &= \frac{\kappa_0 T_i^n}{U_i^n} \frac{T_{i+1}^n - 2T_i^n + T_{i-1}^n}{\Delta z^2} - g\left(T_i^n - U_i^n\right) + S_i^n \\ C_L \frac{U_i^{n+1} - U_i^n}{\Delta t} &= g\left(T_i^n - U_i^n\right) \end{aligned} \tag{A.2}$$

Rewriting into the explicit time-marching format gives:

$$\begin{aligned} T_i^{n+1} &= T_i^n + \frac{\kappa_0 \Delta t}{\gamma U_i^n \Delta z^2}\left(T_{i+1}^n - 2T_i^n + T_{i-1}^n\right) - \frac{g\Delta t}{\gamma}\left(1 - \frac{U_i^n}{T_i^n}\right) + \frac{\Delta t}{\gamma T_i^n} S_i^n \\ U_i^{n+1} &= U_i^n + \frac{g\Delta t}{C_L}\left(T_i^n - U_i^n\right) \end{aligned} \tag{A.3}$$

where all constants and variables have been introduced previously except for T_i^n which is the current time value of the electron temperature at node i and U_i^n, which is the current time value of the lattice temperature at node i.

The above version of the TTM is not completely correct since the thermal conductivity is dependent on temperature and is therefore more appropriately written as:

$$C_e \frac{\partial T_e}{\partial t} = \frac{\partial}{\partial z}\left(\kappa(T_e, T_L)\frac{\partial T_e}{\partial z}\right) - g(T_e - T_L) + S(z,t)$$
$$C_L \frac{\partial T_L}{\partial t} = g(T_e - T_L) \tag{A.4}$$

To discretize the thermal conductivity, in the form of $[a(u)u_x]_x$, we use the following scheme [201]:

$$[a(u)u_x]_x = \frac{\partial}{\partial x}\left(a(u)\frac{\partial u}{\partial x}\right) = \frac{a^n_{i+\frac{1}{2}}\left(u^n_{i+1} - u^n_i\right) - a^n_{i-\frac{1}{2}}\left(u^n_i - u^n_{i-1}\right)}{\Delta x^2} \tag{A.5}$$

where:

$$a^n_{i+\frac{1}{2}} = \frac{1}{2}\left(a^n_{i+1} + a^n_i\right) \tag{A.6}$$

The discrete form of the electron temperature in equation (A.4) is given below since the discrete equation for the lattice temperature in equation (A.3) is still valid:

$$T_i^{n+1} = T_i^n + \frac{1}{2}\frac{\kappa_0 \Delta t}{\gamma T_i^n \Delta z^2}\left(\frac{T^n_{i+1} + T^n_i}{U^n_{i+1} + U^n_i}\right)\left(T^n_{i+1} - T^n_i\right) - \frac{1}{2}\frac{\kappa_0 \Delta t}{\gamma T_i^n \Delta z^2}\left(\frac{T^n_i + T^n_{i-1}}{U^n_i + U^n_{i-1}}\right)\left(T^n_i - T^n_{i-1}\right)$$
$$- \frac{g\Delta t}{\gamma}\left(1 - \frac{U^n_i}{T^n_i}\right) + \frac{\Delta t}{\gamma T^n_i} S^n_i \tag{A.7}$$

For the plasma electron thermal conductivity in equation (2.9), the discretization of the electron temperature equation is similar to that shown above except for the functional form using equations (A.5) and (A.6).

To discretize the laser source, I examined the three laser pulse widths of interest for modeling in the TTM. The Top Hat, constant intensity over the pulse width, is used for simple calculations, though not available experimentally, and the Gaussian pulse and the sech^2 pulse shapes are experimentally available pulse shapes. The source term in the TTM is;

$$S(z,t) = \frac{dI(z,t)}{dz} = \alpha(1-R)I(t)e^{-\alpha z} \quad [\text{W/m}^3] \tag{A.8}$$

where R is the reflectivity and α is the absorption depth (m^{-1}). The intensity distribution can be generalized as:

$$I(x,y,t) = I_{pk} f(x,y)g(t) \quad [\text{W/m}^2] \tag{A.9}$$

where $f(x,y)$ and $g(t)$ are normalized functions giving the shape of the intensity distribution in time and space. We know that:

$$\iiint I(x,y,t)dxdydt = E_{pulse} \quad [\text{J}] \tag{A.10}$$

where E_{pulse} is the pulse energy. By integrating the functions f and g for real pulse shapes, we can extract cofactors that describe the peak intensity of each source in terms of the pulse energy, a measurable quantity in the laboratory. Starting with the spatial term:

$$\beta_1 \iint_A f(x,y)dxdy = 1$$

$$\beta_1 \iint_A \exp\left(-2\frac{(x^2+y^2)}{w_0^2}\right)dxdy = 1$$

$$\beta_1 \int_{-\infty}^{\infty} \exp\left(-2\frac{x^2}{w_0^2}\right)dx \int_{-\infty}^{\infty} \exp\left(-2\frac{y^2}{w_0^2}\right)dy = 1$$

$$\beta_1 \left[2\int_0^{\infty} \exp\left(-2\frac{x^2}{w_0^2}\right)dx\right]^2 = 1 \qquad \text{(A.11)}$$

$$\beta_1 \left[\sqrt{\frac{\pi w_0^2}{2}}\right]^2 = 1$$

$$\therefore \beta_1 = \frac{2}{\pi w_0^2}$$

The integral of the exponential from 0 to infinity was solved using a table of integrals [202]. For the three temporal profiles, we have:

a) Top Hat in time

$$\beta_2 \int_0^{\tau} g_{TH}(t)dt = 1$$

$$\beta_2 t\Big|_0^{\tau} = 1 \qquad \text{(A.12)}$$

$$\therefore \beta_2 = \frac{1}{\tau}$$

b) Gaussian in time

All the pulse widths were described by their FWHM so they can be readily compared to the experimental parameters. For a Gaussian pulse, the relationship between the FWHM, τ, and the characteristic pulse width σ is:

$$g_G(t) = \exp\left(-\frac{t^2}{\sigma^2}\right)$$

$$\ln\left(\frac{1}{2}\right) = -\frac{\tau^2}{\sigma^2} \qquad \text{(A.13)}$$

$$\sigma = \frac{\tau}{2\sqrt{\ln(2)}}$$

Rewriting the Gaussian distribution for the FWHM:

$$\beta_2 \int_{-\infty}^{\infty} g_G(t)dt = 1$$

$$\beta_2 \int_{-\infty}^{\infty} \exp\left(-4\ln 2\frac{t^2}{\tau^2}\right)dt = 1$$

$$2\beta_2 \int_{0}^{\infty} \exp\left(-at^2\right)dt = 1; \qquad a = \frac{4\ln 2}{\tau^2} \qquad \text{(A.14)}$$

$$\frac{2\beta_2}{2}\sqrt{\frac{\pi}{a}} = 1$$

$$\therefore \beta_2 = \frac{1}{\tau}\sqrt{\frac{4\ln 2}{\pi}}$$

c) Hyperbolic secant squared

Applying the same technique as for the Gaussian distribution, the relationship between the FWHM, τ, and the characteristic pulse width σ is:

$$g_S(t) = \operatorname{sech}^2(t/\sigma)$$

$$\operatorname{sech}^{-1}\left(\frac{1}{\sqrt{2}}\right) = \frac{t_{HWHM}}{\sigma}$$

$$\cosh^{-1}\left(\sqrt{2}\right) = \frac{t_{HWHM}}{\sigma} \qquad \text{(A.15)}$$

$$\sigma \ln\left(\sqrt{2} + \sqrt{\sqrt{2}^2 - 1}\right) = \frac{\tau}{2}$$

$$\sigma = \frac{\tau}{2\ln\left(1+\sqrt{2}\right)}$$

Rewriting the pulse shape in terms of the FWHM and integrating:

$$\beta_2 \int_{-\infty}^{\infty} \operatorname{sech}^2\left(\frac{2\ln\left(1+\sqrt{2}\right)t}{\tau}\right) dt = 1$$

$$2\beta_2 \int_{0}^{\infty} \left(\operatorname{sech}(at)\right)^2 dt = 1; \qquad a = \frac{2\ln\left(1+\sqrt{2}\right)}{\tau}$$

$$2\beta_2 \int_{0}^{\infty} \frac{dt}{\cosh^2(at)} = 1 \tag{A.16}$$

$$\frac{2\beta_2}{a} = 1$$

$$\therefore \beta_2 = \frac{1}{\tau}\ln\left(1+\sqrt{2}\right)$$

To determine the peak intensity of the pulse for the TTM, you simply write:

$$I_{pk} = E_{pulse}\beta_1\beta_2 = \phi_{pk}\beta_2 \ \ [\mathrm{W/m^2}] \tag{A.17}$$

with the temporal distribution given by $g(t)$ that matches the β_2 for the particular pulse shape.

The stability analysis was applied to discrete equation for the electron temperature in equation (A.3) by setting the discrete lattice variable U_i^n to T_0 by assuming U_i^n will not change appreciably with rapidly changing T_i^n. The electron-phonon coupling coefficient term (second term on the right of equation (2.4)) was ignored since the time for the lattice to respond to the change in T_i^n is longer than the time for the peak T_i^n to be reached (point of maximum change). The source term was ignored and the electron temperature variable was replaced in equation (A.3) with:

$$\varepsilon^n = \alpha^n \exp\left(j\beta_k z\right) \tag{A.18}$$

and the new equation was simplified to get an expression for $\alpha \leq 1$, which yielded:

$$\Delta t \leq \frac{1}{2}\Delta z^2 \frac{\gamma T_0}{\kappa_0} \tag{A.19}$$

This stability criterion was sufficient for all three forms of the thermal conductivity in this thesis.

A.2 Procedure for running the TTM

The numerical method was written in MATLAB and the main algorithm is given below:

1. The simulation parameters were entered for the TTM. The basic parameters entered were substrate type (ex: Cu, Au), simulation length (L), peak fluence (ϕ_{pk}), pulse shape (Gaussian, Top hat, Hyperbolic secant squared), total simulation time (t_T) and stability fidelity (A). The stability fidelity was a means of testing the stability of the simulation with $A/2$ replacing the ½ in equation (A.19).
2. The simulation subdivided the simulation into M cells resulting in a spacing $\Delta z = L/M$ and the time spacing Δt was calculated using the stability requirement in equation (A.19).
3. The surface boundary layer, $i = 0$, was initialized to T_0 for both the electron and lattice temperature systems at time $n = 0$.
4. The pulse shape was calculated for all time and space nodes with an offset so that the peak of the pulse occurs about five or six e-foldings in time after $n = 0$.

The time steps were iterated with three separate calculations occurring. The surface layer $i = 0$ was calculated, then a matrix calculation on nodes $i = 1$ to $i = M - 1$, followed by the calculation of the rear boundary layer at $i = M$.

A.3 TTM filenames

The following MATLAB scripts are required for running the TTM on a basic installation of MATLAB (no toolboxes required).

TTM_yymmdd.m

The parameters for the simulation are entered in this file. It calls the rest of the scripts. By changing the material name using the full chemical name (Copper instead of Cu) and the wavelength, the optical properties for that wavelength is retrieved from TTM_Material_Parameters.m. This script allows you to select between the *PTS* and *HTS* forms of the TTM, and whether the thermal conductivity is *constant*, equation (A.3), *variable*, equation (A.7), or *plasma*, using equations (A.5) and (A.6) to discretize equation (2.9). The pulse shape is chosen as *TopHat*, *Gauss* or *sech2* and the absorption is *normal* or *ballistic*. The peak fluence, ϕ_{pk}, defined in equation (A.17) and the FWHM pulse width as shown above. The user also selects the *g*-parameter, the full temporal and spatial extent and the spatial divisions.

TTM_Material_Parameters.m

Using data collected from [22, 23, 25, 192], this script loads the material file (Cu.mat, for example) and provides the photon energy, the Sommerfeld parameter, the thermal conductivity coefficient, the lattice heat capacity, the reflectivity, the skin depth, the ballistic absorption depth, the melting temperature, the Fermi temperature and the plasma electron thermal conductivity parameters, if the user did not override them in the TTM_yymmdd.m file.

Cu.mat

This file contains the n and k values for the complex index of refraction, defined as $n + jk$, and the reflectivity for the material [23]. The user creates this file by extracting the data from the source and making a 4-column vector that is photon energy (eV), n, k and R. Files for copper, gold and tungsten exist at this time.

TTM_v2_0.m

This script defines Δz from the total spatial extent and the mesh divisions and calculates Δt from equation (A.19). All nodal positions are created for space and time and the memory for the matrices is allocated for the temporal evolution of the temperature of the surface and rear boundary over time for the electrons and the lattice,

the peak temperature excursion through the material for the electrons and the lattice and the laser pulse width for an entire time sweep. This speeds up the calculations and exploits the matrix mathematics engine of MATLAB. The script named TTM_Finite_Difference_v2_0.m is called and after completion, all the data is saved to files with the parameters as descriptors.

TTM_Finite_Difference_v2_0.m

This script is the discrete TTM for four cases: PTS with constant thermal conductivity, PTS with variable thermal conductivity, PTS with the plasma conductivity and the HTS, which by default has a variable thermal conductivity.

TTM_PDF_Page_Plot_v2_0.m

This script makes a pretty plot of the data for the user's archives.

B. Derivation of the Gaussian Beam Limiting Technique

In this appendix, the GBLT is derived that determines the threshold for material removal by a femtosecond laser pulse by measuring the diameter of each of the ablation spots. Starting from the electric field distribution of a Gaussian beam spatial profile:

$$E(r,z) = E_{pk}\frac{w_0}{w(z)}\exp\left(-\frac{r^2}{w^2(z)}\right)\exp\left(-j\left(kz-\phi(z)-\frac{kr^2}{2R(z)}\right)\right) \text{ (V/m)} \qquad \text{(B.1)}$$

where E_{pk} is the electric field amplitude, r is the radial spatial component and z is the direction along the optical axis. The minimum 1 e-folding electric field beam waist is given by w_0 and its change as the beam propagates away from the minimum beam waist along z is $w(z)$. Other parameters for the electric field distribution are the Guoy phase shift at focus, $\phi(z)$, the phase front curvature, $R(z)$, and the propagation wave vector, k.

This equation becomes the time averaged plane wave intensity field distribution in a medium with impedance η as (p.70 in ref. [203]):

$$I(r,z) = \frac{E(r,z)E^*(r,z)}{2\eta} = \frac{E_{pk}^2}{2\eta}\frac{w_0^2}{w^2(z)}\exp\left(-2\frac{r^2}{w^2(z)}\right) \text{ (W/m}^2\text{)} \qquad \text{(B.2)}$$

Since experiments are made at some point z_1 along the optical axis, we can group the constants into a peak intensity component I_{pk} at z_1 and rewrite equation (B.2) as:

$$I(r,z_1) = I_{pk}(z_1)\exp\left(-2\frac{r^2}{w_1^2}\right) \qquad \text{(B.3)}$$

GBLT experiments are done at the focal spot and the amount of energy that is incident on the sample per unit area is calculated by multiplying the intensity in equation (B.3) by the pulse width τ_p and writing the beam waist at the focal spot as w_0 (now the 2 e-folding intensity beam waist), we get:

$$\phi(r) = \phi_{pk} \exp\left(-2\frac{r^2}{w_0^2}\right) \tag{B.4}$$

By measuring the damage spot diameter and defining this radius as the ablation threshold, ϕ_{th}, equation (B.4) is rewritten as:

$$\phi_{th} = \phi_{pk} \exp\left(-2\frac{\left(D/2\right)^2}{w_0^2}\right) \tag{B.5}$$

Solving for D yields:

$$\begin{aligned} \ln\left(\frac{\phi_{th}}{\phi_{pk}}\right) &= -\frac{D^2}{2w_0^2} \\ D^2 &= 2w_0^2 \ln\left(\frac{\phi_{pk}}{\phi_{th}}\right) \end{aligned} \tag{B.6}$$

Equation (B.6) still has two unknowns and one of the unknowns is determined through independent measurement of pulse energy. The peak fluence from the energy measured in a Gaussian spatial profile pulse is derived as:

$$\begin{aligned} E_{pulse} &= \iint_A \phi(r)\,dA \\ &= \int_0^{\infty}\int_0^{2\pi} \phi_{pk} \exp\left(-\frac{2r^2}{w_0^2}\right) r\,dr\,d\phi \\ &= 2\pi\phi_{pk} \int_0^{\infty} r \exp\left(-\frac{2r^2}{w_0^2}\right) dr \\ &= 2\pi\phi_{pk} \frac{\Gamma(1)}{2} \frac{w_0^2}{2} \\ &= \frac{\pi w_0^2}{2} \phi_{pk} \end{aligned}$$

$$\phi_{pk} = \frac{2E_{pulse}}{\pi w_0^2} \tag{B.7}$$

Substituting equation (B.7) into (B.6) gives an equation used in the methodology for measuring the ablation threshold experimentally from the damage diameters.

$$D^2 = 2w_0^2 \left\{ \ln\left(E_{pulse}\right) - \ln\left(\frac{2}{\pi w_0^2 \phi_{th}}\right) \right\} \tag{B.8}$$

In equation (B.8), a semi-logarithmic plot of the squared damage diameters against the pulse energy yields the 2 e-folding intensity beam waist in the slope of the regression fit. Using this beam waist in equation (B.7), a new semi- logarithmic plot of the squared diameter against the incident fluence gives the ablation threshold at the intersection with the horizontal axis. Instead of making two plots, one can see by substituting for the ablation threshold, ϕ_{th}, by using E_{th} in equation (B.7), gives the energy threshold at the intersection with the horizontal axis:

$$D^2 = 2w_0^2 \left\{ \ln\left(E_{pulse}\right) - \ln\left(E_{th}\right) \right\} \tag{B.9}$$

Using the errors from the diameter analysis, error propagation can be applied to the final ablation threshold value as will be shown in Appendix C.

C. Reporting of the ablation threshold and incubation coefficient

C.1 Error in the beam waist and the threshold energy for ablation

All *independent* errors can be formulated into a error for a formula $y(x_i)$ by the following (p. 75 in ref. [128]):

$$\delta y = \sqrt{\sum_i \left(\frac{\partial y}{\partial x_i}\right)^2 \delta x_i^2} \tag{C.1}$$

where y is the variable of interest, and x_i are the dependent variables in the formula $y(x_i)$, δx_i is the error for the variable x when formulated as $x = (\mu_x \pm \delta x)$, where δx is the one standard deviation error (68.26 %). For the D^2 formula in equation (4.2), the errors in w_0 and E_{pulse} are considered independent since the errors in E_{pulse} arise from the calibration of the photodiode and the w_0 errors arise in user measurement error. The linearized form of equation (4.2) is:

$$D^2 = m \ln\left(E_{pulse}\right) + b \tag{C.2}$$

where m is the slope and b is the intercept ,and a regression to 68.26 % would yield $m = (\mu_m \pm \delta m)$ and $b = (\mu_b \pm \delta b)$. The errors in the beam waist are then:

$$\begin{aligned}
\delta w_0 &= \sqrt{\left(\frac{\partial w_0}{\partial m}\right)^2 \delta m^2} \\
&= \sqrt{\left[\frac{1}{2}\left(\frac{m}{2}\right)^{-\frac{1}{2}}\right]^2 \delta m^2} \\
&= \frac{1}{4}\left(\frac{2}{m}\right)^{\frac{1}{2}} \delta m \\
&= \frac{1}{2} w_0 \left|\frac{\delta m}{m}\right|
\end{aligned} \tag{C.3}$$

As a check we see that the form of this error is similar to $|n|\,|q|\,\delta x/|x|$ for $q = x^n$ (p. 66 in ref [128]).

The error in the energy threshold is obtained by first noting that it occurs when D^2 is zero and $E_{th} = \exp(-b/m)$:

$$\begin{aligned}
\delta E_{th} &= \sqrt{\left(\frac{\partial E_{th}}{\partial m}\right)^2 \delta m^2 + \left(\frac{\partial E_{th}}{\partial b}\right)^2 \delta b^2} \\
&= \sqrt{\left\{\exp\left(-\frac{b}{m}\right)\left(-\frac{b}{m^2}\right)\right\}^2 \delta m^2 + \left\{\exp\left(-\frac{b}{m}\right)\left(-\frac{1}{m}\right)^2\right\}^2 \delta b^2} \\
&= \exp\left(-\frac{b}{m}\right)\sqrt{\left(\frac{\delta m}{m}\right)^2\left(\frac{b}{m}\right)^2 + \left(\frac{\delta b}{m}\right)^2} \\
&= \exp\left(-\frac{b}{m}\right)\sqrt{\left(\frac{\delta m}{m}\right)^2\left(\frac{b}{m}\right)^2 + \left(\frac{\delta b}{b}\right)^2\left(\frac{b}{m}\right)^2} \\
&= \left|\frac{b}{m}\right|\exp\left(-\frac{b}{m}\right)\sqrt{\left(\frac{\delta m}{m}\right)^2 + \left(\frac{\delta b}{b}\right)^2}
\end{aligned} \tag{C.4}$$

The GBLT returns two beam waists to capture the slight ellipticity of the beam waist and therefore has two energy threshold intercepts. To get the final energy threshold, a weighted average of the two energy threshold is reported:

$$E_{th}^{weight} = \frac{\sum_i w_i E_{th}^i}{\sum_i w_i} \tag{C.5}$$

where w_i is the weight for the i^{th} energy threshold, where i represents either the major or minor axis energy threshold and the weight w_i is:

$$w_i = \frac{1}{\left(\delta E_{th}^i\right)^2} \tag{C.6}$$

Once the threshold energy for ablation is known, the threshold fluence is calculated. The ablation threshold fluence is calculated as:

$$\phi_{th} = \frac{2E_{th}}{\pi w_{major} w_{minor}} \tag{C.7}$$

The error in the ablation threshold fluence is calculated from equation (C.1) as:

$$\delta\phi_{th} = \phi_{th}\sqrt{\left(\frac{\delta E_{th}}{E_{th}}\right)^2 + \left(\frac{\delta w_{major}}{w_{major}}\right)^2 + \left(\frac{\delta w_{minor}}{w_{minor}}\right)^2} \tag{C.8}$$

since we continue to assume all the errors are independent from one another.

C.2 Error in the incubation coefficient

The incubation coefficient is evaluated by equation (2.3) and the first step in the error analysis is to linearized it to:

$$\ln(N\phi_{th}(N)) = \ln(\phi_{th}(1)) + \xi \ln(N) \tag{C.9}$$

The incubation coefficient for a sample was evaluated from the single- and multishot ablation thresholds measured during the same experimental run. For several repetitions over different days, the weighted average of the incubation coefficients would be reported and this would be calculated as shown in equations (C.5) and (C.6).

To evaluate the incubation coefficient for a sample, a least-squares fit was made of the collected single- and multishot ablation thresholds as shown in Chapter 8 in ref.[128]. This procedure also returned an uncertainty for the incubation coefficient.

C.3 An example

The following example is a 1, 10, and 100-shot ablation threshold experiment performed on a copper thin film sample.

The calibration of the photodiode, with the voltage measured between the baseline and 100 μs after the voltage peak time, against the Gentec power meter resulted in the calibration data on the left side of Figure C.1. The laser pulse energy was calculated by dividing the measured power by the repetition rate of the laser at 1 kHz.

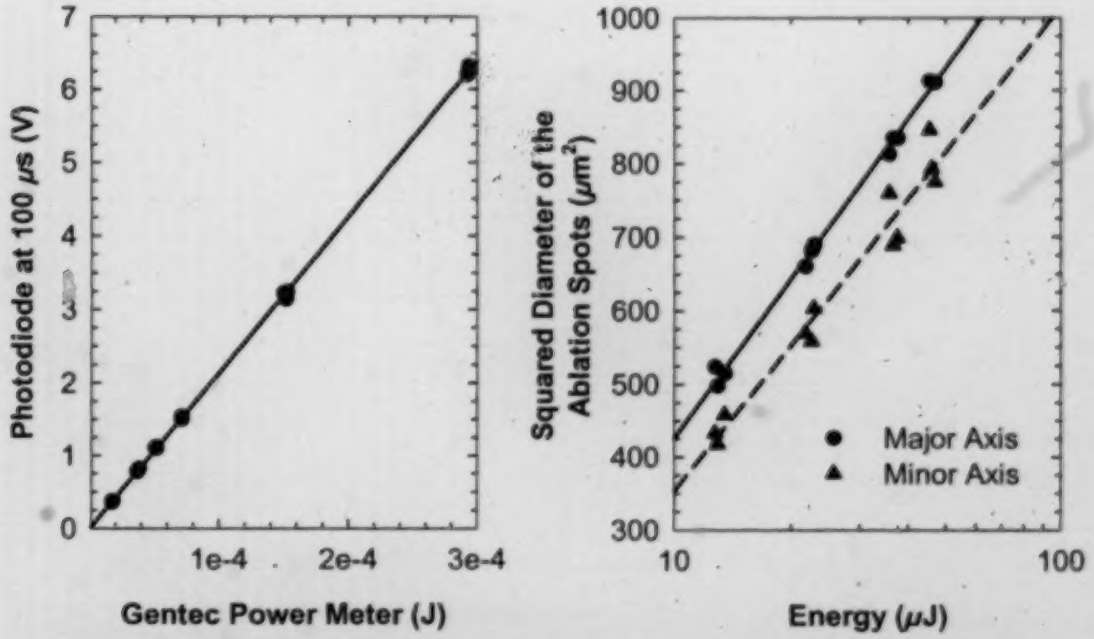

Figure C.1: Example of an energy calibration curve for a photodiode and beam waist measurement for a 100 nm thin copper film sample used in the nanomilling experiments.

The regression line for the energy calibration data returned a slope of 21 327 V/J with an intercept of -2.8×10^{-3} V. The intercept spanned -2.6×10^{-2} V and $+2.0 \times 10^{-2}$ V in a 95 % confidence interval, meaning that the intercept could just as easily have been zero. When the 95 % confidence interval for the intercept spanned the value of zero, the intercept in the regression was ignored (set to zero). If the 95 % confidence interval did not contain span through zero, then the intercept (instrument bias) was used when

calculating the laser pulse energy measured by the photodiode during ablation experiments. Calibrations were never *forced* through zero!

As an indication of the precision of the calibration, the one e-folding error was also calculated for the regression. Careful measurements should, typically return precisions of nearly 1 % (p.29 in [128]) and the above regression had a precision of 0.4 %. The accuracy of the Gentec was listed as 3 % making the overall energy calibration with the photodiode accurate to approximately 3.4 % (treating the errors as additive). This error did not propagate further in the calculations since the regression analysis would need to be multivariate and unnecessarily complex since the major error in the experiments was in the diameter measurements as will be seen in the following discussion.

On the right side of Figure C.1 is the measurement of the D^2 of the major and minor axes of the elliptical ablation spots for single shot ablation on the 100 nm copper thin film substrate. These diameters were measured in the MATLAB script described in Section 3.3.4. A regression analysis was made for each of the axes of the linearized equation shown in equation (C.2). The regression analysis of these axes returned a slope of 314.05 μm^2 and an intercept of -297.09 μm^2 for the major axis and a slope of 287.06 μm^2 and an intercept of -307.19 μm^2 for the minor axis.

The regression was instructed to return a confidence interval of 68.26 %, which represents the one e-folding standard deviation of the fit. This error was used as the standard for reporting errors throughout this thesis. The regression fit for the major axis returned a 68.26 % error (σ) for the slope of $\pm 6.4\ \mu m^2$ and $\sigma = \pm 21.4\ \mu m^2$ for the intercept. The regression fit for the minor axis returned $\sigma = \pm 19.4\ \mu m^2$ for the slope and $\sigma = \pm 64.1\ \mu m^2$ for the intercept.

From equation (B.9) and equation (C.2), the slope and intercept needed to be transformed from the linearized form. The slope was transformed by $w_0 = (m/2)^{1/2}$ and the intercept transformed by $E_{th} = \exp(-b/m)$. The errors in these values were calculated as shown in equations (C.3) and (C.4), respectively, where $\delta m/m$ and $\delta b/b$ are the relative errors for the one e-folding errors reported by the regression fit. For example, $\delta m/m$ for the major axis is 21.4/314.05. The resulting values in this example for the energy threshold and the beam waist were: $(2.58 \pm 0.18)\ \mu J$ (a 7 % error) and $(12.5 \pm 0.13)\ \mu m$

(1 %) for the major axis and (2.91 ± 0.68) μJ (23 %) and (12.0 ± 0.4) μm (3 %) for the minor axis.

The weighted average of the energy threshold was calculated as shown in equations (C.5) and (C.6) to get E_{th} = (2.60 ± 0.18) μJ (7 %). The weighted average gives higher precedence to values with smaller error, which is why the final value of the threshold is closer to 2.58 μJ and the error is the same as the smallest error in the two measurements to within two significant digits. This error is also larger than that reported in the energy calibration and it was expected that a multivariate regression analysis would not have yielded a significantly larger error. If the errors reported by the regression analysis of the squared diameters had been less than that of the energy calibration, then a multivariate approach would have been necessary to examine the contributions of all errors more closely.

Using equations (C.7) and (C.8), the ablation threshold fluence for this sample was calculated to be ϕ_{th} = (1100 ± 80) mJ/cm^2, an 8 % error. Repeated experiments with this sample over several different days yielded other results of (841 ± 44) mJ/cm^2 and (858 ± 89) mJ/cm^2. The weighted average of all three experiments was (890 ± 40) mJ/cm^2 as reported in Section 4.3 for the 100 nm thin copper film.

The experiment to determine the single-shot ablation threshold for the 100 nm thin copper film included experiments to determine the multishot ablation thresholds for 10 and 100 shots on the same day. Using the same techniques as described in this section, the 10-shot and 100-shot ablation thresholds were determined to be (494 ± 17) mJ/cm^2 and (338 ± 11) mJ/cm^2.

To calculate the incubation coefficient, a least-squares fit to the three data points and their respective errors yielded 0.78 ± 0.02. Another measurement of the 100 nm thin copper film gave an incubation coefficient of 0.78 ± 0.01. The 83 % reflective 300 nm thin copper film had an incubation coefficient measured as 0.74 ± 0.02 and since this was close to the measured incubation coefficient of the 100 nm film, the incubation coefficients were combined as a weighted average and reported to be 0.77 ± 0.01 as shown in Section 4.3.